INTERFACE STUDIES OF RARE EARTH OXIDES ON SILICON AND GERMANIUM SUBSTRATES

LIU ZHIQIANG

(B. Eng.(Hons.), NUS)

A Thesis Submitted for the Degree of Doctor of Philosophy

Department of Electrical and Computer Engineering

National University of Singapore

2012

Abstract

In recent decades, the high-k/semiconductor interface is gaining much interest due to miniaturization of devices. Rare earth based oxides are promising candidates to succeed hafnium oxide as the second generation high dielectric constant (high-k) dielectrics. The first part of this dissertation investigates the mechanisms behind interface dipole formation which are responsible for appreciable flatband voltage shifts commonly observed in capacitors involving rare earth oxides. Electron affinity and band offsets are measured using photoemission and with the latter being corrected for differential charging using a novel, time-resolved method. A dipole neutrality concept/model is then introduced after careful evaluation of the use of electronegativity in band alignment models. This novel model allows accurate prediction of interface dipoles which will be beneficial for threshold voltage adjustments in advanced gate stack engineering. The second part looks into manipulation of the interface to improve device characteristics. An ultra-thin yttrium interlayer is found to be able to improve interface trap density, leakage current and thermal stability of lanthanum aluminate capacitors on silicon. Furthermore, an interfacial-layer-free growth of yttrium oxide on germanium is demonstrated using a layer-by-layer approach. This is particularly useful in terms of equivalent-oxide-thickness scaling for next-generation devices.

Acknowledgements

First and foremost, I would like to thank my thesis supervisors: A/Prof. Chim Wai Kin for his support and guidance throughout this four years, and for allowing me freedom to purse my area of interest in my Ph.D. studies; Dr. Pan Ji Sheng for granting access (even after office hours) to the XPS equipment and the memorable experience during the Poland conference trip. I am much indebted to my mentor, Dr. Chiam Sing Yang for being an inspirational figure during these four years. The engaging discussions we shared on XPS and band alignment theories have given me useful insights to carry out my research. I am especially grateful for the countless hours you have spent on correcting my reports and manuscripts, and the moral support you have given me as a friend.

Next, I would like to thank Dr. Lap Chan for imparting his knowledge to us and sharing his life experiences. Your teachings will no doubt be useful during my stay in the industry. I would also like to show my appreciation to Dr. Ng Chee Mang and Mr. Leong Kam Chew for organizing the lessons and Wednesday meetings, and Dr. Du Anyan for helping me with TEM characterization. I would like to express my gratitude to the staff in IMRE for graciously accommodating my presence: Dr. Wang Shijie for kindly giving me some GaN and ZnO substrates, Dr. Zhang Zheng, Ms. Doreen Lai Mei Ying, and Dr. Chai Jian Wei for allowing me to use his growth chamber. I am also very grateful to Prof. Choi Wee Kiong, Walter, and Xiao Yun for granting me access to the Microelectronics Laboratory equipment. I am also grateful to have the companionship of Anna, Jinquan, Pi Can, Ren Yi, and Roger in CICFAR

2 lab, and also my friends in GlobalFoundries: Jason, Shuping, Sumarlina, Raymond, Xuanding, Duen Yang, Vanessa, Irvine, and many others. Also, special thanks go out to Wenhu and Shurong for taking the time to help me with the low temperature electrical measurements and TEM preparation in NTU.

I am eternally grateful to my family, especially my mother for treating me with unconditional love and care. Last but not least, I am extremely grateful for all the support and love from my fiancée, Cheryl, who gave me the strength and courage to survive through the trying times. Thank you for always being by my side.

Contents

List of Tables

List of Figures

1. Introduction and Motivation

1.1. MOS scaling: problems and solutions

Silicon (Si) - based microelectronic devices, in particular complementary metal-oxide-semiconductor (CMOS) transistors, have fundamentally revolutionized the technology of mankind without which many inventions such as the internet and computer would not have existed. In the past few decades, the demand for faster and more powerful processors has skyrocketed with the world-wide proliferation of consumer electronic products such as smart phones, and touch screen tablets. This advancement is achieved through the aggressive scaling of transistor feature sizes, i.e. reduction of channel length accompanied with changes in key device dimensions.[1] This scaling leads to device improvements such as higher speed, lower power dissipation and higher packing density.[2] In 1965, Gordon Moore predicted that the number of components on a chip would quadruple every three years.[3] So far, this has dictated the trend of growth in the semiconductor industry. In 1971, the first 4-bit central processing unit (CPU) released by Intel Corporation only had 2,300 transistors.[4] Across a span of 40 years, the transistor count has reached an alarming number of 2 billion and this scaling is showing no signs of stopping.

Sustaining of this aggressive scaling trend however, requires tremendous efforts. Some of the crucial aspects include lithography, control of threshold voltage, geometric design, and source drain engineering, etc. In recent years, the downsizing of the devices has reached atomic scales whereby intrinsic properties of existing materials have become the roadblock for further CMOS scaling. This

has led to the introduction of novel materials such as high mobility substrates, copper interconnects, low dielectric constant inter-metal dielectrics, high dielectric constant (high-k) gate dielectrics, metal gate electrodes, etc. This approach of material engineering promises continued usage of the CMOS technology without major overhauls of device fabrication and designs. This is highly desirable from the manufacturing point of view given the intensive capital invested in the equipment.

Leading the frontier of this miniaturization is the development of high dielectric constant (high-k) materials since the gate oxide is the thinnest feature in a MOSFET device. At the 90-nm technology node, the silicon dioxide (SiO_2) thickness is already being shrunk to a mere 1.2 nm (only about four atomic layers).[5] This presents two fundamental problems which hinders the continual use of SiO_2 as the gate oxide. First, the gate tunneling leakage current becomes unacceptably large, thus affecting the standby power dissipation.[6] This is largely due to a quantum mechanical tunneling effect which states that the tunneling probability is expected to increase exponentially as the oxide thickness decreases (i.e., based on the Wentzel-Kraners-Brillouin (WKB) formulation).[7] Second, the device reliability is greatly compromised. When the gate oxide thickness is too thin, the critical density of defects (at the Si/SiO_2 interface) required to trigger breakdown is reduced significantly, leading to device failure.[8] It is also worthwhile to note that the fundamental physical thickness limit of SiO_2 is 7 Å, below which its full bandgap is not formed.[9]

The metal-oxide-semiconductor structure can be electrically modeled as a parallel plate capacitor shown in Eq. (1.1) as follows:

$$C = (k\varepsilon_0 A)/t_{ox} = (3.9\varepsilon_0 A)/EOT, \quad (1.1)$$

where A is the capacitor area, k is the relative dielectric constant, ε_0 is the permittivity of free space, and t_{ox} is the gate oxide thickness. Since increasing the device area contradicts the general trend in scaling, the only way an equivalent capacitance (to induce sufficient inversion charges) can be achieved with a thicker oxide is to make use of a material with higher dielectric constant (see Eq. (1.1)). In other words, the equivalent oxide thickness (EOT) of the high-k dielectric, which is a hypothetical thickness assuming that the high-k material has a dielectric constant of SiO_2 (3.9), is always smaller than its actual physical thickness (t_{ox}). This ensures that the gate oxide scaling trend can be prolonged.

1.2. Issues pertinent to the choice of high-k dielectrics

A major component of the success behind the CMOS technology lies in the excellent compatibility of SiO_2 with Si. SiO_2 has a large band gap (~ 9 eV), hence large band offsets with Si and also a high breakdown field, of the order of 13 $MVcm^{-1}$.[10] Moreover, SiO_2 possesses good thermal and chemical stability and is able to withstand high temperature annealing steps (up to 1000ºC) in the fabrication of transistors. If grown properly, SiO_2 is also able to form a high quality interface with Si giving rise to a low density of interface defects.

The task of replacing the SiO_2 gate dielectric with high-k dielectrics is not straightforward and requires careful considerations.[11] Apart from having high

dielectric constant, the high-k material must be able to meet a set of other requirements, namely (1) good thermodynamic stability on Si (or Ge), (2) low density of intrinsic defects at the interface and bulk, (3) sufficiently large energy bandgap in order to provide a sufficiently high energy barrier to reduce leakage current, and (4) be compatible with CMOS processing, i.e. able to sustain high thermal budget.

Based on the requirement of being thermodynamically stable on Si, the remaining high-k material candidates belong to either transition or rare earth metal oxides.[12] Unfortunately, these existing high-k dielectrics do not fare as well as the traditional SiO_2 in terms of the above requirements, except for the dielectric constant. This may very well be attributed to the difference in the chemical bonding nature of the oxides.[13] The delocalized *d* electrons involved in high-k oxides result in a more rigid structure that is more prone to structural defects, such as oxygen vacancies or interstitials. These *d* electrons are also the reason behind the smaller bandgap observed in high-k oxides.[14] This is as opposed to the *sp*-type Si-O bonds which are less rigid and give rise to large splitting of anti-bonding and bonding states (larger bandgap).

1.3. Importance of studying the high-k/semiconductor interface

The high-k/semiconductor interface is particularly important for advanced technology nodes due to the various issues highlighted in the schematic shown in Fig. 1.1. These issues are concerning the formation of interface layer, interface trap charges, and interface dipoles which is discussed in more detail in the paragraphs below.

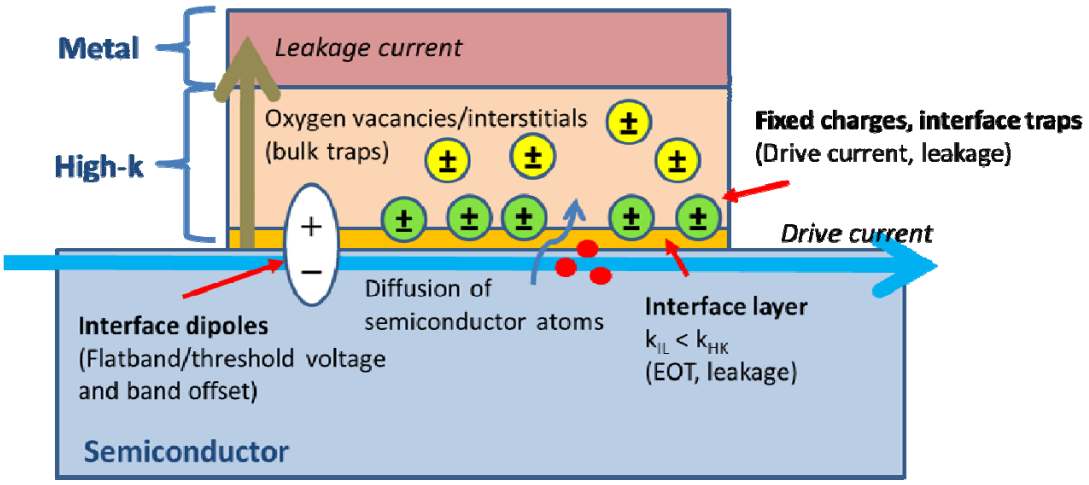

Fig. 1.1: Schematic illustrating the various issues involved at the high-k/semiconductor interface that are crucial to device performance. Note that k_{IL} and k_{HK} represent the dielectric constants for both the interface layer and high-k dielectric respectively.

First and foremost, any formation of an interfacial layer (IL) will play an increasingly dominant role in the overall electrical performance due to the ultra-thin dimension of the gate dielectric as a result of aggressive scaling. One immediate impact is the increase of the equivalent oxide thickness (EOT). This is because IL formation entails the incorporation of underlying semiconductor atoms which will bring the overall dielectric constant down. As such, many have espoused the idea of using a zero interfacial layer (ZIL) structure for future technology nodes to meet the stringent requirement for EOT scaling.[15] This is however not an easy task, as seen from literature, because of thermodynamics and chemical kinetics involved in the deposition process.[16]

Furthermore, crucial electrical parameters such as interface trap density, fixed charge and leakage current are dependent on the quality of the high-k/semiconductor interface. Interface traps degrade the carrier mobility and drive current through Coulomb scattering and electron trapping.[17] Gate stacks

involving high-k oxides with Si usually do not have as low levels of interface trap density (D_{it}) and fixed charges (Q_f) (i.e. 10^{10} and 10^{11} $cm^{-2}eV^{-1}$) as that of SiO_2/Si structure.[18] Moreover, formation of a silicon oxide (SiO_x) interfacial layer, coupled with traps within the high-k dielectric bulk, can lead to leakage current via trap-assisted tunneling mechanisms.[19]

Lastly, charge transfer at the high-k/semiconductor interface affects band alignment through the formation of interface dipoles. This then affects crucial electronic parameters such as the band offset and effective metal work function. These are pertinent to the overall device performance as they control the tunneling leakage current and flatband voltage (and threshold voltage) respectively. Unfortunately, the actual mechanism behind the formation of these interface dipoles is still being extensively debated in the literature. In spite of this, high-k related interface dipoles are already being used to lower the threshold voltage of advanced gate stacks.[20] This is valuable because threshold voltage adjustment is becoming an increasingly difficult task with the miniaturization of devices.

1.4. Organization of thesis

The first three chapters review the background knowledge relevant to this work. Following the present chapter (i.e., chapter 1), chapter 2 reviews the pertinent issues related to the study of the high-k/semiconductor interface, with special emphasis on the existing theories and techniques related to band alignment in the literature. Chapter 3 describes the working principles behind the characterization techniques used in this work, in particular photoemission.

There are four main chapters which discuss on the experimental findings. The first two chapters focus on gaining insights into the oxide/semiconductor band alignment and hence high-k related interface dipoles. Chapter 4 investigates the potential pitfalls involved in band alignment study using photoemission and the necessary measures to correct them. In chapter 5, we re-evaluate the use of electronegativity in the band alignment models for oxide/semiconductor heterojunctions by examining a good range of experimental data. Using a newly established correlation between dielectric work function and electronegativity, we introduce a novel dipole neutrality model that is able to give good predictions for the reported interface dipoles in literature. The next two chapters explore the possibilities of manipulating the high-k oxide/semiconductor interface in order to improve device characteristics. In chapter 6, crucial electrical characteristics (such as interface trap density, fixed charges, and leakage current) after annealing are improved for the lanthanum aluminium oxide/silicon ($LaAlO_3$/Si) capacitors upon insertion of a thin yttrium interlayer. Chapter 7 proposes and investigates a layer-by-layer method to suppress IL formation in the growth of yttrium oxide (Y_2O_3) films on germanium (Ge) substrates to benefit EOT scaling.

Chapter 8 summarizes the findings in this work. A number of possible future directions are then provided as suggestions for future work in the development of rare earth oxide gate dielectrics for Si and Ge MOSFETs.

2. Literature Review

2.1. Basic material properties

Advancement in CMOS technology is based upon the careful selection and integration of novel materials to overcome the physical limitations brought about by the aggressive scaling of devices. This section reviews the fundamental properties of rare earth oxides that make them attractive high dielectric constant (high-k) materials (see section 2.1.1), and motivations and issues involving the use of germanium (Ge) as a high mobility channel material (see section 2.1.2). Hitherto, passivation of the Ge surface remains to be a major obstacle in the implementation of Ge MOSFETs. Section 2.1.3 discusses existing passivation techniques and provides a possible explanation as to why rare earth oxides form good interfaces with Ge.

2.1.1. Rare earth oxides as second generation high-k dielectrics

The criterion of thermodynamic stability on Si limits the choice of high-k dielectrics to transition metal (e.g., Hf and Zr), rare-earth metal (e.g., Y, La and other lanthanides) oxides and some group II oxides (such as SrO, CaO and BaO).[12,21] The group II oxides are not favoured because of their high reactivity with water.[22] Between transition metal oxides and rare earth oxides, the former has already been extensively researched but the latter is only beginning to gain interest in the recent decade.[23,24] Rare earth oxides are regarded as attractive candidates for the second generation oxide to succeed hafnium oxide (HfO_2) due

to more symmetric band offsets with silicon (see Table 2.1), while maintaining comparable or higher dielectric constant.[22,25]

Table 2.1: Summary of the dielectric constant (k), band gap (E_g), conduction (CBO) and valence band offsets (VBO) on Si values for rare earth (RE) oxides and transition metal (TM) oxides. The data marked with asterisks are obtained from this work while the rest of the data are obtained from refs. 22 and 25

		k	E_g (eV)	CBO (eV)	VBO (eV)
	SiO_2	3.9	9.0	3.2	4.7
	Al_2O_3	9.0	8.8	2.8	4.9
RE oxides	$LaAlO_3$	30	6.1	*2.3	*2.7
	La_2O_3	30	6.0	*2.3	*2.6
	Y_2O_3	18	5.7	*2.3	*2.3
	Lu_2O_3	18	5.8	2.3	2.4
	Gd_2O_3	17	5.6	2.2	2.3
TM oxides	HfO_2	20	5.8	*1.7	*3.0
	ZrO_2	25	5.8	1.5	3.2
	TiO_2	80	3.5	0	2.4
	Ta_2O_5	22	4.4	0.35	2.9

Moreover, epitaxial growth of HfO_2 on Si is unlikely, and low-temperature deposition induces defects due to partial amorphocity and residual contamination. Some rare earth oxides on the other hand, have closer lattice mismatch with Si compared to HfO_2 and ZrO_2.[26] This makes them attractive dielectric materials beyond the 45-nm technology node. In addition, rare earth oxides exhibit interesting flatband voltage shifts (see section 2.1.1) that can be manipulated for threshold voltage adjustment. Lastly, rare earth metals tend to possess multiple valency, such as (+2 and +3 oxidation states), which could promote catalytic reactions on semiconductor surfaces, thereby achieving effective passivation of

electrically active defects.[27] This is particularly useful for high mobility substrates such as Ge, where interface passivation remains to be a problem (more details are found in section 2.1.2).

As defined by the International Union of Pure and Applied Chemistry (IUPAC), rare earth metals are a set of seventeen elements in the periodic table, including the lanthanides plus scandium and yttrium.[28] The lanthanide series comprises elements with atomic numbers ranging from 57 to 71. Their oxides are known for their large bandgap, and hence large band offset, which results in low leakage current.[29,30]

Lanthanium (La) is the first element in this series with an electronic configuration of $\{Xe\}5d^16s^2$. Lanthanum oxide, La_2O_3, has a high dielectric constant of ~25. The important physical properties are correlated and follow a distinctive trend across the lanthanide group. Being the lightest element in the group, La_2O_3 has the lowest lattice energy of -12.867 kJ/mol, largest band gap (~5.5 eV) and is the most hygroscopic among the lanthanide group elements. The tendency to absorb moisture poses a major problem in the processing of devices.[31] The formation of its low-density hexagonal hydroxide, $La(OH)_3$, lowers the dielectric constant and degrades the surface roughness of La_2O_3.[32] Fortunately, one can introduce aluminum (Al) into the oxide to increase the resistance to moisture absorption and also to increase the overall bandgap. Furthermore, addition of Al is also expected to increase the crystallization temperature and chemical stability of various high-k materials studied.[33,34,35] This makes lanthanum aluminate ($LaAlO_3$ or LAO) an attractive candidate due to its large bandgap (~5 to 6 eV), high dielectric constant

(~22 to 25), and its stability on Si.[36,37] Using a $SrTiO_3$ template layer, epitaxial LAO can also be grown on Si (001) due to its small lattice mismatch of 1.3%.[38,39] On the other hand, sputtered LAO films have a very high crystallization temperature of 1000^oC.[40]

Yttrium (Y) is often associated with the lanthanide series because of its similar valence electron configuration of $4s^15s^2$. Yttrium oxide, Y_2O_3, has a dielectric constant of ~14 to 18, band gap of ~6 eV and has a possibility of epitaxial growth on Si (111) with a high quality interface.[41,42] The problem of water absorption can possibly be eliminated by *in situ* processing, using a protective capping layer or post deposition annealing.[43] Interestingly, 4% of yttrium doping can increase the dielectric constant of HfO_2 films to as high as 27 due to structural phase transformation.[44]

2.1.2. Germanium as high mobility channel material

Historically, the first transistor was based on Ge. However, the transition to Si was necessary due to various factors such as the excellent SiO_2/Si interface, the larger bandgap of Si compared to Ge, and the abundance of the Si element (raw material for Si is sand). In recent decades, Ge is back on the microelectronic research agenda again because it promises high electron and hole mobilities (see Table 2.2).[45] On the other hand, mobility enhancement by strain is subjected to limitations.[46] In fact, Ge possesses the highest hole mobility of 1900 $cm^2V^{-1}s^{-1}$ compared to other alternative channel materials, making it an attractive material for pMOSFETs.[47]

Table 2.2: Summary of important physical properties of Ge in comparison with Si and other alternative semiconductor channel materials.

	Ge	Si	GaAs	InSb	InP
Bandgap, E_g (eV)	0.66	1.12	1.42	0.17	1.35
Electron affinity, χ (eV)	4.05	4.00	4.07	4.59	4.38
Hole mobility, μ_h ($cm^2V^{-1}s^{-1}$)	1900	450	400	1250	150
Electron mobility, μ_e ($cm^2V^{-1}s^{-1}$)	3900	1500	8500	80 000	4600
Dielectric constant, k	16.0	11.9	13.1	17.7	12.4
Melting point, T_m (^oC)	937	1412	1240	527	1060

Germanium possesses one of the smallest bandgap (E_g) compared to other semiconductors.[48] The drawback of a small E_g is the large band-to-band tunneling leakage current. However, possessing a small E_g is compatible with low supply voltage (V_{dd}) in advanced CMOS devices. This also implies a lower barrier height at the source/drain junction, which is one important factor that affects contact resistance.

2.1.3. Passivation of the germanium interface

The main technical issue hindering the development of Ge MOSFETs is its poor interface quality. Its native oxide (i.e., GeO_2) is unstable, water soluble, and reacts easily with the Ge substrate to form GeO (see Eq. (2.1)), which desorbs as a gas-phase at low temperatures of about 400^{o}C.[49] The desorption process may leave behind a defective interface since GeO has reducing properties.[50] Desorption of GeO at high temperatures (>500ºC) is believed to be the main cause of large

capacitance-voltage (C-V) hysteresis, serious stretch-out of the C-V characteristics and a large flatband voltage (V_{FB}) shift.[51,52]

$$GeO_2 + Ge \rightarrow 2GeO(s) \text{ or } 2GeO(g) \text{ at } \sim 400°C. \quad (2.1)$$

The poor interfacial issue of Ge is further exacerbated by the fact that hydrofluoric acid (HF), which has been known to provide effective passivation for Si devices, does not work well for Ge. One theoretical study showed that Ge dangling bonds form negatively charged electronic states below the valence band maximum (VBM).[53] Unfortunately, interstitial hydrogen (H) in Ge exists also as a stable negatively charged state and is therefore not able to passivate these dangling bonds. Various passivation methods have hence been proposed, with some halogen-based pre-gate deposition methods showing decent results. For example, aqueous $(NH_4)_2S$ can suppress the Ge native oxide formation through the formation of air-stable germanium sulfide (GeS_x), thereby improving the Ge device electrical characteristics.[54,55,56] Also, introduction of nitrogen at the high-k/Ge interface through various methods is shown to be effective in reducing leakage current and interface trap density.[57,58,59,60] However, introduction of nitrogen at the interface possibly degrades the channel carrier mobility, due to increased oxide defects which act as Coulomb scattering centers, in a similar manner to the effect of SiON and/or SiN in Si MOSFETs.[61] Hydrochloric acid (HCl) etching of Ge leads to an air-stable chlorine-terminated Ge surface, although its effects in actual devices have not yet been thoroughly investigated.[62] Surface passivation by Si is also an attractive approach because the Si/Ge epitaxial interface, which is less defective than the Ge-oxide interface, is preserved.[63,64,65] However, this method will inevitably result in a low-k interfacial SiO_x layer which

compromises the effective oxide thickness (EOT) scaling. In addition, the Si conduction band is lower than the Ge conduction band and as such, the electrons will be mostly populated in the Si layer which has lower electron mobility.[66]

Recently, GeO_2 has been reinvestigated as a promising candidate for Ge surface passivation.[67,68] This is because despite GeO_2 being physically unstable as a bulk oxide, it may however be beneficial at the Ge interface. By the analogy from the SiO_2/Si interface using the bonding constraint model, GeO_2 has a large spread in bond angles and a random distribution of dihedral angles, thus promising a potentially good interface.[69] However, formation of a good quality GeO_2/Ge interface (with interface trap density $D_{it} \sim 10^{11}$ cm^{-2} eV^{-1}) requires exclusive techniques such as slot-plane-antenna (SPA) high density radical oxidation or high-pressure oxidation (HPO).

Rare earth oxides, on the other hand, have recently been reported to form good interfaces with Ge as compared to HfO_2.[70,71,72,73] Houssa *et al.* explain this ability to effectively passivate the defective Ge surface through a first principles study on the electronic properties of the relevant interfaces.[74] Their calculations show that Hf-based oxides tend to form Ge-Hf bonds due to the five-fold coordination of Hf in the GeO_x matrix which is responsible for creating defect levels in the upper part of the Ge band gap. On the other hand using La-based oxides, only La-O-Ge bonds are formed because La possesses a lower coordination (four-fold) which leads to a surface-state-free Ge band gap. Since most of the rare earth oxides are six-fold coordinated in its bulk oxide phase, like La_2O_3, one should expect a

similar four-fold coordination in the GeO_x matrix. This explains why rare earth oxides can passivate Ge surfaces effectively.

2.2. Physics of surfaces and interfaces

Understanding of surface properties has always been intriguing for both experimental and theoretical physicists alike, since the situation at the surface is different (and much more complicated) from that within the bulk in many important ways. Wolfgang Pauli, the great Swiss theoretician, once commented that "God created the bulk and the Devil made the surface". The key concepts involved at the surface are crucial, however, to provide useful insights into the study of a more complex issue, that of the interface. For example, interface states in band alignment theories (see section 2.3) are often developed upon the presumption of surface states. This section reviews these key concepts and also the work function parameter.

2.2.1. Deviation of surfaces from bulk

Due to the interference of electron wave functions in a periodic medium, the concept of band theory describes the electronic properties of solids relatively well. However, the electronic structure near the surface is markedly different from the bulk because of the lack of three-dimensional periodicity at the surface. The abrupt termination at the surface will give rise to the formation of surface states since the boundary conditions for the electronic wave functions are changed in the direction normal to the surface. In particular, intrinsic surface states are formed when the truncation results in an ideal surface where the surface atoms are in their bulk-like positions and retaining the in-plane symmetry. In reality, the exact

knowledge of the atomic positions (surface structure) is required and surface relaxations and reconstructions frequently occur. This presents one of the most challenging tasks in surface science. To further complicate matters, imperfections at the surface (for example, missing surface atoms or line defects) will result in extrinsic surface states. These states can also be formed in the presence of contaminants, such as carbon, hydrocarbon or oxygen, and other adsorbed atoms (adatoms).

2.2.2. Electronic states at surfaces

Simple model calculation of the electronic surface states on a crystalline surface is based upon solving of the Schrödinger equation at the surface, i.e. at $z = 0$.[75] The most general one-electron wave function for localized states near the ideal surface has a plane-wave Bloch character for coordinates parallel to the surfaces (ideal 2D periodicity within the surface plane). For simplification, the surface ($z = 0$) is modeled by an abrupt potential step V_0 in a nearly-free electron model. Because of periodicity within the bulk, one can take as the simplest model a semi-infinite chain of identical and periodically arranged atoms, with the end of the chain representing the surface. Here, a cosine variation of potential along the chain is assumed, i.e. $V(z) = 2V\cos(2\pi z/a)$, for $z < 0$. The resulting solutions must be composed of a part compatible with the vacuum energy level, $E_{vac} = qV_0$ on the vacuum side ($z > 0$) and of a part with the cosine potential in the bulk ($z < 0$). This matching is necessary for both the electronic wave function, ψ, and its derivative, $\delta\psi/\delta z$.

Possible surface solutions can be calculated to be standing Bloch waves inside the crystal which are matched to exponentially decaying tails on the vacuum side as shown in Fig. 2.1 (a). By allowing for complex wave vectors, additional surface solutions become possible, giving rise to a standing wave with exponentially decaying amplitude (Fig. 2.1 (b)). The solution then becomes essentially a standing wave with exponentially decaying amplitudes at both sides. Another important consequence of the matching conditions is the restriction on the allowed values of E, i.e. only one single energy level E somewhere within the gap of the bulk states is allowed. The solutions of these discrete states are called *Shockley states*.[76] Using the other limiting case of tightly bound electrons, *Tamm states* can be derived.[77] This is done using an approximate treatment in terms of wave functions that are linear combinations of atomic eigenstates (i.e. LCAO).

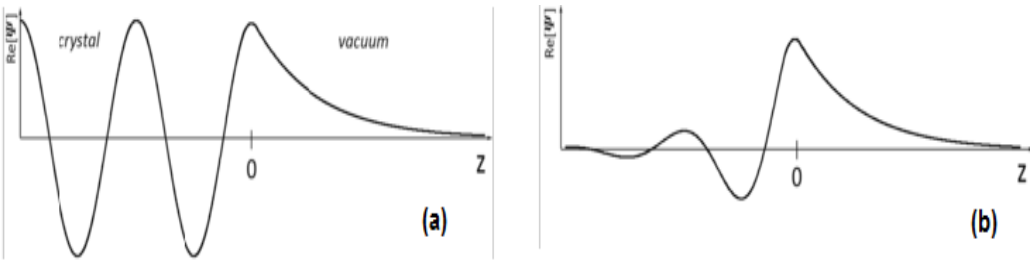

Fig. 2.1: Real part of the one-electron wave function for (a) a standing Bloch wave matched to an exponentially decaying tail in the vacuum and (b) a surface-state wave function localized at the surface (z = 0).

The existence of electronic surface states, with energy levels different from the bulk state, is easy to comprehend within the framework of a tight-binding model. Since the atoms residing in the top-most surface layer is missing their bonding partners (above them), their orbitals have less overlap with orbitals of neighbouring atoms. The splitting and shift in the energy levels of surface atoms will be smaller which therefore introduces energy levels within the band gap. The

breakage of chemical bonds (e.g., sp^3 hybrid in Si or Ge) at the surface results in dangling orbitals and these orbitals also do not experience the same splitting and shift as the bulk atoms. This similarly results in the appearance of energy states within the band gap. The perturbation of chemical bonds due to presence of the surface is not only restricted to the first layer of atoms. Surface-induced modifications of chemical bonds between the top-most layers are called *back bond states*. These states are however generally less disturbed than dangling bonds, giving rise to a smaller shift in energy levels with respect to the bulk.

The respective surface state wave functions are "built-up" from conduction (CB) and valence band (VB) wave functions which, in the absence of a surface, would have contributed to the bulk states. This implies that the character of these states also reflects that of the corresponding bulk states. In particular, a semiconductor is neutral if all the CB states are empty and all the VB states are occupied by electrons. On the other hand, CB states will be negatively charged if occupied (acceptor-like) and VB states will be positively charged if unoccupied (donor-like). As such, surface states derived from the CB are acceptor-like while those from the VB are donor-like in character.

2.2.3. Adatom induced surface band bending

The formation of extrinsic surface states adatoms (adsorbate) results in surface band bending within submonolayer coverage. This has been studied specifically on well cleaved gallium arsenide, GaAs (110) surfaces where the intrinsic surface states are overlapping the bulk bands, i.e. band gap is empty of such states. Cao *et al.* investigated the surface band bending as a function of the metal coverage, for

coverage as low as 10^{-3} monolayers, for In, Al, Ag, and Au deposited at 83 K on p-GaAs surfaces as shown in Fig. 2.2(a).[78]

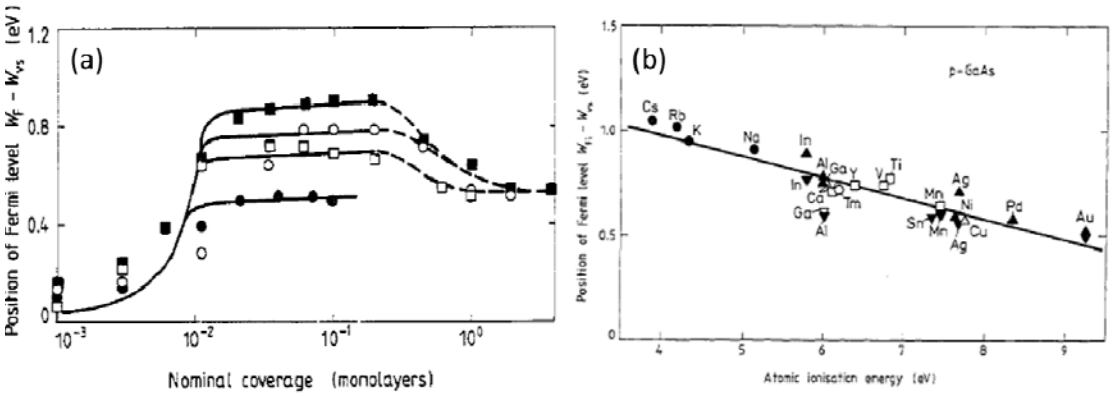

Fig. 2.2: (a) Position of Fermi level above the VBM as a function of the amount of nominal metal coverage on clean p-GaAs. Experimental data for In (■), Al (○), Ag (□) and Au (●) deposited at low temperature from ref. 78 and curves calculated for surface donors at 0.87, 0.76, 0.68 and 0.49 eV, respectively, above the VBM; (b) Initial pinning position of Fermi level above the VBM as a function of the first ionization energy of metal atoms deposited on p-GaAs. (●) data from ref. 81; (▲) from refs. 78, 82; (▼) from ref. 83; (■) from refs. 84, 85.

To interpret these data, we first look at how band bending in the substrate is affected by the presence of adatom induced surfaces states. In order to satisfy charge neutrality, the charges induced by the adatom-induced surface states (Q_{ss}) must balance with the space charge density in the semiconductor (Q_{sc}). With the assumption of discrete donor states at energy E_{ss}, Q_{ss} is given by:

$$Q_{SS} = +qN_{SS}[\exp(\frac{E_{SS} - E_F}{k_B T}) + 1]^{-1}. \quad (2.2)$$

At low temperatures, the space charge density in a depletion layer may be approximated by

$$Q_{SC} = -(2q\varepsilon_S\varepsilon_0 N_A \mid V_S \mid)^{1/2}, \quad (2.3)$$

where q is the electronic charge, N_A is the accepter density of a p-typed doped semiconductor, ε_s is its static dielectric constant, ε_s is the permittivity of free space, and V_s is the resultant surface band bending. The solid curves in Fig. 2.2(a) were

computed by solving Eqs. (2.2) and (2.3) for adatom-induced donor levels at 0.87, 0.76, 0.68 and 0.49 eV above the VBM, with the assumption that each metal atom deposited induces one surface states, i.e. $N_{ss} = \sigma_{110}\theta$. The coverage θ in monolayers (ML) is measured in units of the total density $\sigma_{110} = 8.85 \times 10^{14}$ cm^{-2} atoms in the GaAs (110) planes. For the first ~0.25 ML, there is good agreement with the experimental data, suggesting that the initial band bending is strongly influenced by adsorbate-related surface donors.

The above data suggests the energy of these adatom-induced levels might have a certain chemical trend, which is shown to be possible using a tight-binding approach.[79] In particular, Mönch showed that the energies of these adatom-induced surface donors reveal a pronounced chemical trend when they are plotted against the ionization energies of the respective free metal atoms.[80] This is shown in Fig. 2.2(b).[78,81,82,83,84,85] In addition to data obtained at low temperature, the plot in Fig. 2.2 (b) includes results of transition metals, thulium (Tm) and calcium (Ca), which are evaporated at room temperature. The inclusion of these data is justified by the fact that depositions of manganese (Mn) at room and at low temperatures give the same pinning positions. At room temperature, evaporation of Mn atoms, as with other transition atoms, were found to substitute for gallium (Ga) surface atoms. Such cation-exchange reactions yield isolated adatoms, effectively reducing surface mobility and therefore counteracting the formation of adatom islands. This explains for the similar pinning positions observed for both low and room temperature depositions.

2.2.4. Work function and electron affinity

An important parameter that represents the state of a surface (and arguably the interface) is the work function, Φ_F. The work function plays a crucial role in many important and successful band alignment models which will be discussed in section 2.3.[86] Theoretically, the work function is equal to the minimum work that must be done to remove an electron from the solid at 0K.[87] It can be shown that the theoretical expression for work function is given by two components

$$\Phi_F = \Delta\phi - \bar{\mu}, \tag{2.4}$$

where $\Delta\phi$ is the change in electrostatic potential across the dipole layer created by the "spilling out" of electrons at the surface, and $\bar{\mu}$ is the chemical potential of the electrons in the bulk metal relative to the mean electrostatic potential there.

Experimentally, it is almost impossible to distinguish between these two terms since measurements often include both the surface and bulk contributions. It is however crucial to ensure a clean surface prior to measurement so that adsorbed contaminants do not contribute to additional surface dipoles.(see section 4.1.3.1) The Kelvin probe is one commonly adopted technique for work function measurements. It is based on measuring the contact potential built up between the sample and the probe but requires prior calibration of the work function of the probe tip. Alternatively, ultra-violet photoemission spectroscopy (UPS) can also be used (see section 3.2.1.6). On the device level, the work function difference between the metal and semiconductor in a MOS capacitor structure dictates the flat band voltage (V_{FB}) of the capacitor. Any presence of dipoles at the metal/high-k and high-k/semiconductor interfaces will lead to changes in the

effective metal work function and therefore causes V_{FB} shifts. This effective metal work function can be determined from the V_{FB}-EOT plot by extrapolating to zero EOT.[88,89] (see section 6.1.2)

Due to the lack of a definite Fermi level, it does not make sense to use the work function term for oxide materials. A more appropriate term will be the electron affinity, χ, which is defined as the energy required to remove an electron from the CBM into vacuum. This parameter is important in band alignment models, especially for oxide-semiconductor heterojunctions.

2.3. Band alignment theories

The ability to understand and control band discontinuities has often been viewed as a holy grail in the area of solid-state device engineering. This is because these discontinuities (i.e., Schottky barrier height (SBH) and band offsets) act as barriers to electronic transport across the junction. In the recent decade, there has been a resurgence of interest in studying band alignment due to the introduction of high-k materials. This is primarily due to two reasons. Firstly, high-k materials have a smaller bandgap compared to SiO_2; therefore there is a need to predict and/or measure band offsets which control the leakage current. Secondly, high-k related interface dipoles are believed to cause large flatband voltage shifts which affect the device threshold voltage.[90] This section reviews some of the more popular existing theories behind band lineup for oxide-semiconductor heterojunctions. In addition, this section also shows how band alignment is intimately related to interface (surface) physics.

2.3.1. Ideal Schottky-Mott lineup

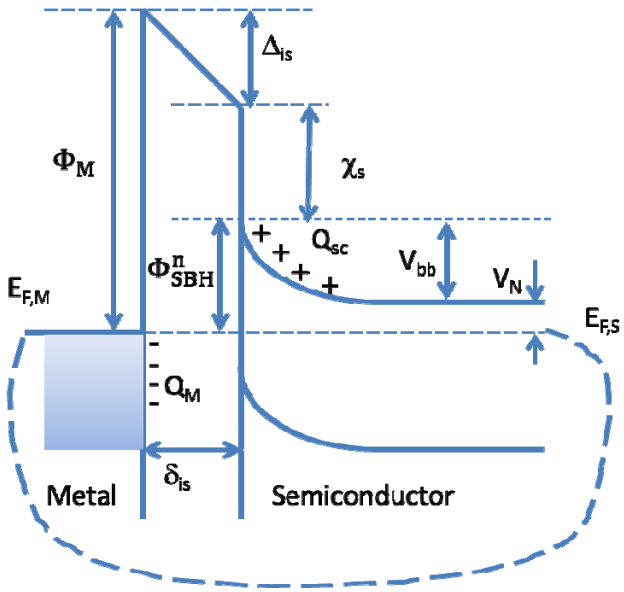

Fig. 2.3: Schematic illustrating the "Gedanken" experiment of forming a Schottky junction without the presence of any interface states. This will eventually imply that the potential due to the interface dipole (i.e., Δ_{is}) must be zero.

The Schottky-Mott model was one of the earliest theories developed to explain the band alignment of metal/semiconductor junctions, or otherwise termed as Schottky junctions.[91] Essentially, the Schottky-Mott model states that the electron Schottky barrier height (Φ^{n}_{SBH}) is given simply by the difference between the metal workfunction (Φ_m) and the electron affinity (χ_S) for n-type Si, Eq. (2.5); or the difference between the ionization energy (I) and Φ_m for p-type Si, Eq. (2.6), whereby $I = E_g + \chi_S$.

$$\Phi^{n}_{SBH} = \Phi_m - \chi_s, \tag{2.5}$$

$$\Phi^{p}_{SBH} = I - \Phi_m. \tag{2.6}$$

Despite its simplicity, the Schottky-Mott model forms the basis of many other models and hence warrants more attention in this thesis. One useful approach to

understanding this model is treating it as a "Gedanken" (thought) experiment, as shown in Fig. 2.3. Suppose the two materials, i.e. metal and semiconductor, are placed parallel to each other with a small gap δ_{is} separating them. An electrical connection is made externally, thereby equalizing the Fermi level at both sides of the junction. Assuming that there are no additional interface states present, the only charges present at the semiconductor side should originate only from the space charge (Q_{SC}) which induces an equal magnitude of charges of opposite polarity at the metal side, akin to that of a parallel plate capacitor. The resultant potential drop across the interface is then given by

$$\Delta_{is} = (\delta_{is} Q_{sc}) / \varepsilon_0. \tag{2.7}$$

To maintain continuity in the band diagram, this potential drop can also be expressed as Eq. (2.8), whereby V_{bb} is the semiconductor band bending and V_N is the Fermi level to conduction band in the bulk.

$$\Delta_{is} = \chi_s + eV_{bb} + eV_N - \Phi_m. \tag{2.8}$$

By bringing the two materials into intimate contact, such that δ_{is} approaches zero, the potential at the interface becomes zero (see Eq. (2.7)), and as such the Schottky-Mott condition is also otherwise known as a vacuum level lineup. In other words, because the interfacial gap vanishes, i.e $\delta_{is} = 0$, the charge transfer cannot occur any finite distance and therefore no interface dipole can be formed. This eventually results in the electron barrier height Φ^n_{SBH} (= $e(V_{bb} + V_N)$) to be equal to $\Phi_M - \chi_s$ in Eq. (2.8). This analysis can be similarly carried out for Φ^p_{SBH}.

Band alignment concepts initially established for metal/semiconductor Schottky junctions can often be carried forth to semiconductor/semiconductor and oxide/semiconductor heterojunctions, since an oxide can simply be regarded as a wide band gap semiconductor. This extension is first made for the Schottky-Mott model, followed by other intrinsic gap state models thereafter. The equivalent of the Schottky-Mott lineup for oxide/semiconductor heterojunctions is termed the Anderson model, which is similarly based on the concept of vacuum level lineup (i.e., zero interface dipole).[92] Accordingly, the conduction band offset, CBO should then be the difference between the two electron affinities, χ, of semiconductors "a" and "b" as follows:

$$\mathrm{CBO} = \chi_a - \chi_b. \tag{2.9}$$

Unfortunately, it is soon found that experimental results often do not comply with this simple rule. Although barrier heights of metal-selenium rectifiers correlate linearly with the metal work function, the slope parameter, $S = -\mathrm{d}(\Phi_{SBH}^{p}) / \mathrm{d}(\Phi_m)$ is 0.08, rather than 1, as required by the Schottky-Mott rule (see Eq. (2.6)). The insensitivity of the barrier height to the metal work function, i.e. S < 1, is otherwise commonly known as Fermi level pinning (FLP).

2.3.2. Concept of charge neutrality: Metal-induced gap states

In 1947, Bardeen introduced the concept of interface states to explain for the FLP effect.[93] In essence, he postulated that prior to the space-charge layer on the semiconductor side, interface states exist (usually within the semiconductor band gap) and contribute charges that affect the band alignment. This came about naturally given that surface states are a natural consequence of solving the

Schrödinger equation at the surface (see section 2.2.2). These states contribute additional charges to the overall system, on top of Q_{SC} (assumed in Eq. (2.7)). This accounts for the deviation of the experimental results from the Schottky-Mott limit (i.e., S = 1), where no interface states are assumed. In the presence of a high density of such states (i.e., Bardeen limit), S approaches zero and the Fermi level becomes fully pinned at a certain energy level.

The concept of interface states eventually developed into the metal-induced gap states (MIGS) model. This theory was initially proposed by Heine in 1965, which was then developed further by Louie, Chelikowsky, Cohen and then Tersoff.[94,95,96] Heine pointed out that the states produced in the semiconductor at the initial interface is due to the intimate contact with the electrons from the metal. In particular, the introduction of the metal perturbs the existing intrinsic surface states. These states exist as a continuum (not discrete) in the in-plane direction within the band gap of the semiconductor, and decay exponentially in the out-of-plane direction. To use this model for quantitative predictions, Tersoff proposed the concept of the charge neutrality level (CNL) which is being used to define the branch-point of the continuum of MIGS states. This hypothetical energy level is defined such that any states below it are predominantly donor-like (VB-like) while those above it are mostly acceptor-like (CB-like). As such, the occupancy of these states (determined by the relative position of E_F) will create additional charges that change the alignment (see Appendix I). The corresponding overall band lineup in this model is then given by

$$\Phi_{SBH}^{n} = S(\Phi_m - \chi_s) + (1-S)\Phi_{CNL}^{CBM}, \qquad (2.10)$$

$$\Phi_{SBH}^{p} = S(I_s - \Phi_m) + (1-S)\Phi_{CNL}^{VBM}, \quad (2.11)$$

where Φ_{CNL}^{CBM} and Φ_{CNL}^{VBM} represent the energy distances from the CNL to the conduction band minimum (CBM) and valence band maximum (VBM) respectively. Note that these two equations contain familiar terms from the Schottky-Mott model (see section 2.3.1). As mentioned, this is because the Schottky-Mott lineup is one of the limits of the MIGS model, i.e. when S = 1. The other limit is the Bardeen lineup which represents the fully pinned condition when S = 0. Under this condition, the Fermi level is aligned exactly to the CNL. Robertson successfully extended the MIGS concept to the oxide/semiconductor heterojunction, where the conduction band offset (CBO) is given by[97]

$$CBO = \chi_a - \chi_b + (S-1)(\Phi_{CNL,a}^{Vac} - \Phi_{CNL,b}^{Vac}), \quad (2.12)$$

where χ represents the electron affinity and Φ_{CNL}^{Vac} is defined as the energy distance from vacuum level to the CNL. Note that subscripts "a" and "b" represent the semiconductor and oxide respectively. Empirically, S is found to obey

$$S = \frac{1}{1 + 0.1(\varepsilon_\infty - 1)^2}, \quad (2.13)$$

where ε_∞ is the electronic part of the dielectric constant of the larger band gap material.[98,97] More details on this relationship can be found in Appendix 1.

2.3.3. Calculation of branch point energies

Tersoff computed one of the most reliable set of branch point energies for 15 semiconductors.[96, 99] He first obtained the energy bands with a linearized augmented plane-wave method (APW) and used the local-density approximation (LDA) for correlation and exchange. The band gaps were then adjusted to the

experimental values by rigid shifts of the conduction bands, i.e. scissors operation. Lastly, a cell-averaged real-space Green's function was computed and decomposed into a valence band (VB) and conduction band (CB) part. The CNL is then defined as the energy at which these two contributions are of equal value. The computed CNL values by Tersoff have proven to be quite reliable but require a lot of computational effort involved in the convergence of the Green's function.

Several other approximate treatments have also been proposed for the calculation of the CNL. Flores and co-workers used the average of the midgap energies at the Γ, X and L points of the Brillouin zone (BZ) for face-centered cubic (fcc) crystals using local-density approximation (LDA).[100] Cardona and Christensen applied the concept of BZ averaging by using Baldereschi's special points to approximate the corresponding k-point sum, which requires less computational effort compared to Tersoff's method.[101,102] More precisely, the CNL is taken as the midgap energy, which is an average of the eigenvalues of the two highest VB and two lowest CB at the first Baldereschi point. This is as opposed to the scissors operation which was used by Tersoff. However, the calculated CNL values by Cardona and Christensen are surprisingly near to Tersoff's values.

2.3.4. Chemical trends: Interface-induced gap states

In section 2.2.3, it is seen that there exists a chemical trend between the energies induced by adatom surface states and its first ionization energy. Upon attaining a continuous metallic film, the final Fermi level positions are plotted against the electronegativity difference between the metal and the substrate, as shown in Fig.

2.4. These final Fermi level positions are identical for both n- and p-type semiconductors and this is well supported by experimental data. This suggests that the charge transfer involved in the interface formation depends strongly on electronegativity. It is also seen that when the electronegativity difference is zero, the Fermi level lies at the CNL of GaAs. In fact, a compilation of reported data in literature shows that the barrier height is dependent on the electronegativity difference for many other Schottky junctions.[98]

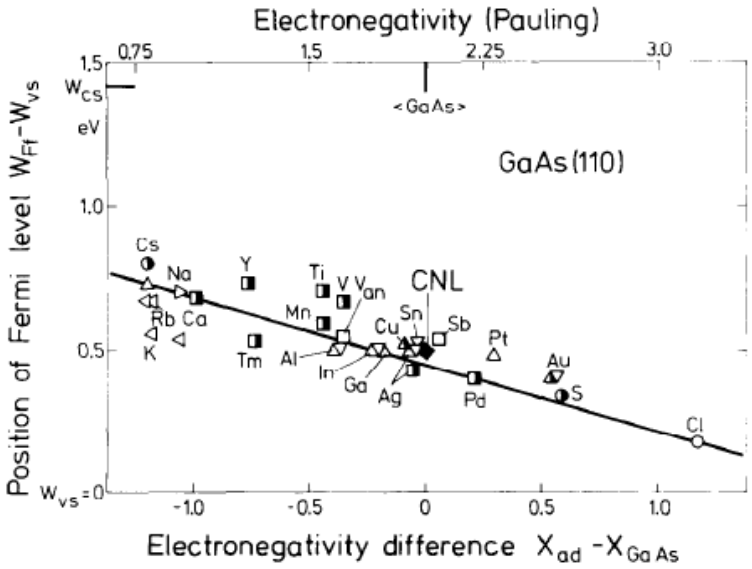

Fig. 2.4: Final pinning positions of the Fermi level above the valence-band maxima versus electronegativity difference. Unfilled and partly filled symbols are labeling data obtained with substrates doped p-type and n-type.[79,96]

Pauling correlated the ionicity of single bonds in diatomic molecules with the differences in their atomic electronegativities. [103] In essence, the more electronegative atom tends to draw more electrons and becomes negatively charged. This concept proved useful in solid state physics. Miedema and coworkers applied it to metal alloys.[104,105] Mönch adopted it to model the charge transfer across heterojunctions and proposed that, to a first approximation, the charge transfer varies proportionally to the difference between electronegativities of the two materials. Furthermore, the electronegativity of compounds can be

calculated based on a geometric mean approach which has been shown to effectively predict Fermi energies.[106] The model proposed by Mönch is termed the interface induced gap states (IFIGS) model. This model recognizes the importance of intrinsic gap states in band lineup but advocates the use of electronegativity instead of electron affinity (or work function). This is because the concept of vacuum level at the interface is not well-defined. Note that in the following review, the term "CNL" is used for consistency, which is actually equivalent to the term "branch point" used in the IFIGS model.

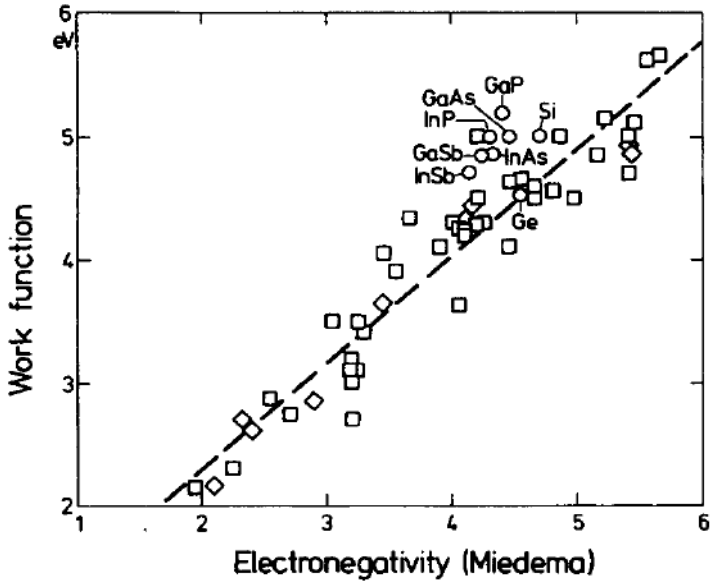

Fig. 2.5: Work function of metals and dielectric work function of semiconductors as a function of Miedema's electronegativites. (□) and (◊) represent data of metals while (○) represents data of semiconductors.

In the derivation of the IFIGS model, it is imperative to establish the relationship between electronegativity and work function. One starts off by considering the contact potential difference between two solids of different work functions:

$$\Delta_{cp} = \Phi_l - \Phi_r. \tag{2.14}$$

Charge transfer will occur in such a way that the solid on the left-hand (l) and right-hand (r) sides will be charged negatively and positively respectively for $\Phi_l >$

Φ_r. As in small molecules, such charge transfer suggests that the work functions of solids correlate with their electronegativities.[107] In fact, experiments show that the work function of polycrystalline metals correlates with Miedema's electronegativities according to Eq. (2.15) below, which is derived from a plot shown in Fig. 2.5. Miedema electronegatvities (EN) are preferred since they were derived from chemical trends in the properties of metallic alloys and compounds.

$$\Phi_M = 0.86\mathrm{EN} + 0.59\mathrm{eV}. \tag{2.15}$$

For semiconductors, the dielectric work function (Φ_{CNL}^{Vac}), defined as the energy distance from the vacuum level to the charge neutrality level, is assumed to scale with electronegativity, in a similar manner for semiconductors. The dielectric work function is defined with respect to the CNL because it is the CNL that eventually determines the charge transfer instead of the Fermi level, E_F. This is to say that there will always be additional charges formed which screens the charge transfer unless the semiconductor is doped in such a way that E_F matches the CNL. This is also justified by the good agreement of the experimental results with the linear fit of the metals (see Fig. 2.5).

Since the charge transfer is given by the difference in the work function, there is an additional "residual" term due to the fact that Φ_{CNL}^{Vac} is defined with respect to the CNL instead of the Fermi level (E_F). The resultant dipole is thus given by

$$\Delta_{is} = \Phi_m - \Phi_s = A_X(\mathrm{EN}_m - \mathrm{EN}_s) - (\Phi_{SBH}^{n} - \Phi_{CNL}^{CBM}), \tag{2.16}$$

where A_X is the proportionality constant between the work function and Miedema electronegativity, and Φ_{CNL}^{CBM} is the energy distance from the CNL to the

conduction band minimum (CBM). On the other hand, the occupancy of the gap states depends on the Fermi level position (E_F) with respect to the CNL (see Appendix 1 for more details). When E_F is above, coincides with or below the CNL, the resultant net charge (Q_{is}) is negative, vanishes or becomes positive respectively. This is given by the following equation:

$$Q_{is} = eD_{is}(\Phi_{SBH}^{n} - \Phi_{CNL}^{CBM}), \tag{2.17}$$

where D_{is} is the density of interface states. Since the charges induced by the space charge density is usually smaller than Q_{is}, the interface dipole (Δ_{is}) across a interfacial thickness of δ_{is}, is then given by

$$\Delta_{is} = \frac{q}{\varepsilon_i \varepsilon_0} Q_{is}\delta_{is} = \frac{q^2}{\varepsilon_i \varepsilon_0} D_{is}\delta_{is}(\Phi_{SBH}^{n} - \Phi_{CNL}^{CBM}). \tag{2.18}$$

By substituting Eq. (2.16) into Eq. (2.18), one obtains the IFIGS equation for a n-type semiconductor in Eq. (2.19) and that for a p-type semiconductor can be similarly obtained in Eq. (2.20).

$$\Phi_{SBH}^{n} = \Phi_{CNL}^{CBM} + D_X(EN_m - EN_s), \tag{2.19}$$

$$\Phi_{SBH}^{p} = \Phi_{CNL}^{VBM} - D_X(EN_m - EN_s). \tag{2.20}$$

These two equations show that the band lineup is composed of a zero-charge transfer term and an electric dipole contribution. The slope parameter indicates two limiting conditions: $D_X = 0$ for the Bardeen condition and $D_X = A_X$ for the Schottky-Mott condition. This can easily be verified since when $D_X = A_X$, Eq. (2.19) gives $\Phi_{SBH}^{n} = \Phi_{CNL}^{n} + \Phi_m - \Phi_{CNL}^{Vac} = \Phi_m - \chi_s$ (Schottky-Mott condition, Eq.

(2.5)). Similarly, the IFIGS model can be carried forth to the oxide/semiconductor heterojunction,[214] and the resulting equation is given by

$$\mathrm{VBO} = \Phi_{\mathrm{CNL,b}}^{\mathrm{VBM}} - \Phi_{\mathrm{CNL,a}}^{\mathrm{VBM}} + \mathrm{D_X}(\mathrm{EN_b} - \mathrm{EN_a}), \tag{2.21}$$

where VBO is the valence band offset, $\Phi_{\mathrm{CNL}}^{\mathrm{VBM}}$ is the energy distance from the CNL to the VBM, and EN is the Miedema electronegativity. Note that this equation takes on a similar form to Eq. (2.20). Subscripts "a" and "b" represent the semiconductor and oxide respectively.

2.3.5. Other extrinsic mechanisms

One major contender against the MIGS model in the early period is the Unified defect model (UDM) proposed by Spicer and co-workers. This model suggests that native defects in the semiconductor are responsible for the Fermi level pinning (FLP). Unfortunately, this model was not well-received because the density of extrinsic defects is not high enough to account for FLP. It is shown that a defect density of at least 10^{14} cm^{-2} is needed for metal-semiconductor interfaces due to the screening effect from the metal.[108] This then favors the MIGS theory since the gap states can be sufficiently high.[213] Furthermore, there is no direct evidence that FLP is associated with defect levels due to the limited sensitivity of spectroscopy techniques in detecting the small amount of defect states.[109]

Subsequently, many other band alignment models have been proposed, one of which is the chemical bond polarization model.[110] This model attempts to explain the FLP effect in terms of polarized chemical bonds at the metal-semiconductor interface. The charge rearrangement at the interface specific region of a

metal/semiconductor interface is driven by the minimization of interface energy. This leads to the polarization of interfacial chemical bonds which is responsible for the interface dipole formation. This can be quantitatively estimated using the electrochemical potential equalization (ECPE) method. In this model, parameters such as density of chemical bonds, bond distance and the sum of all the hoping interactions (involved in bonding) are used. However, the ECPE method becomes inaccurate for materials with bandgaps, and as such, this model is not easily implemented for explaining high-k/semiconductor heterojunctions.

2.4. Band offset measurement techniques

The development of theoretical band alignment models for oxide/semiconductor heterojunctions are based upon accurate measurements of band offsets. These measurements often require techniques that are capable of probing the interface, and these can be broadly classified into two categories: (1) electrical/transport based and (2) photoemission based techniques.[111] In the former case, excited electrons are transported across the actual interface itself, whereby its conduction is governed by the relevant band offsets. In the latter case, band discontinuities are extracted based on referencing of energy levels measured by ejection of the electrons from their filled states to the vacuum level. We will only briefly review some common transport based techniques in section 2.4.1 while the photoemission techniques, used in this work, are discussed in greater detail in section 2.4.2.

2.4.1. Electrical/transport based techniques

Internal photoemission (IPE) and current-voltage (IV) measurements can be used to extract the band offset.[112,6,113] This category of techniques is based on the actual transport of carriers across the interface and therefore requires a metal electrode to provide the electric field. Errors involved in this family of techniques include (1) presence of interfacial charges or traps, (2) presence of additional metal/oxide interface and (3) complications related to modeling of conduction current. An important pre-requisite for using IV measurements to extract band offset is that the conduction mechanism be electrode-limited, i.e. Fowler-Nordheim (FN) tunneling or Schottky emission (SC). This is however, often not the case given the numerous mechanisms cited for high-k oxides (see section 3.2.4.3).

2.4.2. Photoemission based techniques

In comparison with transport based techniques, photoemission measurements are advantageous in various ways. First, these measurements are quick and do not require the deposition of an additional conducting electrode. In addition, the extraction of band discontinuities is based on straightforward referencing of energy levels without the need for complicated conduction models. Lastly, these measurements can be as accurate (±0.1 eV), if not more than most transport based techniques given the typical spectrometer energy resolution of ± 0.05 eV. There are, however, some potential pitfalls associated with this technique which will be discussed in more detail in Chapter 4.

2.4.2.1. Core-level at interface

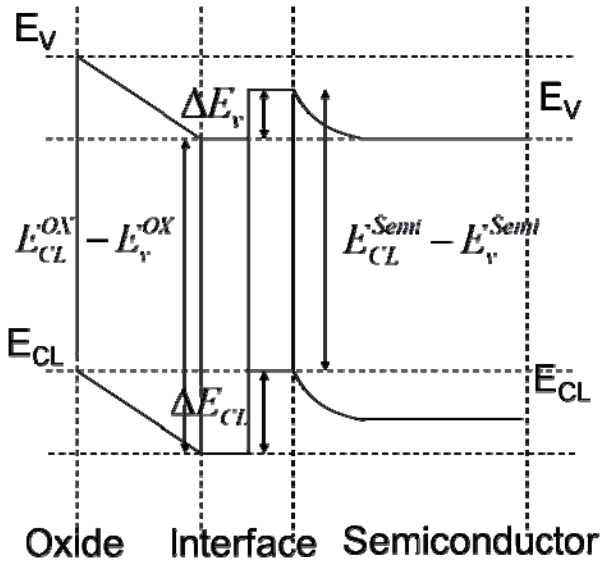

Fig. 2.6: Energy band diagram of an oxide/semiconductor heterojunction showing how the valence band offset (ΔE_V) can be extracted using Kraut's method (not drawn to scale). Note that E_V represents the valence band maximum while E_{CL} represents the core level.

Kraut *et al.* first introduced this referencing method based on core-level photoemission spectroscopy.[114,115] Here, three samples, representing the two bulk materials at both sides and the interface, are required. Depending on the mean free path (MFP) of the photoelectrons, appropriate thicknesses are chosen for the bulk and interface samples. Given a typical Al kα X-ray source of 1487.7 eV, the thickness of bulk samples are often in the range of 13 to 20 nm to ensure that negligible substrate photoelectrons can escape. Following the same argument, thicknesses of interface samples are kept below ~10 nm to ensure that the interface can be probed.

In order to derive the valence band offset (ΔE_V, or VBO), one needs to measure the core-to-valence energy level differences (E_{CL}-E_V) for the two bulk samples and the core level separation (ΔE_{CL}) for the interface sample, as shown in Fig. 2.6.

$$\Delta E_V = (E_{CL}^{Semi} - E_V^{Semi})_{bulk,Semi} - (E_{CL}^{OX} - E_V^{OX})_{bulk,OX} + \Delta E_{CL}, \quad (2.22)$$

where the superscripts "Semi" and "OX" represent the semiconductor and oxide respectively while subscripts "CL" and "V" represent core-level and VBM respectively. The determination of the VBM using photoemission is found to be most accurate using a linear extrapolation method for instruments equipped with monochromatic X-ray sources.[116] As such, this method is most commonly adopted in literature and therefore is used in this work. Note that although in the following examples, Kraut's method is used to measure band offsets, it can similarly be applied to measure the Schottky barrier height (SBH) by replacing (E_{CL}-E_V) with (E_{CL}-E_F) instead for the bulk metal.

2.4.2.2. Valence band at interface

Since photoemission allows one to measure the VBM, it is theoretically possible to directly deduce the valence band offset at the interface if one is able to distinguish the valence bands at the interface. Such measurements would imply that only one interface sample is needed instead of three samples (using the core-level at interface method). However, deconvolution of the valence band spectrum is often not an easy task. Chiam *et al.* investigated the effects of varying film thickness on VBO measurements of Y_2O_3 films on Si using the valence band at interface method.[117]

The valence band spectra plotted in Fig. 2.7 are aligned such that the Si 2p binding energy (BE) matches that of the clean substrate. The initial spectrum (i.e. at t=0 s) is shown to consist of two prominent slopes, i.e. one near the Fermi edge

(Si substrate) and the other indicated by the bold line (O 2p states from Y_2O_3). The VBO is then the difference between the extrapolations of the slopes from Si and Y_2O_3. With the reduction of overlayer film thickness after sputtering, the increased contribution from the Si substrate slope leads to reduction in the steepness of the linearly extrapolated slope. This leads to an apparent lowering of the VBO extracted. This illustrates the possible error involved in this method due to choice of film thickness.

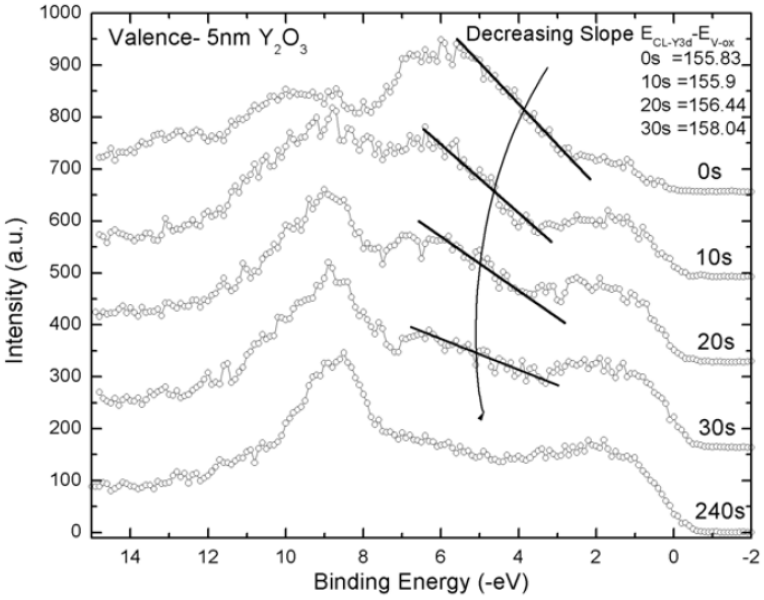

Fig. 2.7: Measured valence band spectra of 5nm Y_2O_3 on Si at different depth profiles. The time indicated for each profile represents the total sputtering time.[117]

3. Experimental Setup and Theory

3.1. Growth setup

In this study, high-k oxide films are grown using either sputtering or UHV evaporation EFM3 deposition, followed by plasma oxidation. The former method is employed for deposition of different high-k oxide films for band alignment studies (see Chapters 4 and 5) and in the fabrication of capacitor structures for electrical characterization (see Chapter 6). The latter UHV technique is used for the growth of yttrium oxide because of its tendency for moisture absorption (see Chapter 7). Fundamental studies involving initial growth and reaction pathways behind interfacial layer formation can thus be studied.

3.1.1. Sample preparation

Prior to deposition, Si substrates n-type (phosphorous dopants, 10^{15} to 10^{16} cm^{-3}) underwent a standard Radio Corporation of America (RCA) cleaning process typically employed by the semiconductor industry.[118] This RCA process starts with a 20 minutes (min) RCA1 dip, which is a solution of NH_4OH (aqueous ammonia), H_2O_2 (hydrogen peroxide) and de-ionized water (H_2O) in the ratio of 1:1:5. This is followed by a 20 min RCA2 dip, which is a solution of HCl (hydrochloric acid), H_2O_2 and H_2O in the ratio of 1:1:6. RCA1 is to remove organic contaminants while RCA2 is used for removing ionic contaminants. Both solutions are maintained at a bath temperature of 80^oC. The substrates were rinsed in de-ionized water for 20 min before and after each chemical rinse. Lastly, the

samples underwent a final dip in 10% hydrofluoric acid for 25 s to produce a hydrogen-terminated sample.[118]

Other substrates were cleaned using standard procedures from the literature. Germanium (Ge) n-type (Sb, 10^{15} - 10^{16} cm^{-3}) and p-type (Ga, 10^{16} cm^{-3}) substrates were cleaned using a cyclic (for 5 times) 10% HF dip and deionized water rinse.[119] Indium gallium arsenide ($In_{0.53}Ga_{0.47}As$) and gallium arsenide (GaAs) p-type substrates with Zn doping of ~10^{16} - 10^{17} cm^{-3} respectively, were dipped in hydrofluoric acid (HF) for 30 s followed by ammonium sulfide, $(NH_4)_2S$, for 5 min.[120] Gallium nitride (GaN) p-type (Mg, 10^{18}-10^{19} cm^{-3}) substrates were dipped in HCl for 5 min while intrinsic zinc oxide (ZnO) underwent ultrasonic cleaning in acetone, ethanol and deionized water for 5 min.[121, 122] For UHV deposition, an additional annealing step (at ~400^{o}C) was carried out once the substrate was loaded into the deposition chamber. This is to degas both the surface carbon contaminants and also any remaining native Ge oxide.

3.1.2. Sputtering, thermal evaporation and annealing

Sputter deposition was carried out using an Anelva L3325FH multi-target (a maximum of three targets) sputterer. Upon loading of the sample, a turbo-molecular pump was used to pump the chamber down to typically a base pressure of ~9 x 10^{-7} Torr. Once the desired base pressure was reached, the chamber was filled with Ar gas at a flow rate of 30 sccm till the chamber pressure stabilized at ~0.3 kPa. Plasma was then generated using the RF generator at 10 W after bringing the pressure to 5 kPa. Once the plasma was ignited, the valve was fully opened and the chamber was pumped back down to ~0.3 kPa. The RF power was

then increased to the desired value. Pre-sputtering was conducted for each target for 10 – 15 min to remove possible surface impurities with the mechanical shutter in place. The actual sputtering commences upon opening this shutter and the sputter time was noted to control the deposition thickness. In this study, the wafer stage was kept at room temperature, i.e. around 28^{o}C. Sputtering targets are three inches in diameter and mounted on copper plates. The sputtered materials include yttrium metal, yttrium oxide (Y_2O_3), lanthanum aluminate ($LaAlO_3$), lanthanum oxide (La_2O_3), aluminum oxide (Al_2O_3), and hafnium oxide (HfO_2), all of 99.9% purity. The RF power used was 100 W, except for Al_2O_3 (30W) and HfO_2 (50W) targets. The deposition rate was calibrated using ellipsometery based on the different refractive indexes of the dielectric films.

The capacitor structures fabricated in this study (i.e. in Chapter 6) consist of aluminum (Al) metal front and back electrodes which were thermally evaporated using an Edwards FL 400 evaporator. The chamber was pumped down to ~10^{-6} Torr before deposition. Evaporation was performed by passing ~1 A of current through a tungsten filament holding small Al wires at a deposition rate of ~1 nm/s. Al metal dots with radius of ~230 μm (measured by an optical microscope) and thickness of ~200 nm (measured by an in-built thickness gauge) are formed using a shadow mask for the front side while the entire back side of the sample was metallized.

Furnace annealing was carried out in a horizontal quartz tube furnace. The three-zone furnace was back filled with nitrogen (N_2) at a flow rate of 3 liters/min. In chapter 6, post (dielectric) deposition annealing was performed at 600^{o}C and

800°C for 30 min, while post metallization annealing was done under forming gas ambience (10% H_2, and 90% N_2) for 10 min at 400°C to improve the metal contact properties.

3.1.3. UHV evaporation

In the growth of high-k oxides, physical deposition methods such as molecular beam epitaxy (MBE) or electron beam (e-beam) evaporation are preferred over chemical based techniques, and even atomic layer deposition (ALD), in terms of control over the interface.[123] This is because of two reasons.[27] Firstly, more advanced physical deposition techniques are carried out in UHV environment which allows for *in situ* desorption of any native oxide to achieve a clean surface prior to the dielectric growth. Secondly, room temperature deposition is possible with physical deposition methods while chemical deposition methods typically require higher temperatures for the reaction of the precursors.

In order to further elaborate on the effects of vacuum on contamination during growth, one can consider the rate of n number of gas atoms impinging on unit area of surface per unit time using the kinetic theory of gases:[124]

$$\frac{dn}{dt} = \frac{P}{\sqrt{2\pi mkT}} cm^{-2}s^{-1} = 3.5x10^{22} \frac{P}{\sqrt{MT}} cm^{-2}s^{-1}, \quad (3.1)$$

where P is the gas pressure (in Torr), m is the atomic mass (in g), k is the Boltzmann constant, and T is the absolute temperature (in K). Converting the atomic mass to molecular weight M, one finds that the arrival rate becomes 3.2 x 10^{14} $cm^{-2}s^{-1}$ under a pressure of 10^{-6} Torr for a typical residual gas molecular weight of 40g and temperature of 25°C. This value is approximately the surface

density of Si. The implication of this is that at a pressure of 10^{-6} Torr, a full monolayer of residual gas atoms arrives at the surface, and the amount of reaction will then depend on the sticking coefficient of these residual atoms. It is then apparent that UHV conditions (preferably 10^{-9} to 10^{-10} Torr) is necessary to minimize surface contamination.

Electron beam evaporation was carried out using the Omicron evaporator with an integral flux monitor (EFM3) in the preparation chamber which is maintained at a base pressure of 10^{-10} to 10^{-9} Torr by a turbo-molecular pump. The preparation chamber is connected to the analysis chamber and therefore allows in situ XPS and UPS characterization. By using the electron beam (instead of thermal energy), evaporation can be carried out with lesser contamination, better thickness control, and at a higher temperature range over a more localized area. This allows for a wider range of materials (with higher melting points) to be used. The electron beam source is generated through thermionic emission by passing a current through the filament. A high voltage between the filament and the rod then controls the energy of the impinging electrons (on the evaporant rod) which affects the heating power. Once the temperature of the evaporant rod is sufficiently high such that the material reaches a semi-molten state, a small blob will form which is being kept bonded to the tip by surface tension. One then waits for the deposition flux to become stabilized before opening the shutter to begin the actual deposition. It is important at this point not to further increase the energy of the e-beam as the deposition flux can suddenly increase drastically. During deposition, the copper shroud is cooled with circulation of chilled water so as to prevent overheating. The film thickness during deposition was monitored using a

quartz crystal modulator (QCM). Essentially, the QCM makes use of the piezoelectric property of quartz to measure the resonance frequency shift which changes according to the film thickness. The QCM in this study is operated at an oscillator frequency of 5.14 MHz, and thickness is determined using a yttrium bulk density of 4.34 g/cm^3 with an impedance factor of 0.835.

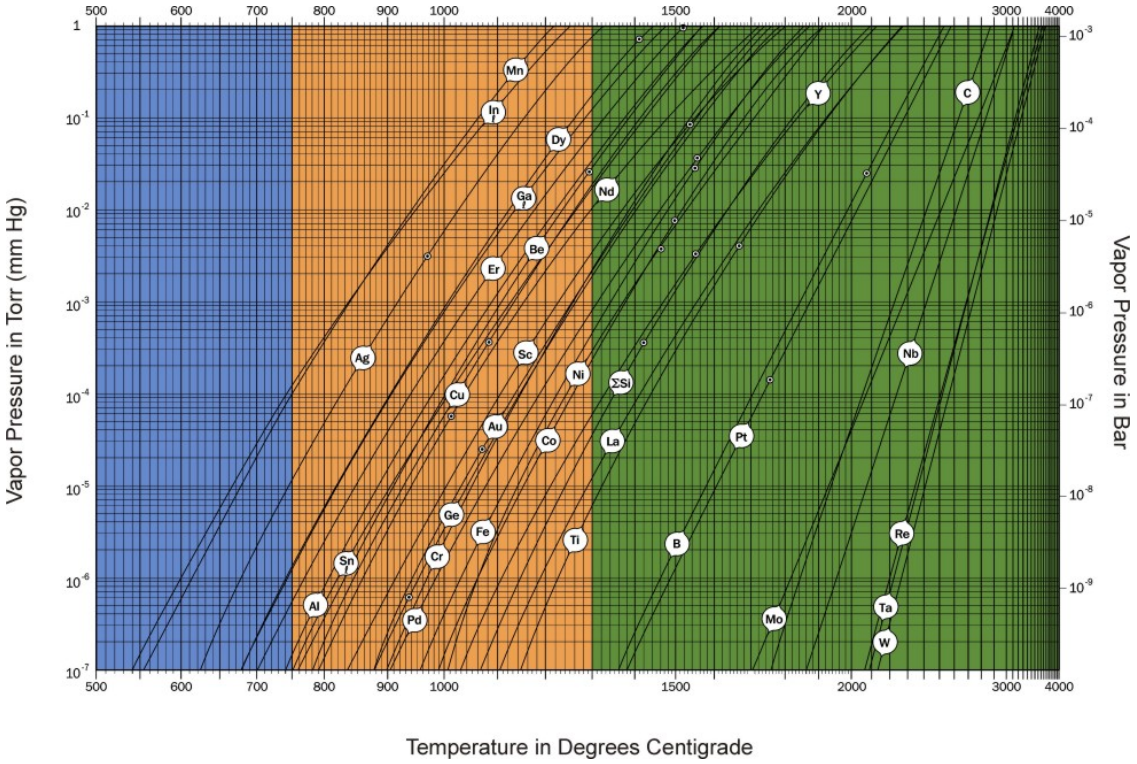

Fig. 3.1: Vapor pressure curves for different elements.[126]

It is known that at a given temperature (T), the vapour pressure (p) varies according to the Clausius-Clapeyron relation:[125]

$$p = A\exp(-\Delta H_{vap}/RT), \qquad (3.2)$$

where A is the rate constant, ΔH_{Vap} is the enthalpy of vapourization and R is the gas constant, i.e. 8.3145 J mol^{-1} K^{-1}. This dependence of vapour pressure with temperature is shown in Fig. 3.1 for different elements.[126] As shown by the plot, a

useful vapour pressure of 10^{-4} Torr can be obtained when yttrium reaches a temperature of ~1600 K. This is close to the specifications from other sources.[127]

In equilibrium, one assumes that the amount of particles leaving the evaporant equals to the flux of particles impinging on the substrate surface, using the similar kinetic theory of gases as in Eq. (3.1). Assuming that all the molecules from the gas phase are deposited on the surface, the maximum value for the deposition rate D (molecules $cm^{-2}s^{-1}$) is calculated to be:

$$D = \frac{p r^2}{L^2\sqrt{2\pi mkT}} = 3.5x10^{22}\frac{p r^2}{L^2\sqrt{MkT}} cm^{-2}s^{-1}, \qquad (3.3)$$

where M is the molecular weight (in g), p is the vapour pressure (in Torr), and r is the radius of evaporant rod (cm), L is the distance from source to substrate (cm), and T is the temperature of the evaporant (K). Calculating based on r = 0.1 cm, T = 300 K, L = 22 cm, and M = 88.9 g, a vapour pressure of 10^{-4} Torr leads to a deposition rate of 0.04 ML/min. (surface density of Ge (001): 6.25 x 10^{14} atom/cm^2 = 1 ML) Assuming 1 ML is equivalent to 3Å based on a hexagonal close packed structure for the Y atoms, a typical value for the deposition rate should be around 0.13 nm/min.

The maximum filament current and voltage are 1.9 A and 1000 V as indicated in the Omicron manual. A thorough degas step was carried out for both the shroud and rod beforehand to ensure a low chamber pressure of ~3 x 10^{-9} Torr during our deposition. Deposition was carried out under a constant flux of ~ 30 nA, with an emission current of ~15 mA and the beam diameter lies in the range of 8.5 – 15 mm. This gives a heating power of ~ 15W. The calibration (shown in Appendix II)

shows that the deposition rate should be ~0.096 nm/min. This implies that the temperature of the rod has reached ~1600 K.

3.2. Characterization techniques

In this study, the characterization tools can be divided into two broad categories, namely physical (and chemical) and electrical characterization techniques. The former includes X-ray photoelectron spectroscopy (XPS) to study the chemical profile and electronic properties at the interface, (see section 3.2.1), ultra-violet photoelectron spectroscopy (UPS) to measure the work function and electron affinity, and transmission electron microscopy (TEM) to physically identify interfacial layer formation (see section 3.2.2). Other important techniques such as X-ray diffraction (XRD) to check the crystallinity of the film and ellipsometery to measure the film thickness are briefly explained in section 3.2.3. On the other hand, electrical measurements using capacitance-voltage (CV), conductance and current-voltage (IV) measurements provide important parameters that are often used to assess the quality of the high-k/semiconductor interface, which directly affects device performance (see section 3.2.4).

3.2.1. Photoelectron spectroscopy

Photoelectron spectroscopy, or photoemission, allows one to probe the electronic properties of solids, their surfaces and interfaces.[128] This is essentially carried out by analyzing the binding energy (BE) distribution of the emitted photoelectrons (i.e. electrons emitted due to excitation by the incident photons). The energy of the incoming photon can be in the ultraviolet regime (5 to 100 eV) for ultraviolet

photoelectron spectroscopy (UPS), or in the X-ray regime (> 1000 eV) for X-ray photoelectron spectroscopy (XPS). By using different photon energies, different information can be obtained. For instance, XPS looks mainly at core-level photoelectrons which are sensitive to the chemical bonding environment (see section 3.2.1.2). On the other hand, UPS looks at valence electrons, which reflect the occupied density of states (DOS) in the material (see section 3.2.1.6). Despite the differences, the fundamental concepts behind these two techniques are identical.

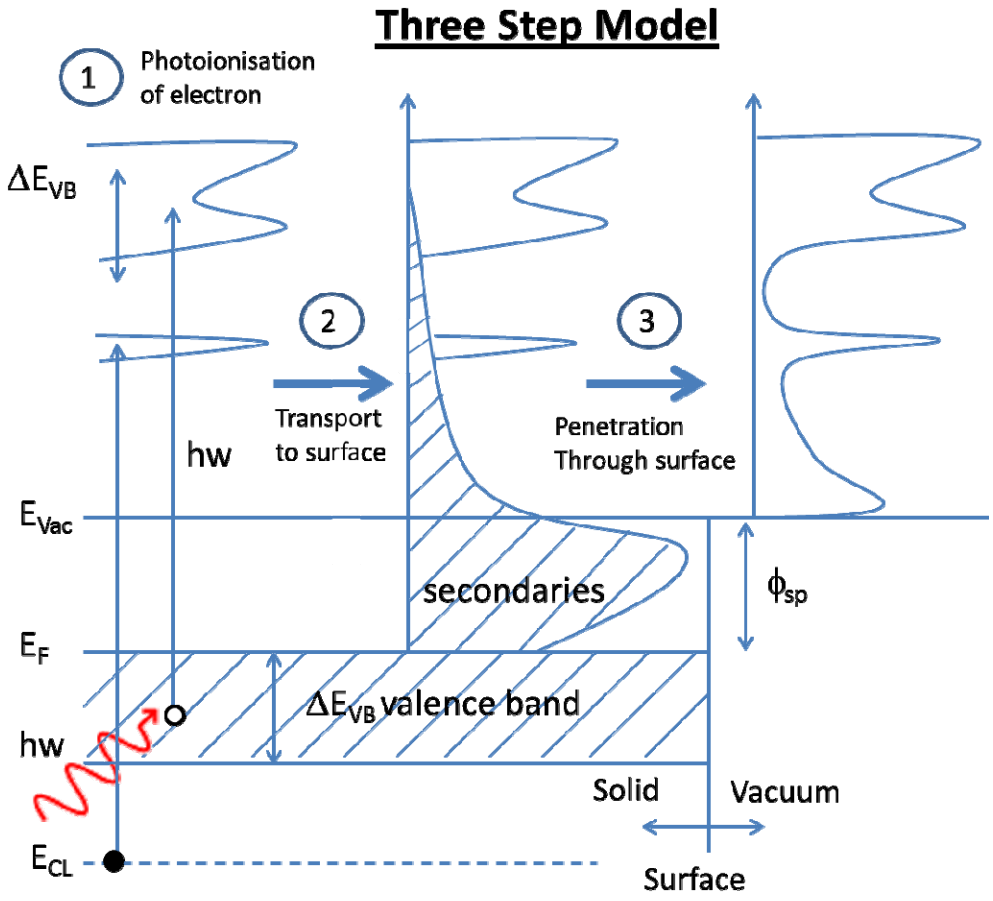

Fig. 3.2: Schematic illustrating photoemission as a three-step process: (1) Photoionization of electrons with incident photons with energy of hv; (2) Emitted travel to the surface with production of secondaries (shaded) as a result of inelastic scattering; (3) Electron penetration through the surface and escape to vacuum. Note that electrons can be emitted from the valence band (empty circle) or deeper in the core levels (filled circle) and ϕ_{sp} represents the work function of the spectrometer. This schematic is a variation adapted from ref. 128.

Photoemission can be understood as the excitation of an electron from an initial bound state to a final state that can be described by a damped wave function (which includes matching of momentum at the surface). Despite the photoemission process being inherently a one-step process, the three-step model (shown in Fig. 3.2) is particularly useful in summarizing the essential theories involved in XPS.[129] The first step is the photoionization process, which involves the interaction of the electromagnetic wave with the electrons in the solid, and it is described by the "Fermi's golden-rule" transition probability.[75] This optical excitation essentially results in a direct vertical transition in the reduced zone scheme. When the electron does not encounter any loss mechanisms, a photoelectron with kinetic energy equal to the incident photon energy minus its binding energy (BE) is emitted.[130] Initial and final state effects can affect the BE at this point and these are discussed in section 3.2.1.2.

The second step involves the transport of the electron from the bulk to the surface. A large number of electrons undergo inelastic scattering processes such as electron-plasmon or electron-phonon scattering and contributing to a secondary background, or otherwise known as secondaries. Besides forming secondaries, other important processes like bulk plasmon losses occur during this step, which contributes to the important spectral features discussed in section 3.2.1.3. Furthermore, the probability that an electron can reach the surface without inelastic scattering is described phenomenologically by the mean-free path, λ (see section 3.2.1.5). Photoemission is a highly surface sensitive technique because of the typically low λ values.

The third step accounts for surface effects which affect the photoemission spectrum. This is described by the scattering of the Bloch electron wave from the surface-atom potential. The vertical component of the electron wave vector is changed due to the need to overcome the work function of the spectrometer (seen in Fig. 3.2). This has implications in the measurement of lower kinetic energy electrons in work function measurements. In addition to this, other pertinent surface effects include surface plasmons and surface dipoles, which can possibly affect the kinetic energy of the photoelectrons and these are discussed in sections 3.2.1.3 and 3.2.1.6 respectively.

3.2.1.1. Instrumentation

Before describing the XPS spectral analysis, it is useful to review the instrumentation. The primary components include the vacuum system, X-ray source and electron energy analyzer.[131] In this study, our photoemission experiments are performed in a VG ESCALAB 220i-XL system with the background pressure in the analysis chamber kept in the low 10^{-10} Torr range using an ion gettering pump and a titanium (Ti) sublimation pump. The latter can be switched on to lower the chamber pressure by coating the surrounding chamber walls with a thin film of clean Ti that helps to getter residual gas (e.g. oxygen and moisture). This ultra-high vacuum (UHV) condition is necessary due to three reasons. Firstly, the photoelectrons must be able to travel from the sample to the analyzer without colliding with the gas phase particles. Secondly, the X-ray source requires vacuum conditions to remain operational. Thirdly, this is to ensure a clean sample surface since contaminants can easily affect this surface sensitive technique. The loading of samples is performed using a load-lock chamber

(supported by a turbomolecular pump) which is isolated from the main analysis chamber.

The X-ray source is produced by impinging a high energy electron beam (~10 keV) onto a target. This process creates core holes which in turn generate fluorescence X-rays that is used for the XPS experiments. The characteristic X-ray fluorescence possesses different energies and natural line width for different materials. In this study, a monochromatic Al Kα source is being used. This is a common energy source for laboratory use because it is able to provide a sufficient energy source of 1486.6 eV with a narrow line width of 0.85 eV which is capable of giving a good energy resolution. The use of a monochromatic energy source is important to avoid other weaker (satellite) fluorescence lines and Bremsstrahlung radiation which may contribute to ghost peaks. Also, the monochromatic source is able to narrow the energy spread of X-rays to give a better energy resolution. The spot size of the XPS equipment used in this study is 700 μm in diameter.

Lastly, this system uses a concentric hemispherical energy analyzer with a magnetic immersion lens (XL lens) to maximize the photoelectron signals. The analyzer was calibrated with pure gold, silver, and copper (polycrystalline) standard samples by setting the Au $4f_{7/2}$, Ag $3d_{5/2}$, and Cu $2p_{3/2}$ peaks at BE of 83.98 ±0.02 eV, 368.26 ±0.02 eV, and 932.67 ±0.02 eV respectively. The Fermi edge was calibrated using a pure nickel sample. In addition to collecting the photoelectrons, the lens system also retards the electrons such that their kinetic energy (KE) becomes close to the pass energy of the energy analyzer. The concentric hemispherical energy analyzer contains two concentric hemispheres

with radius R_1 and R_2. A potential of ΔV is applied across both hemispheres such that the outer one is negative with respect to the potential at the centre line, $R_0 = (R_1 + R_2)/2$. This centre line potential is also equivalent to the pass energy (E_p) which affects the energy resolution (ΔE) of the photoelectron peaks. By keeping E_p constant, ΔE is maintained constant since the analyzer resolution, defined as $\sim\Delta E/E_p$, is fixed at a certain value. This relationship shows that to achieve a better resolution ΔE, one needs to lower the pass energy E_p. In this study, the high energy resolution and survey scans are recorded with pass energies of 10 eV and 150 eV, respectively. Because of the lower signal intensity (as a result of lower E_p), at least ten scans are typically carried out for the high energy resolution spectra. Once the electrons have passed through the analyzer, they are counted using a multichannel array.

3.2.1.2. Binding energy shifts

The crux in the interpretation of the photoelectron spectrum lies in the understanding of binding energy (BE) shifts. The BE of a photoelectron is simply the difference in energy of the (n-1) electron final state and the initial n electron state. A first approximation for BE comes from the Koopman's theorem which states that the BE is simply the negative orbital energy calculated from the Hartree-Focke method.[132] In other words, this theorem adopts a "frozen orbital approximation" whereby the remaining orbitals are the same in the final state as in the initial state. However, in reality, final state effects must be accounted for. These final state effects occur because of the rearrangement of electrons to screen

or minimize the electrostatic effect due to the sudden creation of the core hole when the electron is emitted.

Initial state effects will firstly be discussed. The initial state is defined as the ground state of the atom prior to the photoemission process. This effect contributes greatly to chemical shifts which defines one of the main uses of XPS. As such, XPS is also known as electron spectroscopy for chemical analysis (ESCA). Such effects are best observed using core electrons which exhibit sharp peaks. Typically, when the atom becomes a positive ion, i.e. gains positive charges, Q, the BE of the remaining electrons increases. This is because losing electrons implies lesser screening of the positive nucleus on the remaining electrons. As such, the core electrons become more tightly bounded to the nucleus, i.e. higher BE. Taking into account the additional influence of fields produced by other atoms (giving rise to potential energy, V), the resultant BE shift (ΔBE) between two compounds A and B can be quantitatively described using a simple charge potential model as follows:[133]

$$\Delta BE(A,B) = K(Q_A - Q_B) + (V_A - V_B), \qquad (3.4)$$

where K is the coupling constant which is related to the Coulomb interaction between the valence and core electrons.

As mentioned earlier, final state effects can also have a significant impact on the overall BE. Due to the creation of a positive core hole, electron rearrangement on a faster time scale can occur, thus resulting in a change of the BE. One of these effects is relaxation and this is usually dependent on the density of free and mobile electrons. This can be classified in terms of intra-atomic and extra-atomic

relaxation. The former arises due to electrons within the atom while the latter is due to electrons from surrounding atoms (see section 4.1.2.2). Other types of final state effects include multiplet splitting and shakeup satellites. These often show up as distinctive spectral features and are described in section 3.2.1.3.

Besides initial and final state effects, a change in the reference energy level can also affect the BE. These external effects are not directly related to the photoemission process itself and include other electrostatic effects such as band bending, interface dipoles and charging. Since the measured BE is always referenced to the Fermi level of the spectrometer, which is tied to that of the sample, band bending will cause a shift in the entire photoelectron spectrum.[134] A typical band bending region can cover up to a range on the order of hundred nanometers as opposed to the probing depth of about 3 to 12 nm for XPS. As such, unless the substrate is heavily doped, such band bending effects can be negligible. On the other hand, dipoles present at the interface manifest as a potential drop at the vacuum level, which once again results in a change of the reference energy level.[135,136]

Lastly, charging in dielectric films can lead to BE shifts, and even spectral peak broadening (see section 3.2.1.4), because the insulating film is unable to compensate for the electrons lost in the photoemission process. Correction for this charging effect in insulators is a tricky problem. Some methods have been proposed in the literature to overcome this. One way is to flood the sample with a monoenergetic source of low-energy (< 20 eV) electrons in order to neutralize the generated core holes.[131] Another common approach is to align the shifted

photoelectron spectrum to a reference peak, i.e. adventitious carbon C1s energy at 285 eV.[137] This allows a fairer comparison across samples. However, these methods have their disadvantages and in this work, the use of a novel time-dependent method is proposed to correct for charging effects (see section 4.1.2.1).

The theory behind the time dependence of insulator charging will next be discussed. In electrostatics, in the absence of an external electric current, an electric charge density (ρ) will decrease according to an exponential time dependence manner (shown in Eq. (3.5)) when embedded in a medium of electrical conductivity (γ) and permittivity (ε), as follows:[138]

$$\rho(t) = \rho(0)\exp(-t/\tau), \tag{3.5}$$

where the dielectric time constant, $\tau = \varepsilon/\gamma$, is a measure of the residence time of a mobile charge locally set at a point inside a material. Note that $\varepsilon = \varepsilon_0\varepsilon_r$, where ε_r is the relative dielectric constant of the material and the permittivity of free space $\varepsilon_0 = 8.85 \times 10^{-12}$ F/m. The recombination rate equation shown by Eq. (3.2) is derived from the conservation of electric charge, Ohm's law, and Gauss's theorem.[139] Expectedly, τ is negligibly small ($< 10^{-3}$ s) for both metals and most semiconductors due to their low resistivity ($1/\gamma$) values ($< 10^{-2}$ Ω–m).[140] However, typical resistivity values for common oxides like Al_2O_3 or SiO_2 can range from 10^{12}-10^{14} Ω–m, which amounts to τ values of between 77 to 7800 s.[141] During X-ray irradiation, trapped charge densities are expected to increase as a function of time. Assuming these charges increase linearly as a first approximation, then the resultant variation of charge density with time after considering the recombination rate is

$$\rho(t) = \rho(\infty)[1 - \exp(-t/\tau)], \quad (3.6)$$

where $\rho(\infty)$ is the charge density when the system reaches steady state. As expected, τ can vary due to various factors such as actual grounding conditions, and different conductivity of the film due to different processing conditions. Furthermore, the focusing of X-rays affects τ because the conductivity changes under X-ray irradiation.

3.2.1.3. Spectral features

In this section, common features such as the rising background, X-ray induced Auger electrons, spin-orbit doublets, plasmon losses and other satellite features are discussed. These distinctive features are generally discernable as opposed to the more subtle shifts mentioned in the previous section. The common rising background (with increasing BE) easily observed from wide survey scans is attributed to inelastic scattering of the photoelectrons during the second stage in the three step model. Due to the nature of the collisions within the solid, there is a continuum of energies (not discrete) of such escaping photoelectrons, therefore forming the cumulative background signal.

In addition to photoemission related peaks, prominent peaks such as *X-ray induced Auger electron peaks* can ride upon the secondaries background. The Auger electron emission is a consequence of the relaxation of the excited core hole. Here, the Auger electron is ejected because of the energy gained from the filling of the core hole by an electron from a higher energy level. The Auger peaks

are generally much broader than core level peaks but are still useful for obtaining information such as extra-atomic relaxation (to be discussed in section 4.1.2.2).

Spin orbit splitting exists for all photoemission (zero loss, main) peaks except for the *s* orbitals, because of the possibilities of two final states, i.e. spin up and spin down. If there is an open shell (quantum number $l > 0$, i.e. *p*, *d*, or *f* orbital) with two states of the same energy (orbital degeneracy), a magnetic interaction between the spins of the electron and its orbital angular momentum leads to a splitting of the degenerate state into two components. This is also known as spin-orbit coupling or *j-j* coupling ($j = l + s$) where $s = +1/2$, or $-1/2$. The ratio of their respective degeneracies, $2j+1$ determines their respective intensities with the higher *j* number having a lower BE. Furthermore, the doublet separation increases for orbitals further from the nucleus, i.e. $p > d > f$ within a given atom.

Another important component of spectral features is that of *plasmon losses*. Plasmon is a quantum of oscillations of collective longitudinal excitation of the conduction electron gas. The charge of the electron can couple with the electrostatic field fluctuations of the plasma oscillations resulting in a periodic energy loss of the electron which is equal to integral multiples of the plasmon energy. It is equally possible to obtain plasmons in dielectrics, as well as in metals, when the entire valence electron gas oscillates back and forth with respect to the ion cores. These excitations of the conduction-electron system (plasmons) can originate from (1) the de-excitations of the photohole during the photoemission process (intrinsic) or (2) electron-electron or electron-ion interactions as the photoelectron is being transported to the surface (extrinsic).[128]

Due to many body effects, *satellite peaks* can also be observed. These peaks are not explicable on the basis of a simple one-electron transition theory for an ionization process. For instance, these satellites can occur in a dielectric because of inelastic losses due to inter-band excitations, or shake processes. Shake processes are final state effects which occur when the photoelectrons are excited into unoccupied states above the Fermi level (shake up) or into continuum states (shake off).[142] On the other hand, inter-band transition losses occur for dielectrics when the photoelectron loses energy to excite an electron from the valence to conduction band.[143] This is particularly useful since this energy is equivalent to the band gap of the dielectric.[144] Also fortunately, for most dielectrics, the nearest valence-electron plasmon loss is generally much larger than the inter-band transition losses.[145] As such, extraction of the onset of inter-band transition loss (i.e. bandgap value) can be made by determination of the threshold energy in the energy loss spectrum (shown in section 4.1.1).

Another common satellite peak which occurs due to formation of more than one final state is the *charge transfer satellite*. These are often observed in systems containing *d* and *f* orbitals such as transition and rare earth metals and their compounds.[146,147] The formation of a core hole due to photoemission produces an addition Coulomb interaction (U_{cd}). For example, in Cu dihalides, the Cu 3*d* shell is situated in energy above the ligand valence orbitals in its ground state ($3d^9\underline{L}$ configuration). However, the extra U_{cd} energy can pull this level below the top of the ligand valence band, making it energetically favourable for the valence ligand electrons to be transferred to the empty 3*d* orbital ($3d^{10}\underline{L}^{-1}$ configuration). These two different final states then make up the satellite and main lines respectively.[128]

3.2.1.4. Peak fitting

Accurate peak fitting is necessary to distinguish spectra that overlap each other and also to carry out quantitative analysis. This work uses the Thermo Avantage v4.12 software for peak fitting. The more complicated peaks (such as that of metals) require additional parameters such as the tail mix, height and exponent due to their asymmetry, while most peaks only involve simple parameters such as the full-width at half-maximum (FWHM) and Lorentzian/Gaussian mix ratio. The first step in peak fitting involves subtraction of the spectrum background (i.e. contributed by secondaries or plasmon losses). This is important especially for weak scans with low signal-to-noise ratio as the background affects the accuracy of the quantification results. In this study, a Shirley subtraction is adopted.[148] This method involves iterative analysis which is shown to be more accurate in most cases.

The FWHM is an important parameter in peak fitting which is affected by mainly the natural line-width and instrumentation contributions. The natural line-width of a photoemission spectrum is of Lorentzian lineshape and is determined only by the life-time of the core hole state (τ). This intrinsic peak width (in eV) can be obtained from Heisenberg's uncertainty relationship as follows:

$$\Gamma = h/\tau, \qquad (3.7)$$

where h is Planck's constant (in eV s). Generally for a given element, the value of Γ increases (i.e. τ decreases) for shell orbitals closer to the nucleus (i.e. inner shell orbitals). This is because inner shell orbitals tend to be more easily filled by electrons from outer shells, i.e. smaller τ. Subsequently, with increasing atomic number, the probability of filling the core hole increases (with increasing valence

electron density), and hence the core hole life-time also decreases (i.e. Γ becomes larger). Besides intrinsic factors, instrumentation effects such as (1) the energy spread of the incident X-rays and (2) the resolution of the analyzer can broaden the width of the photoemission peak. These effects are usually of Gaussian lineshape. In an insulator, differential charging effects can result in a broadening of the Gaussian contribution to the line-width. Satellite features, as discussed earlier, can also contribute to peak widths. These can arise from vibrational broadening, multiplet splitting and shakeup satellites.

In order for accurate quantification of the photoelectron spectrum, it is imperative to take into account the sensitivity factor. This is because different elements (and its respective subshells) have different sensitivity to photoionisation. The photoionization cross-section σ_{ij} is the probability that an incident X-ray will create a photoelectron from the *j*th orbital of element *i*. It is given by an overlap of the initial and final state wavefunctions. These values have been theoretically tabulated by Scofield and also experimentally determined by Wagner.[149,150] Lower atomic number elements tend to have lower σ_{ij} implying that such elements are less sensitive to photoionization.

3.2.1.5. Electron mean free path and quantification

The usefulness of photoemission for interface study of thin films is largely due to its desirable sampling depth, i.e. ~3 – 12 nm (depending on the energy source).[131] This small sampling depth, implying surface sensitivity, is a consequence of the low photoelectron mean free path. Since this parameter affects the film thickness

determination and other quantitative analysis, there have been extensive studies conducted on it.[151,152] In essence, the inelastic mean free path, (IMFP) has been defined as the average distance an electron can travel before undergoing an inelastic scattering. However, it was soon found that elastic-electron scattering on the trajectories of photoelectron signals can contribute to additional losses.[151] With this, the term attenuation length (AL) was introduced to give a more accurate description. Having taken into account the elastic scattering effects, AL is found to be less than the related IMFP by 30%.[153]

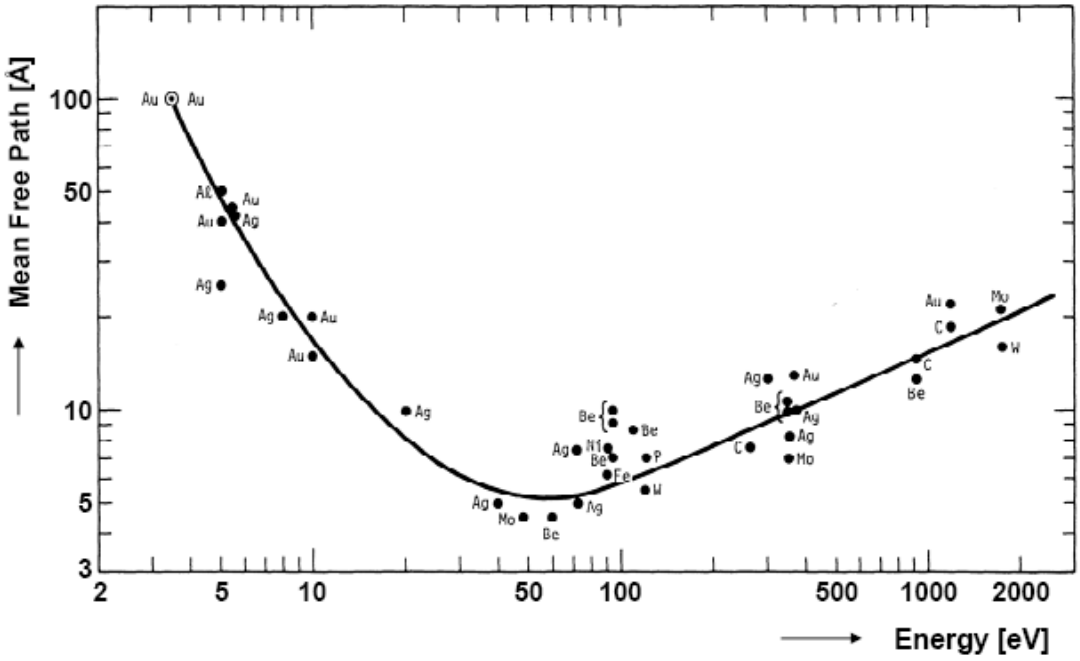

Fig. 3.3: Experimental and theoretical mean free path plotted against the electron kinetic energies for various elements. [154]

Another important observation from the mean free path studies in the literature is that of the universal mean free path, shown in Fig. 3.3. Interestingly, the mean free path depends strongly on the electron kinetic energy but not on the material itself. A least square fit of the experimental results show that the IMFP generally

follows a relationship given by Eq. (3.8) and Eq. (3.9) for elements and inorganic compounds, respectively.

$$\lambda = 538/E^2 + 0.41(aE)^{1/2} \text{ monolayers} \quad (3.8)$$

$$\lambda = 2170/E^2 + 0.72(aE)^{1/2} \text{ monolayers} \quad (3.9)$$

where a is the monolayer thickness (nm) and E is the electron kinetic energy (eV). The relationships shown above were developed empirically and shown to be consistently invariant of the matrix element. The theoretical explanation for this invariance is that the IMFP is mainly determined by electron-electron collisions as opposed to electron-phonon collisions which only occur at very low electron energies.[128] For electron energies of interest (excluding the very low energies), the electrons in the solid behave like a free-electron gas whereby the bonding properties are not significant. This loss function is then only a function of the electron density which does not vary much across materials.[128]

As mentioned, the measurement of IMFP (λ) is not a trivial problem. Nonetheless, for the purpose of the work in this project, λ is obtained through overlayer experiments. This will be sufficient to provide quantification analysis with reasonable accuracy. Beer's law equation states that electrons will be attenuated from its original intensity (I_0) and transmitted with an intensity of I_k through a specimen of thickness (d) as shown in Eq. (3.10).

$$I_k = I_0 \exp(-d/\lambda \cos\theta). \quad (3.10)$$

In Appendix III, attenuation equations are derived for some cases which are particularly useful for film thickness determination.

3.2.1.6. Valence band and work function measurements

Due to the low incident photon energy for ultra-violet rays (He I: 21.2 eV, He II: 40.8 eV), the photoionization cross-section for the valence electrons is greatly increased along with higher surface sensitivity (see Fig. 3.3).[131] This makes UPS a useful tool for fundamental studies of the valence band electronic structure, such as the density of states (DOS). Occupied surface states due to dangling bonds, dimers or back-bond states can also be observed for clean, cleaved semiconductor surfaces.[155] For instance, the change in the electronic structure upon submonolayer coverage of metal atoms on the Si surface can be investigated.[156] It is sometimes also possible to deduce additional surface structural information. The UPS technique is also useful for the identification of molecular species on organic surfaces by measurement of the molecular orbital energies.[157] Moreover, angular resolved UPS can be used to investigate the occupied component of the electronic band structure.[75]

In this work, UPS (with a He I energy source) is used to measure electron affinities and work functions for high-k oxides and metals, respectively. Electron affinity (χ) can be obtained using Eq. (3.11), which is derived based on the conservation of energy, where W is the spectral width defined as the energy distance from the valence band maxmium (VBM) to the secondaries cut-off energy (denoting the vacuum level). Both of these energies can be determined using a linear extrapolation method.[158]

$$\chi = hv - E_g - W. \qquad (3.11)$$

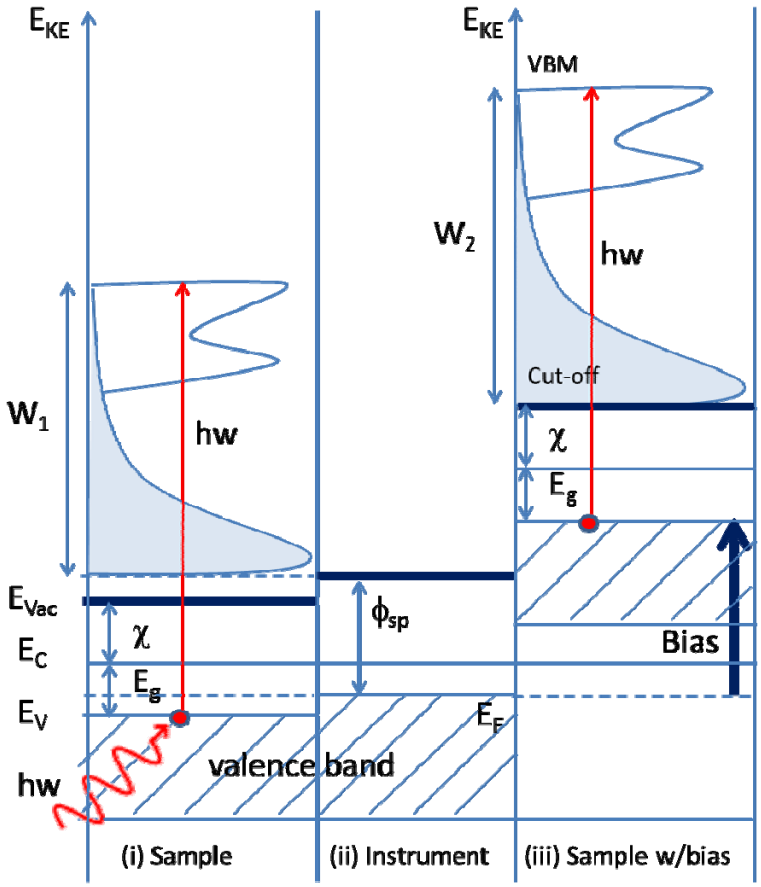

Fig. 3.4: Energy diagram schematic illustrating the measurement of electron affinity χ using UPS with a photon energy of hv = 21.2 eV. Application of a negative bias (black bold arrow) is necessary to overcome the spectrometer work function ϕ_{sp} so that χ can be accurately extracted from the measured spectral width of W_2. This width is defined as the energy distance from the cut-off energy of the secondaries (shaded) to the valence band maximum (VBM).

Figure 3.4 shows that the application of a negative bias to the sample is important in order to accurately determine χ. This is because without the application of a bias, the secondaries from the sample (of lowest energy) may be lost since they cannot overcome the spectrometer work function (see Fig. 3.4(i) and 3.3(ii)). This reduces the value of the measured spectral width, W. Furthermore, the secondaries can also be generated from the spectrometer itself which may complicate the measured spectrum.[159] Application of a large enough bias can separate this contribution from the true secondaries from the sample. The other issue comes

from the high surface sensitivity of the UPS technique as compared with XPS. In particular, the effects of surface carbon contaminants on UPS measurements are investigated in section 4.1.3.1.For metals, UPS can be used to measure its work function (Φ_m) in a similar manner:

$$\Phi_m = hv - W', \tag{3.12}$$

where W' is defined as the energy distance from the secondaries cutoff to the Fermi edge. The Fermi edge should ideally be infinitely abrupt but is however broadened due to the limited spectrometer resolution and thermal effects.[160] The Fermi edge is typically determined as the center of the slope, as shown in Fig. 3.5.

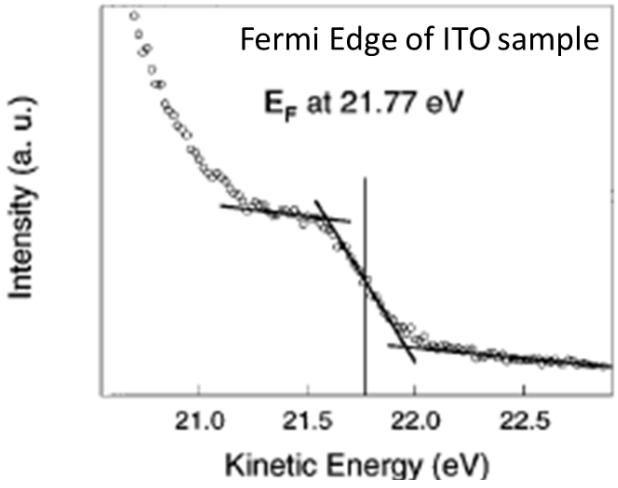

Fig. 3.5: UPS Fermi edge region of an ITO film.[160]

3.2.2. Transmission electron microscopy

Transmission electron microscopy (TEM) is a technique which can be used to study the interfaces of thin films due to its atomic scale resolution.[161] In this technique, a high energy electron beam (typically 100 to 400 keV) is transmitted through a very thin sample to form a high resolution image. In this regard, TEMs are similar to optical microscopes in principle, but use high energy electrons instead of photons. This is because the resolution of the optical microscope is

limited by the wavelength of light (410-660 nm) as dictated by the Rayleigh criterion.[162] Due to the wave-particle duality relationship from De Broglie, the wavelength of electrons becomes smaller when their momentum increases. For instance, a 200 keV electron possesses a wavelength of ~0.025 Å which is much smaller than visible light wavelengths. Theoretically, this small wavelength allows one to achieve extremely high resolution of around 1.5 Å within sub-atomic scale, as dictated by the diffraction limit. In reality, this resolution is also affected by other factors related to wave optics given by the Scherzer resolution equation, Eq. (3.13).[163] The minimum feature size that can be resolved, d_{min}, is given by

$$d_{min} = 0.43(C_S\lambda^3)^{1/4}, \quad (3.13)$$

where C_s is the spherical aberration coefficient and λ is the electron wavelength. On the other hand, higher accelerating voltage in the TEM can have drawbacks such as irradiation damage to the sample and high equipment cost.

3.2.2.1. Instrumentation

In this study, HR-TEM imaging was carried out using a Philips CM300 TEM system, equipped with a field emission gun (FEG), to investigate the interfaces of Y_2O_3 films on Ge on the atomic scale. The TEM analysis is carried out using an accelerating voltage of 300 kV giving a point-to-point spatial resolution of 1.7 Å. This can be approximately derived by using a spherical aberration coefficient of 0.65 mm in Eq. (3.13). The Philips CM300 TEM also has an “ultra-twin” objective lens and is able to resolve atomic columns which allows for crystal structure determination using bright-field images, dark-field images and diffraction patterns.

Besides HR-TEM imaging, this instrument is also equipped with an energy dispersive X-ray spectrometer (EDS) which is used to provide elemental information. Essentially, it measures the energy of the X-ray fluorescence which is characteristic of the electron transitions between inner orbits (i.e. relaxation process) after inner-shell ionization.[164] Note that the spectral resolution of X-ray fluorescence techniques is generally very poor and the peaks from different elements can also overlap. As such, typical EDS can only provide elemental information even though it can theoretically yield chemical information. Furthermore, the sensitivity of this technique varies with the thickness of the sample but is generally low due to the low X-ray yield.

3.2.2.2. Sample preparation

Due to the requirement of very thin samples for the electron beam to be transmitted, sample preparation becomes a crucial part of TEM measurements. Traditionally, mechanical lapping-polishing and ion milling was used and successful sample preparations were not easy.[165] In this work, focused ion beam (FIB) milling is being employed.[166] This is carried out in the FEI Nova Nanolab DualBeam 600i system with an electron beam (0.2 - 30 kV, < 20nA) capable of 1.1 nm spatial resolution and a Ga^+ ion beam (0.5 – 30 kV, 20nA) capable of 7 nm spatial resolution. The ion beam is used to raster over given portions of the sample in order to obtain a cross-sectional specimen of the sample while the imaging is achieved using the electron beam. Prior to FIB, the samples in this study were coated with a layer of gold (Au) of ~200 nm to protect the surface of the film. Upon loading into the FIB chamber, another ~1 μm of platinum (Pt) capping layer

is further deposited in order to protect the surface from damage done by ion bombardment. The introduction of FIB has made TEM sample preparation easier and can significantly reduce the amount of time spent compared to traditional sample thinning methods.

3.2.3. X-ray diffraction and ellipsometery

The X-ray diffraction (XRD) technique makes use of the coherent elastic scattering (i.e. Rayleigh scattering) of incident X-rays to determine the structure of a crystalline solid. Typically, interatomic distances in a solid are of the order of angstroms. In order to investigate microscopic structures of this scale, electromagnetic probes must have wavelengths of at least the angstroms scale, corresponding to energies of tens of keV.[167] By treating a crystal as consisting of parallel planes of atoms, with lattice spacing of d, intense peaks of scattered X-rays (i.e. Bragg peaks) are observed when there is constructive interference. This occurs when the path difference is an integral number (n) of wavelengths (λ) according to the Bragg condition:

$$n\lambda = 2d\sin\theta, \tag{3.14}$$

where θ is the angle of incidence of the X-ray. The von Laue formulation presents an alternative approach by using reciprocal lattice planes (as opposed to direct lattice planes in the Bragg formulation) to describe constructive interference of X-rays. Accordingly, the use of the Ewald sphere allows one to determine which reciprocal lattice points will result in a diffraction signal for a given wavelength of incident radiation.[164] In order to experimentally search for Bragg peaks, one can vary the incident wave vector **k**, by varying either the wavelength of the incident

beam or its direction (i.e. orientation of the crystal with respect to the incident direction). The interference of these scattered rays is represented by a geometrical structural factor which affects the overall intensity of the Bragg peak. Due to this structural factor, specific crystal structures (e.g. body-centered cubic) will yield characteristic periodic Bragg peaks which can be used for identification. On the other hand, lack of Bragg peaks across a reasonable range of 2θ values signifies the lack of crystallinity.

Ellipsometery is a sensitive and quick technique to characterize thin dielectric films, based on the reflection of polarized light. When a linearly polarized light of a known orientation is reflected at oblique incidence by a surface, the reflected light becomes elliptically polarized. This polarization change is described by the ratio of the Fresnel reflection coefficients for p- (r_p) and s- polarized (r_s) light, which are related to the two measurable values, ψ and Δ.[168]

$$r_p / r_s = \tan \Psi \exp(j\Delta). \qquad (3.15)$$

Physically, $\tan \Psi$ represents the measured ratio of the modulus of the amplitude reflection ratio while Δ represents the phase difference between p- and s-polarized reflected light. The propagation of plane waves through a single film on a substrate is modeled after two propagation matrices built from the Fresnel coefficients. The reflectivity coefficient derived will then be a function of the film thickness, and the refractive indexes of the substrate and the film. By knowing the refractive indexes, one can then obtain the value of film thickness. Due to the periodic nature of both the p- and s-polarized reflectivities, the reflectivity at a given angle of incidence (φ) is the same for film thicknesses differing by

$$D = \frac{\lambda}{2\sqrt{n_1^2 - (n_a \sin\varphi)^2}}, \tag{3.16}$$

where n_1 and n_a are the refractive indexes of the film and ambient, and λ is the wavelength of light. In this study, the ellipsometer L2W26D 488 is being used to measure the thickness of the deposited high-k oxide films. By using fixed refractive indexes of 1.80, 1.86, 1.90, 1.88, and 1.79 for $LaAlO_3$, Y_2O_3, HfO_2, La_2O_3, and Al_2O_3, the respective film thicknesses can be obtained.

3.2.4. Electrical measurements

Electrical characterization of MOS capacitors is necessary to study important device parameters such as the equivalent oxide thickness (EOT), flatband voltage (V_{FB}), interface trap density (D_{it}), and leakage current. These parameters are intimately related to the quality of the high-k oxide/semiconductor interface but are not obtainable from the physical characterization methods discussed earlier.

3.2.4.1. High frequency capacitance-voltage measurements

The high frequency capacitance-voltage (HFCV) measurement allows one to obtain important parameters such as the equivalent oxide thickness (EOT) and the flatband voltage (V_{FB}). Firstly, EOT is defined as the equivalent hypothetical thickness of a high-k film supposing it possesses the same dielectric constant as SiO_2. Typically, this value is deduced from the maximum capacitance (C_{max}) in the HFCV plot where in the accumulation mode, the total measured capacitance, $C_{tot} = C_{max} = (1/C_{ox} + 1/C_{sub})^{-1}$ is approximately C_{ox}. This is based on the fact that the majority carriers can respond to the electrical bias and substrate capacitance

(C_{sub}) becomes much larger than C_{ox}. However, this approximation does not hold when the oxide capacitance C_{ox} becomes comparable to C_{sub}. One indication of this is a non-saturating C_{max} even under very strong accumulation. A few techniques are proposed to improve the accuracy of EOT determination. These are discussed in more detail in section 6.1.2.1.

Next, the determination of V_{FB} is discussed. V_{FB} is a condition whereby the semiconductor (Si in this case) is free of any electric field (i.e., no band bending). It can be obtained experimentally by reading off the experimental HFCV plot at the theoretical flatband capacitance (C_{FB}) which is based on the substrate doping concentration (N_{sub}) and C_{OX}. It can be shown that C_{FB} is given by:[169]

$$C_{FB} = [1/C_{FB,sub} + 1/C_{ox}]^{-1} = [1/\sqrt{kT/(q\varepsilon_{Si}N_{sub})} + 1/C_{ox}]^{-1}, \quad (3.17)$$

where $C_{FB,sub}$ is the substrate flatband capacitance, k is the Boltzman constant, T is the temperature, q is the electronic charge, and ε_{si} is the dielectric constant of Si. N_{sub} can be derived from the minimum capacitance (C_{min}) from the experimental HFCV curve.

Since V_{FB} is defined as the condition that is free of internal electric field, it is therefore sensitive to any oxide charges within the gate stack and the relative alignment of the two materials. Equation (3.18) shows a simplified expression for V_{FB} taking into account the work function difference and oxide trap charges, Q.

$$V_{FB} = \frac{\Phi_{ms}}{q} - \frac{Q}{C_{OX}} = \frac{\Phi_{ms}}{q} - EOT\frac{Q}{\varepsilon_0\varepsilon_{ox}}, \quad (3.18)$$

where Φ_{ms} is the metal work function, EOT is the equivalent oxide thickness, q is the electronic charge, ε_0 is the permittivity of free space and ε_{ox} is the dielectric constant of silicon oxide. Q represents the trap charges at the interface.

In reality, an interfacial layer (IL) often exists during the fabrication of the MOS device and different interface dipoles and charges can be present at the interface, in addition to the oxide charges in the bulk oxide. In order to separate the effects from the charges and the dipoles, one can plot V_{FB}-EOT for a whole range of varying oxide thickness and this is discussed in section 6.1.2.3. It is primarily because the dipoles are not affected by changes in EOT.

3.2.4.2. Conductance measurements

In 1967, Nicollian and Goetzberger proposed a conductance method to determine the interface trap density (D_{it}). Hitherto, this is one of the most sensitive methods, which is capable of detecting D_{it} of the order of 10^9 $cm^{-2}eV^{-1}$ and lower. In addition, the conductance technique is also able to provide additional information, such as the carrier lifetime (τ) and also information on surface potential fluctuations. Measuring conductance is advantageous as compared to other capacitance based methods, such as Terman's (high frequency capacitance) method, Berglund's (low frequency capacitance) method, and the combined high-low frequency capacitance method. In the capacitance methods, differences in capacitances must be calculated because the depletion capacitance is in parallel with the interface trap capacitance (see Fig. 3.7), resulting in large experimental errors. The conductance method, on the other hand, directly measures the energy

loss during the capture and emission of carriers by the interface traps. This conductance parameter will not depend on the substrate capacitance (i.e. C_D in Eq. (3.19) below).

Essentially, the conductance method is based upon modeling of the behaviour of traps as passive elements in an equivalent circuit. For simplification purposes, this method is usually carried out in the depletion region where effects from minority carriers can be neglected. Through some derivations shown below, a model is developed to extract D_{it} from a plot of G_p/ω versus frequency. Note that gate bias can be varied instead of frequency.

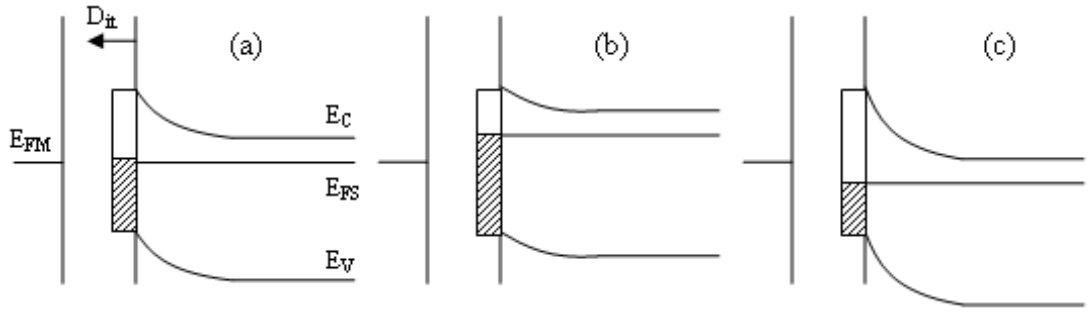

Fig. 3.6: Band bending diagram showing how gate bias affects the occupancy of interface traps for a n-type substrate. (a) No gate bias; (b) small positive gate bias; and (c) small negative gate bias.

Consider the case of a n-type substrate. Interface traps communicate with the substrate by exchanging charges, i.e. capturing or emitting electrons with the Si CB and holes with Si VB. Interface traps below E_F will be filled, while those above E_F will be empty. By applying small variations in the gate bias, the interface traps are filled as illustrated in Fig. 3.6.

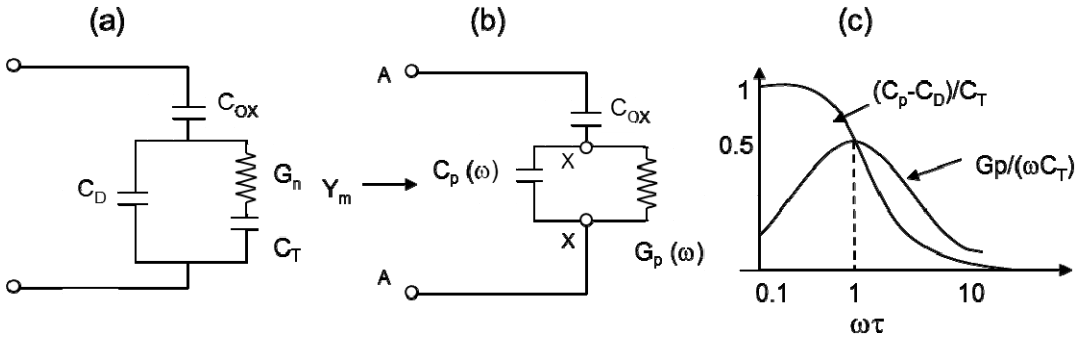

Fig. 3.7: (a) Equivalent circuit for a single-level interface trap with capacitance C_T , and conductance G_n , related to the capture of majority carriers, substrate capacitance of C_D in depletion, and oxide capacitance C_{ox}. (b) Measured admittance, Y_m across terminals A-A using the equivalent parallel capacitance C_p, and conductance G_p. (c) Plot of $(C_p-C_D)/C_T$ and $(G_p/(\omega C_T))$ as a function of ωτ.

The energy loss associated with the capture or emission of carriers (i.e. G_n for electrons) depends both on the speed of response of interface traps (τ) which is determined by their capture probability, and also on the interface trap level density, D_{it}. The ability of interface traps to store/trap charges (C_T) is proportional to its density, i.e. $C_T \approx qD_{it}$. One starts off by considering a single level trap. Its equivalent circuit is shown in Fig. 3.7(a). In this resistor-capacitor (RC) circuit, the time constant τ is given by C_T/G_n , which only varies with band bending, i.e. changes in bias. In Fig. 3.7(b), the circuit is simplified such that the parallel capacitance C_p and conductance G_p are used instead. Considering the depletion case without effects from minority carriers, C_p and G_p can be modeled as follows:

$$G_p/\omega = C_T\omega\tau[1+(\omega\tau)^2]^{-1}, \tag{3.19}$$

$$C_p = C_T[1+(\omega\tau)^2]^{-1} + C_D. \tag{3.20}$$

Using Eqs. (3.19) and (3.20), one can derive a plot shown in Fig. 3.7(c). At low values of ωτ, the interface traps can respond immediately to the slow changes in gate voltage. As such, $(C_p - C_D)/C_T \approx 1$ because $C_p = C_D + C_T$. As ωτ increases, the

interface traps will start to lag behind, resulting in a decrease in C_T. When $\omega\tau$ becomes very large, $(C_p - C_D)/C_T \approx 0$ because $C_p = C_D$. On the other hand, $G_p/(\omega C_T)$ reflects the energy loss when the interface traps lag behind the gate voltage. As discussed earlier, the interface traps will only lag behind for moderate $\omega\tau$ values, but not for very large and small $\omega\tau$ values. As predicted by Eq. (3.19), this energy loss reaches a peak value of 0.5 when $\omega\tau = 1$.

In reality, single-energy level traps do not exist. As such, one can model a distribution of such traps, i.e. parallel combination of single level traps with constant density and capture probability. To further generalize this model, one can take into account band bending fluctuations which lead to a dispersion of interface trap time constants. Expectedly, the general shape of the both plots, in particular $G_p/\omega C_T$ versus $\omega\tau$ (in Fig. 3.7(c)) is preserved even when the trap distribution is modeled differently because each individual trap is still modeled as an R-C circuit. Next, we discuss in particular how the $G_p/\omega C_T$ versus $\omega\tau$ plot can be obtained using the actual measurable quantities. G_p/ω can be calculated from the measured admittance, i.e. $(G_m + j\omega C_m)$ across terminals A-A. As shown in Fig. 3.7(b), this includes the oxide capacitance C_{ox}. Therefore correcting for C_{ox}, G_p/ω can be derived to be

$$\frac{\langle G_p \rangle}{\omega} = \frac{\omega C_{OX}^2 G_m}{G_m^2 + \omega^2 (C_{OX} - C_m)^2}. \tag{3.21}$$

In terms of varying $\omega\tau$, one can either change the frequency or gate bias. The latter is possible because τ varies as a function of band bending. As mentioned, the variation in frequency is being used in this study. Despite the general shapes

of the plots being similar, modeling of the trap distribution will introduce some corrections to Eqs. (3.19) and (3.20). With regards to the interface trap time constant dispersion model, the interface trap density (i.e. $D_{it} \approx qC_{it}$) is shown to be

$$D_{it} = (G_p/\omega)_{fp} / [qA.f_D(\sigma_s)], \tag{3.22}$$

where the subscript fp denotes the frequency at the peak of the conductance plot, $f_D(\sigma_s)$ is a function to account for band bending variations, q is the electronic charge of 1.6 x 10^{-19} Coulombs, and A is the area of the capacitor.

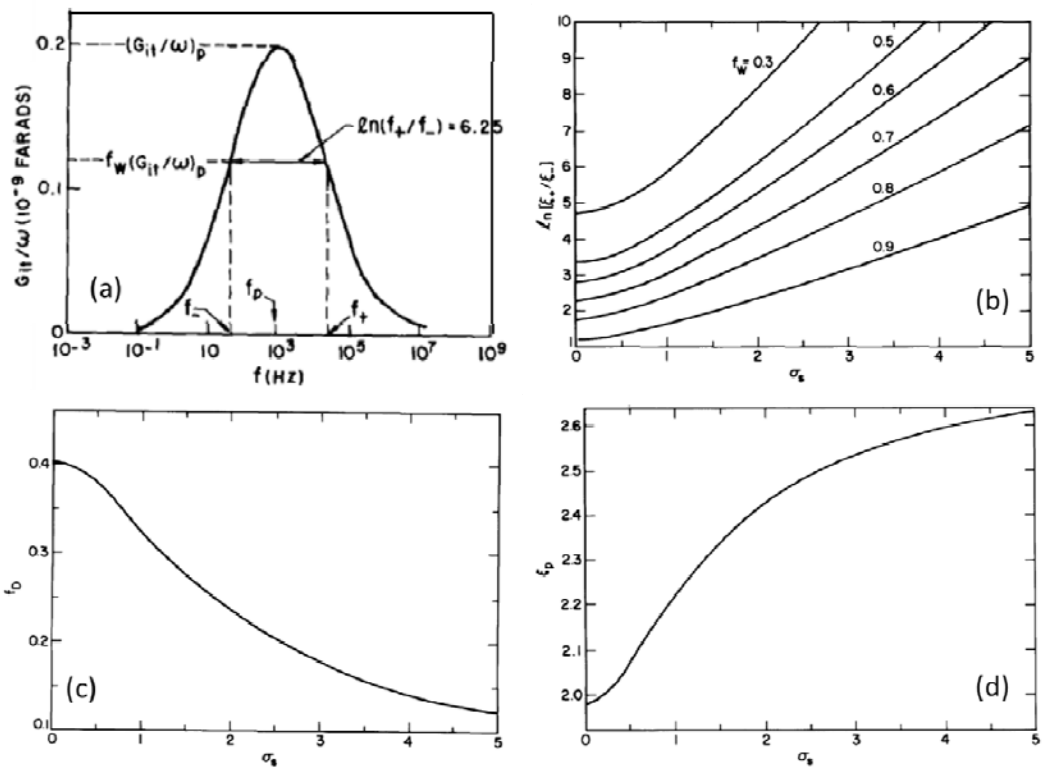

Fig. 3.8: (a) Plot of G_p/ω versus frequency whereby the width of the peak varies with the standard deviation of band bending (σ_s) in a manner shown in (b); the dependence of the function f_D and ξ_p on σ_s are shown in (c) and (d) respectively. Note that $\xi_p = \omega_p\tau_p$ [169]

First, the width of the peak is found to vary with σ_s in a manner shown in Fig. 3.8(b) which is always broader than the case of the single level trap model. Second, the maximum value for $G_p/(\omega C_T)$ is replaced with a function, $f_D(\sigma_s)$, which varies with the standard deviation of band bending (σ_s) as seen in Fig.

3.8(c). Note that the single energy trap model originally predicts the value of $f_D(\sigma_s)$ to be 0.5. Lastly, the $\omega\tau$ value where the peak occurs, i.e. $\omega_p\tau_p$, also varies according to σ_s. Note that the single energy level trap model predicts this to be 1 while the distribution of traps with constant density and probability predicts this to be 1.98. The interface time constant dispersion model gives a relationship shown in Fig. 3.8(d) whereby $\xi_p = \omega_p\tau_p$. By knowing ξ_p, one can calculate τ_p. To apply the corrections as mentioned above, one can simply read off from the universal plots in Fig. 3.8(a) to 3.7(d).[170]

Unfortunately, the conductance method is shown to be not as accurate for smaller bandgap semiconductors (such as Ge devices) due to the faster capture and emission of its minority carriers.[171] These contribute to an additional interaction between the traps and the minority carrier band at room temperature (biased in weak inversion) which was previously negligible for the case of Si because of its larger band gap. As such, conductance measurements for Ge capacitors have to be conducted under low temperatures.[172]

3.2.4.3. Leakage current-voltage measurements

This section reviews some of the common conduction mechanisms for high-k dielectrics, which includes the space-charge limited conduction (SCLC), Poole-Frenkel (PF) and Schottky (SC) emission mechanisms. Investigation of the current density versus voltage (J-V) relationship is useful for understanding of the conduction mechanism because each of the mechanisms usually shows characteristic J-V profiles.

Space-charge limited conduction (SCLC) can often play an important role in insulator leakage profiles. This is due to the low density of free carriers which easily results in space charge forces. A space-charge effect occurs when the injected carrier concentration is larger than its thermal equilibrium value, and the current generated is termed the space charge limited current. The SCLC theory comprises three limiting mechanisms, namely (I) Ohm's law ($J \propto V$), (II) space-charge limit, SCL ($J \propto V^2$) and (III) trap-filled limit (TFL).[173,174] Any presence of localized traps in the band gap affects mainly the transition between the regions, as will be discussed in detail later. The characteristic J-V equations involved in these mechanisms can be derived using the Poisson and continuity equations.

In the first region (Ohm's law), under extremely low gate voltage, the electrons trapped in the bulk oxide are thermally excited giving rise to a larger concentration of free charge carriers in thermal equilibrium (n_0) compared to the concentration of the injected carriers. Here, n_0 contributes to the current flow which is given by:

$$J_{Ohm} = qn_0\mu\frac{V}{d}, \tag{3.23}$$

where q is the electronic charge, μ is the electron mobility in the oxide film, V is the applied voltage, and d is the oxide thickness. This ohmic mode exists in an electrically quasi-neutral state where not all trap centers are filled at weak injection.

As the gate voltage is increased, the current injection is increased till a threshold voltage of V_{tr} which demarks the transition from the Ohmic to SCL region. This transition takes place when the carrier transit time (τ_c) becomes equal to the

dielectric relaxation time (τ_d). In this case, the injected excess carriers dominate the thermally generated carriers, and this threshold voltage is given by:

$$V_{tr} = \frac{8qn_0d^2}{9\varepsilon_r\varepsilon_0\theta}, \tag{3.24}$$

$$\theta = \frac{N_C}{g_n N_t}\exp(\frac{E_t - E_C}{kT}), \tag{3.25}$$

where ε_0 is the permittivity of free space, ε_r is the dielectric constant, θ is the ratio of free-carrier density to total carrier (free and trapped) density, N_t is the trap density, N_C is the density of states in the conduction band, g_n is the degeneracy of the energy state in the conduction band (~2), k is the Boltzmann constant, and E_t is the energy level of the traps below E_C. Upon reaching the second region (SCL), the J-V relationship is described by the Child's law:[175,176]

$$J_{Child} = \frac{9}{8}\mu\varepsilon_r\varepsilon_0\theta\frac{V^2}{d^3}. \tag{3.26}$$

The parameter θ represents the influence of the traps as not all the traps are being filled in this region. Another transition takes place from the SCL to the TFL region when the traps are filled. This second threshold voltage is given by:

$$V_{TFL} = \frac{qN_td^2}{2\varepsilon_r\varepsilon_0}. \tag{3.27}$$

In the third region (TFL), the current increases drastically and is given by:

$$J_{TFL} = B(\frac{V^{l+1}}{d^{2l+1}}), \tag{3.28}$$

where B is an l-dependent parameter, l = (T_C/T). The term T_C refers to a characteristic temperature related to the trap distribution and T is the absolute temperature. Upon filling of all the traps, the J-V profile reverts back to the trap-

free Child's law, i.e. Eq. (3.26) when θ = 1. A typical J-V profile describing the SCLC conduction mechanism is shown in Fig. 3.9. Each of the three regions are characterised by the slope of the log-log plot and the transition voltages, V_{tr} and V_{TFL}, can be used to calculate important parameters (see Eqs. (3.24) and (3.27)).

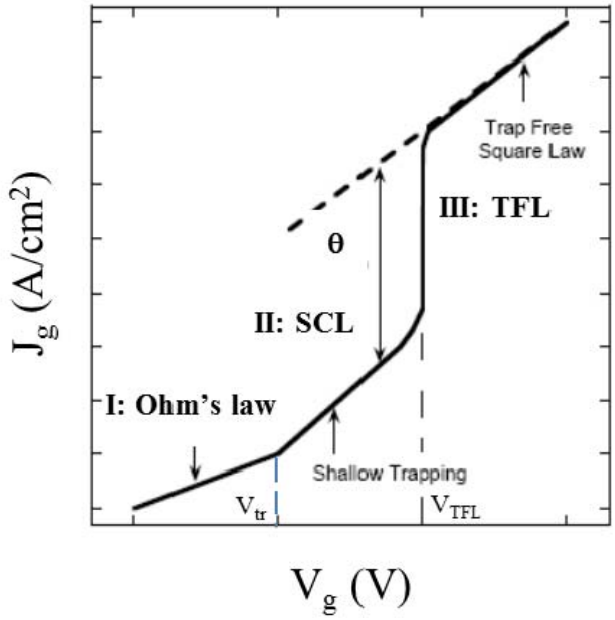

Fig. 3.9: A log-log plot of current-voltage characteristic for SCLC conduction mechanism.

Other possible conduction mechanisms are Schottky (SC) and Poole-Frenkel (PF) emission. [177] The SC emission process involves a field-assisted thermionic emission of electrons over a surface barrier. The J-V equation for SC emission is given by:

$$J_{SC} = (A^{*}T^{2})\exp[\frac{-q(\phi_B - \sqrt{qE/4\pi\varepsilon_0\varepsilon_r}}{kT}], \qquad (3.29)$$

where A* is the Richardson constant (120 A/cm^{2}k^2) and ϕ_B is the barrier height (which is the CBO for substrate injection). If the mechanism involved is SC emission, a plot of $\ln(J_{SC}/A^{*}T^{2})$ versus $E^{1/2}$ must be linear and ε_r and ϕ_B can be obtained from the slope and intercept, respectively. On the other hand, PF

emission involves a field-assisted thermal de-trapping of the carriers from the bulk oxide into the conduction band. The J-V equation for PF emission is given by:

$$J_{PF} = (qN_C\mu)E\exp[\frac{-q(\phi_t - \sqrt{qE/\pi\varepsilon_0\varepsilon_r}}{kT}], \quad (3.30)$$

where N_C, μ, ϕ_t are the density of states in the conduction band, μ is the mobility, and the trap energy level in the oxide, respectively. By rearranging the terms, ε_r can be extracted from the slope of a $\ln(J_{PF}/E)$ versus $E^{1/2}$ plot, while ϕ_t can be obtained from the y-intercept.

The choice of the value of ε_r used to describe the above conduction mechanisms depends on the mobility of the carriers in dielectric materials.[178] Generally, carriers move very slowly in insulator films (i.e. 10^{-7} – 10^{-10} cm^2/Vs, compared to 1 – 10^3 cm^2/Vs in semiconductors) and therefore the static dielectric constant should be used to model these polaron-like movement of the carriers.[179]

4. Challenges in interface dipole measurements: Corrections and Implications

The electric field strength of the electrostatic dipole at the interface of a heterojunction is an elusive property that cannot be measured directly. Yet, these dipoles are of paramount importance in the understanding of heterojunction physics. Recent growing interest in interface dipoles at the heterojunctions of high dielectric constant (high-k) materials on semiconductors has been motivated by the possibility of tuning the threshold voltage to alleviate Fermi level pinning issues in advanced complementary metal-oxide-semiconductor (CMOS) devices.[180,181] As such, it is essential to measure these interface dipoles accurately for the modeling and understanding of heterostructure interface physics. One approach to measure the dipoles is to investigate the dependence of the flatband voltage (V_{FB}) with oxide thickness.[169, 182] However, this method involves the fabrication of the entire gate stack structure, which includes an additional metal electrode, and complications from various oxide trap charges could result. The former introduces an additional interface that complicates the overall interface dipole analysis while the latter could also be a significant source of error in the case of most high-k oxide materials due to the higher concentration of oxide defects compared to silicon dioxide. This chapter investigates the use of photoemission to determine interface dipoles at high-k oxide/semiconductor interfaces. As an example, the interface dipoles at the $LaAlO_3$/Si and $LaAlO_3$/Ge heterojunctions are studied. This chapter is separated into two parts. In the first part, potential pitfalls involving photoemission measurements are discussed and

appropriate solutions to correct for these artifacts are proposed. In the derivation of the interface dipole, inaccuracies from each of these individual measurements can easily add up to contribute to the overall ambiguity in the eventual dipole value. The implications of the erroneous measurements on our understanding of the formation of these interface dipoles are then discussed in the second part.

4.1. Accurate determination of relevant parameters

The interface dipole potential (Δ) can be indirectly derived from the measured values of band gap (E_g), valence band offset (VBO) and electron affinity (χ) as shown in Fig. 4.1. For consistency in this study, the direction of this dipole is defined as positive when the negative polarity is on the semiconductor (smaller bandgap) side as in the diagram. This section looks at the three relevant parameters, E_g, VBO and χ, of which the first two is obtained using XPS while the third parameter is obtained from UPS measurement.

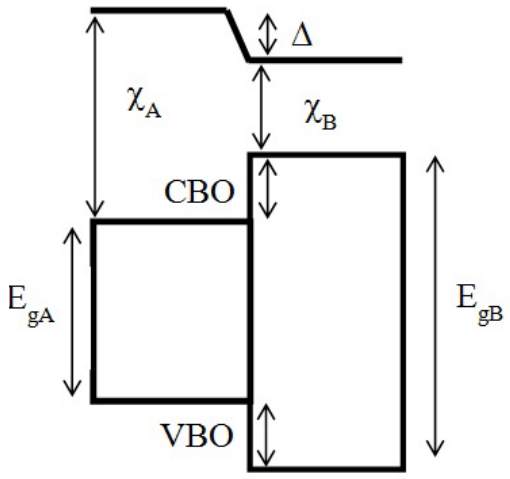

Fig. 4.1: Energy band diagram schematic showing how the interface dipole potential (Δ) in a heterostructure of two materials (A and B) is related to the valence band offset (VBO), conduction band offset (CBO), electron affinity (χ) and band gap (E_g). Note that the direction of the interface dipole is defined to be positive, when the charge transfer is such that the semiconductor side is negative (as shown in diagram).

A necessary first step to obtaining reliable information using XPS involves correct interpretation and selection of the core-level peaks. This is especially important since the XPS spectrum for La involves complicated satellite peaks due to the presence of d orbitals.[183,184] In this study, the La 3d spectrum is chosen to represent $LaAlO_3$ (or LAO), and later also La_2O_3 (refer to Appendix IV for more details). The issues involving the use of different orbitals for the substrates (i.e. Ge and Si) are also explained in Appendix IV. After the careful interpretation and selection of the core-level peaks, one is then able to obtain useful chemical information of the film under study. After taking into account the instrument transmission function, together with the Scofield photoionisation sensitivity factor as discussed in section 3.2.1.4, our quantitative analysis confirms an Al to La ratio of ~0.5 (±0.05) for our bulk LAO film across different batches of deposition since similar deposition conditions are ensured.[149]

Common pitfalls involving photoemission measurements are investigated in the following subsections. These include differential charging and extra-atomic relaxation effects for VBO measurements using XPS, and the effect of surface carbon contaminants on χ measurements using UPS. We have proposed the relevant correction methods to resolve these artefacts.

4.1.1. Band gap

We first briefly discuss the measurement of the band gap, which is relatively straightforward compared to VBO and χ measurements. The bandgap measurement, which involves the energy loss spectrum of O 1s core-level, is

usually carried out on bulk films so as to avoid contributions from any interfacial layer. Energy loss can occur when the photoexcited electron couples with the valence electrons during its emission.[143] For losses that result in an interband transition, the loss energy is quantized. This enables the measurement of the insulator bandgap as the energy difference between the zero loss peak and the onset of the transition loss as shown in Fig. 4.2(a).[144] The electron energy loss spectrum for our LAO samples, shown in Fig. 4.2(b), is obtained by using the main O1s as the zero-loss peak. The bandgap was extracted by taking the intersection between the background and the linear interpolation of the initial slope of the loss peak, as this marks the onset of the energy loss process. Across different batches of deposition, we obtain bandgap values of 6.13 (± 0.1) eV due to the minimal Al to La ratio variations. This is in excellent agreement with the reported bandgap energy (6.2 eV) of amorphous LAO films obtained using spectroscopic ellipsometery.[185]

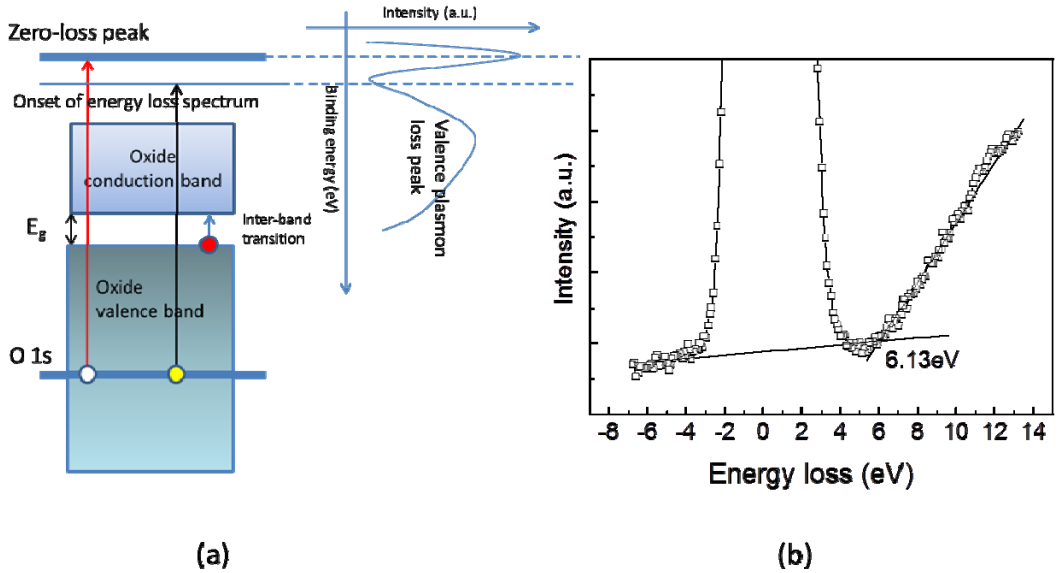

Fig. 4.2: (a) Schematic of the O1s interband transition loss mechanism. (b) O1s energy loss spectrum for a bulk (15 nm) LAO film on Si. The band gap is taken as the intersection between the background and the linear interpolation of the initial slope of the loss peak.

4.1.2. Valence band offset

Valence band offsets (VBOs) can be determined with X-ray photoelectron spectroscopy by making use of the Kraut's method (see section 2.4.2.1 for more details). The method gives the VBO using the core-to-valence level separation of the bulk that is referenced by the interface core-level separation (ΔE_{CL}). This is shown for the case of measurement on a LAO/Ge heterostructure as follows:

$$VBO = (E_{CL}^{Ge3d} - E_v)_{bulk,Ge} - (E_{CL}^{La3d} - E_v)_{bulk,LAO} + \Delta E_{CL} . \quad (4.1)$$

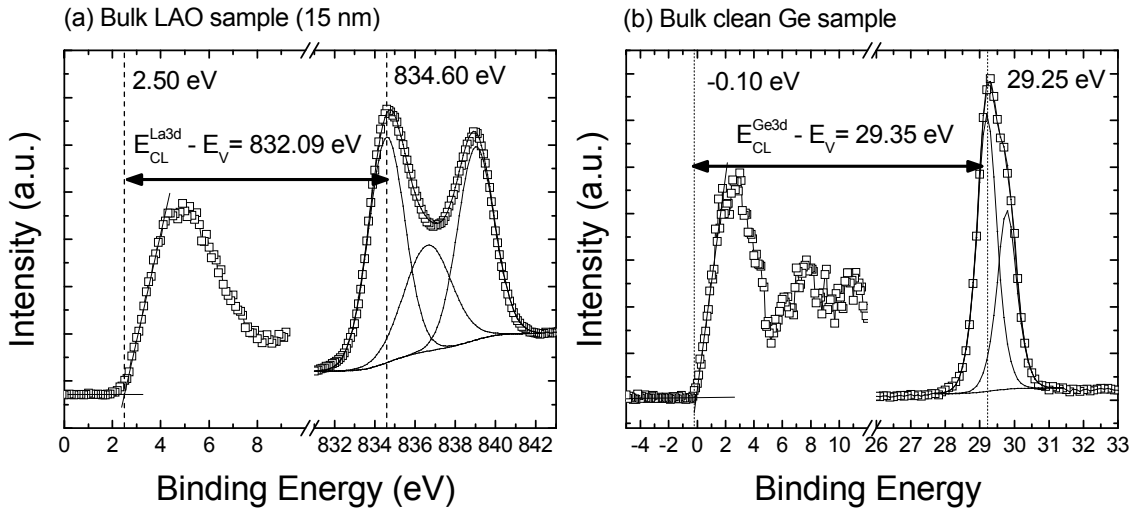

Fig. 4.3: (a) High-energy resolution XPS spectrum showing (a) valence and La 3d core-level peaks for a bulk (15 nm) LAO sample and (b) valence and Ge 3d core-level peaks for a clean Ge bulk sample.

As discussed in section 2.4.2, this method is more accurate than direct comparisons using purely valence band profiles. We first look at the bulk core-to-valence separations given by the first two terms in Eq. (4.1). Figures 4.3(a) and (b) show the determination of the bulk core-to-valence separation values of 832.09 and 29.35 eV for a thick LAO film and a clean Ge substrate respectively. In a similar manner, the core-to-valence separation, i.e $(E_{CL}^{Si2p} - E_v)$, for clean Si sample is determined to be 98.96 eV.

While the measurements of the bulk core-to-valence separations are relatively straightforward, various potential pitfalls can affect the experimental determination of the interface core-level separation (ΔE_{CL}). These include band bending, charging, and extra-atomic relaxation effects. Band bending effects are negligible in this study as the substrates used are moderately doped. On the other hand, differential charging is a serious problem in the measurement of VBO in oxide-semiconductor heterostructures.[186,187] This arises due to the differing ability to replenish the lost electrons in the oxide layer as compared to the semiconductor substrate, thereby resulting in unequal peak shifts that affect the interface core-level separation. Thus, peak shifts due to electrostatic potential changes from interface dipoles cannot be easily distinguished, rendering the measured VBO inaccurate. Another possible source of error for VBO measurements comes from the contribution of extra-atomic relaxation effects, which has been reported to have resulted in peak shifts of more than 0.5 eV for ultrathin oxide films on Si.[188] This final state effect involves the remote-screening of core-holes in the oxide film from the semiconducting substrate. Such relaxation energy is expected to be sensitive to the oxide thin film thickness. As this relaxation energy does not reflect the initial energy alignment between the materials, any difference in the relaxation across different samples will necessarily lead to a spurious change in the measured band offset. These issues will be dealt with in the subsequent subsections.

4.1.2.1. Differential charging effects

Charging is one of the tricky issues in photoemission measurements of insulating films. Static charging involves an equal shift in the core-level peaks and hence

does not pose a problem since Kraut's method involves taking core-level separations at the interface. Differential charging, on the other hand, cannot be easily corrected and is believed to be the main cause behind the large variations in the measured VBO values for high-k oxides.[39,189,190] The semiconductor, which is grounded through the sample holder, can replenish the electrons lost through photoemission reasonably well, while the high-k oxide overlayer cannot do so due to its poor conductivity.[186] The oxide core-level peaks thus shift to higher binding energy while the semiconductor core-level peaks do not, causing unequal core-level shifts. This affects the interface core-level separation, ΔE_{CL} in Eq. (4.1), leading to inaccurate VBO measurements.

In this work, we can monitor the effects of differential charging through our proposed time-resolved photoemission method using single scans for better time resolution. The time taken for a typical scan with energy window of 15 eV is about 25 s while the time lag between the exposure to the X-rays and the recorded photoelectron signals is 20 to 25 s, owing to the focusing of the X-rays and delay in the instrument response. The time-lapsed measurement of the core-level peaks for the high-k oxide and the semiconductor will be used to determine ΔE_{CL} (see Eq. (4.2) below). It is important to choose the highest intensity orbitals (see Appendix IV) for this method because only single scans are recorded. Fig. 4.4 (a) shows the actual photoemission peaks used to define ΔE_{CL} and their relative shifts over X-ray irradiation times of 37, 221 and 1243 s. It is observed that the E_{CL} of the semiconductor substrate (Ge $3d_{5/2}$) peak remains relatively consistent (within the experimental error of 0.05 eV) while the E_{CL} of the oxide (La $3d_{5/2}$) peak increases by as much as 0.37 eV over time.

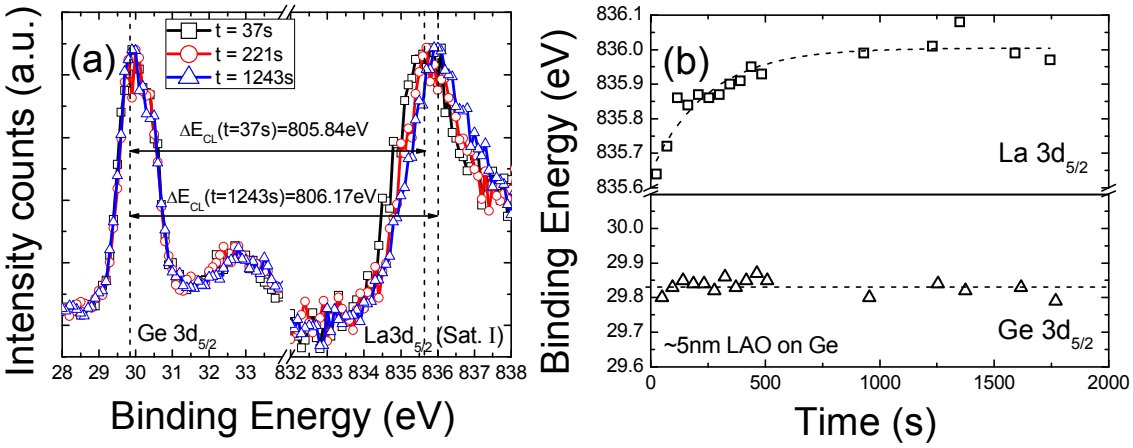

Fig. 4.4: (a) Photoemission peaks of Ge $3d_{5/2}$ and La $3d_{5/2}$ (satellite I [Sat. I] representing the substrate and oxide overlayer film, respectively, at different x-ray irradiation (exposure); (b) binding energies of the substrate (Ge $3d_{5/2}$) and oxide (La $3d_{5/2}$) core-level peaks plotted as a function of the x-ray exposure time. The dotted line for La $3d_{5/2}$ plot is a best fit function.

The presence of the differential shift of 0.37 eV is considerable and it directly affects the accurate determination of band offsets. The time-lapsed manner of measurement that we employed allows us to examine the charging effect through a detailed plot as shown in Fig. 4.4(b). It is noted that charging induced Gaussian broadening is not observable as seen from a typical (10 scans) La 3d spectrum taken after saturation of the BE shift, i.e. after 600 s as seen in Fig. 4.4(b). On the other hand, apparent changes in the FWHM due to summation effects of different BE shifts are possible within the steep charging profile slope shown in Fig. 4.4(b). Careful fitting of the single scan peaks give a consistent FWHM of 2 eV. This suggests that within our time window of ~15 s per scan, the subtle increase in BE over time does not result in noticeable alterations in the peak width. More importantly, the FWHM of single scans after saturation is also ~2 eV. This suggests that the FWHM change resulting from ~0.3 eV of BE shift due to charging is not substantial. However, if the time-resolved method is to be used for oxide films with substantial charging shifts of 2 to 10 eV (FWHM changes of ~0.5

to 1.0 eV from our previous experiments), a more complicated peak analysis needs to be used to accurately account for the charging profile. This is unlikely for properly grounded heterojunctions of a thin film oxide on semiconductor. Therefore, barring errors in estimation of the time of X-ray exposures, the extrapolation of the plots to time zero essentially gives the "charge-free" state of the heterostructure and this will be important in accurate photoelectron spectroscopy on oxide-semiconductor structures. In this aspect, we are able to obtain repeatable and consistent trends through the proposed time-resolved method and this will be demonstrated subsequently.

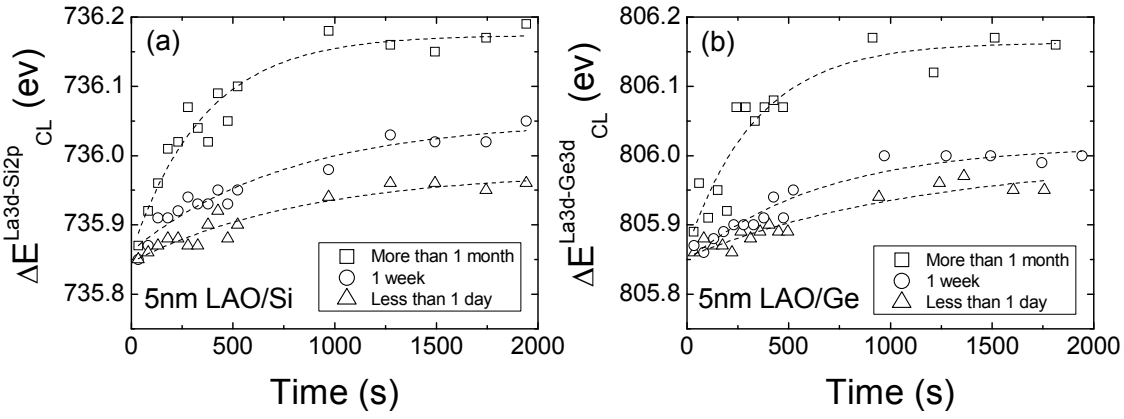

Fig. 4.5: Time-resolved plots showing core-level separations (ΔE_{CL}) vs X-ray exposure time for (a) 5nm LAO/Si and (b) 5 nm LAO/Ge heterostructures after different durations of ambient exposure. The dotted lines are best fit functions, and the convergence of the lines at time zero represents the zero-charge state, $\Delta E_{CL(0)}$.

To further investigate on the effectiveness of the proposed method, not only were different runs conducted, but the samples were also left exposed to ambient condition for different periods of time. We observed that the differential charging effects are more pronounced with longer exposure to ambient conditions. This is shown in Fig. 4.5(a) and 4.5(b) where the resultant ΔE_{CL} for LAO/Si and LAO/Ge heterostructures obtained after curve fitting is plotted with respect to the X-ray

irradiation time. The dotted lines represent the following fitted exponential relationship:

$$\Delta E_{CL} = C_1[1 - \exp(-t/C_2)] + \Delta E_{CL(0)}, \quad (4.2)$$

where C_1 and C_2 are fitting constants, while $\Delta E_{CL(0)}$ represents the charge-free ΔE_{CL} at time t = 0 s. This BE time dependence follows a similar relationship as the prediction based on electrostatics involving the dielectric time constant (τ) in section 3.2.1.2. The fitting constants C_1 and C_2 correspond to $\rho(\infty)$ and τ respectively. The τ parameter represents the average time before a core hole is being filled, and an average value of ~696 s is obtained based on the fitting shown in Fig. 4.5. This is reasonable given typical τ values ranging from 77 to 7800 s for insulators with resistivity values between $10^{12} – 10^{14}$ Ωm. On the other hand, the other parameter, i.e. $\rho(\infty)$, represents the amount of charge density when the system reaches a steady state. The extracted values of $\rho(\infty)$ are observed to increase from ~ 0.13 to 0.31 eV with increasing exposure time. This is probably due to the fact that the amount of adventitious carbon surface contaminants increases with longer exposure time, thereby reducing the amount of charge compensation from stray electrons in the vacuum chamber. As such, there is a larger density of charges built up at steady state, i.e. $\rho(\infty)$.

In any case, we show and emphasize that the time-resolved measurements provided adequate correction even for the more severe extent of differential charging. This can be seen by the similar $\Delta E_{CL(0)}$ for LAO/Si and LAO/Ge heterostructures, obtained to be 735.86 and 805.86 (± 0.1) eV respectively, for all levels of differential charging. This translates to a calculated VBO of 2.73 and

3.12 (±0.1) eV respectively, after obtaining bulk core-to-valence separation measurements of the respective materials using Kraut's method.[114] It is important to highlight that a typical core-level measurement, averaging over 10 scans, naturally results in a higher ΔE_{CL} value as compared to our measured $\Delta E_{CL(0)}$ value that is free from differential charging.

Our experimental VBO value for the LAO/Si heterostructure is smaller than that obtained from photoemission measurement (3.2 eV) by Edge *et al.*[185] If we do not correct for the differential charging, we will obtain a VBO of 3.03 eV that is closer to the value from Edge *et al*. The larger VBO obtained in Edge *et al.*'s work is therefore likely to be an effect of differential charging. In support of this, we note that our measured VBO of 2.73 (±0.1) eV for LAO/Si is closer to the VBO of 2.60 (±0.1) eV as derived from internal photoemission (IPE) and photoconductivity (PC) measurements.[191] The VBO values determined using IPE and PC are not affected by charging effects since these involve measurements on a metal-oxide-semiconductor structure under applied external bias.[112] We also note that VBO values measured by XPS without charge correction tend to be larger than that using IPE for other oxide-semiconductor structures.[190]

The comparison of our measured VBO with the results of Mi *et al.* (2.86 eV and 3.06 eV for LAO/Si and LAO/Ge, respectively) shows some disagreement.[39,189] The discrepancy can be attributed to the different VBO determination method where Mi *et al.* examines the valence band profile at the interface instead of core-level separations (see section 2.4.2). The derived VBO can thus be affected by both differential charging and the VBO determination errors, resulting in a larger

deviation observed even with the same material system. Instead, with our proposed time-resolved measurement, we can accurately account for differential charging effects, giving an accurate and consistent valence band offset that will be important for subsequent interface dipole analysis. Also note that the accuracy and consistency is dependent on good estimation of the X-ray exposure time.

4.1.2.2. Extra-atomic relaxation effects

We now turn our attention to relaxation screening in final state effects that may affect the accuracy of VBO measurements. This is because a slight change in the distance between the oxide and the substrate may lead to a drastic change in the remote-screening effects of the core-hole as discussed. This extra-atomic relaxation effect can be important for ultra-thin SiO_x films on Si substrates and it will be prudent to examine the relaxation effects of our samples.[192] Here, we investigated the effects of extra-atomic relaxation by using the Auger parameter and a classical electrostatic model. The Auger parameter (AP or α) has been proven to be effective in quantifying changes in extra-atomic relaxation energy in thin films. Briefly, AP is defined as the sum between the kinetic energy of the Auger electron and the binding energy of the photoelectron. Since the AP considers the relative separation between two energy lines, static charge and work function corrections are not needed.[193] Using reasonable assumptions, it can be derived that AP shifts are equivalent to twice the difference in the relaxation energies experienced by an atom in two different environments (i.e. $\Delta\alpha = 2\Delta R_{ea}$).[194] Here, we investigate the effects of extra-atomic relaxation shifts on thin oxide films by comparing the AP of a 4 nm thick LAO film on Si

with that of a 15 nm thick LAO film on Si. The latter is being used to as a control since extra-atomic relaxation shifts are reasonably assumed to be negligible for thick films.

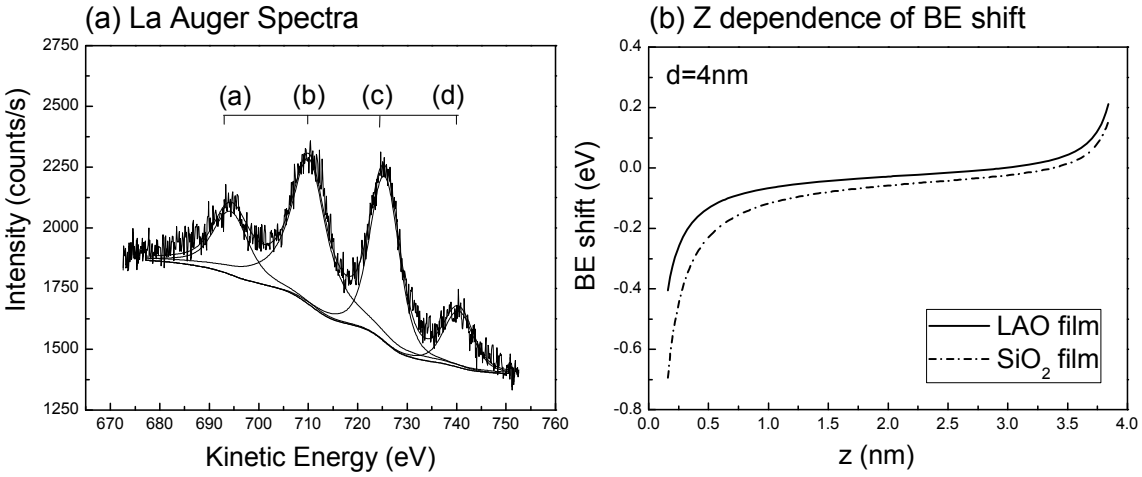

Fig. 4.6: (a) Typical Auger spectrum obtained using X-ray source in an XPS experiment. The La Auger peaks consist of a series of transitions, namely: peak a: $M_4N_{4,5}O_1$; peak b: $M_5N_{4,5}O_{2,3}$; peak c: $M_5N_{4,5}N_{6,7}$, $M_4N_{4,5}O_{2,3}$; and peak d: $M_4N_{4,5}N_{6,7}$. Peaks a and b are chosen to be used in the AP calculations tabulated in Table 4.1. (b) Binding energy (BE) shifts due to core-level relaxations at different positions (z) based on an image charge model.

Figure 4.6(a) shows a series of X-ray induced La Auger peaks (see section 3.2.1.3) of the following transitions: peak (a): $M_4N_{4,5}O_1$; peak (b): $M_5N_{4,5}O_{2,3}$; peak (c): $M_5N_{4,5}N_{6,7}$, $M_4N_{4,5}O_{2,3}$; and peak (d): $M_4N_{4,5}N_{6,7}$.[195] We note that the Auger transition for peaks (c) and (d) involves the occupancy of the initially empty 4f orbital (valence shell) due to hybridization of the 4f level and the valence electronic states.[196] Therefore, the use of peaks (a) and (b) to compute the AP will be more accurate in reflecting the relaxation effects since these Auger peaks do not involve non-local valence bands.[197] The resulting AP obtained for our thin films are shown in Table 4.1. The comparison between the AP shifts in the thin and thick samples showed negligible differences (< 0.06 eV), implying that the extra-atomic relaxation effects did not contribute to the observed core-level shifts in this work.

Table 4.1: Summary of the measured Auger parameter (AP) values. Units for binding energy (BE) and kinetic energy (KE) values are in eV. $\Delta\alpha$ is the difference in the AP between the bulk (15 nm) and thin (4 nm) LAO sample, where AP 1 = BE ($La3d_{3/2}$) + KE ($M_4N_{4,5}O_1$) and AP 2 = BE ($La3d_{5/2}$) + KE ($M_5N_{4,5}O_{2,3}$) respectively.

	Thick (15 nm)	Thin (4 nm)	$\Delta\alpha$
$La3d_{3/2}$ BE	851.53	851.55	
Peak a ($M_4N_{4,5}O_1$) KE	694.4	694.35	-0.03
AP 1	1545.93	1545.90	
$La3d_{5/2}$ BE	834.65	834.70	
Peak b ($M_5N_{4,5}O_{2,3}$) KE	1545.11	1545.12	-0.06
AP 2	2379.76	2379.82	

We can further understand this by modeling the remote core-hole screening using a series of image charges across heterojunctions.[198] This model, which makes use of an infinite series of image charges, has demonstrated energy shifts that are in good agreement with experimental data.[199] Briefly, the effective energy shift expected across a dielectric discontinuous interface of vacuum/oxide/semiconductor can be expressed as

$$\Delta E = \frac{q^2}{8\pi\varepsilon_{oxide}} \sum_{n=0}^{\infty} (k_1 k_2)^n \left[\frac{k_1}{2z - 2nd} + \frac{k_2}{(2n+2)d - 2z} + \frac{2k_1 k_2}{(2n+2)d} \right], \quad (4.3)$$

where the reflection coefficients, k_1 and k_2, are given by

$$k_1 = \frac{\varepsilon_{oxide} - \varepsilon_{Subs}}{\varepsilon_{oxide} + \varepsilon_{Ssubs}}, \quad (4.4)$$

$$k_2 = \frac{\varepsilon_{oxide} - \varepsilon_0}{\varepsilon_{oxide} + \varepsilon_0}. \quad (4.5)$$

Equation (4.3) describes the overall electrostatic effect experienced by a core-hole located at position z (where z = 0 corresponds to the substrate/oxide interface) due to the creation of the infinite series of image charges. This translates to the shift in the core-level binding energy of the measured photoelectron emitted from the core-hole. The reflection coefficients in Eqs. (4.4) and (4.5), given by the difference in dielectric constants, account for the electrostatic screening of the image charges and are therefore the key to the equation. By making use of the above equations with attenuation considerations, one can obtain the overall BE shift due to extra-atomic relaxation for a given oxide thickness. We obtained the simulation results shown in Fig. 4.6(b) by using an optical dielectric constant of 3.24 for LAO and 2.1 for SiO_2.[200] Figure 4.6(b) predicts that a lower BE shift arising from extra-atomic relaxation effects is expected for LAO thin films as compared with that of silicon dioxide (SiO_2). This is a consequence of the higher optical dielectric constant of the high-k oxide. With the prediction of less than 0.1 eV shift for a 4 nm thick SiO_2, our simulation result affirms our experimental observation of a negligible effect from the remote screening.[199] The simulation also shows that extra-atomic relaxation effects will be of little significance for most high-k oxides of similar or greater thicknesses.

4.1.3. Electron affinity

The dipole value at the heterostructure interface is defined as the difference in the vacuum level between the two materials (see Fig. 4.1). To relate the interface dipole to the valence band offset value, electron affinities must be measured. UPS is often preferred due to the lower secondary electrons intensity since the secondary cut-off edge needs to be measured. In such measurements, the valence

band maxima (VBM) and the secondary electron emission edge (representing the vacuum level, V_0) is used to compute the spectrum width, W. The electron affinity for the oxide can then be found using Eq. (4.6): [159]

$$\chi = hv - E_g - W = hv - E_g - (V_0 - VBM), \quad (4.6)$$

where h is Planck's constant, v is the frequency of the excitation and hv is the energy of the UPS excitation source. For accurate measurements, it is important to understand that a negative sample bias has to be applied to provide sufficient energy for the secondary electrons to reach the electron detector. Our control experiments (not shown) indicate that a bias of -15 V is sufficient for this purpose, as judged from the unchanging spectrum width with a range of bias applied beyond this value. As such, all our subsequent UPS measurements are carried out with -15 V bias in order to obtain a true secondary electron cutoff. We believe that applying a sufficiently large bias is important, which is sometimes neglected in other works. [201, 202] In all cases, examining changes in the spectrum width, secondary edge and the valence edge with bias can be performed to determine the range of voltages that is suitable for the material. With this, we are able to obtain work function values of 5.01 eV and 4.92 eV for sputtered clean Au and Ni metal samples respectively, which are in good agreement with their expected work function values.

4.1.3.1. Effects of surface carbon contaminants

Next, we turn our attention to examine the detrimental effects of carbon contaminants on UPS measurements of χ for oxides, since it is not always practical to carry out *in situ* characterization. This is important because the extremely high surface sensitivity of the UPS technique means that the measured

spectrum will be extremely sensitive to surface conditions.[203] Despite the fact that the hydrocarbon peak at 285 eV is commonly used as a standard for referencing, the seemingly insignificant overlayer of contaminant species can contribute greatly either in forming surface dipoles (affecting V_0) or distorting the valence band profile (affecting VBM).[204] As such, these carbon contaminants can give rise to inaccuracies in *ex situ* electron affinity measurements for thin films without prior surface treatment.[117,205,206]

We can clearly show the effects of the carbon contaminant by the use of three different *in situ* surface treatments to remove the surface carbon overlayer and the results are summarized in Table 4.2. Our UPS measurement of the untreated (As Dep) sample gives a χ value of 1.94 eV which decreases drastically to 1.24 eV after sputtering to remove the carbon contaminant. The large decrease in χ can possibly be attributed to carbon contamination removal. Although unlikely, as the sputtering could be minimal, it can also be argued that the drastic reduction in the χ value may be due to the preferential sputtering of the Al oxide in the LAO film, given that the Al atom has a similar mass as the sputter (Ar) ion as compared to La.[207] Therefore, we employ a second method of carbon contaminant removal by annealing the samples at a temperature of 450 ^{o}C in a low vacuum pressure of 10^{-8} mbar. The annealing process can effectively remove most of the surface carbon and expectedly, we see the drastic decrease in the χ value to 1.26 eV. Although we expect LAO to be stable at the annealing temperature used, one can still argue on the presence of subtle chemical or structural changes with annealing, thereby affecting the results.

Table 4.2: Measured electron affinity (χ) values and the spectrum width (W) for the LAO/Ge heterostructure before (As Dep) and after various surface treatments. The spectrum width (W) is defined as the difference between the valence band maximum and the cutoff of the secondary electron spectrum measured using UPS.

	Spectrum width W (eV)	Electron affinity χ (eV)
As Dep	13.13	1.94
Sputtered	13.83	1.24
Annealed 450^{o}C, 1 hour	13.81	1.26
Oxygen plasma 15 mins	13.80	1.27
Oxygen plasma 30 mins	13.78	1.29
Exposure to ambient	13.30	1.77

As such, we also carried out an *in situ* oxygen plasma treatment using the Oxford Applied Research atomic oxygen source at a low radio-frequency plasma power of 150 W at room temperature to clean the oxide surface; the low power is preferred to ensure minimal changes to the surface roughness. Table 4.2 shows that we similarly recorded reduction in χ to values of 1.27 to 1.29 eV after the oxygen plasma treatment. The similar range of χ values obtained for different surface cleaning methods is conclusive evidence that the main contributing factor observed in all three surface treatments is the removal of the surface contamination. In addition, we did a simple test by exposing the oxygen plasma cleaned sample to ambient conditions for 30 minutes before loading it back into the analysis chamber. The contamination upon ambient re-exposure restores the measured χ value to 1.77 eV, which is close to the value of 1.94 eV before the plasma treatment.

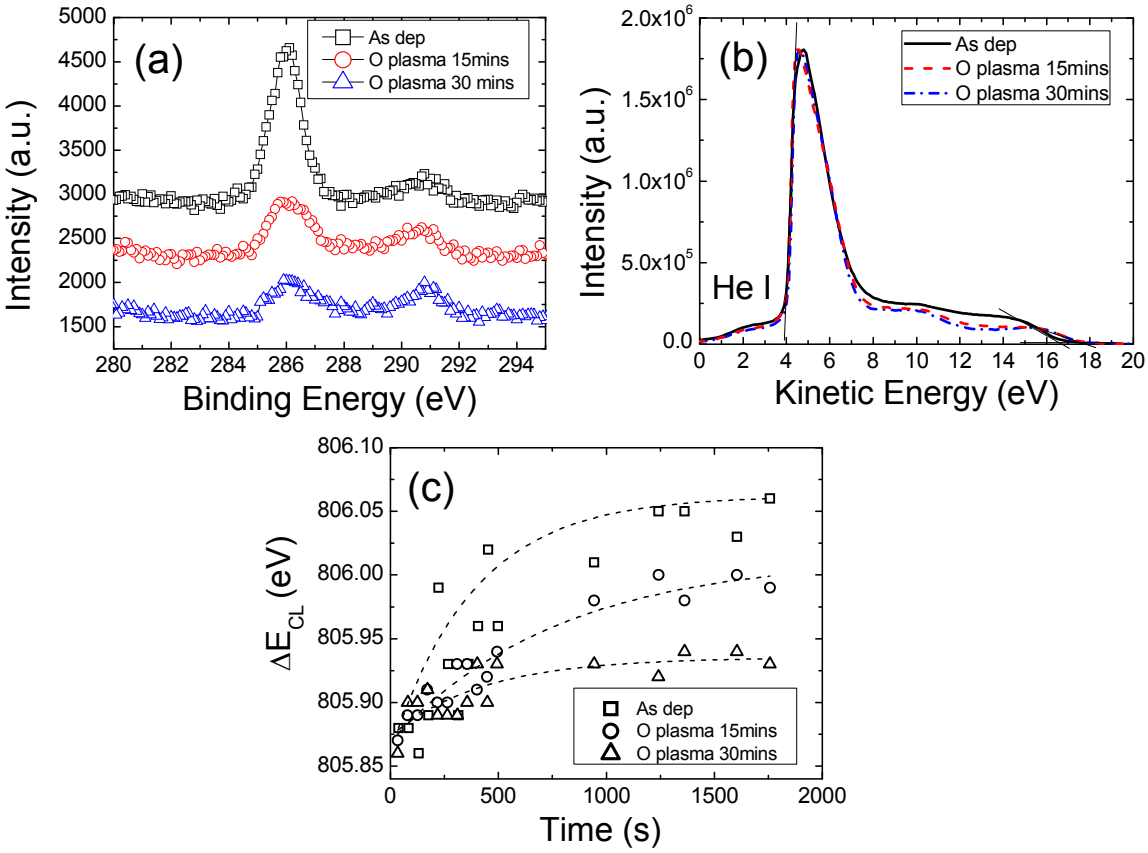

Fig. 4.7: (a) C 1s photoemission peaks before and after low power (150 W) oxygen plasma treatment of the LAO/Ge heterostructure with thickness of 5nm. (b) The corresponding He I spectrum showing the changes caused by the removal of surface carbon contaminants. The inset in (b) shows a magnified view of the changes near the valence band maxima after the removal of surface carbon contaminants. (c) Measured time-resolved plots of the core level separations (ΔE_{CL}) for the as-deposited (As dep) sample and after different durations of oxygen (O) plasma treatment. The lines are best fit functions and show the correction of differential charging when extrapolated to time zero.

The reason for the apparent change can be clearer if we examine the photoelectron spectrum. Figure 4.7 (a) shows the carbon C 1s core level peaks before and after the low power oxygen plasma treatment. It is seen that after 15 minutes (mins) of plasma treatment, the hydrocarbon peak is reduced (~17% remains as estimated by the integrated intensity). The accompanying UPS He I spectrum is shown in Fig. 4.7(b). Our analysis shows that the secondary cut-off of the spectrum remains largely unchanged and this implies that the carbon does not greatly alter the surface dipoles since the film is amorphous. However, the presence of the carbon

changes the spectrum width by changing the valence band profile, as shown in the inset in valence states can be observed. After the contamination removal, the band at 13 eV disappears and a valley-shaped plot can be clearly observed in Fig. 4.7(b). The additional valence band states contributed by the hydrocarbons therefore gave an erroneous measurement of the valence band edge and hence the spectrum width. We highlight that this does not affect XPS measurements of the valence band edge (important for band offset measurement) due to the negligible photoionization cross section for C 2p states as compared to O 2s and O 2p states.[208] In agreement to what is expected from our findings on the effect of contamination on differential charging, Fig. 4.7(c) shows that a longer duration oxygen plasma treatment results in lower differential charging. More importantly, the ability to obtain accurate core-level separation values again shows the efficacy of the time-resolved photoemission method introduced earlier.

4.2. Importance of accurate measurements

In this section, we will focus on the implications of the errors in the derivation of the interface dipole value. With the experimentally measured VBO of 2.73 eV (free of differential charging) and band gap of 6.13 eV, Fig. 4.8(a) and 4.8(b) show graphically how different values of interface dipoles can be obtained when different values of χ are being used. This is summarized for both LAO/Si and LAO/Ge heterostructures in part (a) of Table 4.3. It can be seen that when the χ value of 1.29 eV (after surface treatment) is used, we obtain a dipole value of +0.48 V, with the positive sign symbolizing a dipole with the negative polarity at the semiconductor side with respect to the oxide in a manner as shown

schematically in Fig. 4.1. However, if we simply take the χ values for the as-deposited samples or that as obtained from the literature (ref. 209), the derived dipole values will be -0.17 V and -0.73 V. This means that not only are the magnitude of the dipoles different, the direction of the dipoles are also reversed. This is a significant error and can be misleading as it erroneously represents the charge transfer direction at the heterojunction.

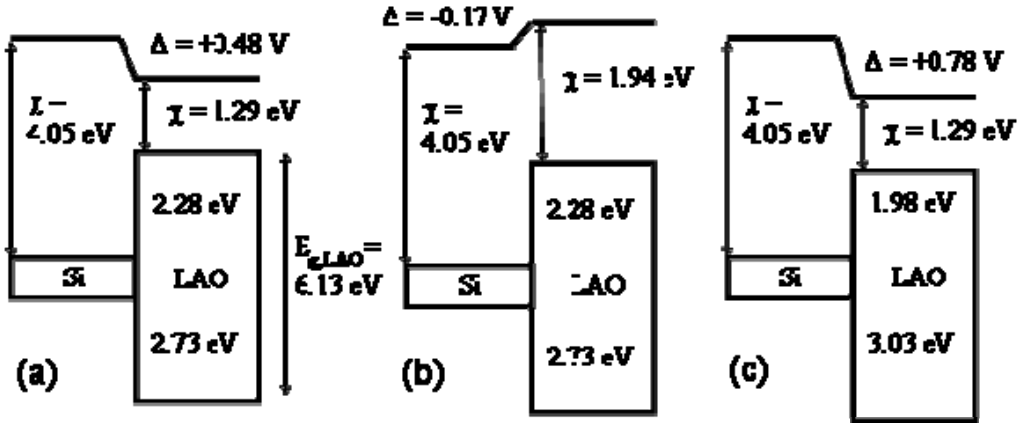

Fig. 4.8: Energy band diagram for the LAO/Si heterostructure, derived using the measured electron affinity (χ) of (a) as-deposited samples and (b) after surface treatment that removes the carbon contaminants. (c) Resultant band lineup using a measured VBO without the time-resolved charge correction method ($\Delta E_{CL(0)}$ +0.3 eV).

The determination of the interface dipole can also be affected by errors in the VBO measurement as shown in Fig. 4.8(c). For example, if differential charging is not accounted for, Fig. 4.5 shows that $E_{CL(0)}$ can be increased by 0.3 eV as indicated by the saturation of the charging. The incorrectly measured VBO would then be 3.03 eV and 3.42 eV for the LAO/Si and LAO/Ge heterostructures, respectively, as shown in part (b) of Table 4.3. The corresponding derived interface dipole would then be significantly larger at +0.78 V and +0.80 V, respectively.

Table 4.3: Ambiguity in magnitude and polarity of the derived interface dipole potential (Δ) value should incorrect measurements of (a) χ or (b) valence band offset (VBO) be used. The values outside the brackets are experimentally determined while those within the brackets correspond to the predictions by the MIGS model. The direction of Δ is as defined in Fig. 4.1

	χ (eV)	LAO/Si		LAO/Ge	
		VBO (eV)	Δ (V)	VBO (eV)	Δ (V)
(a):	1.29	2.73 (2.81)	+0.48 (+0.56)	3.12 (3.09)	+0.50 (+0.47)
	1.94	2.73 (3.15)	-0.17 (+0.25)	3.12 (3.43)	-0.15 (+0.16)
	2.50	2.73 (3.45)	-0.73 (-0.01)	3.12 (3.73)	-0.71 (-0.10)
(b):	1.29	3.03 (2.81)	+0.78 (+0.56)	3.42 (3.09)	+0.80 (0.47)

4.2.1. Validation of the MIGS model

It can thus be seen that the magnitude and polarity of the interface dipole is easily altered by errors in measurements of VBO and χ. This has far reaching impact in many models and studies that rely on accurate dipole values to give meaningful and consistent description of the physics at the heterostructure interface, of which we highlight the band alignment model that uses the charge-neutrality level (CNL) concept.[111,181,187] The excellent agreement with correctly determined values will also be added proof, not only of the accuracy in the measurements, but also as a validation for this model.

It will be useful to briefly discuss the CNL model. The model is an extension from the metal-induced gap states (MIGS) theory for metal-semiconductor heterojunctions where the semiconductor takes on the role of the metal.[97,180,209,212] This is discussed in section 2.3.2.For this reason, we will refer to this model as the MIGS model to distinguish it from other similar models, later in this dissertation.

The resultant conduction band offset (CBO) of the heterostructure is obtained as follows:

$$\mathrm{CBO} = (\chi_A - \chi_B) + (S-1)(\Phi^{Vac}_{CNL,A} - \Phi^{Vac}_{CNL,B}), \quad (4.7)$$

where Φ^{Vac}_{CNL} represents the energy distance from the vacuum level to the CNL, A and B represent the two materials of the heterostructure and S is a pinning parameter. From Eq. (4.7), it is seen that the electron affinity plays an important role in this model since it determines the condition of zero charge transfer dipoles (i.e. S = 1), or otherwise known as the Schottky-Mott limit (see section 2.3.1). As such, our experimentally obtained value of the electron affinity plays an important role in order to conduct a meaningful analysis of the MIGS model, in addition to deriving an accurate interface dipole.

The pinning parameter of LAO is calculated to be 0.53 and its CNL is derived to be 3.8 eV above from its valence band maxima.[209] If we use the χ value of 1.94 eV (without surface treatment), the MIGS model will predict a VBO for LAO/Si and LAO/Ge to be 3.15 eV and 3.43 eV respectively, with corresponding interface dipoles of +0.25 V and +0.16 V. This differs greatly from our experimentally determined VBO values of 2.73 eV and 3.12 eV, and dipoles of -0.17 V and -0.15 V, for LAO/Si and LAO/Ge respectively as shown in Table 4.3. This can put an undeserving erroneous judgment on the validity of the MIGS model. The model fares even worse when a χ value of 2.50 eV is used. Not only are the VBO differences between the predicted and experimental values greater (e.g., LAO/Si: 3.43 eV vs. 2.73 eV), the band lineup will fall out of range of the two limits imposed by the MIGS model. This suggests a failure in the MIGS model, which

can lead to the presumption that intrinsic gap states are not important in oxide-semiconductor band lineups. If we now use the correct χ value of 1.29 eV, we obtain excellent agreement with the MIGS model as shown in Table 4.3. The predicted dipoles of +0.56 V and +0.47 V for LAO/Si and LAO/Ge respectively are also in good agreement with the measured dipole values, unlike the earlier cases whereby even the dipole polarity is wrongly predicted. This is excellent proof that the values of VBO and χ obtained are accurate and above all, it demonstrates the good prediction of the MIGS model that is otherwise not possible. It is therefore important to re-visit previous disagreements of the model with more accurate measurements to test if the deviations can possibly be reconciled.[117,158,121,180,190]

We add that there is a wider implication for the accurate prediction by the MIGS model. It demonstrates that χ is a valid parameter in the prediction of interface band alignment. Although there are suggestions that χ values may not be valid at the interface given that it is a bulk property and that it is highly surface dependent, the correct prediction demonstrates otherwise. We attempt to justify its relevance by arguing from a conservation of energy point of view. If vacuum level references exist for bulk electrons, its continuity must be met even at the interface. This continuity is necessary to ensure that an electron that makes a complete loop does not gain any energy in the cycle. The continuity is also exactly the basis for defining that the values of the interface dipoles exist as the vacuum level differences.

4.2.2. Comparison with existing V_{FB} shifts

Finally, we examine the obtained dipole values by looking at their effects on V_{FB} shifts. This is particularly of great interest since these shifts will eventually alter the threshold voltage, which is a crucial parameter in CMOS devices. Unfortunately, the overall V_{FB} is also heavily influenced by the effects of the different oxide trap charges (see section 3.2.4.1). These oxide charges are sensitive to the actual processing conditions and can be present in large amounts in novel high-k dielectrics, such as LAO, due to the high defect density. Our proposed photoemission measurement, however, should not be affected by these oxide trap charges significantly. From what we have gathered from the literature and our electrical data from chapter 6, experimental V_{FB} shifts of LAO/Si based capacitors tend to range from positive to close to zero after considering the metal electrode work function.[210,211] Considering reasonable contributions from fixed oxide charges to the overall V_{FB}, our experimentally derived interface dipole value of +0.48 V accounts for a large component of the positive V_{FB} shift. The methodology discussed in this work thus provides a platform to measure interface dipoles which is not affected by oxide charges, thereby allowing one to better understand the origin and cause of the V_{FB} shifts.

5. Dipole neutrality point: Re-evaluating the use of electronegativity in band alignment

Accurate band alignment prediction of semiconductor-oxide heterostructures is important and useful for device technologists since band discontinuities can affect both electrical and optical properties.[111] In particular, the band alignment between high dielectric constant (high-k) materials on alternative channel materials influences both leakage current and the overall threshold voltage of the transistors.[14,180] Over the decades, several models to predict band alignments have been developed. However, a large number of these models are based on metal-semiconductor interfaces and thus are not easily translated to predict band offsets in semiconductor-oxide heterostructures, e.g. the chemical bond polarization model.[110] As mentioned in the previous chapter, it is found that the metal induced gap states (MIGS) model is able to give good predictions of the band alignment of LAO/Si and LAO/Ge heterostructures. This is primarily due to the dominating role of intrinsic gap states, which will be further shown in this chapter. However, the MIGS model requires the knowledge of electron affinity, which requires careful measurements and these data are not readily available in the literature. Furthermore, some researchers have questioned the use of electron affinity (or work function) in band alignment models because the vacuum level at the interface is not well-defined. For these reasons, electronegativity is used instead, as in the interface induced gap states (IFIGS) model in section 2.3.4. As an example in this study, we evaluated the experimental slope parameter, in section 5.1, from a range of $LaAlO_3$ (or LAO) heterostructures using both models (i.e.

MIGS and IFIGS) in order to shed light on the use of electronegativity in band alignment models. This is done by measuring the valence band offsets (VBO) using the proposed methodology in chapter 4. Use of electronegativity (EN) also presents another important dilemma in band alignment prediction despite its strong correlation with the strength of interface dipoles. This is the inevitable prediction of unidirectional dipoles at high-k oxide/Si interfaces due to the fact that most, if not all, of the high-k oxides possess larger EN when compared to Si. This is contrary to the common experimental observation of opposing dipole polarities shown in the literature, e.g. negative for La_2O_3 and positive for Al_2O_3. In section 5.2, we show how this dilemma can be resolved by introducing a novel dipole neutrality point (DNP) model in our work.

5.1. Evaluation of current band alignment models

Two widely accepted band alignment models utilize the concept of the charge neutrality level (CNL), whose importance was briefly demonstrated in the previous chapter. These are the metal induced gap states (MIGS) and interface induced gap states (IFIGS) models. These models have been successfully applied to various semiconductor-oxide heterojunctions and can frequently achieve good predictions of band offsets.[97, 212, 213, 214] Equations (5.1) and (5.2) show the prediction of the conduction band offset (CBO) and valence band offset (VBO) for the MIGS and IFIGS models respectively.

$$\mathrm{CBO} = \chi_a - \chi_b + (S-1)(\Phi^{\mathrm{Vac}}_{\mathrm{CNL,a}} - \Phi^{\mathrm{Vac}}_{\mathrm{CNL,b}}), \tag{5.1}$$

$$\mathrm{VBO} = \Phi^{\mathrm{VBM}}_{\mathrm{CNL,b}} - \Phi^{\mathrm{VBM}}_{\mathrm{CNL,a}} + D_X(\mathrm{EN}_b - \mathrm{EN}_a). \tag{5.2}$$

In Eqs. (5.1) and (5.2), subscript "a" represents the semiconductor while subscript "b" represents the oxide (or larger bandgap semiconductor) in both equations. Equation (5.1) is generally termed the MIGS model since it is an extension from the metal-semiconductor junction to a semiconductor-oxide lineup.[97] Here, the concept of CNL still plays a key role but the metal and semiconductor are replaced by a semiconductor and oxide, respectively. The term, Φ_{CNL}^{Vac} in Eq. (5.1) represents the energy separation from the CNL to the vacuum (Vac) level. The difference in the electron affinities (χ), represented by the first two terms in Eq. (5.1), gives the conduction band offset in the canonical lineup whereby there is no charge transfer, i.e. the Schottky-Mott limit (when $S = 1$). As the CNL is the neutral energy level for gap states, the driving force to achieve charge neutrality at the interface will try to align the two CNLs at each side.[96] The last two terms in Eq. (5.1) represents the gap states dipole contribution which is further mediated by the pinning or slope parameter (S). This parameter is semi-empirically shown to be proportional to the electronic polarizability of the oxide. On the other hand, the IFIGS model shown in Eq. (5.2) describes the resultant VBO as a combination of the effects of the intrinsic gap states and chemical dipoles. In this approach, the CNLs (or branch points) of both materials will, again, tend to align to minimize the intrinsic gap states dipole and achieve a charge neutral interface and this shown by the first two terms in Eq. (5.2). Here, we note that the concept of branch points used in the IFIGS model is identical to that of the CNL used in the MIGS model and we will use CNL henceforth for consistency. One difference is, however, that the CNL in the IFIGS model is usually referenced to the valence band maximum (Φ_{CNL}^{VBM}) instead of the vacuum level (Φ_{CNL}^{Vac}). The absence of the vacuum level in the equation is useful since the concept of vacuum level at the

interface is not well-defined. The last two terms in Eq. (5.2) of the IFIGS model then describe the formation of chemical dipoles that results from the difference in electronegativities (EN) of the two materials. This is again mediated by a slope parameter, D_X, which is similar to the usage of S in Eq. (5.1). Despite the use of different parameters in both equations, we note that intrinsic gap states play a key role for both models. It appears that the gap states act as a starting lineup for the IFIGS model but serve as a driving force in charge transfer and alignment for the MIGS model.

5.1.1. Band offset measurement of LAO heterostructures

To evaluate the MIGS and IFIGS models, band offsets of a range of LAO heterostructures were measured. Amorphous 5 nm thick LAO films were sputter-deposited (at 100 W under room temperature) on six different semiconductor substrates, i.e. silicon (Si), germanium (Ge), indium gallium arsenide ($In_{0.53}Ga_{0.47}As$), gallium arsenide (GaAs), gallium nitride (GaN) and zinc oxide (ZnO). The cleaning of the substrates was described in section 3.1.1. The core-level orbitals used for our analysis were carefully chosen and these are shown in Table 5.2 in a later section. As much as possible, orbitals with overlaps were avoided to minimize errors due to fitting. For example, due to the proximity of the O 2s and In 4d signals, the Ga 3d core level was not used for InGaAs.

Differential charging can be a major source of error for oxide-semiconductor structures whereby the charging of the oxide and semiconductor occurs at different rates. As mentioned in the previous chapter, this is expected due to the difference in conductivity between the two materials leading to a comparatively

diminished capability of the oxide in compensating for electrons lost via photoemission. When this occurs, a different charge state of the semiconductor and oxide will give inaccurate band offset measurements. A clear indication of differential charging effects is apparent in cases whereby the semiconducting substrates are suitably conductive. This is shown in the stability of the BE position of the substrate peaks over time in contrast to the BE of the oxide peaks that exhibit an exponential increase. This trend is observed for Si, Ge, $In_{0.53}Ga_{0.47}As$ and GaAs substrates in this work as they exhibited good conductivity. The time-resolved XPS method is also useful when the substrates are not as conducting (e.g., ZnO and GaN). In this case, both the oxide and the semiconductor will exhibit different rates of charging due to both conductivity differences and proximity to the supply of electrons (i.e. grounding, flood gun or stray electrons).

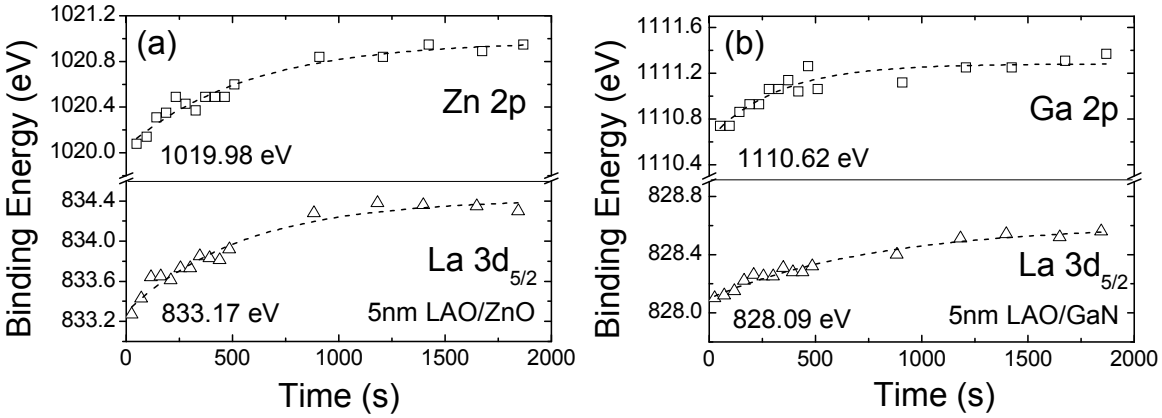

Fig. 5.1: Time resolved plots showing the respective binding energies (BE) vs. X-ray irradiation time for 5 nm thick LAO films on (a) ZnO and (b) GaN substrates, with application of a low energy electron flood gun (3V, 0.1 mA).

An example of the charging profiles of LAO on both ZnO and GaN are plotted in Fig. 5.1(a) and 5.1(b). The eventual charge-free BE values are then obtained from the time-zero intercept from the fitted plots in a similar manner as discussed in section 4.1.2.1. As such, the true interface core-level separations are then derived

and used for calculation of the band offset. Table 5.1 shows a comparison between our experimental band offsets that are free from differential charging, and those that are available from the published literature.

Table 5.1: A comparison of our experimental valence band offset (VBO) values against those that are available in the literature. Note that the data in literature obtained by both photoemission techniques using core level, XPS (ΔE_{CL}), and valence band, XPS (ΔE_V), separation at the interface do not explicitly account for differential charging. The VBO values obtained using internal photoemission (IPE) and photoconductivity (PC) is also shown. VBO is derived from the band gap values measured using PC and the conduction band offset obtained from IPE. All values are expressed in electron volt (eV) with an experimental error of ± 0.1 eV.

	LAO/GaN	LAO/GaAs	LAO/Si	LAO/Ge	LAO/InGaAs	LAO/ZnO
This work	1.21	2.56	2.73	3.12	2.66	0.22
IPE/PC	-	2.65[a]	2.60[b]	-	-	-
XPS (ΔE_{CL})	-	-	3.20[c]	-	3.10[e]	-
XPS (ΔE_V)	-	-	2.86[d]	3.06[d]	-	-

a. See Ref. 215
b. See Ref. 191
c. See Ref. 185
d. See Ref. 189
e. See Ref. 216

We have shown in section 2.4.2.2 how the band offset measurements using valence bands at interfaces (denoted as XPS (ΔE_V)) can be less accurate as compared to that by core-level separations (denoted as XPS (ΔE_{CL})). The range of possible errors involved with using XPS (ΔE_V) can over- or under-compensate the true band offset values because this measurement is dependent on both thickness and differential charging (which can act in an opposing manner) of the oxide film. Next, it is seen that the existing available measurements by internal photoemission (IPE) and photoconductivity (PC) are always smaller than those obtained from

XPS (ΔE_{CL}). The larger values obtained is an indication of differential charging. This trend can be similarly observed in other independent studies on insulators such as hafnium oxide on Si (HfO_2/Si).[190] The close agreement of our results with that of IPE/PC measurements (which is not affected by differential charging) suggests strongly that some values previously obtained can be influenced by differential charging and our time-resolved XPS method can effectively correct for this artifact to reconcile the data obtained from the two different measurements. This gives us good confidence in our experimental measurements.

5.1.2. Derived slope parameters for MIGS and IFIGS models

As discussed in section 5.1, the slope parameter provides a useful test for the MIGS and IFIGS models and can be derived from the range of LAO heterostructures. This is because the slope parameter depends largely on the polariziablity of the larger band gap material (see section 2.3.2), i.e. LAO which is fixed in this study involving LAO heterostructures. The motivation behind the choice of the substrates is two-fold: firstly, the provision of a good range of CNLs for a fair examination of both models; and secondly, the relevance of the respective heterojunctions formed in terms of potential applications. Possible applications of LAO include uses as a charge trapping layer in nonvolatile memory devices (LAO/Si) or as a gate dielectric in high speed transistors that employs high mobility channel materials (LAO/InGaAs, or LAO/Ge) or wide bandgap semiconductors (LAO/GaN) for high power applications.[209,217] In both scenarios, the resultant band offset is important as it influences electron tunneling, charge trapping and the resultant charge storage behaviour (charge trapping layer)

and controls the leakage current in the CMOS gate stack (gate dielectric). After obtaining the experimental slope parameter for LAO, one can then extrapolate to predict for other novel unknown LAO heterojunctions, such as LAO/InSb or LAO/SiC.

The charge neutrality level (CNL), or branch point, is also important in the evaluation of the slope parameter, as can be seen Eqs. (5.1) and (5.2). Since various theoretical computational methods are available to calculate CNL, it is useful to first understand some of the issues involved in these calculations. Most of the CNL values are obtained from theoretical studies that take the weighted average of valence and conduction band density of states (DOS) at special points of the Brillouin zone.[101] However, for semiconductors, such as GaN and ZnO, with conduction bands that have a lower energy in the vicinity of Γ, we use the values obtained from calculations with quasi-particle band structures.[218] These values indicate that the CNLs for ZnO and GaN lie respectively above and close to their CBM. The recent experimental observations of n-type surface conductivity of ZnO due to surface electron accumulation demonstrate the accuracy of these theoretical calculations.[219]

A compilation of our experimental VBO values and the chosen CNLs is shown in Table 5.2. Other values, such as the electron affinity and electronegativity values for the semiconductors used in this study, can be easily obtained from the literature. The electron affinity for LAO, on the other hand, has been determined from the previous chapter. Using these values, we can then provide more insights into both models as will be discussed in the following sections.

Table 5.2: Summary of intrinsic properties of the semiconductors for electron affinity (χ), bandgap (E_g) and energy distance from the valence band maximum to the charge neutrality level (Φ_{CNL}^{VBM}).[209,97] The difference between the electronegativity of lanthanum aluminate (LAO) and the respective semiconductors is given by ΔEN. The conduction band offset (CBO) and valence band offset (VBO) of each semiconductor with LAO as predicted by the metal induced gap states (MIGS) and interface induced gap states (IFIGS) models are shown. Experimental VBO (± 0.1 eV) values are obtained in this work by measuring the bulk core-level separation (E_{CL} - E_V) and the interface core-level separation (ΔE_{CL}) of the selected core level orbitals to represent the substrate. The measured CBO (± 0.2 eV) is obtained by using the measured bandgap value of 6.13 eV for LAO. ΔEN is presented in Miedema units while the rest of the values are in electron volts (eV).

		Theoretical Models					Experimental data				
			MIGS		IFIGS						
	E_g	χ	Φ_{CNL}^{VBM}	CBO	ΔEN	VBO	Orbitals	$E_{CL} - E_V$	ΔE_{CL}	VBO	CBO
GaN	3.35[b]	3.30	2.31[b]	1.67	0.23	1.59	Ga 2p	1115.83	-282.53	1.21	1.57
GaAs	1.45	4.15	0.50	2.16	1.15	3.82	As 3d	40.43	794.22	2.56	2.12
Si	1.12	4.05	0.36	2.20	0.88	3.84	Si 2p	98.96	735.86	2.73	2.28
Ge	0.67	4.13	0.18	2.37	1.03	4.09	Ge 3d	29.35	805.86	3.12	2.34
InGaAs	0.75[c]	4.54[d]	0.60[d]	2.75	1.21	3.75	As 3d	40.35	794.40	2.66	2.72
ZnO	3.21[b]	4.25[a]	3.40[b]	2.75	0.08	0.44	Zn 2p	1019.12	-186.81	0.22	2.70

a. See Ref. 101
b. See Ref. 219
c. See Ref. 220
d. Estimated from Vegard's law

Equation (5.1) for the MIGS model shows that an experimental value of the slope parameter S can be derived by plotting the (CBO - χ) versus Φ_{CNL}^{Vac} as is shown in Fig. 5.2. The gradient of the plot will yield (S - 1) and from which, one can easily derive the experimental value of S. The linear least square fit (dashed line in Fig. 5.2) of our data points gives a slope of -0.40 ± 0.07, yielding an S value of 0.60 ± 0.07. This is very close to the theoretical prediction of 0.53 from the electronic polarizability of the oxide. The slight difference in the values can be due to

possible differences in atomistic details at the interface that are not accounted for in the MIGS model.[212]

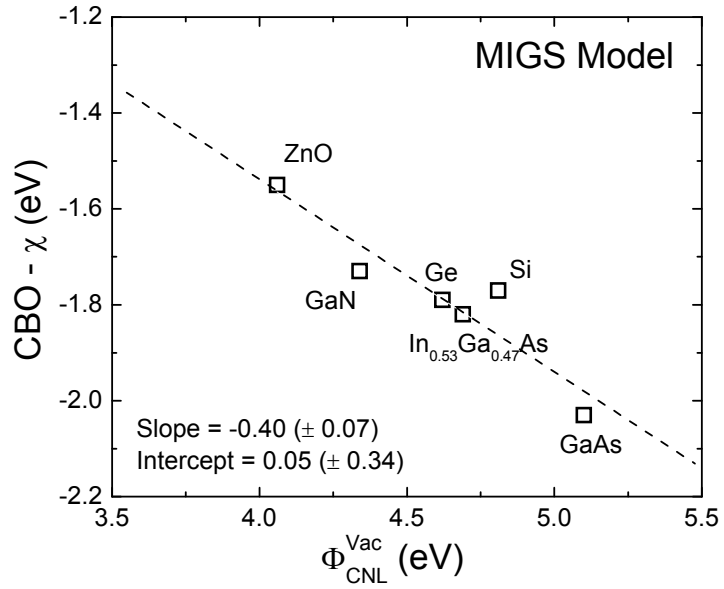

Fig. 5.2: Plot of experimental conduction band offset (CBO) minus the electron affinity (χ) of the semiconductor versus the energy distance from the charge neutrality level (CNL) to the vacuum level (Φ_{CNL}^{Vac}) for LAO on various semiconductor substrates. The plot yields an experimental slope parameter of 0.6.

One reason for the good agreement can be attributed to more accurate band offsets determination after the differential charging effects were corrected. Moreover, it is emphasized again that accurate measurement of electron affinities χ of novel high-k oxide materials are also crucial, as seen from Eq. (5.1), since there is a lack of reliable data in the literature hitherto. These two parameters have to be carefully measured, as was the case in this work, in order to accurately examine or use the MIGS model. Using the experimental slope parameter, we can predict the CBOs (VBOs) of LAO on InSb and 4H-SiC substrates to be 2.85 eV and 1.67 eV (3.11 eV and 1.21 eV), respectively. These values, which have not been reported in the literature thus far, show that LAO can be a suitable high-k dielectric on these substrates in terms of leakage current considerations. However, judging from the

CNL of LAO on 4H-SiC, the derived VBO suggests a low hole barrier height, which implies that leakage current might be a problem for p-type 4H-SiC devices.

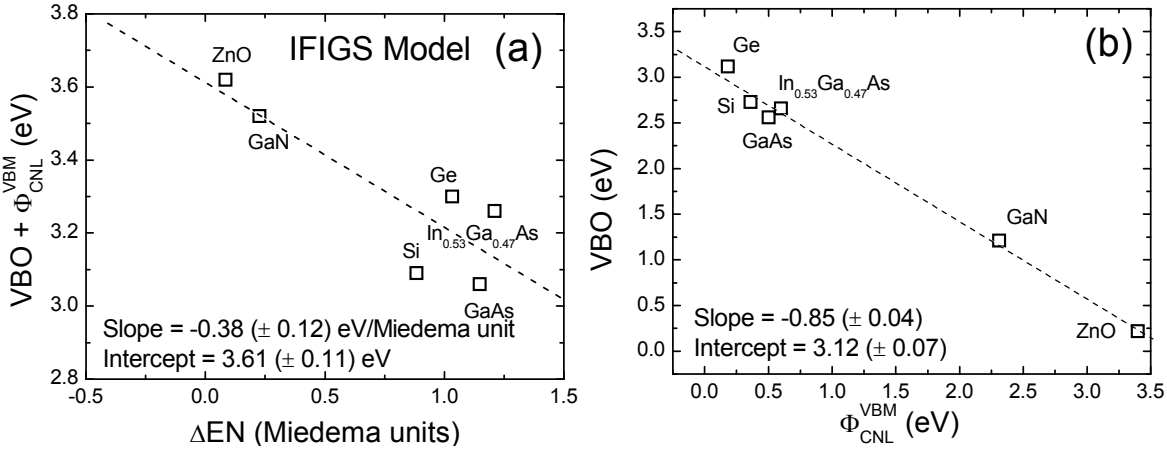

Fig. 5.3: (a) Plot of experimental valence band offset (VBO) plus the energy distance from the valence band maximum (VBM) to CNL (Φ_{CNL}^{VBM}) versus the difference in electronegativity (ΔEN) between LAO and the various substrates. The plot yields an experimental slope parameter (D_X) of -0.38 eV/Miedema unit. (b) Plot of the experimental valence band offset (VBO) versus energy distance from the valence band maximum to the charge neutrality level (CNL), Φ_{CNL}^{VBM}.

The IFIGS model can be similarly examined by plotting (VBO + Φ_{CNL}^{VBM}) against ΔEN as shown in Fig. 5.3(a). The Miedema electronegativities (ENs) of the compound materials are obtained based on a geometric mean approach introduced in ref. 213 and ΔEN ($EN_{oxide} - EN_{semiconductor}$) is as defined in Eq. (5.2) . In this plot, the slope yields the value of D_X which turns out to be -0.38 (± 0.12) eV/Miedema units. Unlike the MIGS model, this experimental slope parameter differs from the theoretical predictions. If we use the theoretical pinning parameter of 0.53 and the semi-empirical proportionality constant (A_X) of 0.86 eV/Miedema unit, we will obtain a value of 0.46 for D_X using Eq. (5.5). The experimentally obtained value of -0.38 is therefore significantly different (of opposite signs) from the theoretical derivation of 0.46.

The obtained negative value for D_X is counter intuitive to the role of the mediating slope parameter that should be within the range of 1 and 0. This discrepancy is not obvious if the slope parameter is not explicitly examined and this occurs if the EN is not appropriately included in the axis of the plot.[214] This is because Eq. (5.2) shows that the slope parameter acts solely on ΔEN and therefore can easily be overlooked if the variation in EN is not examined. In fact, using the plot of VBO vs Φ_{CNL}^{VBM} as shown in Fig. 5.3(b), we can similarly obtain the frequently reported negative relationship (slope of -0.85 ± 0.04) with the same set of data. While this is often taken as a proof for the accuracy of the model, we stress that such plots will only affirm the domineering role of gap states in the overall band lineup as shown by our results. The examination of the slope parameter, as shown in Fig. 5.2 and Fig. 5.3(b), allows for a more stringent and rigorous test of the two models.

5.1.3. Implications of negative slope parameter

The following section discusses on the implications of D_X being negative. Since the gap states, and hence the CNL, play a domineering role in both models, it is perhaps surprising that the corresponding slope parameter, and hence band offset predictions, can differ greatly. We first show how the MIGS and IFIGS models are related. By substituting into Eq. (5.1) (MIGS model) with CBO = ($E_{g,b}$ – $E_{g,a}$ – VBO) and making VBO to be the subject matter, we can derive the following equation:

$$VBO = \Phi_{CNL,b}^{VBM} - \Phi_{CNL,a}^{VBM} + S[\Phi_{CNL,b}^{Vac} - \Phi_{CNL,a}^{Vac}]. \quad (5.3)$$

The derived Eq. (5.3) now bears a resemblance to the IFIGS model in Eq. (5.2). It is useful to note that the term Φ_{CNL}^{Vac} is also referred to as the dielectric work function in the derivation of the IFIGS model (section 2.3.4).[213] Comparing Eqs. (5.3) and (5.2), it is seen that if there exists a clear correlation between the dielectric work function and the EN, these two models will be identical. This correlation between the (dielectric) work function with the electronegativity, i.e. $\Phi_{CNL}^{Vac} \sim A_X.EN$, will thus be the critical bridge between these two models. By substituting the Φ_{CNL}^{Vac} parameter in Eq. (5.3) with ($A_X.EN$), we obtain

$$VBO = \Phi_{CNL,b}^{VBM} - \Phi_{CNL,a}^{VBM} + S \cdot A_X[EN_b - EN_a]. \quad (5.4)$$

Comparing Eq. (5.4) with Eq. (5.2), it is now clear that

$$D_X = S \cdot A_X. \quad (5.5)$$

Since the slope parameter lies within the range $1 < S < 0$, the negative D_X obtained in our study suggests that A_X is negative for oxide-semiconductor heterojunction. This is possible because the commonly assumed value of 0.86 eV/Miedema units for A_X (in the IFIGS model) is derived only for metals and some semiconductors, but not for oxides (section 2.3.4).[213] This then motivates us to investigate further on this correlation for oxides using a series of heterostructures involving some commonly used high-k oxides.

5.2. Introduction of a novel dipole neutrality point model

This section investigates the band alignment of various common high-k oxides on Si and Ge to (1) further study the correlation between Φ_{CNL}^{Vac} and EN for oxides and (2) test the validity in using electronegativity to predict interface dipoles. As

mentioned in chapter 4, interface dipoles can contribute to significant flatband voltage (V_{FB}) shifts in novel gate stacks involving high-k dielectrics which can directly affect the threshold voltage of the MOS transistor. Hitherto, there has been no consensus as to the actual mechanism behind interface dipole formation. Many models or theories were proposed to predict the dipole formation, including the interface induced gap states (IFIGS), dielectric contact induced gap states (DCIGS), electrochemical potential equalization, oxygen vacancies and oxygen areal density models.[181,227,221,222] However, no simple predictive model has been established so far. Using the IFIGS model, one can derive a simple relationship between the electronegativity difference between the high-k oxide and semiconductor and the dipole strength (to be shown below).[223,224,225] However most, if not all, of the high-k oxides possess larger EN when compared to silicon (Si) and therefore only dipoles in one direction should form considering the unidirectional charge transfer.[181] This is contrary to the experimental findings whereby Al_2O_3 and La_2O_3 give rise to positive and negative dipole directions, which is used for tuning threshold voltages for p- and n-MOSFETs, respectively.[226,227] Yet, there remains strong evidence for the correlation of EN to the strength of interface dipoles.[223,224,225] In this section, this dilemma is resolved through the introduction of a dipole neutrality point concept that is derived based on a new correlation found between the electronegativity and dielectric work function (for oxides).

Our results in section 5.1.2 show a strong dependence of band offsets on the charge neutrality level (CNL), demonstrating the importance of intrinsic gap states in band alignment models. In order to achieve charge neutrality at the interface,

charge transfer occurs in a manner to minimize the CNL difference at both sides of the high-k oxide/semiconductor heterojunction (see Fig. 5.4).[213,97] This is mediated by the electronic polarizability of the oxide, represented by a pinning parameter (S). The charge transfer behind the formation of this intrinsic dipole (Δ) is driven by the difference in the dielectric work functions, and is derived to be

$$\Delta = (1-S)(\Phi^{Vac}_{CNL,semi} - \Phi^{Vac}_{CNL,oxide}), \quad (5.6)$$

where Φ^{Vac}_{CNL} is the dielectric work function, which is defined as the energy distance from the vacuum level to the CNL, while the subscripts "semi" and "oxide" denote that for the semiconductor and high-k oxide.[97] More details on this derivation can be found in Appendix V.

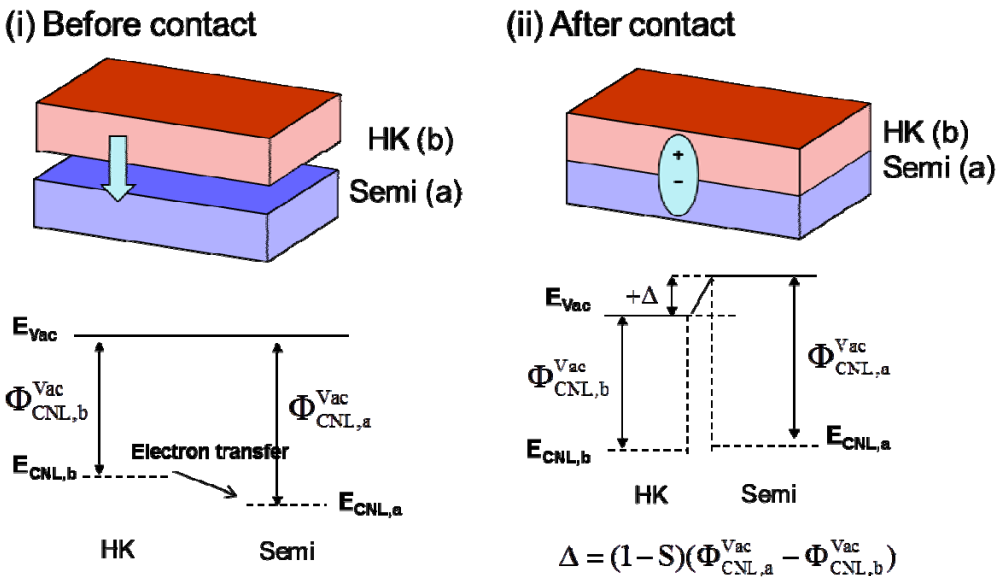

Fig. 5.4: Illustration of the charge transfer responsible for formation of the interface dipole at the high-k oxide/semiconductor interface (i) before and (ii) after contact. This charge transfer occurs due to the difference in the charge neutrality levels (CNLs). We will define a positive dipole formation as shown in (ii) and this occurs when the dielectric work function (Φ^{Vac}_{CNL}) of the high-k (HK) oxide is smaller than that of the semiconductor (Semi).

In this work, the direction of the interface dipole is defined as positive when the negative polarity resides at the semiconductor side for a high-k oxide/semiconductor interface shown in Fig. 5.4. Unfortunately, one needs to

know Φ_{CNL}^{Vac}, which is sometimes unavailable especially for new materials, often because of the lack of data for electron affinity (χ) and the need for theoretical computation of the CNL.[97] Any existing experimental values of χ should also be scrutinized since such measurements are highly sensitive to surface contamination (see section 4.1.3.1). As such, the prediction of dipoles for new material interfaces is often not a straightforward task when using the gap states model approach.

5.2.1. Investigation of correlation for high-k oxides

Given the accuracy of the gap states model and the simplicity of using EN, it is of great interest to reconcile the two approaches and this can be done by examining the correlation between EN and Φ_{CNL}^{Vac}. This approach has been adopted by the IFIGS model and EN suitably replaces χ to describe the Schottky lineup between metals and semiconductors.[213] This is achieved through a good semi-empirical relationship between EN and work function for metals.[107] However, the extension to wide band gap materials, such as high-k oxides, proved to be more involved as their dielectric work function appears to be negatively correlated with EN. Here, we further explore and clarify this relationship for the case of high-k oxide/semiconductor heterojunctions. By obtaining a general relationship to map EN to Φ_{CNL}^{Vac} for high-k oxide materials, a prediction of dipoles for any new high-k oxides can be made easily using only EN instead of Φ_{CNL}^{Vac} (see Eq. (5.6)). In contrast, EN data for elements are widely available and EN for compounds can be easily computed using a geometric mean approach.

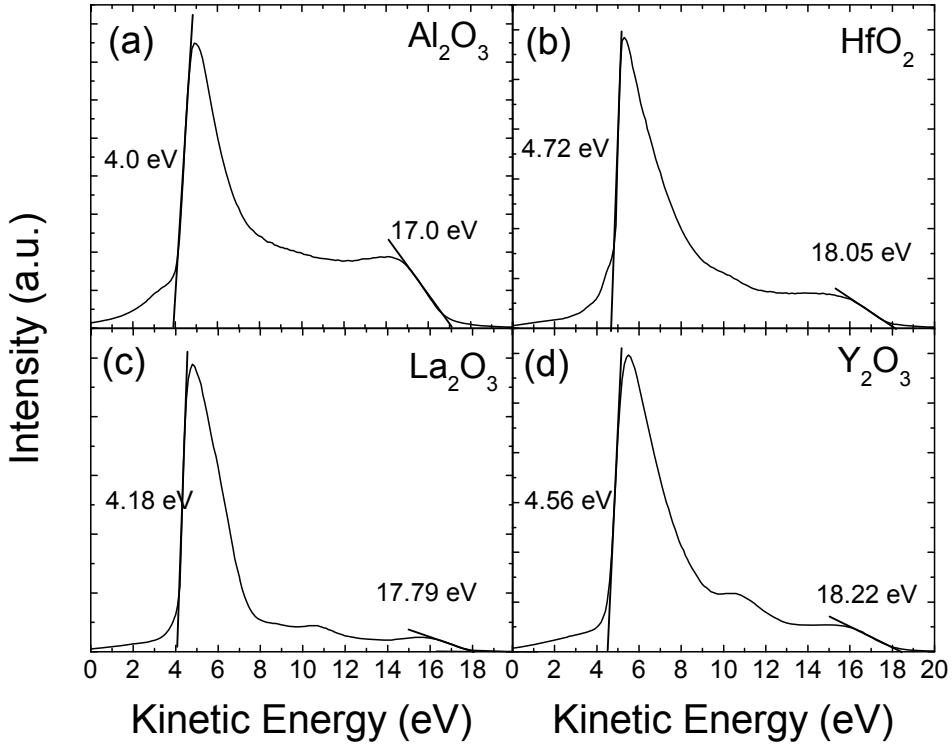

Fig. 5.5: UPS measurements of the high-k oxides used in this study, ie. (a) Al_2O_3, (b) HfO_2, (c) La_2O_3, and (d) Y_2O_3. Note that for all samples, a bias of -15 V is applied, and the surface carbon contaminants are removed after application of low power (150 W) oxygen plasma treatment.

The mapping of EN to Φ_{CNL}^{Vac} requires accurate measurements of χ values for the high-k oxides, which is obtained using UPS (see Fig. 5.5) in this work. The chosen oxides to establish this general relationship are such that they represent both positive (e.g. hafnium oxide (HfO_2) and aluminum oxide (Al_2O_3)) and negative (e.g. yttrium oxide (Y_2O_3) and lanthanum oxide (La_2O_3)) dipole shifts based on the common flatband voltage shifts observed in the literature. Briefly, carbon contaminants were removed using *in situ* low-power oxygen plasma cleaning before UPS measurements (see section 4.1.3.1 for more details).

In addition to χ, the energy distance between the conduction band minimum and the CNL, i.e. Φ_{CNL}^{CBM} or $(E_g - \Phi_{CNL}^{VBM})$ is needed to compute Φ_{CNL}^{Vac}. However, both

the experimental and theoretical Φ_{CNL}^{VBM} values reported in the literature can be noticeably different. It should be noted that the experimental Φ_{CNL}^{VBM} values in the literature are obtained assuming a positive correlation and they are most likely not accurate for oxides.[228] Therefore in this study, theoretical Φ_{CNL}^{VBM} values will be used instead.[97,209] We note that the different computational methods can yield different theoretical CNL values. The range of these reported values will be considered in this study and they are shown in Table 5.3. Lastly, we note that our measured band gap ($E_{g,meas}$) of Al_2O_3 is 7 eV, which differs significantly from the theoretical band gap ($E_{g,th}$) of 8.8 eV that is used in the calculations. As such, the CNL used will be rescaled accordingly using the theoretical CNL (i.e., CNL_{th}) via the relation, $CNL = CNL_{th}$ ($E_{g,meas}$ / $E_{g,th}$).[229] This is valid because the position of the CNL is directly affected by the relative position in energy of the occupied and unoccupied states, as dictated by the band gap.

Table 5.3: Summary of the measured band gap (E_g), electron affinities of high-k (HK) oxides used in this study and the derived dielectric work functions, Φ_{CNL}^{Vac} based on the range of CNL values from literature. Miedema electronegativity values (EN) are also shown. The measured E_{CL}-E_V values for the bulk high-k oxides are used to calculate the experimental valence band offset (VBO). The experimental (Exp.) interface dipole (Δ) of the various high-k oxides on silicon (Si) and germanium (Ge) are shown along with the predicted dipoles (DNP) from our dipole neutrality point model.

Oxide	E_g (eV)	χ (eV)	Φ_{CNL}^{VBM} (eV)	Φ_{CNL}^{Vac} (eV)	EN	E_{CL}-E_V (eV)	VBO (eV)		$\Delta_{HK/Si}$ (V)		$\Delta_{HK/Ge}$ (V)	
							HK/Si	HK/Ge	Exp.	DNP	Exp.	DNP
Al_2O_3	7.0	1.20	4.38 -5.2	3.00-3.82	5.95	71.10	3.45	3.54	0.42	0.49	0.13	0.41
HfO_2	5.8	2.17	3.7-4.0	3.97-4.27	5.85	14.01	3.02	3.23	0.22	0.39	0.05	0.31
Y_2O_3	5.7	1.84	2.3-2.7	4.84-5.24	5.34	154.27	2.32	2.70	-0.05	-0.12	-0.05	-0.20
La_2O_3	6.0	1.89	2.4-2.5	5.39-5.49	5.24	832.15	2.59	2.78	-0.13	-0.22	-0.41	-0.30

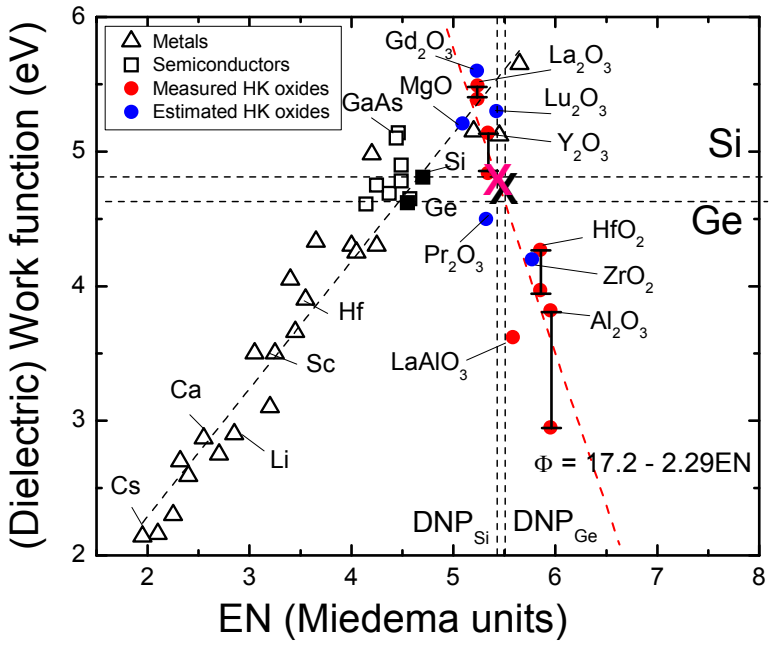

Fig. 5.6: Plot of (dielectric) work function with electronegativity (EN) for different classes of materials including metals (triangles) and semiconductors (squares). Values of high-k oxides using our measured data (red circles) and values from literature (blue circles) are also shown, yielding the negative relationship between the dielectric work function and EN (red dashed line).[97,209,213,230,231,232] The black error bar represents the spread in the CNL values obtained theoretically. It can be seen that the differences from various simulation works do not affect the negative correlation shown. The dipole neutrality points (DNPs) for Si and Ge (shaded black squares) are indicated as red and black crosses (refer to text for explanation).

A summary of the experimental data is shown in Table 5.3. Using our measured values, Φ_{CNL}^{Vac} is plotted versus EN in Fig. 5.6. This plot also includes values for different metals, semiconductors and high-k oxides that are available from the literature. The experimental data for Φ_{CNL}^{Vac} (i.e. HfO_2, Al_2O_3, La_2O_3 and Y_2O_3) obtained in this work and lanthanum aluminate ($LaAlO_3$) in chapter 4, are shown as red circles while those obtained from literature (i.e. Lu_2O_3, G_2dO_3, MgO, Pr_2O_3 and ZrO_2) are shown as blue circles.[97,209,230,231,232] Generally, the compiled data show a negative correlation between Φ_{CNL}^{Vac} and EN. It is important to understand that despite the spread in the Φ_{CNL}^{VBM} values, due to the use of different computational methods, all the resultant Φ_{CNL}^{Vac} still lies within our fitted line (red dashed line). From the slope of this fitted line, we derive a proportionality

constant ($A_{X,HK}$) of -2.29 ± 0.40 eV/Miedema unit for the high-k (HK) oxides used in this study. This negative trend is consistent with the negative D_X obtained previously in section 5.1.3.

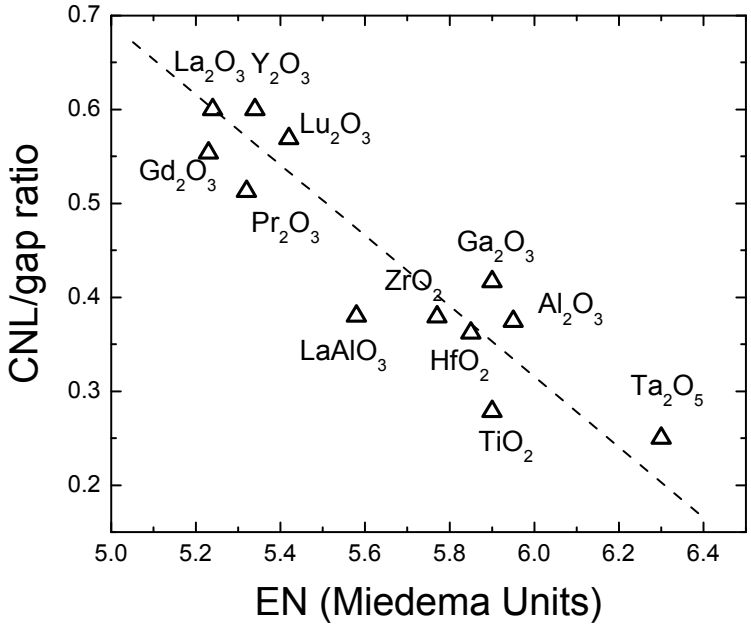

Fig. 5.7: Plot of the CNL/gap ratio (i.e., Φ_{CNL}^{CBM}/E_g) versus electronegativity (EN) for high-k oxides, where Φ_{CNL}^{CBM} is defined to be the energy distance from the charge neutrality level (CNL) to the conduction band minimum (CBM). The values are taken from refs. 97 and 230.

The negative relationship between Φ_{CNL}^{Vac} and EN can be understood further and the main difference can be attributed to the large band gap (E_g). As mentioned earlier, Φ_{CNL}^{Vac} essentially comprises two terms, the electron affinity (χ) and the energy distance between the conduction band minimum (CBM) and the CNL (Φ_{CNL}^{CBM}). For wide band gap materials, such as high-k oxides, the significant E_g values will tend to dominate Φ_{CNL}^{Vac} (as opposed to the smaller χ values) and thus play a major role in affecting its trend. However, there are no clear trends for E_g versus EN. This then prompted us to look at the dependence of the ratio of

CNL/band gap (i.e., Φ_{CNL}^{CBM}/E_g) on EN instead. According to Robertson *et al.*, this parameter varies with different chemical properties and can therefore possibly explain the negative correlation between EN and Φ_{CNL}^{Vac}.[209,97] A plot of the Φ_{CNL}^{CBM}/E_g versus EN is shown in Fig. 5.7 for a range of high-k oxides.[97,230] We observe that oxides of lower EN generally have CNLs further to the CBM (i.e. larger Φ_{CNL}^{CBM}/E_g values). The EN values used in the plot are the geometric means calculated for the compound oxides. We believe that this is more representative than using the individual EN since the geometric mean approach has been successfully used to predict Fermi energies.[106] The use of the geometric mean EN encompasses both effects of anion-to-cation stoichiometry and ionicity which are reported to be correlated with the CNL/bandgap ratio. For example, semiconductors with higher ionicity tend to have CNL that are closer to the CBM (i.e., smaller Φ_{CNL}^{CBM}/E_g).[209] In addition, a higher anion-to-cation stoichiometry for metal oxides also causes the CNL to be closer to the CBM, due to considerations of changes in the density of states in the valence band and conduction band that are dominated by oxygen (anion) and metal (cation) respectively.[97] As such, we conclude that our experimental observation of the negative correlation between EN and Φ_{CNL}^{Vac} can be largely explained by the dependence of the CNL/bandgap ratio on EN related properties such as ionicity or even anion-to-cation stoichiometry. Interestingly, this relationship can also possibly explain the symmetric band offsets of rare earth oxides as compared to most transition oxides which tend to favour VBO (see section 2.1.1). By being more electropositive (i.e. low EN) in nature, the rare earth oxides tend to have CNL values lower within the band gap, thereby achieving a more balanced VBO/CBO ratio.

5.2.2. Dipole neutrality point (DNP) model

After this general relationship is established, we introduce here the concept of a dipole neutrality point (DNP) for semiconductors. The DNP defines the equivalent EN of a semiconductor should the semiconductor possess a similar proportionality constant (A_X) as the high-k oxides. The following equations will show the derivation of the DNP parameter in the use of EN in the dipole equation (i.e., Eq. (5.7)) when different proportionality constants are needed for different materials:

$$\begin{aligned}\Delta &= (1-S)(\Phi^{Vac}_{CNL,semi} - \Phi^{Vac}_{CNL,oxide}) \\ &= (1-S)([A_{X,Semi}EN_{Semi}] + C_{Semi} - [A_{X,oxide}EN_{oxide}] - C_{oxide}) \\ &= (1-S)A_{X,oxide}([A_{X,Semi}EN_{Semi} + C_{Semi} - C_{oxide}]/A_{X,oxide} - EN_{oxide}) \\ &= (1-S)A_{X,oxide}(DNP_{semi} - EN_{oxide})\end{aligned} \tag{5.7}$$

where the subscripts “semi” and “oxide” represent the semiconductor and oxide respectively and C represents the y-intercept of the fitted trend (red dashed line in Fig. 5.6). The equivalence of solving the above equations is to deduce the DNP through simple mapping. In this work as shown in Fig. 5.6, the DNPs for Si and Ge are 5.46 and 5.54 Miedema units as shown by the respective red and black crosses. Here, we can simplify the equation further (i.e., Eq. (5.8)) since the value of S is about 0.5 for most of the high-k oxides and $A_{X,oxide}$ is previously found to be approximately -2 for high-k (HK) oxide materials.

$$\Delta \approx (EN_{HK} - DNP_{semi}). \tag{5.8}$$

The polarity of the impending dipole formation at any high-k/semiconductor interface can hereby be predicted easily using Eq. (5.8). It is seen that the DNP essentially represents a comparison point for a semiconductor with high-k oxides whereby zero interface dipole formation is expected when $DNP_{semi} = EN_{HK}$. In an attempt to justify Eq. (5.8), we look at how changing the bulk chemical

composition of ternary compound oxides affects dipole formation, which can be observed from V_{FB} shifts. For example, the addition of La into bulk HfO_2 dielectric (to form $Hf_{(1-x)}La_xO_y$) reduces the overall bulk EN (geometric mean of contributing elements). Our DNP concept predicts a negative net change in interface dipoles and expectedly, a negative V_{FB} shift is observed.[233] Conversely, another independent study that incorporates Al into bulk HfO_2 reported positive V_{FB} shifts for the $Hf_{(1-x)}Al_xO_y$ compound oxide; a result that is also predicted by the DNP concept since Al increases the overall bulk EN.[234] Apart from these bulk oxides, modification of the effective EN at the interface using interlayers also give rise to agreements in the expected trends. Reports indicate that interlayer modifications at the high-k oxide/Si interface with TiO_2 (larger EN) tend to shift the V_{FB} towards positive values while MgO and Gd_2O_3 (smaller EN) shift the V_{FB} towards negative values.[235,236,237] All these expected V_{FB} shifts or interface dipole formation can be easily predicted by examining the EN of the oxide in comparison with the DNP_{Si}. The vertical line in Fig. 5.6 clearly demarcates the region of zero dipole formation; easy assessment for the dipole directions for new high-k oxides can be clearly read off from the diagram, where positive and negative dipoles are expected on either side of the DNP.

5.2.3. Comparison with experimental interface dipoles

Next, we examine the feasibility of quantitative prediction of dipoles using our DNP concept. This is firstly done using our experimental measurements of the interface dipoles (see Chapter 4), which require the measurement of the valence band offset (VBO) in addition to χ. The measurement of the VBO is carried out

following Kraut's method with correction for differential charging effects using the time-resolved XPS plots (refer to section 4.1.2.1 for more details).

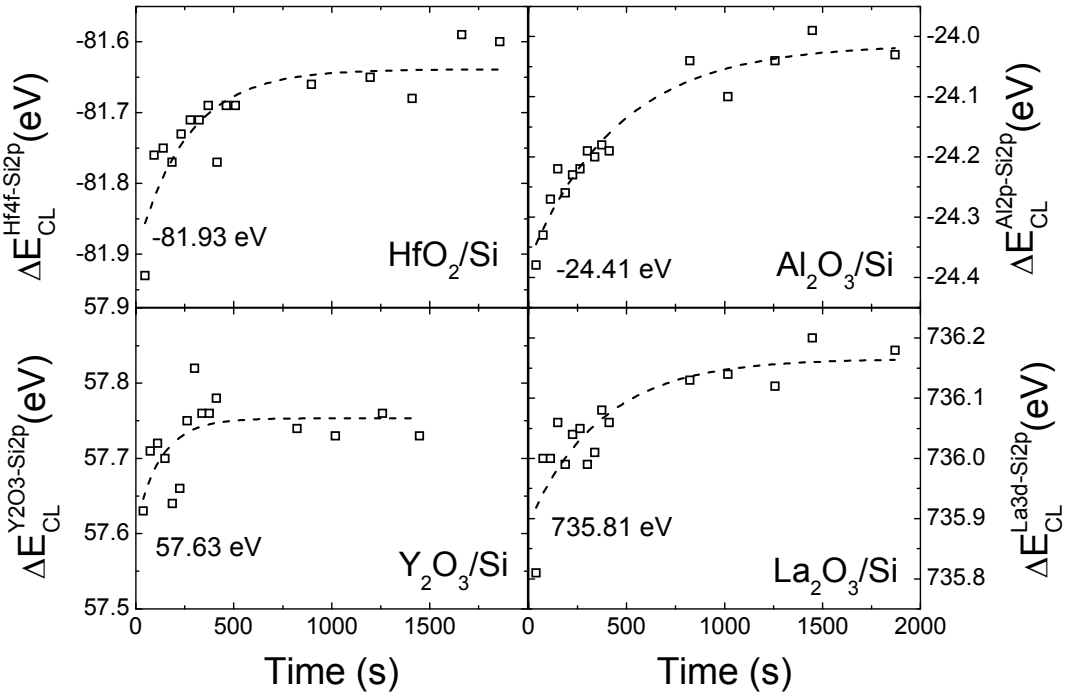

Fig. 5.8: Time-resolved plots used in obtaining the core-level separations for thin high-k oxides on silicon.

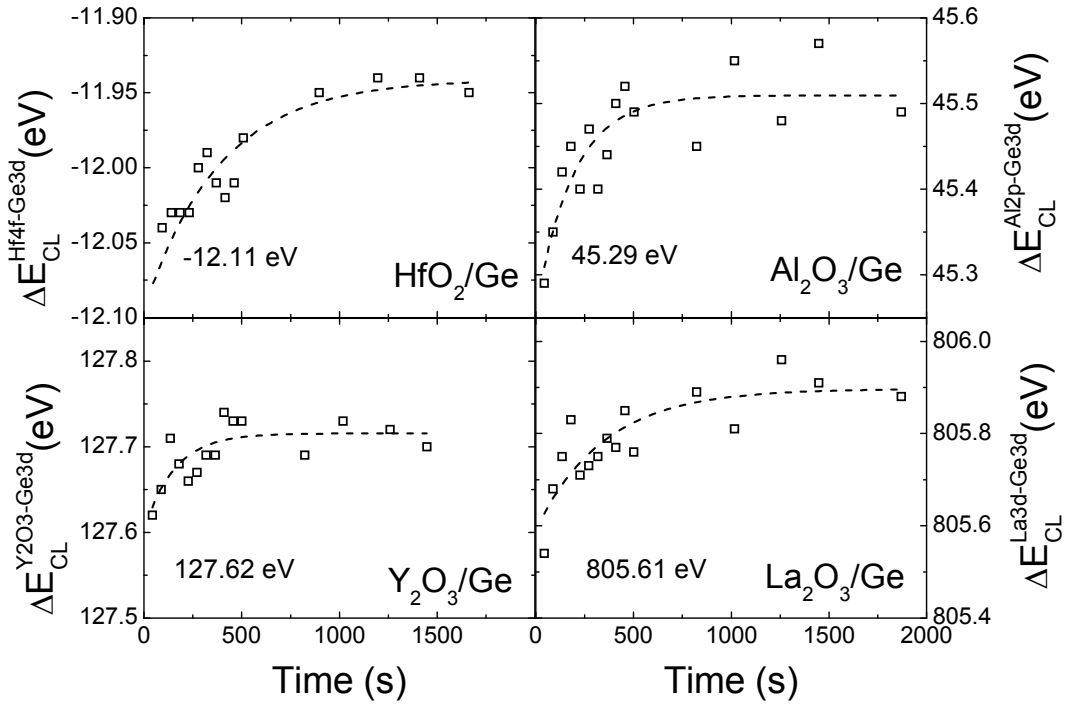

Fig. 5.9: Time-resolved plots used in obtaining the core-level separations for thin high-k oxides on germanium.

Using these plots (Fig. 5.8 and Fig. 5.9), the true core-level separation at the interface is obtained at time zero. The experimental interface dipole, Δ (Exp.), is obtained as the difference in vacuum levels at the interface. The predicted interface dipoles are obtained using DNP_{Si} and DNP_{Ge} of 5.46 and 5.54 Miedema units for Si and Ge, respectively, using Eq. (5.8). A comparison between the experimental and predicted interface dipoles is shown in Table 5.3. It is seen that the simple DNP model predicts the dipole polarities well and also gives reasonable predictions for their strength. In particular, oxides that possess a higher EN (i.e. HfO_2 and Al_2O_3) than DNP will give a positive dipole value while those with a smaller EN (i.e. La_2O_3 and Y_2O_3) will yield a negative dipole.

5.2.4. Comparison with flatband (V_{FB}) voltage shifts

The prediction of the dipole strength is further verified by comparisons with the V_{FB} shifts of the above-mentioned high-k oxides as shown in Fig. 5.10. These V_{FB} shifts are attributed to effects from the interface dipole because they are carefully gathered from a series of systematic capacitance-voltage measurements of bi-layer structures with varying thickness combined with band bending measurements by XPS.[225,238,239] We note that the V_{FB} shifts have been previously attributed to differences in oxygen areal densities and these densities are calculated from bulk oxide structures.[181] However, the effective EN used in the DNP approach also includes oxygen density variations. Unlike the former, the geometric EN mean approach encompasses effects of the metal ions that are not accounted for and their inclusion can be crucial considering findings from interlayer insertion studies.[223,225] We observe that the V_{FB} shifts follow closely with ΔEN (i.e.,

$EN_{HK} - DNP_{Si}$), which is predicted by Eq. (5.8). The largest error between the experimental data and our predictions is ~ 0.13 eV. Lastly, we add that the presence of a SiO_x interfacial layer should not affect the analysis using our DNP concept. A simple calculation will show that SiO_2 has a similar dielectric workfunction compared with Si. This implies that dipoles for high-k oxides on Si should yield identical polarity and similar dipole strength compared to the case on SiO_x and this can suitably explain observed influence of (or lack of) the interfacial oxide.

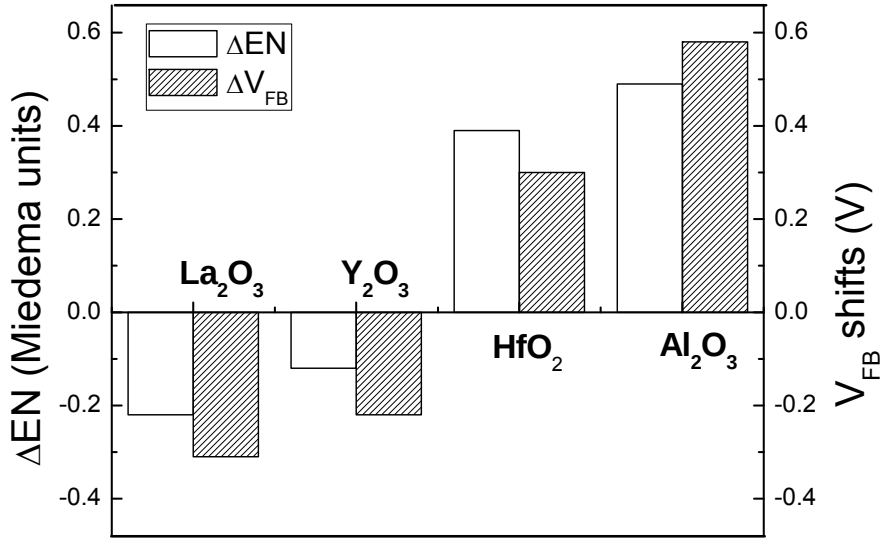

Fig. 5.10: Experimental values of V_{FB} shifts due to interface dipoles and ΔEN (where ΔEN = $EN_{high-k} - DNP_{Si}$, and DNP_{Si} is equal to 5.46 Miedema units) for various labeled high-k oxide/Si capacitor structures are shown as shaded and non-shaded bars, respectively.[225,238,239] The bars are shown in order of increasing EN of the high-k oxides. The plot clearly shows a good correlation between ΔEN and the V_{FB} shifts, thereby supporting our DNP concept for interface dipoles.

Lastly, our model can also be applied to material systems involving insertion of interfacial interlayers. Our previous work demonstrates that enriching the interfaces between Y_2O_3 and various semiconductors with yttrium yields a consistent ~ 0.1 to 0.2 eV reduction in the VBO.[117] This can be explained by the modification of the effective EN near the interface, which results in additional

charge transfer (due to a change in the effective dielectric work function) as predicted by the DNP concept. If we apply the proposed model to other common semiconductors, we can now easily explain the similar V_{FB} shifts on different semiconductor substrates given a certain high-k oxide.[240,241,242] This is because many of the small band gap semiconductors tend to have similar DNPs (from 5.26 to 5.54 eV) and our model therefore predicts similar charge transfers at these interfaces, yielding almost similar dipole values. Our model can also successfully predict the V_{FB} shifts of Ge capacitor structures after insertion of high-k oxide interlayers to improve the interface quality. In particular, high-k oxides that have lower EN (e.g. Y_2O_3 and La_2O_3) than DNP_{Ge}, are observed to result in negative V_{FB} shifts while those with higher EN (e.g. Al_2O_3) results in positive V_{FB} shifts as expected from our simple model.[240-242]

In conclusion, we have introduced a simple concept of dipole neutrality point which allows easy assessment of the interface dipole at the high-k/semiconductor heterojunction without the need to know the electron affinity or CNL values. This model is extremely simple and allows quick and accurate predictions of interface dipoles for new material interfaces. This will be of great value in terms of threshold voltage adjustments in the development of advanced gate stacks using high-k oxide related dipoles.

6. Improving the thermal stability of the $LaAlO_3$/Si interface: Band offset and other electrical properties

Lanthanum aluminate ($LaAlO_3$ or LAO) is a promising candidate as a high-k dielectric because of its large bandgap (6.13 eV), sufficiently large and symmetric band offsets which are both larger than 2 eV (see Chapter 4), and high dielectric constant (22 to 25). This study investigates the thermal stability of this oxide on Si, which is crucial in the conventional CMOS process flow that involves high temperature steps, such as the source-drain activation anneal. Such high temperatures can result in changes at the interface which can lead to alterations of crucial properties such as band offset, interface trap density, and leakage current. Recent works have demonstrated that thermal annealing of high-k oxide films on Si results in undesirable reduction of the conduction band offset (CBO) that can be detrimental in terms of threshold voltage instability and/or increased device leakage current.[243,244] This can be attributed to the changes of the dipole at the interface after high temperature annealing processes. Degradation of the interfacial electrical properties after annealing, such as increase in the density of interface traps, can also be a problem in other high-k oxide materials such as zirconium oxide gate stacks.[245,246] The presence of these interfacial charges can significantly degrade the carrier mobility and drive current in the transistor device through Coulomb scattering and electron trapping, thereby negating the beneficial effects of using the high-k oxide material.[17]

Interface engineering allows one to ameliorate the above issues without affecting the bulk properties of the high-k dielectric, such as wide band gap and high permittivity. In particular, yttrium (Y) can suitably be used as an effective interlayer because yttrium oxide (Y_2O_3) has been shown to improve the thermal stability of the La_2O_3/Si interface by acting as a barrier layer in suppressing the formation of lower dielectric constant interfacial layers.[247] Furthermore, the addition of Y can possibly reduce the gap states densities and alter the interface dipoles.[248,117] Annealing of LAO/Si films is found to lead to degradation in terms of increased interface trap density, larger leakage current, and significant change in the band offset. By addition of a yttrium interlayer, the thermal stability, in terms of the band offset (section 6.1) and other electrical properties such as the interface trap density and leakage current (section 6.2), are improved.

In this study, amorphous LAO films were sputtered deposited on n-type Si (001) wafers. Post deposition furnace annealing was carried out for 30 min at either 600^{o}C or 800^{o}C. Blanket deposited films were used to study the band offsets in section 6.1.1. From section 6.1.2 onwards, capacitors of oxide thicknesses in the range of 8-25 nm were fabricated (for more details see section 3.1.2). Yttrium interlayer samples were fabricated by sputtering a few monolayers of Y (deposition duration of ~3 s), without breaking the vacuum, prior to LAO deposition. A step profiler and atomic force microscopy was used to measure the thickness of a series of sputtered Y metal films to yield a calibrated sputtering rate of 7.7 nm/min for the sputtering conditions used in this work. As such, the expected thickness of Y deposited is ~ 0.39 nm based on this calibration rate.

6.1. Improvement in the thermal stability of band offset

We first investigate the thermal instability of the band offset of LAO thin films on Si using XPS and show subsequently how the instability can be alleviated using a Y interlayer. In this study, variations of band offsets after annealing are determined using photoemission (section 6.1.1) and later verified by electrical methods (section 6.1.2). To ensure that this change in band offset is purely an interfacial effect, the properties of the bulk oxide after annealing is investigated in section 6.1.3, along with the changes in interfacial chemistry. We then propose the mechanism behind the formation of these interface dipoles in section 6.1.4.

6.1.1. Photoemission method

Band offset measurements are carried out using Kraut's method as described in section 4.1.2. Since the bulk core-to-valence separation for the oxide is shown to be the same, any variations in interface core-level separation (ΔE_{CL}) will directly translate to variations in the valence band offset (refer to Eq. (4.1)). Fig. 6.1(a) shows the interface core-level separation of LAO/Si before and after annealing. The La 3d spectrum is fitted with contributions from both La_2O_3 and LaSiO (at ~1 eV higher BE).[249] The respective satellite peaks for La 3d are also fitted consistently with respect to the core La 3d peak with a FWHM of ~2 eV. The measured spectrums show that annealing at 800^{o}C resulted in an increase of ~0.78 eV in ΔE_{CL}. On the other hand, the inclusion of a Y interlayer reduces this variation to ~0.39 eV, as shown in Fig. 6.1(b).

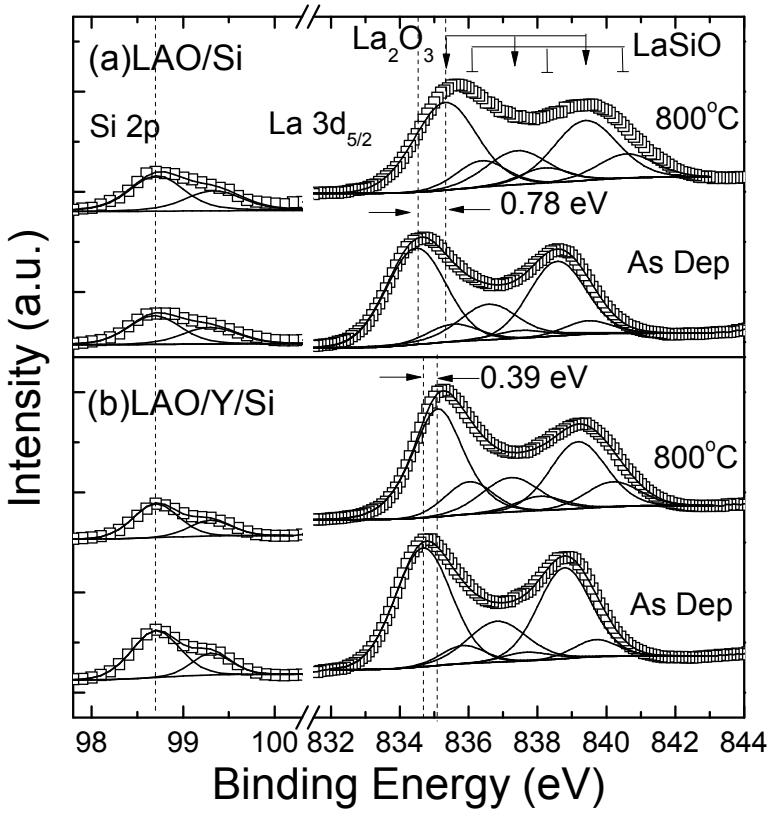

Fig. 6.1: Interface core-level separations of 4 nm (a) LAO/Si and (b) LAO/Y/Si samples before and after 800°C annealing.

At this point, we further emphasize that the difference in these measured ΔE_{CL} values is significant and will directly translate to appreciable VBO changes that can possibly affect the overall threshold voltage stability. It is therefore crucial to ensure the accuracy of these measurements. As mentioned in section 4.1, ΔE_{CL} can be affected by other factors such as band bending, extra-atomic relaxation, and differential charging effects. Band bending effects are reasonably assumed to be negligible since moderately doped substrates are used. On the other hand, extra-atomic relaxation shifts were shown to be minimal for as-deposited (as-dep) samples thicker than 4 nm. For annealed samples, because of the increase in interfacial layer thickness (to be shown in section 6.1.3), this relaxation shift is expected to be lesser since LAO oxide is further from the substrate. This is further confirmed using the experimental Auger parameter measurement (data not shown).

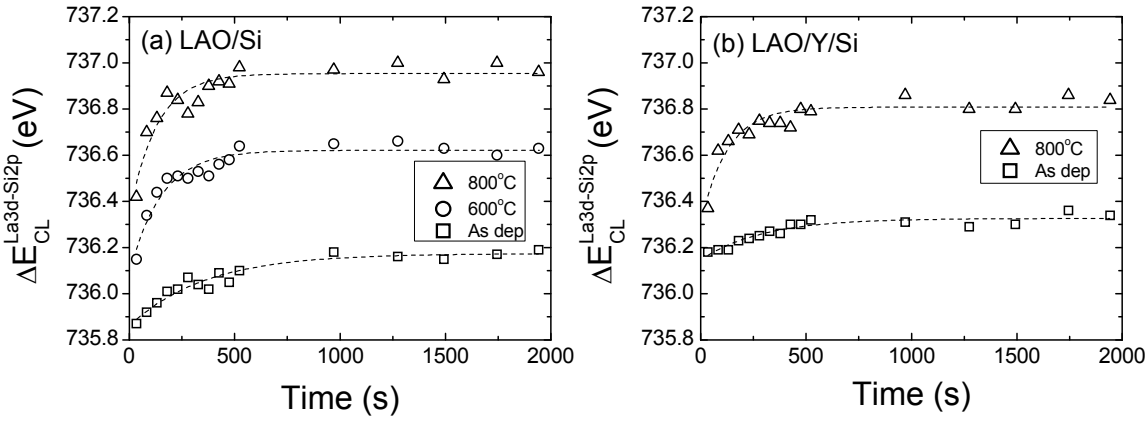

Fig. 6.2: Time-resolved plots showing core-level separations (ΔE_{CL}) vs x-ray exposure time for 4 nm (a) LAO/Si and (b) LAO/Y/Si under different annealing conditions.

Figure 6.2 shows the time-resolved XPS measurements (used to correct for differential charging) of the same LAO/Si and LAO/Y/Si films for the as-dep samples and samples after annealing at different temperatures. The true $\Delta E_{CL(0)}$ values are obtained as the time zero value (see section 4.1.2.1), with an average extracted dielectric time constant of ~212 s. It is seen that after correction for differential charging, a significant increase in $\Delta E_{CL(0)}$ of ~0.48 eV is observed for the LAO/Si sample after annealing at 800°C (as compared to the as-dep sample) while a slight increase of ~0.16 eV is observed for the LAO/Y/Si samples after annealing at 800°C.

Table 6.1: Experimental valence band offsets (VBO) of LAO/Si and LAO/Y/Si films under different annealing conditions, determined using XPS. The experimental error is ±0.1 eV.

		$\Delta E_{CL(0)}$ (eV)	VBO (eV)
LAO/Si	As Dep	735.86	2.73
	600°C	736.08	2.95
	800°C	736.34	3.21
LAO/Y/Si	As Dep	736.14	3.01
	800°C	736.30	3.17

The actual bands offset values of both LAO/Si and LAO/Y/Si films, calculated using Kraut's method, are shown in Table 6.1. The variation in the band offsets is greatly reduced for the samples with a Y-interlayer as the VBO experiences a smaller increase ~0.16 eV after 800^{o}C annealing compared to a ~0.48 eV increase for the sample without a Y-interlayer.

6.1.2. Electrical method: V_{FB}-EOT plots

It is known that flatband voltage (V_{FB}) vs. equivalent oxide thickness (EOT) plots can also provide information on the interfacial band alignment, due to the influence of the interface dipole on the effective metal work function.[182,250] Since this is an electrical measurement, it is entirely of a different nature from the XPS measurements and is a good method to affirm that variation in the interface dipoles is the reason for the band offset changes after annealing. In the following sections, EOT and V_{FB} are individually obtained based on high frequency capacitance voltage (HFCV) measurements carried out on LAO/Si capacitors of different oxide thicknesses from 8-25 nm. These HFCV measurements are carried out at 100 kHz using the HP4284 LCR meter. The V_{FB}-EOT plots are then used to obtain the effective metal work function, which is able to provide information on the interface dipole.

6.1.2.1. EOT determination

We first discuss some of the methods for accurate EOT determination, which is of importance in deriving the effective metal work function. Typically, the EOT can be obtained experimentally from the maximum capacitance (C_{max}) in the

accumulation region of the C-V measurements, if the approximation of $C_{max} \approx C_{ox}$ (where C_{ox} is the oxide capacitance) is valid. However, the approximation can be inaccurate when the silicon space charge capacitance in accumulation ($C_{sc,acc}$) is comparable to C_{ox}. One indication of this is a non-saturating C_{max} even under very strong accumulation. In order to determine EOT accurately, we looked at various techniques as will be described further. The McNutt and Sah (Mc) technique invokes the assumptions of negligible contributions from interface trap capacitance (at 100 kHz) and bulk oxide trap density while quantization effects are also excluded.[251] The Maserjian (Mas) technique makes use of the same assumptions except that it attempts to approximate for the quantization effects.[252] Thirdly, Samares Kar proposed two techniques (denoted as Kar 1 and Kar 2) for accurate EOT extraction by assuming that $C_{sc,acc}$ and the interface trap capacitance (C_{it}) are exponential functions of the surface potential.[253] With this assumption, a linear relationship between $|C^{-1}\, dC/dV|^{1/2}$ versus C is derived, from which C_{ox} can be obtained from the intercept with the C-axis (Samares Kar 1 in Fig. 6.3(a)). Similarly, a plot of $|dC^{-2}/dV|^{1/2}$ versus 1/C can also be used to extract the *EOT* since the x-axis now yields $1/C_{ox}$ (Samares Kar 2 in Fig. 6.3(b)). Comparison of the extracted C_{max}, from which the *EOT* is determined, based on these extrapolation plots is shown in Fig. 6.3(a) and 6.3(b) using a 9 nm thick LAO capacitor structure (as-deposited) as an example. Generally, we managed to obtain reasonably linear plots using the above-mentioned extrapolation techniques. Lastly, a quantum mechanical C-V simulator (QMCV) developed by the Berkeley group is also employed.[254] The simulated C-V is matched with the experimental C-V data to obtain EOT from C_{max}. In this simulator, quantum mechanical (QM) effects were accounted for by solving Schrodinger and Poisson equations self-

consistently with the Fermi-Dirac distribution for the electron/hole distributions in both inversion and accumulation conditions. An example of matching the simulated C-V curve with the experimental data using EOT as a fitting parameter is shown in Fig. 6.3(c).

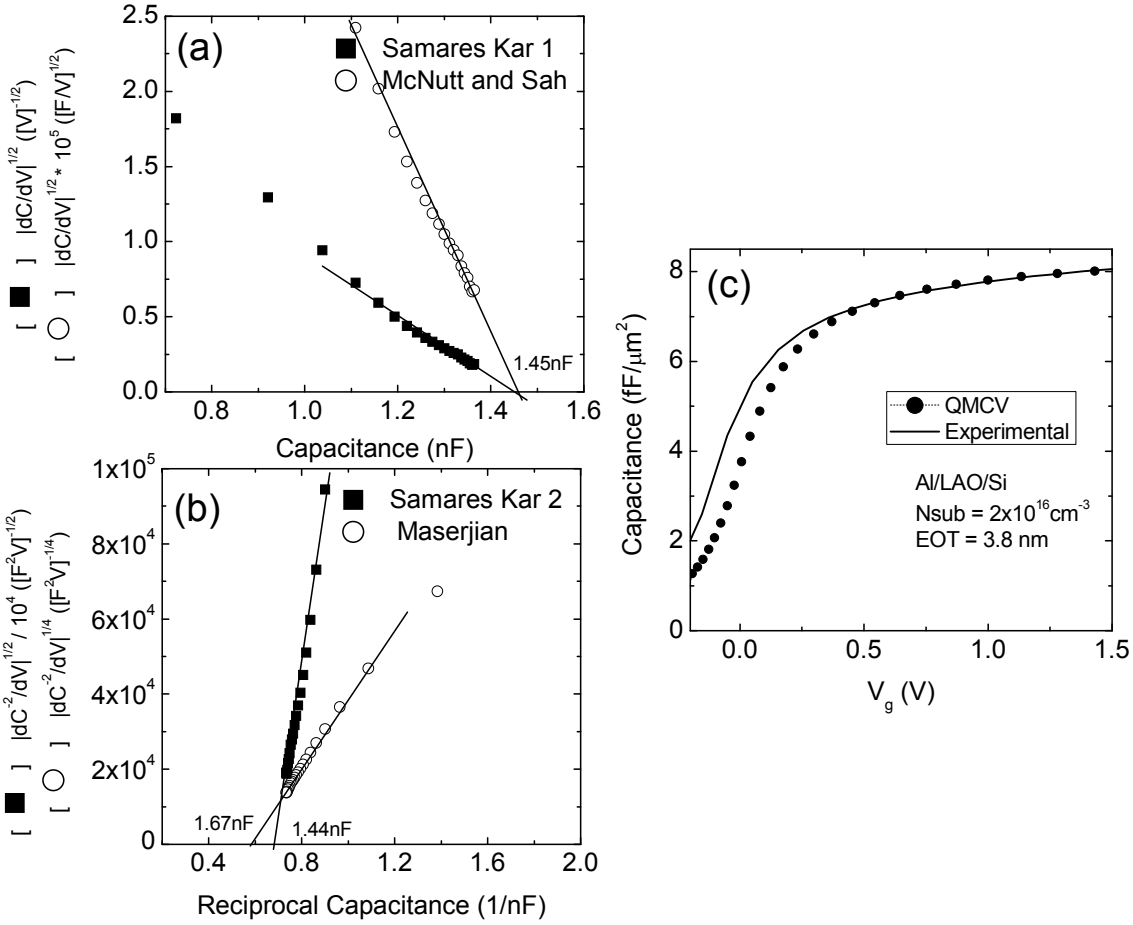

Fig. 6.3: Comparison of various extrapolation based methods to determine EOT for Al/LAO(9nm)/Si capacitors (as-deposited). (a) McNutt and Kar 1 and (b) Maserjian and Kar 2 techniques are shown with the extracted EOT values as indicated; (c) Fitting of the experimental C-V data in strong accumulation using the quantum mechanical C-V simulator (QMCV) from the Berkeley group.

A summary of the EOT determined using all the above-mentioned techniques is shown in Table 6.2. Generally, the results differ by an average of ~5% (largest deviation of ~11%). We take the QMCV method as the most accurate procedure and will base our analysis on this. This is because when QM effects are accounted for, smaller EOT values are generally obtained and this is what we observe.

Table 6.2: Comparison of the equivalent oxide thickness (EOT) values extracted using different extrapolation based techniques, namely McNutt and Sah (Mc), Maserjian (Mas) and Samares Kar (Kar 1 and Kar 2) techniques. Fitting using a quantum mechanical C-V simulator (QMCV) developed by the Berkeley group generally gives a lower EOT value and it differs by an average of ~5% compared with the extrapolation methods mentioned above.[254] The largest difference is ~11%.

			EOT (nm)				
			Mc	Kar 1	Mas	Kar 2	QMCV
LAO/Si	9.0 nm	Bef. Anneal	3.96	3.96	3.46	3.99	3.80
		800˚C PDA	4.38	4.70	4.28	4.82	4.40
	12.5 nm	Bef. Anneal	5.93	6.00	5.26	5.86	5.70
		800˚C PDA	6.25	6.29	5.83	6.38	6.10
	15.0 nm	Bef. Anneal	6.41	6.40	5.36	6.38	6.00
		800˚C PDA	5.68	5.74	5.31	5.74	5.40
	22.5 nm	Bef. Anneal	10.12	10.27	9.60	10.18	9.70
		800˚C PDA	8.27	8.35	7.71	8.26	8.20
	27.5 nm	Bef. Anneal	10.73	10.73	10.00	10.75	10.30
		800˚C PDA	10.30	10.43	10.05	10.45	9.80
LAO/Y/Si	8.0 nm	Bef. Anneal	4.22	4.22	4.22	4.16	3.80
		800˚C PDA	4.74	4.78	4.48	4.86	4.50
	12.0 nm	Bef. Anneal	5.17	5.22	4.48	4.99	4.80
		800˚C PDA	5.79	5.83	5.52	5.86	5.50
	13.0 nm	Bef. Anneal	5.90	5.89	5.26	5.80	5.65
		800˚C PDA	6.02	6.03	5.57	5.91	5.70

6.1.2.2. V_{FB} determination

The flatband voltage (V_{FB}) was obtained by reading off the experimental C-V curve at a calculated flatband capacitance (C_{FB}) based on extracted doping concentration, N_{sub} and EOT parameters (refer to section 3.2.4.1 for more details). N_{Sub} is obtained from the minimum capacitance of the HFCV curves. It is found that the range of values obtained lie within 1 x 10^{16} to 2 x 10^{16} cm^{-3}, which is in good agreement with the doping as indicated by the wafer supplier.

6.1.2.3. V_{FB}-EOT plots: Changes in effective metal work function

After determining both V_{FB} and EOT experimentally, we will show the relationship between these two parameters, and how information on interface

dipoles can be obtained. Flatband corresponds to a condition whereby the semiconductor (Si in this case) is free of any electric field (i.e., no band bending). It is therefore sensitive to any oxide charges within the gate stack and the relative alignment of the two materials as shown in Eq. (6.1) below. The equation shows the contribution of the oxide charges and the importance of the relative band alignment manifested through contributions from interface dipoles. Equation (6.1) is for a high-k oxide on Si with the presence of SiO_x in the interfacial layer as shown in Fig. 6.4 (a),[255] and given as

$$V_{FB} = -EOT_{HK}\left(\frac{Q_0 + Q_1}{\varepsilon_0\varepsilon_{ox}}\right) - EOT_{HK}EOT_{IL}\frac{\rho_{IL}}{\varepsilon_0\varepsilon_{ox}} - \frac{Q_0 EOT_{IL}}{\varepsilon_0\varepsilon_{ox}} - \frac{EOT_{IL}^2}{2}\frac{\rho_{IL}}{\varepsilon_0\varepsilon_{ox}}$$
$$-(EOT_{HK}^2)\left(\frac{\rho_{HK}}{2\varepsilon_0\varepsilon_{ox}}\right) + \frac{\Phi_{ms}}{q} + (\Delta_{MG/HK} + \Delta_{HK/IL} + \Delta_{IL/Si}). \quad (6.1)$$

where EOT represents the equivalent oxide thickness for the high-k (HK) material and interfacial layer (IL) as indicated by the subscript. The symbol q is the electronic charge, ε_0 is the permittivity of free space and ε_{ox} is the dielectric constant of silicon oxide. Q_0 and Q_1 represent the total amount of Q_f and Q_{it} at the (IL)/Si and high-k (HK) oxide/SiO_2 interface respectively, while ρ_{IL} and ρ_{HK} represent the bulk charge density within the IL and high-k oxide films respectively. Δ represents the potential change induced by the respective dipole (the various subscripts denotes the interface at which the dipole resides). The effective metal-semiconductor workfunction, $\Phi_{eff,ms}$, is defined as the eventual difference between the vacuum workfunctions of the metal and semiconductor and this is obtained as the y-intercept of a V_{FB} vs. EOT_{HK} plot (see Eq. (6.1)).

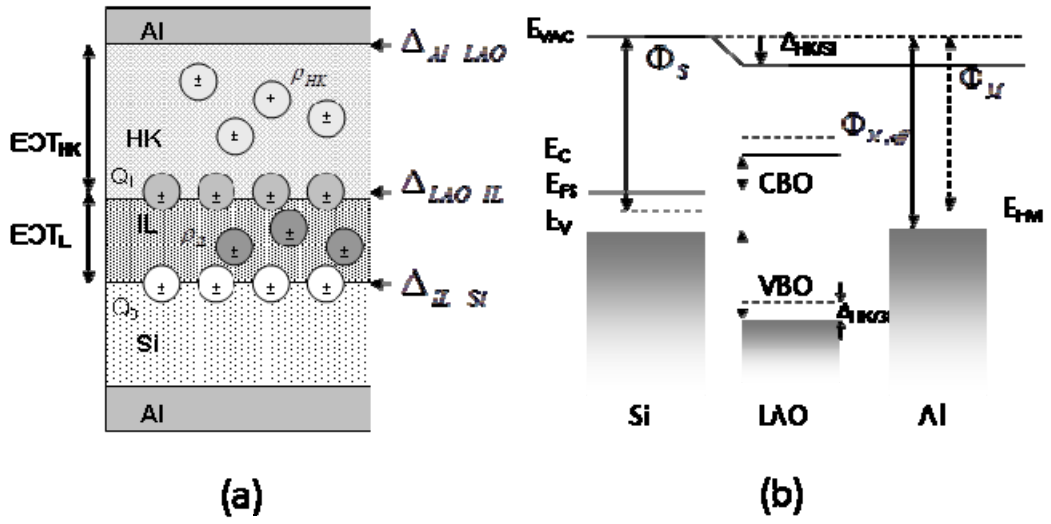

Fig. 6.4: (a) Schematic of Al/HK/IL/Si/Al capacitor structure and the relative positions of the oxide charges and dipoles involved, and (b) Energy band diagram showing the influence of the dipole at the high-k/Si interface, $\Delta_{HK/Si}$ (which could be $\Delta_{HK/IL}$ and/or $\Delta_{IL/Si}$) on the effective metal workfunction, $\Phi_{eff,ms}$. The alignment of the system without interface dipoles is denoted by dash lines while the shift in the effective vacuum level after the annealing is shown by the direction of the arrow. An increase in $\Phi_{eff,ms}$ can then be derived for the direction of the interface dipole induced.

As illustrated in Fig. 6.4(b), $\Phi_{eff,ms}$ is modulated by contributions from any interface dipole within the gate stack and this makes $\Phi_{eff,ms}$ an important parameter in measuring interface dipoles and hence the band alignment. However, in order to correctly extract the true $\Phi_{eff,ms}$ using the V_{FB} vs. EOT plot, the oxide charges should be reasonably accounted for. Bulk oxide charges are oxide trapped charges that are distributed throughout the oxide film while Q_f and Q_{it} reside mainly at the interface. As such, the total bulk oxide charges are expected to vary with thickness while Q_f and Q_{it} can be considered to be thickness-independent. Our V_{FB} vs EOT plots exhibit reasonably linear relationships as shown in Fig. 6.5. Hence from Eq. (6.1), we can deduce that the bulk oxide charges within the high-k oxide layer (ρ_{HK}) do not play a major role and thus these were not considered to simplify the analysis. However, even for different EOTs of the high-k oxide film, the thickness of the interfacial layer can be approximated to be constant for a

given annealing condition and this is especially true for the relatively thick oxides (> 8 nm) used in our V_{FB} vs. EOT analysis. This meant that we cannot rule out effects of the interfacial bulk oxide charges (ρ_{IL}) within the IL despite the linear relationship we obtained. This is because these charges have a linear (or no dependence) on EOT_{HK}. Therefore, the effects of ρ_{IL} have to be considered and this is accounted for in our subsequent analysis. It should also be noted that we assume zero dipole variations at the LAO/metal interface since our comparisons are made across the LAO films (which remain stoichiometric after annealing) that underwent the same metal contact fabrication and processing conditions. Furthermore, we simplified our analysis by reasonably neglecting non-uniformities in the doping concentration of the Si substrates used. From our measurements of the doping variations used in this work, the resultant variation in Φ_{ms} is calculated to be less than 0.01 eV, which is a reasonable value considering our measurement accuracy. Finally, we do not expect the post-metallization anneal at 400ºC to induce any changes in the band offset at the HK/Si interface as shown by relatively consistent band offsets (data not shown) for the as-deposited and 400ºC annealed samples.

The resultant plots of V_{FB} vs. *EOT* for LAO/Si and LAO/Y/Si capacitors are shown in Fig. 6.5 (a) and 6.5(b), respectively. We examine in detail the $\Phi_{eff,ms}$ values between the as-deposited (As Dep) and annealed samples to correlate the electrical measurements with the observed variations in VBO as measured using XPS. For the LAO/Si samples in Fig. 6.5(a), we measured a difference in the intercept of 1.81 V (± 0.2 V) before and after annealing, while for the LAO/Y/Si samples, the difference is reduced to 1.36 V (±0.2 V) after inclusion of a Y

interlayer, as shown in Fig. 6.5(b). The difference in the intercept amounts to a change in the $\Phi_{eff,ms}$ value and this is partly contributed by the interface dipoles.

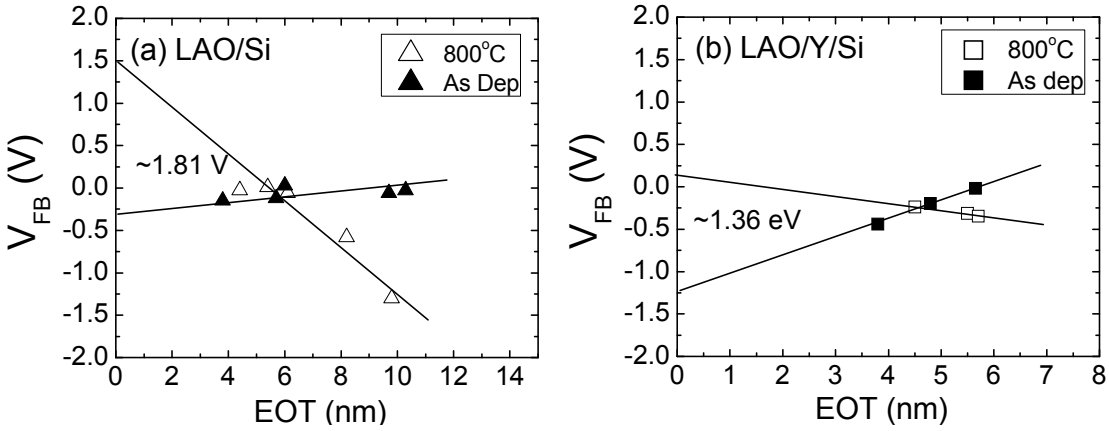

Fig. 6.5: V_{FB} plots for (a) Al/LAO/Si and (b) Al/LAO/Y/Si structures vs. EOT_{HK} before (solid symbols) and after annealing (open symbols). The y-intercept (V_{FB} at EOT_{HK} = 0) is determined from the best fit line shown. The indicated value is the derived difference of the $\Phi_{eff,ms}$ before and after the 800°C anneal.

As discussed, XPS measurements yield a VBO change of 0.48 eV for the as-deposited sample and a difference of 0.16 eV for the Y-stabilized sample after annealing. This difference is attributed similarly to the alterations of the interface dipoles. The larger variations of the $\Phi_{eff,ms}$ as compared to XPS measurements can then be explained by the additional contributions to the intercept by the oxide charges within the IL as previously mentioned. Specifically, the terms $Q_0 EOT_{IL}/\varepsilon_0\varepsilon_{ox}$ and $\rho_{IL} EOT_{IL}^2/2\varepsilon_0\varepsilon_{ox}$ in Eq. (6.1) can lead to changes in the intercept value, especially when EOT_{IL} is high. Since the interfacial oxide is most probably of a lower quality than thermally grown SiO_2, we use an estimated value of -2 x 10^{12} cm^{-2} for Q_0, obtained from the data of a thermally oxidized SiO_2 on Si.[182] Along with a value of -3.0 x 10^{19} cm^{-3} for ρ_{IL}, the total contribution to the intercept is about 0.47 to 0.91 V for a 2 to 3 nm thick IL. This thickness range is measured from attenuation considerations of photoelectron intensities using the

Beer-Lambert's equation. Another possible reason can be from the influence of hysteresis, though we believe this is not significant from our measured hysteresis of 18 to 66 mV. With these as considerations, the values we obtained from both XPS and electrical measurements match reasonably well. In short, electrical measurements show that the addition of the Y-interlayer reduced the band offset variations by 0.45 V while the XPS data shows a reduction of 0.32 eV after a high temperature anneal. The reasonably good agreement of the two measurements suggests that the variations in the band offset after annealing can be suppressed with the addition of a Y-interlayer.

6.1.3. Changes in chemical profile investigated by XPS

This change in the band offsets can either arise due to a change in the bulk properties or because of the formation of interface dipoles. To ensure that there were no changes in the bulk properties after annealing, analysis of thick LAO films (~15 nm) was carried out. Using a quantitative analysis (similar to section 4.1), we obtained a consistent Al to La ratio of ~0.5 (± 0.05) for all our samples, across different batches of deposition and different annealing temperatures. Similarly, the core-level separations between La $3d_{5/2}$ and Al 2p peaks across the different annealed bulk samples were measured to be ~761.3 eV (± 0.1 eV). Expectedly, the bulk core-to-valence separation, i.e $E_{CL}^{La3d} - E_v$ remains consistent at 832.09 eV. Furthermore, the bandgap values were measured to be 6.13 eV (± 0.1 eV) across samples subjected to different annealing temperature using the O 1s energy loss spectrum (see section 4.1.1). With supporting evidence from X-ray diffraction scans to show that the bulk films remain amorphous even after

annealing at 800ºC, we can conclude that the bulk properties of the film remains stable under such processing conditions. This therefore implies that this variation of band offsets is due to formation of interface dipoles.

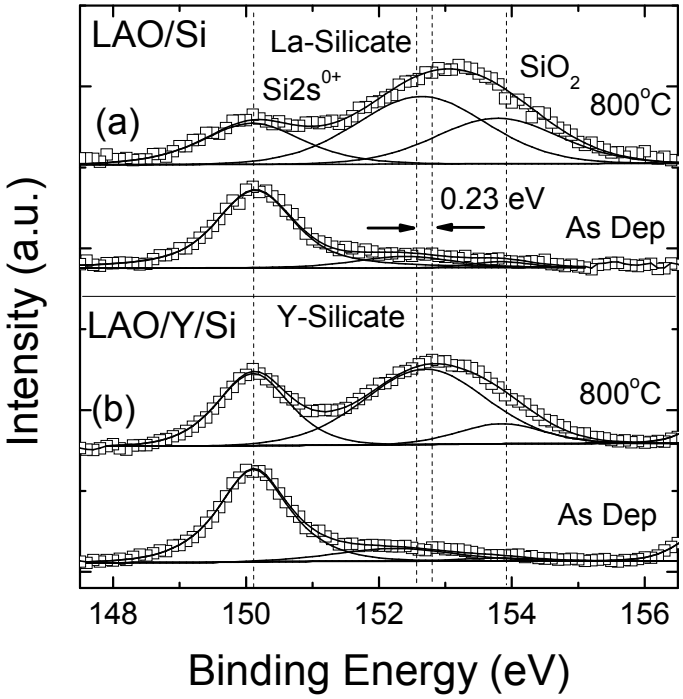

Fig. 6.6: Si 2s XPS peaks before (As Dep) and after 800ºC annealing for 4 nm (a) LAO/Si and (b) LAO/Y/Si. Comparison of the ratio of Si 2s substrate and the oxide peak intensities shows that the addition of the Y-interlayer retards growth of the interfacial oxide.

Next, the changes in the interfacial chemistry are investigated using XPS which will be useful to explain the various improvements observed after addition of the Y interlayer. This is done using the Si 2s photoelectron spectrum as shown in Fig. 6.6. While the Si 2p orbitals have higher intensity, they are not used because the SiO components of Si 2p overlap with the La 4d spectrum. The peaks shown are aligned with respect to the Si substrate peak, Si $2s^{0+}$, at 150.10 eV. The contribution from SiO_2 is represented by a fitted peak at a higher chemical BE shift of 3.7 eV from the substrate peak. The remaining fitted peak is attributed to the contribution from the interfacial silicate. The BE of the silicate after annealing is thus found to be 152.70 eV and 152.47 eV for the samples with and without the

Y-interlayer respectively. The higher BE difference of 0.23 eV from the sample with the Y-interlayer suggests a silicate layer that is richer in Y due to the higher electronegativity of Y (1.05) as compared with La (0.88). From the attenuation measurements of the photoelectron peaks, the thicknesses of the interfacial layers for LAO/Si and LAO/Y/Si samples are obtained to be 0.25 and 0.37 nm before annealing and 3.11 and 2.15 nm after annealing, respectively. The thickness determination is performed by taking the ratio of the substrate and interface oxide component in the Si 2s spectrum (more details can be found in Appendix III). The larger interfacial oxide thickness is thus indicated by the larger oxide-to-substrate peak intensity ratio for the samples without the Y-interlayer as seen in Fig. 6.6. The presence of the Y-interlayer is therefore effective in retarding the formation of the interfacial oxide after annealing and this is consistent with observations from other independent work.[247]

Figure 6.7 shows the interfacial chemistry of the Y-interlayer samples before and after annealing. It is first seen that the yttrium in our samples are oxidized from the Y $3d_{5/2}$ peaks, otherwise the metallic (Y-Y) and silicide (Y-Si) components should be present at 156.1 and 156.4 eV, respectively. For the as-deposited LAO/Y/Si, the Y $3d_{5/2}$ peak is at ~158.4 eV, which is higher than that of Y-O (~157.3 eV), thereby implying silicate formation. This higher BE shift for silicate formation is a result of the second nearest neighbour effect due to the higher electronegativity of Si.[256] Upon annealing, the BE further shifts by ~0.48 eV, which is most likely due to a higher amount of Si incorporation (which is less electron donating) in the silicate compound. This observation of larger Si incorporation is most likely due to higher diffusivity for Si at higher annealing

temperatures to react with Y-O at the interface. This corresponds well with the fitted Si 2s spectrum in Fig. 6.7 and shows that yttrium silicate is present in the annealed LAO/Y/Si sample.

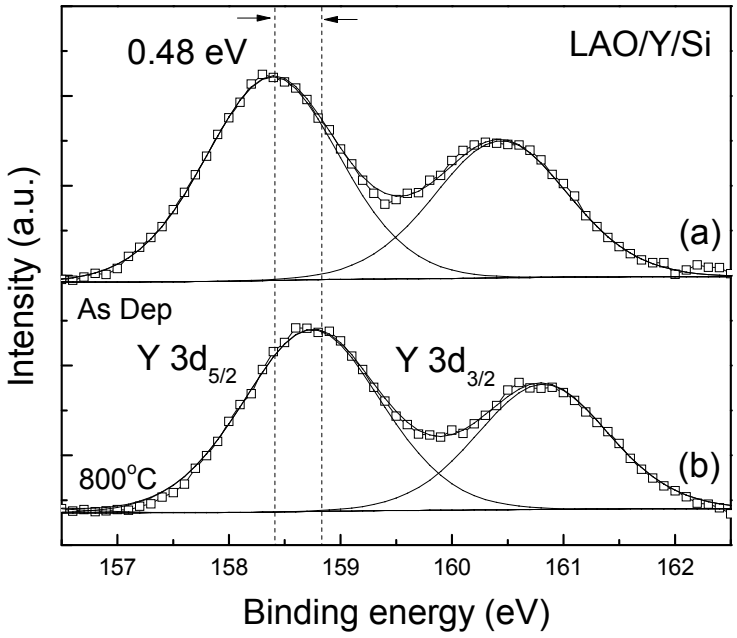

Fig. 6.7: Fitted Y3d XPS peaks of the sample with a Y-interlayer (a) before and (b) after 800°C annealing. The peaks are aligned to the Si2s substrate peak. It can be seen that the fitted $Y3d_{5/2}$ peak of the sample after annealing is at a higher BE (i.e. by ~0.48 eV).

6.1.4. Mechanism for interface dipole formation

Table 6.3: Comparison of conduction band offset (CBO) and interface dipole potential (Δ) for as-deposited and annealed LAO/Si and LAO/Y/Si samples.

		CBO (eV)	Δ (V)
LAO/Si	As Dep	2.28	0.48
	600°C	2.06	0.70
	800°C	1.80	0.96
LAO/Y/Si	As Dep	2.00	0.76
	800°C	1.84	0.92

In this section, the mechanism responsible for the formation of the interface dipole is discussed. The interface dipole potential (Δ) can be experimentally obtained as (χ_{Si} - χ_{LAO} – CBO) as shown in section 4.1, whereby χ_{Si} and χ_{LAO} are 4.05 and 1.29 eV, respectively. It is seen from Table 6.3 that the overall dipole strength increases with annealing temperature. One approach to explaining the changes in interface dipoles is through the formation of extrinsic dipoles (see section 2.3.5). However, here we focus on applying our dipole neutrality point (DNP) developed in chapter 5 to explain the changes in these interface dipoles. The effects of annealing on interface dipoles are first discussed. After annealing (see section 6.1.3), there is significant silicate formation due to the diffusion of Si atoms towards the high-k oxide. According to the DNP concept, the dielectric work function, which affects the charge transfer at the interface (and hence interface dipoles), is negatively correlated with the electronegativity at the oxide/semiconductor interface. Due to the incorporation of electronegative Si atoms, the overall electronegativity at the interface is expected to be increased. This can possibly explain the consistently larger positive interface dipoles observed after annealing for both LAO/Si and LAO/Y/Si. Next, we discuss the effects of adding a Y interlayer on interface dipoles. Similarly, this can be explained using the DNP concept. Addition of Y at the interface tends to substitute mostly La, thereby leading to an increase in the overall electronegativity. This causes the interface dipole to be more positive.

6.2. Improvement of other electrical properties

In addition to improving the thermal stability of band offsets, the inclusion of a Y-interlayer can also improve other electrical characteristics at the interface after annealing. These include the interface trap density (section 6.2.1), and leakage current (section 6.2.2).

6.2.1. Interface trap density

The frequency-dependent conductance method is employed to investigate the interface trap density (D_{it}) for the as-deposited and annealed samples before and after addition of the Y-interlayer (section 3.2.4.2).[169,170] This method essentially measures conductance as a function of frequency in the depletion region whereby the energy loss, defined as the ratio of the effective parallel conductance to frequency (G_p/ω), reflects the density of the interface traps. The occupancy of these traps changes with small variations in the applied gate bias due to band bending, giving rise to a spread of values over different energy level locations.

Table 6.4: Summary of interface trap densities (D_{it}) extracted from conductance measurements before (Bef. Anneal) and after 800°C post deposition annealing (PDA). It can be seen that D_{it} is relatively constant, as expected, with variation in the oxide thickness. Each data point represents the average value from 2 to 3 different capacitors.

		Thickness (nm)	D_{it} (x 10^{12} $eV^{-1}cm^{-2}$)
LAO/Si	Bef. Anneal	12.5	0.678
	800˚C PDA	14.0	2.590
	Bef. Anneal	22.5	0.288
	800˚C PDA	24.0	4.110
LAO/Y/Si	Bef. Anneal	13.0	0.289
	800˚C PDA	14.5	0.138
	Bef. Anneal	12.0	0.320
	800˚C PDA	14.0	0.169

Our analysis provides D_{it} values of good accuracy by correcting for oxide capacitance and considering interfacial broadening effects as described in ref. 170. The D_{it} values obtained are averaged across 2 to 3 samples for each data point and the summarized result is shown in Table 6.4. Actual energy loss curves for LAO/Si samples before and after annealing are shown in Fig. 6.8(a) and 6.8(b) respectively. These curves exhibit typical interface trap behaviour, in which the frequency corresponding to the peak G_p/ω value changes exponentially with bias, showing the spread of D_{it} values across the upper half of the Si bandgap. The D_{it} values of the as-deposited samples are calculated by taking the maximum value of G_p/ω in the conductance plots shown in Fig. 6.8. The corresponding C-V plots obtained at 100 kHz are shown in the insets. The C-V slope in depletion for the annealed samples is much gentler compared to that of the as-deposited (before anneal) samples. This is consistent with an increase in D_{it} after annealing that agrees well with the increase in peaks at higher frequencies of the conductance plots. Overall, the D_{it} obtained from the conductance plots for the as-deposited samples range between ~2.88 x 10^{11} to 6.78 x 10^{11} eV^{-1} cm^{-2} and show a significant increase after annealing (> 2 x 10^{12} $eV^{-1}cm^{-2}$). Interestingly, while the addition of the Y-interlayer yields D_{it} of similar order before annealing, the D_{it} increase was more than suppressed as we observe a modest reduction in the D_{it} values to ~1.5 x 10^{11} $eV^{-1}cm^{-2}$. The increase in D_{it} after annealing is common for amorphous La-based high-k oxide films on Si and this can be attributed to the desorption of hydrogen in forming overcoordinated oxygen centers.[245, 257] Hydrogen can escape freely from the LAO/Si interface resulting in the depassivation of the P_{b0} centers that leads to an increase in D_{it}.[258] The Y-richer silicate formed after the annealing can thus be an effective barrier to block this

desorption or even help in the passivation of the dangling Si bonds, thereby resulting in a lower D_{it}.

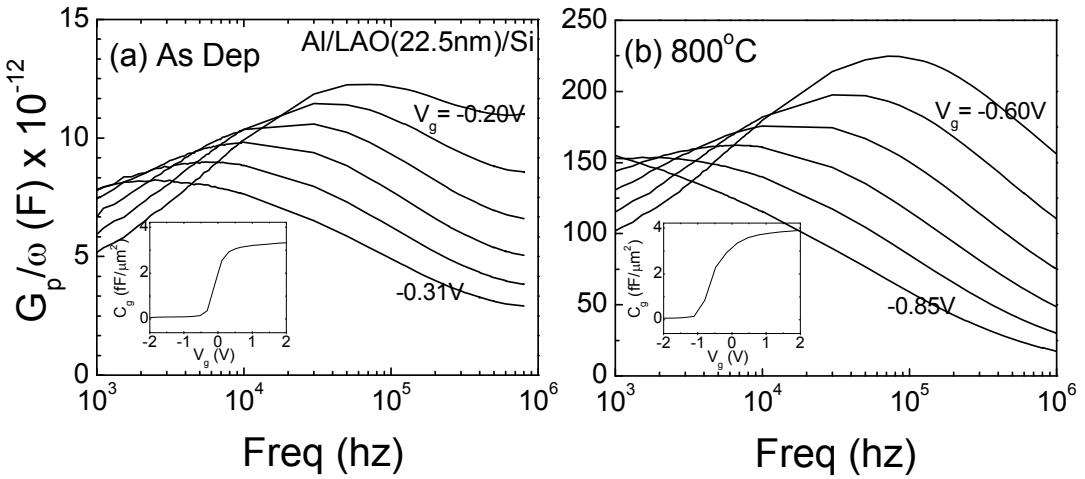

Fig. 6.8: Frequency dependent conductance measurements for Al/LAO(22.5nm)/Si capacitors (a) before and (b) after 800°C annealing for a series of applied gate bias Vg, showing the spread of D_{it} over the upper half of the Si bandgap. The inset shows the corresponding high frequency C-V plots (100 kHz) and it is observed that the stretch-out of the slope after annealing corresponds to the increase in D_{it}.

It is also worthwhile to note that the improved electrical results and the observed dipole changes may be correlated.[259] Although interface traps or oxide charges (or oxygen vacancies) are point defects and therefore do not directly alter the interface potential, these defects can influence the dipoles indirectly through interfacial stress. It has been shown that the concentration of P_b centers at the Si/SiO_2 interface can be correlated with interfacial stress.[260] This stress can subsequently induce changes to the dipole strength, thereby affecting the resultant band alignment measured.[10]

6.2.2. Leakage current

Lastly, the leakage current profiles for the different capacitors are investigated. The samples used in the leakage current density versus gate voltage (J_g-V_g) plots (i.e. Fig. 6.9) have similar LAO thicknesses (~12 nm) to ensure a fair comparison. Since our primary interest is the high-k oxide/semiconductor interface, we will

focus on positive gate voltages whereby the electrons (majority carriers in n-Si) are injected from the substrate towards the metal electrode.

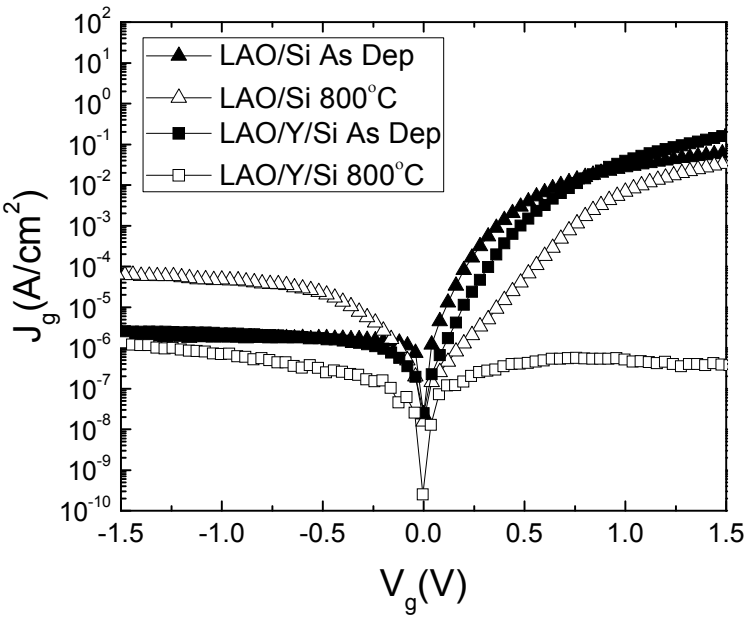

Fig. 6.9: Gate current density vs. gate voltage (J_g - V_g) measurements of LAO(12.5nm)/Si and LAO(12nm)/Y/Si structures before and after 800°C annealing. The corresponding *EOT*s before and after annealing are 5.70 nm and 6.10 nm respectively for LAO/Si, and 4.80 nm and 5.50 nm respectively for LAO/Y/Si

A log-log J_g-V_g plot in Fig. 6.10 shows that the leakage profile of LAO/Si As-dep (as-deposited), LAO/Si 800°C anneal and LAO/Y/Si As-dep capacitors can be described by the space-charge limited conduction (SCLC) theory, while the LAO/Y/Si 800°C anneal capacitor cannot be fitted with the SCLC mechanism. The dashed line with slope of 1 represents the first region described by the Ohm's law, while the other line with slope of 2 represents the space-charge limited (SCL) region described by the Child's law. The deviation of the slopes for LAO/Y/Si As-dep and LAO/Si 800°C samples at higher V_g values from the value of 2 suggests additional contributions from other mechanisms (to be discussed later).

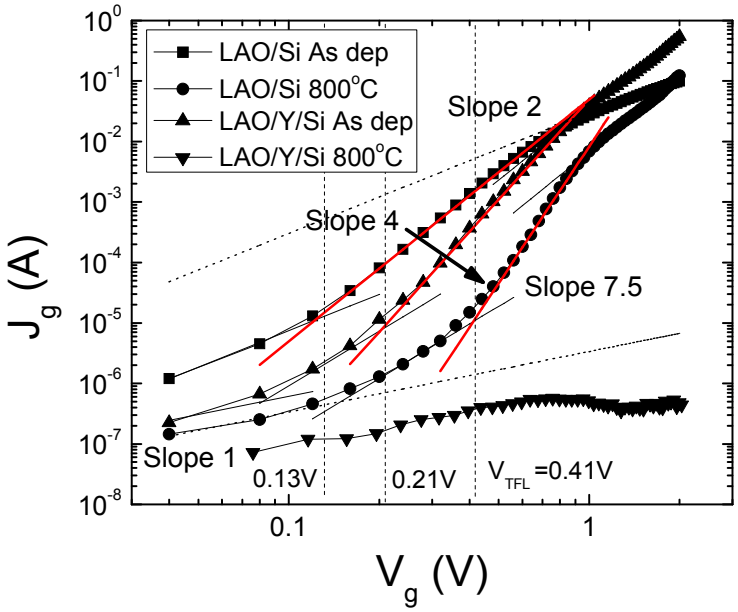

Fig. 6.10: A log-log J_g-V_g plot for the different capacitors fabricated.

The transition voltages between the Ohmic-SCL and SCL-TFL regions, V_{tr} and V_{TFL} respectively, are shown in Table 6.5 along with the calculated values of the trap density (N_t), ratio of free-carrier density to total carrier density (θ), density of thermally generated free carriers (n_0), and electronic mobility in the oxide (μ) based on equations in section 3.2.4.3. It is noted that the V_{tr} value for the LAO/Si As-dep sample is out of range of our data plot and thus not shown in Table 6.5. It is first observed that V_{TFL} increases in the order of LAO/Si As-dep, LAO/Y/Si As-dep, and then LAO/Si 800°C. The trend of our N_t values derived from V_{TFL} correlates well with that of the magnitude of Q_f derived from the slopes of the V_{FB} vs EOT plots in Fig. 6.5. The slope of trap-filled limit (TFL) region also increases from 4 to 7.5. We believe that this can be due to the effects of interface traps on the SCL current, since a higher density of traps at the oxide/semiconductor interface is expected to result in a steeper slope.[261] This explains why the LAO/Si 800°C sample which is found to possess the highest D_{it} (from section 6.2.1)

exhibits the steepest slope in Fig. 6.10. The rest of the parameters extracted based on the SCLC theory are shown in Table 6.5.

Table 6.5: Parameters extracted based on the SCLC equations for the different capacitors.

	d (cm)	V_{TFL} (V)	N_t (cm^{-2})	θ (ppm)	V_{tr} (V)	n_o (cm^{-3})	μ (cm^2/Vs)
LAO/Si As-dep	12.5	0.13	1.01×10^{18}	929	-	-	-
LAO/Si 800°C	14.0	0.41	2.55×10^{18}	2500	0.15	1.31×10^{15}	1.24×10^{-7}
LAO/Y/Si As-dep	12.0	0.21	1.77×10^{18}	593	0.0855	2.41×10^{14}	4.50×10^{-8}

We are able to derive reasonable electron mobility values of 1.24×10^{-7} cm^2/Vs and 4.50×10^{-8} cm^2/Vs for the LAO/Si 800°C and LAO/Y/Si As-dep samples which are of similar order as compared with other high-k dielectrics.[174,262,263] The low extracted electron mobility values also justify the use of static dielectric constant values for our analysis (see section 3.2.4.3).

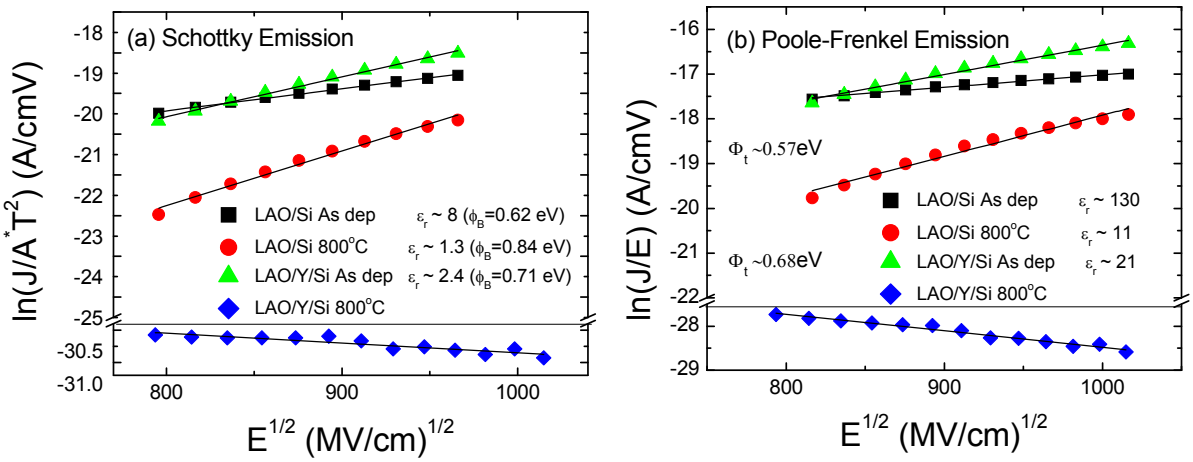

Fig. 6.11: Plots of fitted (a) Schottky (SC) emission and (b) Poole-Frenkel (PF) emission equations for the different capacitors with the extracted parameters, i.e. dielectric constants (ε_r), barrier height (Φ_B), which is the CBO for substrate injection, and trap energies (Φ_t).

Given the high density of traps in the annealed LAO/Si sample, it is not surprising that conduction at high electric fields occurs via Poole-Frenkel (PF) emission.[178]

In Fig. 6.11(a), a plot of $\ln(J_{SC}/T^2)$ versus $E^{1/2}$ reveals that Schottky (SC) emission is not likely for all samples since the obtained CBO values (i.e. 0.62 – 0.71 eV) are all much smaller than that expected (i.e. 1.80 – 2.28 eV) and the dielectric constant values are all smaller than the static dielectric constant of 11 (see section 3.2.4.3). On the other hand, in Fig. 6.11(b), the extracted dielectric constant values from a plot of $\ln(J_{PF}/E)$ versus $E^{1/2}$ at $V_g \sim 1$ confirms that the J-V characteristics at that region resembles that of the PF mechanism for the LAO/Si 800^{o}C sample, and possibly also for the LAO/Y/Si As-dep sample. This agrees with the findings that LAO/Si 800^{o}C sample has the largest amount of oxide traps (see section 6.1.2.3). From the y-intercept, the trap barrier height, Φ_t values for the LAO/Si 800^{o}C and LAO/Y/Si As-dep samples are 0.68 and 0.57 eV, respectively. The leakage current profile of the other two samples however, cannot be described by PF emission. This is because the derived dielectric constant is too large for the LAO/Si As dep sample while the LAO/Y/Si 800^{o}C sample possesses a negative slope.

Despite the fact that no specific conduction mechanism was confirmed using our previous analysis for the LAO/Y/Si 800^{o}C sample, we attribute the drastic improvement in the leakage current profile to both the (1) enhancement of band gap and (2) reduction of oxide traps. Firstly, a theoretical study showed that by alloying LAO with yttrium aluminate ($YAlO_3$), the band gap can be increased by ~1 eV at high concentrations of yttrium, i.e. $0.2 < x < 0.4$ for $La_xY_{1-x}AlO_3$ (LYAO).[264] This enhancement in the band gap is due to the fact that yttrium introduces states 0.1 eV above the delocalized s and p states of the conduction band and causes little change to the large alumina band gap.[265] It is possible that

thermal annealing drives the diffusion of yttrium at the interface to form the LYAO complex for the case of the LAO/Y/Si 800^{o}C sample. The presence of this large band gap at the interface can thus impede carrier injection, explaining the absence of the transition to the SCL regime. Moreover, annealing of the LAO/Y/Si structure is also observed to ameliorate both interface and fixed oxide traps, thereby reducing leakage contributions due to traps responsible for PF emission.

7. Control of the Y_2O_3/Ge interface by understanding of the initial growth processes

Due to the aggressive scaling of complementary metal-oxide semiconductor (CMOS) devices, control of the interface between the high dielectric constant (high-k) oxide and semiconductor is becoming increasingly important to the overall device performance. This interface is especially pertinent for high mobility substrates such as germanium (Ge) due to the poor thermal stability of the Ge native oxide.[266] Yttrium oxide (Y_2O_3), as compared with hafnium oxide (HfO_2), can form a higher quality interface with Ge in terms of interface trap density and leakage current.[70,240, 267] However, interfacial layers (ILs) comprising yttrium germanate (YGeO) are commonly observed at the Y_2O_3/Ge interfaces, much similar to the formation of yttrium silicate for growth of Y_2O_3 on silicon (Si).[268,269,270] It is hard to avoid these germanate and silicate interfacial layers as they may be the most thermodynamically stable compounds, thereby having a large driving force towards their formation.

Generally, IL formation of any kind is not preferred. Although it is possible that the IL can alleviate remote phonon scattering, recent studies have shown that this effect might be small.[271,272] Instead, unintentional IL formation usually creates a defective interface that leads to many detrimental effects such as scattering of carriers in the channel, fixed charges and charge trapping.[273] This subsequently complicates threshold voltage control and degrades the reliability of the devices.[45,54,274] Most importantly, a zero IL structure is necessary to meet the

stringent equivalent oxide thickness (EOT) requirements in order to sustain the aggressive device scaling trends.[15]

Several studies in the literature show that it is necessary to maintain high substrate temperatures (~800^{o}C) during deposition in order to achieve interfacial-layer-free growth of Y_2O_3 on Si and this is not desired for a few reasons.[275,276] Use of Ge substrates requires lower processing temperatures since the Ge substrates has a lower melting point than Si. High-temperature processing can also leave behind a defective interface because at temperatures higher than 400^{o}C, germanium dioxide (GeO_2) tends to consume Ge at the interface to form germanium monoxide (GeO), which then desorbs as a gas-phase (section 2.1.3). Finally, the high-temperature growth always yield polycrystalline Y_2O_3 film that results in high leakage current densities making it unsuitable for high-k oxide applications.[277] While low temperature growth of interfacial layer-free amorphous films is preferred, this is not an easy task. This is because removal of interfacial oxide through desorption cannot proceed at lower temperatures. This makes the control of any substrate oxidation or intermixing highly important since this will lead to unintentional IL growth. This is not only obvious from growth involving powerful oxidizing agents such as ozone, but can also be observed under oxygen limited conditions.[267,269,270,278,279]

In this chapter, we aim to grow an interfacial-layer-free Y_2O_3 on Ge by oxidation of Y metal since this method can yield high quality oxide films with good thickness control.[268] As mentioned above, it is difficult to achieve an interfacial-layer (IL)-free growth without a good understanding of growth processes. In this

study, we acquire this knowledge through a systematic approach. In section 7.1, we first investigated the formation of the yttrium/germanium interface to understand the intermixing and Fermi level pinning phenomena during the early stages of metallic Y growth. In section 7.2 , the subsequent oxidation of the Y/Ge interface is carried out to form Y_2O_3 with the aim to minimize interfacial layer formation.

7.1. Initial growth of yttrium on germanium

In this section, the formation of the yttrium/germanium interface was first investigated using *in situ* XPS. Upon loading into the UHV chamber, the substrates were thoroughly outgassed by resistive heating at 350 to 400 ^{o}C for 1 hour to ensure that the surface carbon contaminants and Ge native oxide (GeO_x) were thermally desorbed. Deposition of yttrium was carried out using an Omicron UHV standard evaporator (EFM 3) under room temperature (section 3.1.3). The deposition rate of yttrium was measured by a quartz crystal microbalance (see calibration in Appendix II). It is noted that our coverage for 3 Å will constitute one monolayer (ML) based on the hexagonal close packed structure assumed for Y atoms. After each deposition cycle, the same sample was transferred *in situ* for XPS characterization of the chemical and electronic properties during Y/Ge interface formation.

The intensity ratio of the attenuated substrate peaks to that of the clean substrate peaks ($I_{Ge}/I_{Ge,\infty}$) was plotted on a natural logarithmic scale against the deposition thickness in Fig. 7.1. Using the attenuation equations, the resultant mean free path (MFP) for Ge 2p (i.e., λ_{Ge2p}) and Ge 3d (i.e., λ_{Ge3d}) photoelectron signals was

obtained to be 8.56 Å and 18.50 Å, respectively, from the inverse of the negative slope of the plots. The extracted MFP values agree well with the expected values estimated from the universal MFP plot, thus showing the accuracy of the thickness determination.

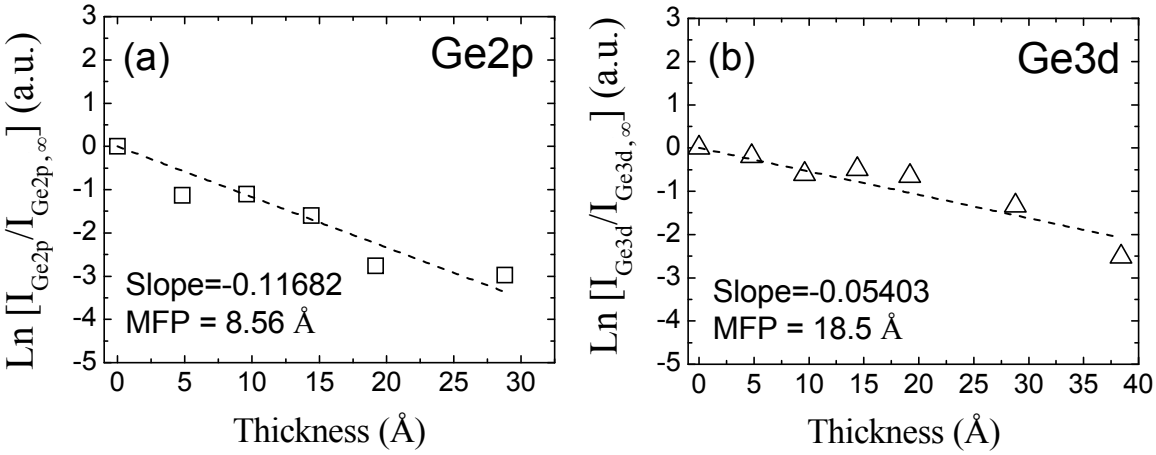

Fig. 7.1: Attenuation plots of Ln $[I_x/I_{x,\infty}]$ versus deposited thickness, where x represents (a) Ge 2p or (b) Ge 3d signal. The mean free path (MFP) for Ge 2p and Ge 3d can be calculated from the slope of the plots to be 8.56 and 18.5 Å, respectively.

Figure 7.2 shows the thickness dependent profiles of (a) Ge 3d, (b) Ge $2p_{3/2}$ and (c) Y 3d photoelectron spectra of Y deposited on p-type Ge and (d) Ge 3d on n-type Ge. In Fig. 7.2(a), the Ge 3d spectrum (27 to 36 eV) can be differentiated from the neighbouring Y 4p and O 2s contributions (22 to 27 eV) and this can be verified by the Ge 2p spectrum in this work. The Ge 2p also provides additional chemical depth information because of its lower MFP. The surface Fermi level observed for UHV-cleaned p-type and n-type Ge substrates (in Fig. 7.2(a) and 7.2(d)) are close to its valence-band maximum (less than 0.1 eV), which is consistent with previous measurements.[280] Given the doping level, this represents significant band bending for the n-type Ge in comparison with the p-type Ge. This can be driven by Fermi-level pinning to surface band states on the Ge (100) surface.

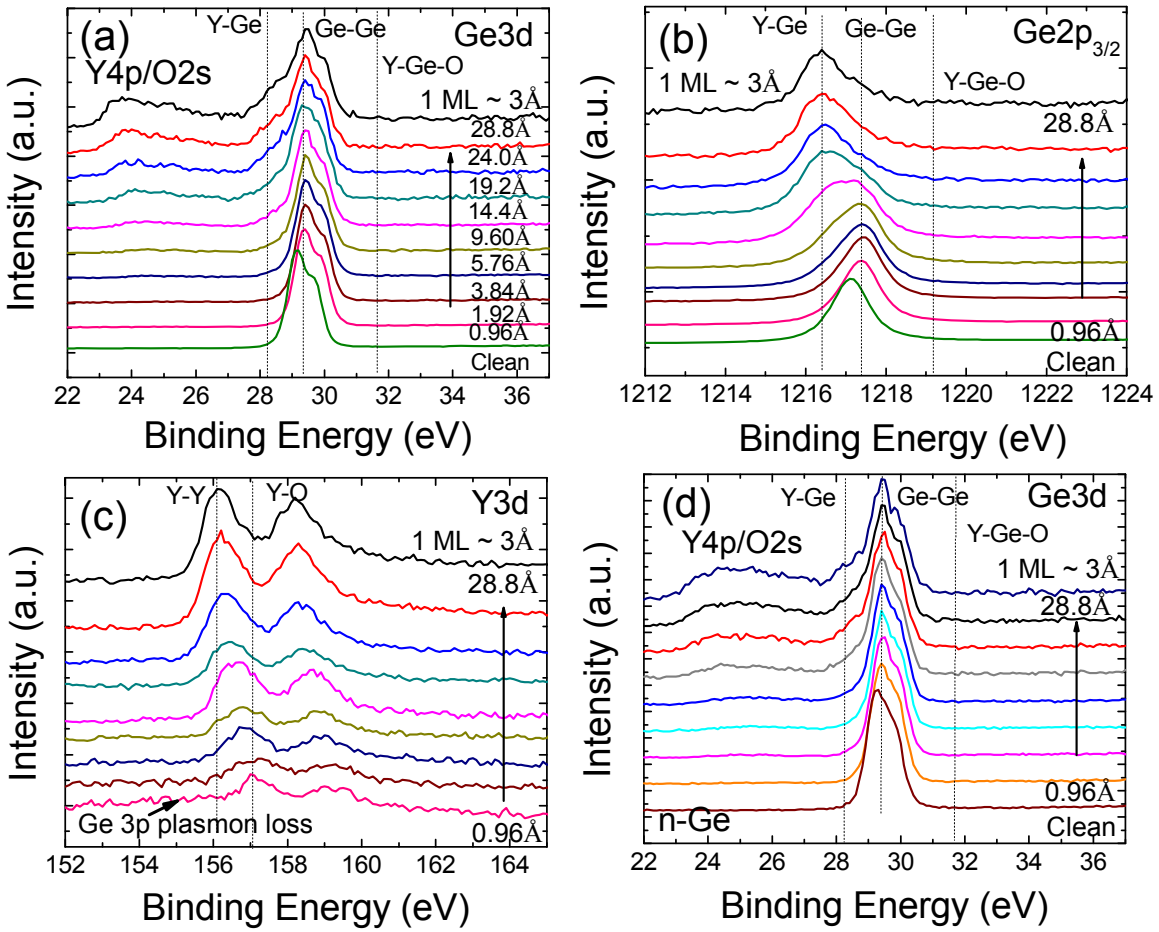

Fig. 7.2: *In situ* XPS spectra for different Y thicknesses (i.e., 0 Å (Clean), 0.96 Å, 1.92 Å, 3.84 Å, 5.76 Å, 9.60 Å, 14.4 Å, 19.2 Å, 24.0 Å and 28.8 Å) on p-type Ge showing (a) Ge 3d, (b) Ge $2p_{3/2}$ and (c) Y 3d orbitals, and on n-type Ge showing (d) Ge 3d orbitals. The peaks have been normalized while the indicated thickness is on a cumulative basis.

In the next few sections, the spectra in Fig. 7.2 will be used to describe the subsequent stages of growth, which essentially can be categorized into three different stages. Firstly, adatom-induced band bending occurs at low coverages, followed by significant intermixing and lastly formation of metallic yttrium.

7.1.1. Stage I: Adatom induced band bending

It is observed in Fig. 7.2 (a), (b) and (d) that the Ge substrate peaks of Ge 3d and Ge $2p_{3/2}$ show an abrupt binding energy (BE) positive shift upon the first few Y

coverages for both the n-type and p-type Ge. After peak fitting of the spectra in Fig. 7.2(a) and 7.2(b), the substrate binding energies were plotted against the deposition thickness in Fig. 7.3(a).

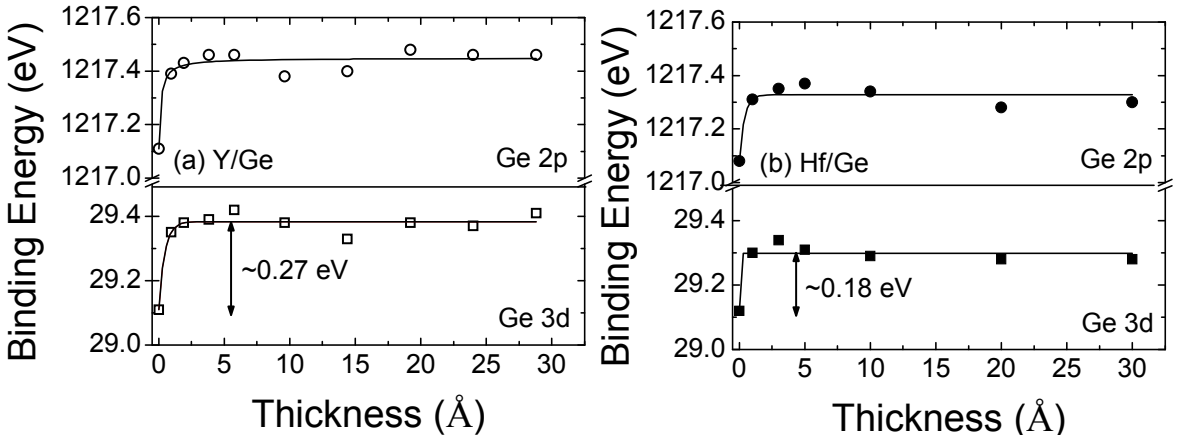

Fig. 7.3: Ge 3d and 2p core level shifts due to (a) Y and (b) Hf metal adatom induced band bending effects at different deposition thickness.

It is seen that the core-level BE shifts by ~ 0.27 eV and saturates within the first monolayer. We could not attribute this to a Y-induced chemical shift since we expect the bulk substrate signals to dominate the Ge 3d spectrum at such low Y coverages, which will mask the limited, if any, Y-induced Ge core level shifts. This shift could possibly represent changes in band bending at the early stages of Schottky barrier formation. At low (sub-monolayer) coverages, deposition of metal adatoms can give rise to discrete surface states, as discussed in section 2.2.3.[281] The downward band movement of both n-type and p-type Ge shows that these adatom-induced states are donor-type in nature. To further ascertain the role of this adatom-induced band bending in the early stages of growth, a thickness dependent BE plot is shown in the case of hafnium (Hf)/Ge in Fig. 7.3(b), using similar deposition conditions as that of yttrium. The core-level shift for Hf/Ge is ~0.18 eV which is lesser than that of Y/Ge. This is because the atomic ionization

energies of Hf and Y are ~6.8 eV and 6.2 eV, respectively and agrees with the trend observed for the energies of the adatom-induced surface donors with the ionization energies of the respective free metal atoms (see section 2.2.3).

In Fig. 7.2(c), the BE of the Y $3d_{5/2}$ signal is at 157.1 eV, which is higher than the bulk BE value of 156 eV, and this provides evidence of charge transfer. The higher binding energy shows the reduced screening effects in yttrium due to the strong electron transfer from yttrium to germanium atoms in forming the Y-Ge bond.[282] We also observe that the background of the Y 3d spectrum changes after full monolayer coverage due to the rapid decrease of the higher order excitation Ge 3p bulk plasmon loss, i.e. the broad peak at ~158 eV seen in Fig. 7.2(c). Beyond that, the core-levels of Ge remained constant with increasing Y thickness. This shows that the band bending changes only occurs within the first monolayer coverage. Thus any adjustments of Schottky barrier heights through band bending can possibly be achieved by the initial monolayer.

7.1.2. Stage II: Intermixing

The next stage of growth is strongly characterized by significant intermixing of Y and Ge at intermediate thicknesses. This is demonstrated in Fig. 7.2(a) and 7.2(b) by the formation of Y-Ge bonds as shown through the increase in the peak intensity of the lower BE shoulder of the Ge 3d (at 28.4 eV) and the Ge 2p (at 1216.4 eV) spectra.[283] This is accompanied by a monotonic shift of the Y 3d peaks (shown in Fig. 7.2(c)) towards lower BE that shows a higher Y-to-Ge ratio in the germanide, resulting in the gradual increase of the screening effect for the Y atoms. The lower BE can also be explained by the gradual formation of pure

metallic Y since only a percentage of the Y is intermixed with Ge (as will be discussed later). The Y-Ge contributions to the Ge 2p signals (with MFP of 8.56 Å) detected at 28.8 Å of Y suggest that this mixing is dominated by Ge out-diffusion.

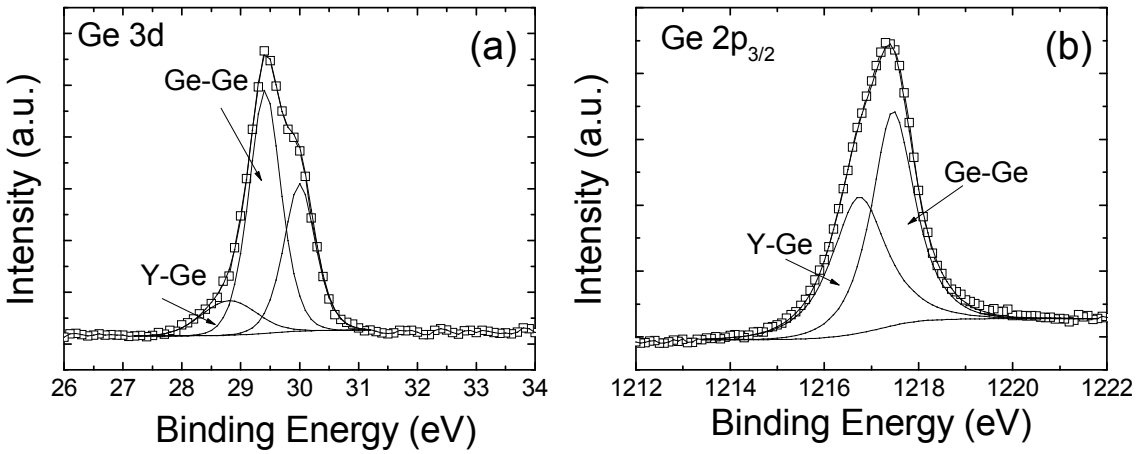

Fig. 7.4: Fitted (a) Ge 3d and (b) Ge $2p_{3/2}$ XPS spectra after 5.76 Å of Y on p-type Ge. The fitted Y-Ge contribution is ~1 eV lower than the Ge 3d substrate peak (which is fitted using two spin-orbits) while the Y-Ge peak is fitted using a single peak.

Figure 7.4 shows an example of the detailed curve fittings for plots of (a) Ge 3d and (b) Ge 2p spectra at a deposited Y thickness of 5.76 Å to quantify the amount of intermixing. In both spectra, the interfacial YGe_x peak is fitted with chemical shifts of -0.72 eV and -0.90 eV for Ge 2p and 3d respectively, in relation to their substrate peaks. The broader Lorentzian line shape observed for the Ge 2p spectrum is largely due to the shorter intrinsic core-hole lifetime that leads to the broadening effect in an adiabatic approximation in XPS experiments.[284] Based on fitted results for different Y thickness, a detailed profile of the intensity ratio between the Y-Ge and Ge-Ge (I_{YGe}/I_{Ge}) versus Y deposition thickness can then be obtained, as shown in Fig. 7.5.

From attenuation equations, the I_{YGe}/I_{Ge} ratio can be described by Eq. (7.1), whereby the subscript ∞ represents the signal intensity from a sample of infinite

thickness (i.e., thicker than probing depth) where $I_{\infty,YGe}/I_{\infty,Ge}$ is a constant.[152] Note that we have assumed a structure of Y/YGe/Ge that is the most reasonable arrangement for a layered structure. The thickness of any unreacted yttrium (t_Y) is absent in Eq. (7.1) because it cancels out from the ratio.

$$\frac{I_{YGe}}{I_{Ge}} = \frac{I_{\infty,YGe}}{I_{\infty,Ge}}[\exp(\frac{t_{YGe}}{\lambda_{Ge}}) - 1]. \qquad (7.1)$$

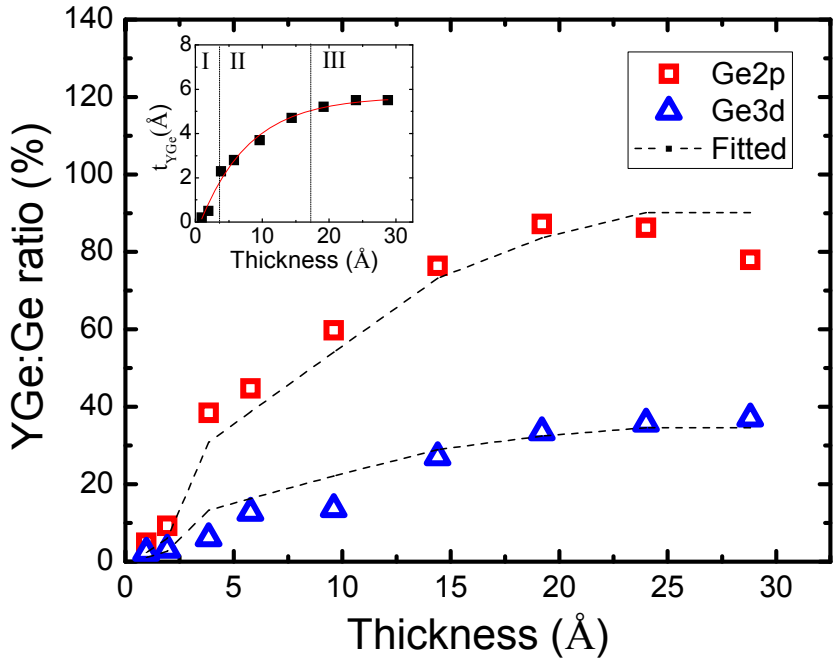

Fig. 7.5: Plot of the intensity ratio between the fitted yttrium germanide (YGe) and the substrate (Ge-Ge) component against the thickness of the Y film deposited. The dotted line shows the calculated intensity ratios using the derived growth profile of the actual Y thickness (t_{YGE}) versus the total deposited thickness in the inset.

From Eq. (7.1), it can be seen that, I_{YGe}/I_{Ge} will vary at different stages of growth as the thickness of yttrium germanide (t_{YGe}) changes. We can then obtain the YGe thickness profile (inset in Fig. 7.5) based on a best match of values from the model in Eq. (7.1) (dotted lines) with the experimentally obtained I_{YGe}/I_{Ge} ratios (square and triangle open symbols) using our derived values of 8.56 Å (λ_{Ge2p}) and 18.5 Å (λ_{Ge3d}) from Fig. 7.1. A reasonable agreement can be obtained for both

Ge 3d and Ge 2p profiles, giving confidence in the determined thickness profile and our initially assumed layered structure. This profile seems to suggest a diffusion-limited reaction process, which is commonly observed for many metal-Si reactions.[285] We can now quantify that formation of YGe occurs during stage II of the growth (3 to 17 Å of Y) and saturates once it reaches stage III (>17 Å of Y), showing the self-limiting nature of intermixing.

This phenomenon of facile intermixing is interesting because the out-diffusion of Ge signifies the breaking of the strong covalent Ge-Ge bonds at room temperature. The chemical bonding model proposes possible bond weakening via charge transfer during the formation of chemical bonds.[286] Since the electronegativity difference between Y and Ge (1.22 and 2.01 using Pauling's scale) is large, charge transfer and hence the bond weakening can be significant. Room temperature mixing is also observed for Si and the concept of metallic screening of covalent bonds is used to explain the bond weakening.[287] A combination of these two models can explain the observed room temperature intermixing. The driving force behind the intermixing is to minimize the Gibbs free energy in germanide formation and/or achieve concentration equalization through diffusion. In the first few monolayers, the bond breaking is assisted by chemical bond weakening while the metallic screening effect takes over at intermediate thicknesses. The latter effect allows for the tunneling of electrons into the Ge-Ge bonds which increases the bonding distance between the atoms.[287] Increasing tunneling thickness therefore makes the electron transfer harder to occur and can explain the self-limiting mechanism in the intermixing. The above findings now suggest the possibility of reducing the intermixing in a layer-by-layer approach.

7.1.3. Stage III: Formation of metallic yttrium

In the last stage, metallic Y is formed as intermixing ceases and the Y 3d BE saturates at ~156.0 eV as seen in Fig. 7.2(c). This is close to the range of 155.8 to 156.1 eV reported in literature for the metallic Y-Y bond.[288,289] Moreover, this transition to bulk metallic film is supported by the asymmetric line shape for both Y 3d (Fig. 7.2(c)) and Y 4p spectra (Fig. 7.2(a)).[290] Upon reaching its metallic state, we then investigated the band alignment of the Y/Ge interface to gain some insights on Fermi level pinning (FLP), which is a prevalent issue in Ge MOSFETs.[291] The Schottky barrier height (SBH) is obtained through Kraut's method (see section 2.4.2.1), in which the interface core-level separation is measured using this ~3 nm thick Y film, while the bulk core-to-valence separation is measured using a bulk (~12 nm) film The obtained p-SBH value of 0.27 ± 0.1 eV is slightly higher than values obtained by electrical p-SBH measurements of Y/Ge (0.14 to 0.19 eV).[292]

On the other hand, the work function (Φ) of yttrium is determined to be 2.82 eV by UPS (see section 3.2.1.6), using the bulk Y film as shown in Fig. 7.6(a), which is close to the reported value of 3.10 eV.[293] Using this measured work function value, deviation of the measured p-SBH (0.27 eV) from the Schottky-Mott model (1.98 eV) becomes apparent.[10] This implies the presence of significant potential drop due to the large vacuum level discontinuity. The theoretical charge neutrality level (CNL) of Ge (0.18 eV above the valence band) is in close proximity to the final position of the Fermi level, indicating the effects of FLP.[294] Using our measured work function value and Miedema electronegativity values of 3.2 (for Y) and 4.55 (for Ge), we obtained p-SBH values of 0.26 and 0.24 eV using the metal

induced gap states (MIGS) and interface induced gap states (IFIGS) models respectively.[213,97]

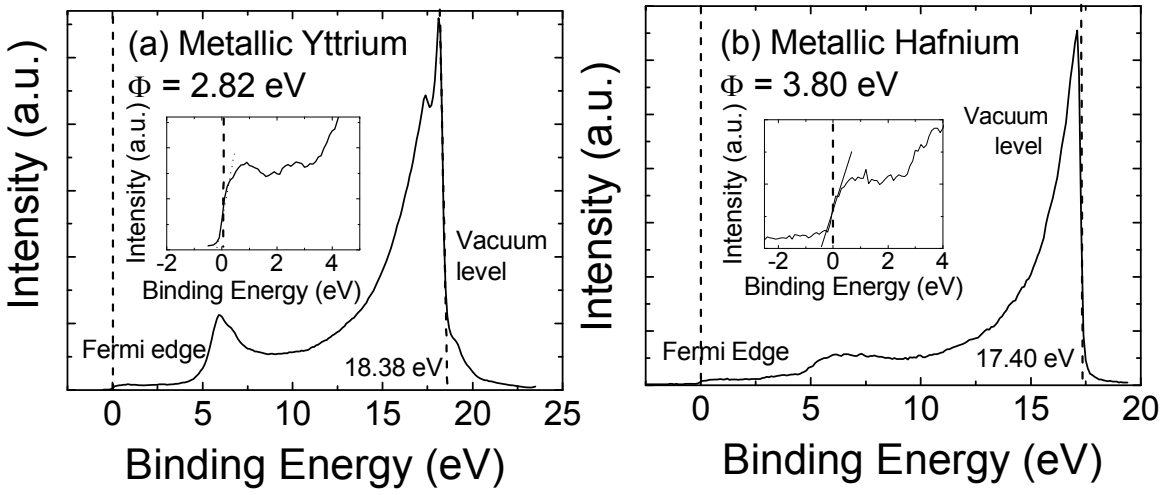

Fig. 7.6: *In situ* UPS spectrum of a 12-nm thick (a) bulk yttrium film and (b) bulk hafnium film on p-type Ge. The inset shows the presence of the Fermi edge at close to zero BE.

Table 7.1: Summary of the measured work function (Φ) and Schottky barrier height (Exp.) in comparison to the predicted values by the MIGS and IFIGS theories. Experimental error of ±0.1 eV.

	Φ (eV)	EN	Schottky barrier height (eV)		
			MIGS	IFIGS	Exp.
Y	2.82	3.20	0.26	0.24	0.27
Hf	3.80	3.55	0.21	0.22	0.20

Similarly, these two parameters are also obtained for the Hf/Ge interface (see Fig. 7.6(b), and Table 7.1 shows a compilation of these measurements with the theoretical predictions. Firstly, it is seen that Hf which possesses a higher electronegativity (EN) compared to Y, and also has a higher measured work function. This agrees well with the empirical trend reported in the literature (see section 2.3.4). Secondly, it is observed that the experimental SBH is very close to both the predicted models, showing the domineering role of the intrinsic gap states in band alignment. The convergence of both the MIGS and IFIGS models is

expected for metals and small band gap semiconductors because (dielectric) work function and electronegativity are strongly correlated for metals.[293]

The agreement with our experimental data also shows that FLP by gap states is important. A large buildup of negative charges in the gap states is probable in Ge devices due to its CNL and this makes inversion for nMOSFETs more difficult.[291] The insensitivity of SBH changes to the metal electrode work function is also a consequence of the FLP and this may pose a problem for lowering source/drain contact resistance. This is especially a serious problem for nMOSFETs since the electron SBH will be lower than the hole SBH. A right choice of material that gives sufficiently low SBH of < 0.1 eV will be required for future scaling of the transistor.[295] The discussion above, however, can possibly explain the poor performance of Ge nMOSFETS commonly observed in the literature.

7.2. IL-free growth of Y_2O_3 on Ge using a layer-by-layer method

In the growth of high-k dielectrics on Ge, formation of lower dielectric constant IL is very hard to prevent.[296] Figure 7.7 shows Ge 3d profiles of Y_2O_3/Ge films grown by (a) sputtering and (b-e) oxidation of evaporated Y film. Oxidation is carried out *in situ* using either molecular oxygen (O_2), or oxygen plasma (OP) generated from the Oxford Applied Research atomic oxygen source at 300 W under a pressure of 5 x 10^{-5} mbar for 20 minutes (min). These plots are aligned to the substrate peak, Ge^{0+} at a binding energy (BE) of 29.5 eV, and the rising edge at BEs lower than ~27 eV originates from Y 4p and O 2s peaks at ~25 eV. The formation of ILs will be reflected in the Ge 3d spectrums as negative and positive shifts (with respect to the substrate peak) when Ge reacts to form germanide (YGe)

and germanate (YGeO) compounds, respectively. It is found from the earlier section that the Y-Ge type bonding yields a BE shift of -0.90 eV. On the other hand, the Y-Ge-O bonding configuration give rises to a BE shift within the range of +2.2 to 2.5 eV due to a second nearest-neighbour effect, which is distinctly different from a O-Ge-O type bonding (+4 eV shift).[297,256] The presence of either higher or lower BE peaks (relative to Ge^{0+}) due to IL formation is observed in Fig. 7.7(a) to 7.7(d), showing how easy the IL forms under typical deposition conditions. The thickest IL formation occurs in the sputtered film (Fig. 7.7(a)). This is most likely due to the traces of oxygen present in the sputtering chamber amidst the high energy plasma environment.

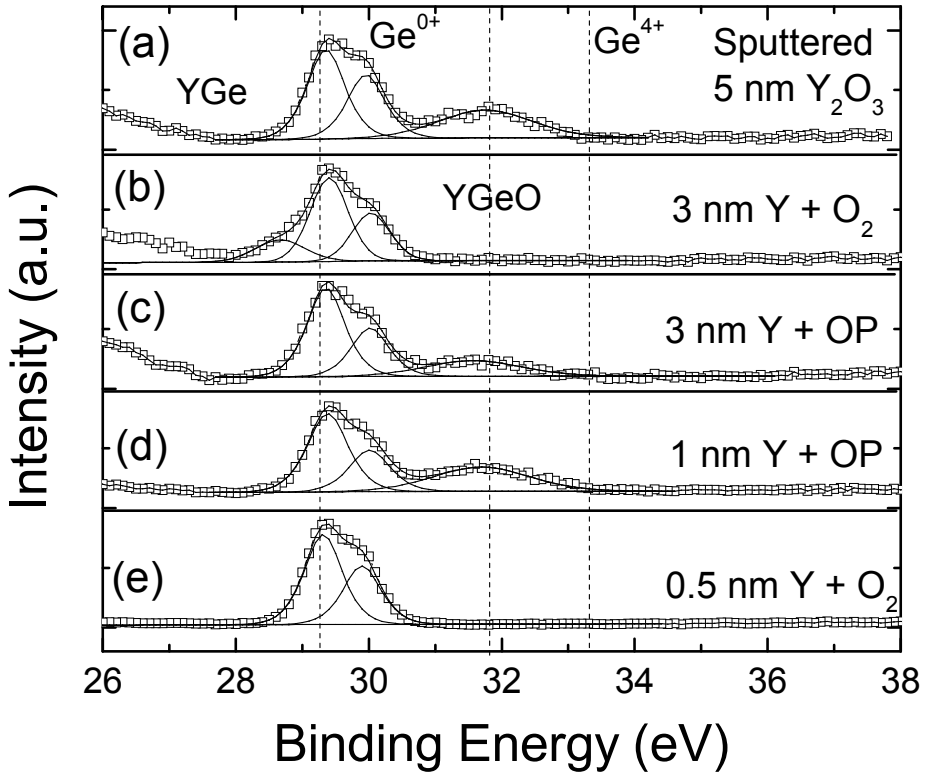

Fig. 7.7: Ge 3d XPS spectrum showing the interfacial chemistry of the samples deposited by (a) sputtering of 5 nm Y_2O_3; evaporation of 3 nm of Y followed by (b) molecular oxygen oxidation (3 nm Y + O_2) and (c) oxygen plasma oxidation (3 nm Y + OP); (d) evaporation of 1 nm Y followed by oxygen plasma (1 nm Y + OP) and (e) evaporation of 0.5 nm Y followed by molecular oxygen oxidation (0.5 nm Y + O_2).

7.2.1. Effects of different oxidation sources on IL formation

The IL formation for growths using the oxidation of evaporated yttrium metal is noticeably lesser, since we have a better control of the oxidation environment. However, the use of molecular oxygen (O_2) is not sufficient to fully oxidize a 3 nm overlayer thin film (i.e. 3 nm Y + O_2). This is observed firstly from the Y 3d BE that is measured at ~157.6 eV, which is different from that of Y_2O_3 at ~157 eV (data not shown). More importantly, YGe is detected in the Ge 3d plot as shown in Fig. 7.7(b) which clearly proves that the oxidation did not proceed to the interface. On the other hand, the use of oxygen plasma (OP) gives a more complete oxidation and the resultant Y 3d BE shifts to 157.1 eV. Unfortunately, as observed in both Fig. 7.7(c) and 7.7(d), YGeO formation can be seen from the appearance of the higher BE peak in the Ge 3d plots. The above observations have a few consequences. Firstly, as mentioned in section 7.1.2, significant intermixing in forming YGe occurs when Y deposition exceeds a critical thickness even at room temperature and this is also seen in Fig. 7.7(b). Secondly, comparing Fig. 7.7(b) and 7.7(c), we can conclude that OP has a higher diffusion length than O_2. This is because for the same oxidation duration across identical films, OP oxidizes YGe into YGeO while O_2 did not. Furthermore, we can also conclude that the reactivity of OP is also much higher than that of O_2. This is based on the observation shown in Fig. 7.7(d), whereby a thinner deposited Y yields significant YGeO formation, which is over and above that expected from the oxidation of YGe from initial intermixing. In this case, YGeO most likely formed from the mixing of the Y overlayer and the oxidized Ge substrate. In contrast, Fig. 7.7(e) shows that O_2 oxidation of an even thinner 0.5 nm Y overlayer does not result in any IL formation. This proves firstly the requirement of a critical thickness for Y-

Ge intermixing, and secondly gives a good indication of the reactivity and/or diffusivity of O_2.

7.2.2. Novel layer-by-layer method to suppress IL formation

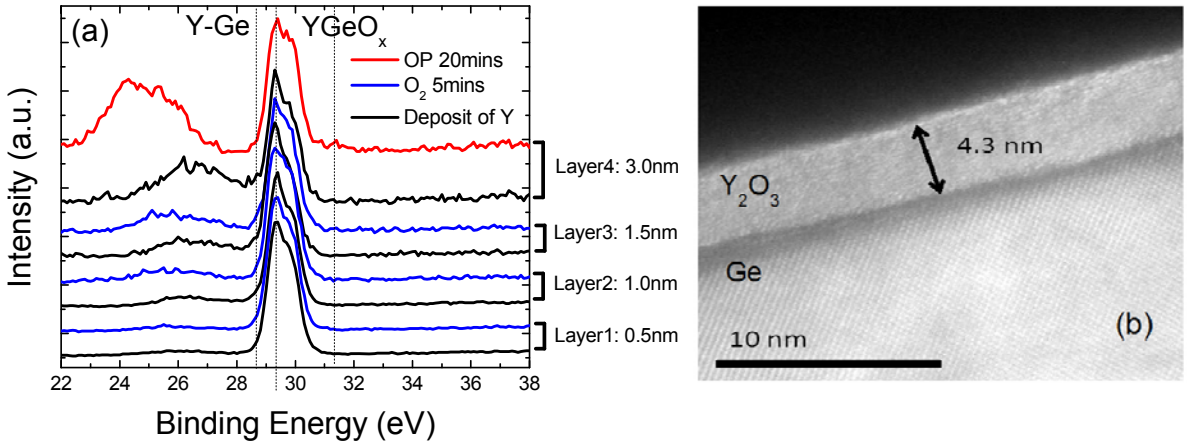

Fig. 7.8: (a) XPS Ge 3d spectrum of layers grown using a layer-by-layer method at different intervals. The Ge 3d spectrums (black lines) show the deposition of 0.5, 1, 1.5 and 3 nm of Y at each indicated layers. Corresponding oxidation at each thickness using 5 min molecular oxygen oxidation, O_2 (blue line) and 20 min oxygen plasma oxidation, OP (red line) is shown together with respective deposition layers as indicated in the plot. Cross-sectional HRTEM image of a layer-by-layer grown Y_2O_3 on Ge is shown in (b).

The above observations also predict that the key to minimizing IL formation when using evaporation of pure yttrium metal is firstly to eliminate the YGe formation, i.e. intermixing. Section 7.1.2 shows the need for a critical metallic thickness in order to trigger the metal-induced weakening of Ge-Ge substrate bonds for intermixing to occur. As such, a layer-by-layer growth method can be employed to prevent intermixing and achieve IL-free growth. The principle is to lightly oxidize the Y metal at regular intervals before the critical thickness is achieved and this should adequately eliminate the metallic screening effect. The light oxidation is suitably accomplished using molecular oxygen since we understood from Fig. 7.7(e) that the reactivity of O_2 is insufficient to oxidize the interface at our conditions of growth.

Figure 7.8 (a) shows the Ge 3d spectrums of the film at different stages using this layer-by-layer approach. The pairs of Ge 3d spectra, labeled as different layers, represent the deposition of a Y layer at the indicated thicknesses (black line) with a 5 min O_2 oxidation (blue line). We highlight that this layer-by-layer approach for the initial growth showed zero intermixing and oxidation of the Ge substrate because of the effective passivation at the early stages of growth. The observation of zero interfacial layer growth is also supported by the Ge 2p spectrum (not shown). At this stage, the Y 3d spectrum showed multiple oxidation states probably due to the incomplete light oxidation steps as was expected from our discussion above. The final layer of Y deposition gives a cumulative deposited Y thickness of 3 nm before a final oxidation step using OP for 20 min (red line). This oxidation step shifts the Y $3d_{5/2}$ BE from ~157.6 to 157 eV, which is a value we would expect from that of Y_2O_3. The Ge 3d spectrum, in Fig. 7.8(a), similarly showed no formation of YGeO or YGe after this final oxidation step. This is consistent in terms of the diffusivity and reactivity of OP from our earlier observations. The peaks around the region 24 – 27 eV originates from both Y 4p and O 2s photoelectron signals. This is further affirmed by the fact that their intensities increased significantly upon the complete oxidation of yttrium (OP). The cross-sectional HR-TEM image of the Y_2O_3/Ge sample grown using the layer-by-layer method is shown in Fig. 7.8(b). The abrupt interface shown in the micrograph confirms the lack of IL formation. The TEM image measures a thickness of 4.3 nm for the Y_2O_3 film representing a ~50% expansion of the Y metal film upon oxidation, which is within expectations.[298]

7.2.3. Effects of different substrate surfaces on IL formation

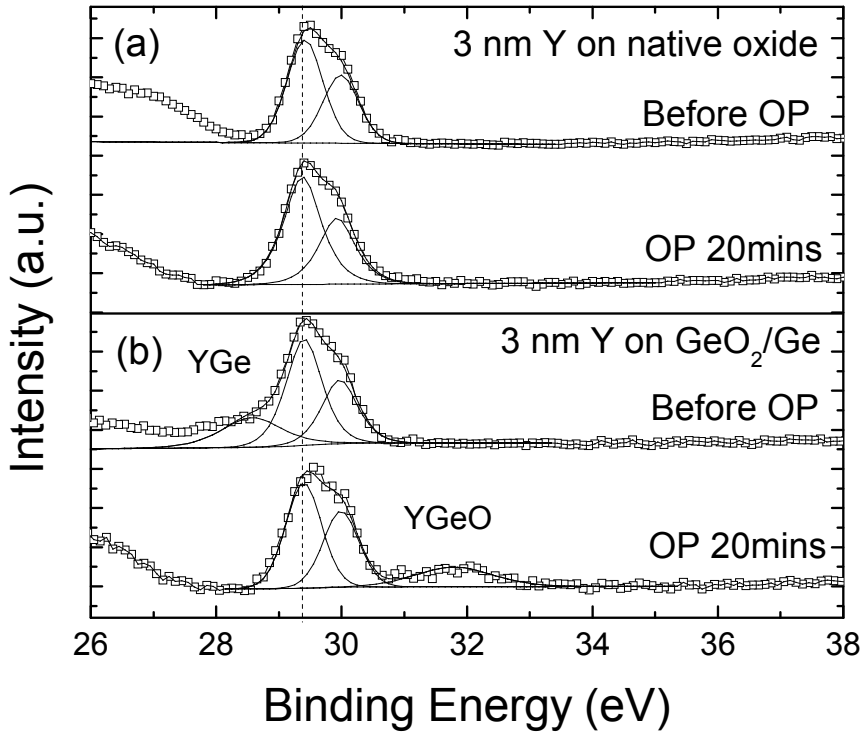

Fig. 7.9: Ge 3d XPS spectrum before and after a 20 min oxygen plasma (OP) for a 3nm evaporation of Y on (a) Ge substrate without prior degas (with native oxide and surface carbon contaminants) and (b) Ge substrate with thin GeO_2 formed by *in situ* oxidation using oxygen plasma (OP).

The key to the interlayer suppression in the layer-by-layer growth method is the prevention of intermixing of Y and Ge. This is achieved by preventing the formation of metallic Y on Ge through initial light oxidation in the method introduced. The importance of initial reactions can be shown by the following experiment. Two different substrate surfaces are investigated: (1) one with native Ge oxide and surface carbon contaminants (by skipping the *in situ* degas step) and (2) one with ~ 0.85 nm of GeO_2 grown by direct OP (1 min) on a degassed Ge substrate. Figure 7.9(a) shows the Ge 3d XPS spectra of 3 nm Y deposited on Ge without prior degas, before and after 20 min of oxygen plasma oxidation. It is noted that upon deposition of 3 nm of Y, the native GeO_x which is initially present

is being consumed as shown by the absence of higher BE chemical shifts in Fig. 7.9(a). This is because Y competes with Ge for oxygen due to its more negative formation enthalpy (-19.7 compared to -6.01 eV/formula unit), and as a result forming YO_x instead.[299] The important observation is that both spectra showed no IL formation, which proves that the intermixing is prevented. Surprisingly, for the second case where GeO_2 is grown on a degassed substrate, intermixing can be seen before and after OP as shown in Fig. 7.9(b). Here, oxygen is only contributed from the initial Ge oxide, which is insufficient to fully oxidize the entire deposited Y. As such, the remaining deposited Y remains metallic and a metal-induced screening effect, which dissociates the Ge-O bonds (shown in Fig. 7.9(b)) to form Y-Ge and Y-O bonds, can occur. Thermodynamically, this observed reduction of GeO_x by Y is consistent with the findings from metal-SiO_2 interactions, whereby the reaction is increasingly favored (i.e., more negative heat of reaction) for more electropositive metals.[300,301] However, for the case of the sample without a prior degas step, the lack of intermixing can be due to the presence of carbon contaminants that prevents the direct contact of Y and Ge and act as a barrier to the screening effect. Moreover, yttrium is also known to react readily with the hydrocarbonates (from the carbon contaminants), therefore forming Y-O-C bonds that acted as additional barriers to prevent intermixing.[302] Subsequent oxidation of these films then converts the YGe into YGeO as shown after the oxygen plasma step.

7.2.4. Discussion on pathways of IL formation

The pathways of formation for $YGeO_x$ can now be better understood as shown in the overall unbalanced chemical equations:

$$YGe + O \rightarrow YGeO \quad (7.2)$$

$$Y + GeO \rightarrow YGeO \quad (7.3)$$

$$YO + Ge \rightarrow YGeO \quad (7.4)$$

Pathway (1) represents the most kinetically favorable reaction since YGe readily oxidizes at room temperature in forming YGeO (as shown in Fig. 7.7(c) and Fig. 7.9(b)). Pathway (2) is not preferred since our experiments show the formation of YGe and YO_x instead when Y interacts with GeO. However, we note that in forming YGe, YGeO can then readily form via pathway (1) in an oxidizing environment. Lastly, pathway (3) does not occur, at least at room temperature, shown by our lightly oxidized film of YO on Ge in the layer-by-layer method. In preventing this low kinetic pathway to YGeO formation, it is probable that a higher temperature is required to disrupt the Ge-Ge substrate bonds, thus explaining the absence of YGeO formation at room temperature.

8. Summary and Conclusion

8.1. Summary of findings

In this section, a summary of the key experimental findings in this work will be reported. In this study, chapter 4 first looks at the common pitfalls involved in photoemission studies of band alignment for semiconductor-oxide heterostructures. In the XPS measurement of valence band offset (VBO) using Kraut's method, it was found that the measured interface core level separation can be significantly affected by differential charging of the overlayer oxide film (up to ~0.3 eV shift). This arises due to the inability of the insulator film to compensate for the electrons lost during the photoemission process. This can be corrected for using a time-resolved XPS method that was proposed in this work. On the other hand, extra-atomic relaxation effects do not affect our measurements. This conclusion was based on an Auger parameter experiment and supported by a theoretical image charge model. In the UPS measurement of electron affinity, it was found that surface carbon contaminants can lead to drastic errors in the measurements. We proposed using a low power oxygen plasma *in situ* cleaning method to remove these contaminants. Using these measurements, we were then able to obtain a good agreement of our results with the metal-induced gap states (MIGS) model based on the charge neutrality level (CNL) concept. This agreement would not have been possible without the accurate measurements from this study.

In chapter 5, we used our proposed methodology to investigate the role of electronegativity in band alignment models and eventually develop a novel dipole

neutrality point (DNP) model to predict high-k oxide related interface dipoles. Firstly, we focused on the interface induced gap states (IFIGS) model, which is similar to the MIGS model but uses electronegativity (EN) in place of electron affinity. The slope parameter can be derived from these two models using our measured band offsets from a good range of LAO heterostructures. It was found that our experimental VBO data of a series of LAO heterostructures agreed well with the MIGS model, but did not agree well with the IFIGS model, thereby questioning the use of the electronegativity parameter. It was found that this discrepancy can be attributed to the use of an inaccurate correlation between the dielectric work function (for oxides) and electronegativity in the IFIGS model. Secondly, this relationship was further explored by measuring the electron affinities of a few common high-k oxides. The compilation of our experimental data and values from the literature showed that the correlation between (dielectric) work function and electronegativity should be negative for oxides, giving a proportionality constant of close to -2.29 eV/Miedema units, as opposed to 0.86 eV/Miedema units for metals. Using this new correlation, we then developed a new model, termed as the dipole neutrality point (DNP) model. The DNP is defined as the effective electronegativity of the semiconductor, supposing it possesses a similar correlation as that of the oxides. Using this concept, we are able to explain the strong dependency of dipole shifts on EN, and more importantly account for the observation of dipoles with opposing polarities which was previously not possible using the IFIGS model. This simple concept allows one to use only electronegativity to predict dipoles at high-k oxide/semiconductor interfaces, which can benefit threshold voltage tuning in the development of advanced CMOS gate stacks.

In chapter 6, the effects of annealing on the LAO/Si capacitors in terms of instability of the VBO, increase in interface trap density, and increase in leakage current were investigated. Subsequently, the beneficial effect of including an ultra-thin yttrium interlayer on the overall device performance was demonstrated. These include a smaller variation in band offset (i.e. by ~0.4 eV), reduction in the interface trap density (from 2 x 10^{12} to 1 x 10^{11} $eV^{-1}cm^{-2}$) and a reduction in leakage current after 800°C thermal annealing. The variation in VBO was measured by XPS and further verified by the V_{FB}-EOT plots. Since XPS measurements verified that annealing did not change the bulk properties (bandgap and stoichiometry) of the LAO oxide, this variation in the band offset was attributed to interface dipole effects. The improvement in the thermal stability and leakage current at the LAO/Si interface by using a Y-interlayer is beneficial for low standby power devices.

In chapter 7, an interfacial-layer-free growth of Y_2O_3 on Ge, through successive oxidation of the yttrium metal in a layer-by-layer fashion, was successfully achieved. In the first section, the initial formation of the yttrium/germanium interface was investigated in a systematic manner. Upon the first monolayer coverage, adatom-induced band bending occurs which is responsible for the eventual Fermi level pinning effect. At intermediate thickness, intermixing (i.e. YGe formation) commenced beyond a critical thickness of ~3 Å, driven by a metal-induced bond weakening mechanism. In the second section, this yttrium film was subsequently oxidized to form Y_2O_3. It was found that the interfacial layer (i.e. YGeO formation) was unavoidable as long as there was initial YGe present. The layer-by-layer method was therefore proposed with an aim to lightly

oxidize the deposited yttrium metal, before the critical thickness for intermixing was reached. This interfacial-layer-free growth method will be especially useful for the fabrication of high performance devices with low EOT.

8.2. Conclusion and future work

This study highlights the importance of the interface between the gate dielectric and semiconductor substrate on the overall device performance. It was demonstrated, that with the appropriate processing conditions, a high quality high-k oxide/semiconductor interface can be realized with the use of rare earth oxides such as Y_2O_3. This suggests that other rare earth oxides (ranging from CeO_2 to Lu_2O_3) can be promising candidates as well for passivation of Ge (and Si) substrates; therefore these materials should be thoroughly explored, in terms of their effects on the interface trap density, leakage current, overall EOT, and the thermal stability of the interface.

Our proposed layer-by-layer method demonstrates a novel method to suppress the interfacial layer formation by oxidation of metal films. It might be interesting to study the use of our layer-by-layer method for the growth of other lanthanide oxides, given the interest in the high-k oxide community. The electrical properties of this IL-free interface should be investigated to ensure that other important characteristics such as leakage current and interface trap density are not compromised for the increase in EOT. Further structural information such as the crystallinity can also be studied since this can also affect the overall dielectric constant of the oxide film. The use of a buffer film layer, such as $LaNiO_3$, can

help promote crystallization of the oxide film, but the leakage current should be monitored closely since current can conduct through the grain boundaries.

The work in this dissertation also looks into the artifacts involving the photoemission characterization of interfaces related to high-k oxides. Using our proposed methodology for studying the band alignment at semiconductor-oxide interfaces, it is suggested to investigate the electron affinities and band offset data for various other rare earth oxides (such as CeO_2, Er_2O_3, etc.) to further verify our proposed dipole neutrality point (DNP) model. Another good test of our model would be to investigate the effects of varying the composition of a complex dielectric material (e.g. $La_{1-x}Al_xO$) on the dipole strength.

References

[1] R. Dennard, F. Gaensslen, H. Yu, V. Rideout, E. Bassous, and A. LeBlanc, *IEEE J. Solid-State Circuits,* **SC-9**, 256 (1974).

[2] E. J. Nowak, *IBM Journal of Research and Development*, **46** (2-3), 169-80 (2002).

[3] G. Moore, *Electronics*, **38**, 144 (1965).

[4] G. George, *Microcosm: the quantum revolution in economics and technology*, p. 107 (Simon and Schuster, 1990).

[5] M. T. Bohr, R. S. Chau, T. Ghani, and K. Mistry, *IEEE Spectrum* **44**, 29 (2007).

[6] S. M. Sze, *Physics of Semiconductor Devices* (Wiley, New York, 1981).

[7] A. T. Fromhold, *Quantum Mechanics for Applied Physics and Engineering* (New York: Dover).

[8] J. H. Stathis, and D. J. DiMaria, *IEDM Tech. Dig.* p.167 (1998).

[9] D. A. Muller, T. Sorsch, S. Moccio, F. H. Baumann, K. Evans-Lutterodt and G. Timp, *Nature* **399**, 758 (1999).

[10] M. Houssa, *High-k Dielectrics*, (Institute of Physics Publishing, Bristol and Philadelphia, 2003), p. 293.

[11] G. D. Wilk, R. M. Wallace, and J. M. Anthony, *Appl. Phys. Rev.* **89**, 5243 (2001).

[12] K. J. Hubbard, and D. G. Schlom, *J. Mater. Res.* **11**, 2757 (1996).

[13] G. Bersuker, P. Zeitzoff, G. Brown, and H. R. Huff, *Mat. Today* **7**, 26, (2004).

[14] H. Wong, and H. Iwai, *Microelect. Engin*. **83**, 1867 (2006).

[15] J. Huang, D. Heh, P. Sivasubramani,P. D. Kirsch, G. Bersuker, D. C. Gilmer, M. A. Quevedo-Lopez, M. M. Hussain, P. Majhi, P. Lysaght, H. Park, N. Goel, C. Young, C. S. Park, C. Park, M. Cruz, V. Diaz, P. Y. Hung, J. Price, H. -H. Tseng, and R. Jammy, *2009 Symposium on VLSI Tech. Dig.* p.34 (2009).

[16] S. Ferrari, S. Spiga, C. Wierner, M. Fanciulli, and A. Dimoulas, *Appl. Phys. Lett.* **89,** 122906 (2006); M. D. Ulrich, J. E. Rowe, D. Niu, and G. N. Parsons, *J. Vac. Sci. Tech. B* **21**, 1792 (2003).

[17] G. Bersuker, J. Barnett, N. Moumen, B. Foran, C. D. Young, P. Lysaght, J. Peterson, B. H. Lee, P. M. Zeitzoff, and H. R. Huff, *Jap. J. Appl. Phys.* **43**, 7899 (2004).

[18] M. Houssa, L. Pantisanom, L. –A. Ragnarsson, R. Degraeve, T. Schram, G. Pourtois, S. De Gendt, G. Groeseneken, and M. M. Heyns, *Mat. Sci. and Engin*. **R 51**, 37 (2006).

[19] M. Houssa, M. Tuominen, M. Naili, V. Afanas'ev, A. Stesmans, S. Haukka, and M. M. Heyns, *J. Appl. Phys.* **87**, 8615 (2000).

[20] H-H. Tseng, *Solid State Circuit Technologies*, pp. 157-202, Chapter 8, edited by J. W. Swart, (InTech, Vukovar, Croatia, 2010).

[21] D. G. Schlom, J. H. Haeni, *MRS Bull.* **27**, 198 (2002).

[22] J. Robertson, *Eur. Phys. J. Appl. Phys*. **28**, 265 (2004).

[23] H. J. Osten, J. P. Liu, P. Gaworzewski, E. Bugiel, and P. Zaumseil, *IEDM Tech. Dig*., 2000, p. 653.

[24] S. Jeon, K. Im, H. Yang, H. Lee, H. Sim, S. Choi, T. Jang, and H. Hwang, *IEDM Tech. Dig*., 2001, p. 471 (2001).

[25] J-P. Locquet, C. Marchiori, M. Sousa, J. Fompeyrine, and J. W. Seo, *J. Appl. Phys.* **100,** 051610 (2006).

[26] M. Leskela, K. Kukli, and M. Ritala, *J. Alloys and Compounds* **418**, 27 (2006).

[27] *Rare earth oxide thin films growth characterization and applications*, edited by M. Fanciulli, G. Scarel, pp. 379-390 (Springer, Heidelberg, Germany, 2007).

[28] *Nomenclature of Inorganic Chemistry: IUPAC Recommendations 2005*, edited by N. G. Connelly, T. Damhus, R. M. Hartshorn and A. T. Hutton, (Cambridge, RSC Publ.).

[29] Y. H. Wu, M. Y. Yang, A. Chin, W. J. Chen, C. M. Kwei, *IEEE Elect. Dev. Lett*. **21**, 341 (2000).

[30] H. Iwai, S. Ohmi, S. Akama, C. Ohshima, A. Kikuchi, I. Kashiwagi, J. Taguchi, H. Yamamoto, J. Tonotani, Y. Kim, I. Ueda, A. Kuriyama, Y. Yoshihara, *IEDM Tech. Dig.,* 2002, p. 625.

[31] A. Kikuchi, S. Akama, S. Ohmi, H. Iwai, *Proc. Electrochem. Soc.* **2002-22,** 157 (2003).

[32] Y. Zhao, M. Toyama, K. Kita, K. Kyuno, and A. Toriumi, *Appl. Phys. Lett.* **88,** 072904 (2006).

[33] H. Y. Yu, M. F. Li, and D. L. Kwong, *Thin Solid Films* **462-463**, 110 (2004).

[34] W. J. Zhu, T. Tamagawa, M. Gibson, T. Furukawa, and T. P. Ma, *IEEE Elect. Dev. Lett*. **23**, 649 (2002).

[35] D. Tahir, E. H. Choi, Y. J. Cho, S. K. Oh, H. J. Kang, H. Jin, S. Heo, J. G. Chung, J. C. Lee, S. Tougaard, *Surf. Int. Anal.* **42**, 1566 (2010).

[36] S. G. Lim, S. Kriventsov, T. N. Jackson, J. H. Haeni, D. G. Schlom, A. M. Balbashov, R. Uecker, P. Reiche, J. L. Freeouf, and G. Lucovsky, *J. Appl. Phys.* **91**, 4500 (2002).

[37] B. E. Park and H. Ishiwara, *Appl. Phys. Lett.* **82,** 1197 (2003).

[38] J. W. Reiner, A. Posadas, M. Wang, M. Sidorov, Z. Krivokapic, F. J. Walker, T. P. Ma, and C. H. Ahn, *J. Appl. Phys.* **105**, 124501 (2009).

[39] Y. Y. Mi, Z. Yu, S. J. Wang, P. C. Lim, Y. L. Foo, A. C. Huan, and C. K. Ong, *Appl. Phys. Lett*. **90**, 181925 (2007).

[40] P. Sivasubrmani, J. Kim, M. J. Kim, B. E. Gnade, and R. M. Wallce, *Appl. Phys. Lett*, **89**, 152903 (2006).

[41] J. Kwo, M. Hong, B. Busch, D. A. Muller, Y. J. Chabal, A. R. Kortan, J. P. Mannaerts, B. Yang, P. Ye, H. Gossmann, A. M. Sergent, K. K. Ng, J. Bude, W. H. Schulte, E. Garfunkel, T. Gustafsson, *J. Cryst. Growth* **251**, 645 (2003), and references therein.

[42] E. K. Evangelou, C. Wiemer, M. Fanciulli, M. Sethu, and W. Cranton, *J. Appl. Phys.* **94**, 318 (2003).

[43] D. Niu, R. W. Ashcroft, and G. N. Parsons, *Appl. Phys. Lett*. **80**, 3575 (2002).

[44] K. Kita, K. Kyuno, and A. Toriumi, *Appl. Phys. Lett.* **86**, 102906 (2005).

[45] Y. Kamata, *Mater. Today* **11**, 30 (2008).

[46] S. Takagi, T. Mizuno, T. Tezuka, N. Sugiyama, T. Numata, K. Usuda, Y. Moriyama, S. Nakaharai, J. Koga, A. Tanabe, N. Hirashita, and T. Maeda, *IEDM Tech. Dig.,* 2003, p. 57.

[47] C. O. Chui, H. Kim, D. Chi, B. B. Triplett, P. C. McIntyre, and K. C. Saraswat, *IEDM Tech. Dig.,* 2002, p. 437.

[48] C. Claeys, and E. Simoen, *Germanium-Based Technologies: From Materials to Devices*, (Elsevier, Amsterdam, 2007).

[49] K. Prabhakaran, F. Maeda, Y. Watanabe and T. Ogino: *Appl. Phys. Lett.* **76**, 2244 (2000).

[50] N. N. Greenwood, and A. Earnshaw, *Chemistry of the Elements*, Pergamon, Oxford, (1997).

[51] K. Kita, S. Suzuki, H Nomura, T Takahashi, T. Nishimura, and A. Toriumi, *Jap. J. Appl. Phys.* **47**, 2349 (2008).

[52] S. Suzuki, K. Kita, H. Nomura, T. Takahashi, T. Nishimura, A. Toriumi, *Ext. Abst. Int.Conf. Solid State Device and Materials*, 2007, p. 20.

[53] J. R. Weber, A. Janotti, P. Rinke, and C. G. Van de Walle, *Appl. Phys. Lett*. **91**, 142101 (2007).

[54] R. Xie, and C. X. Zhu, *IEEE Electron Dev. Lett*. **28**, 976 (2007).

[55] M. M. Frank, S. J. Koester, M. Copel, J. A. Ott, V. K. Paruchuri, and H. Shang, *Appl. Phys. Lett.* **89**, 112905 (2006).

[56] G. W. Anderson, M. C. Hanf, P. R. Norton, Z. H. Lu, and M. J. Grahamn, *Appl. Phys. Lett.,* **66**, 1123 (1995).

[57] M. K. Bera, C. Mahata, A. K. Chakraborty, S. K. Nandi, J. N. Tiwari, J. Y. Hung and C. K. Maiti, *Semicond. Sci. Technol.* **22**, 1352-1361 (2007).

[58] E. P. Gusev, H. Shang, M. Copel, M. Gribelyuk, C. D'Emic, P. Kozlowski, and T. Zabel, *Appl. Phys. Lett.* **85,** 2334 (2004).

[59] T. Takahashi, T. Nishimura, L. Chen, S. Sakata, K. Kita, and A. Toriumi, *IEDM Tech. Dig.* p. 697 (2007).

[60] J. J. Chen, N. A. Bojarczuk, J. H. Shang, M. Copel, J. B. Hannon, J. Karasinski, E. Preisler, S. K. Banerjee, and S. Guha, *IEEE. Trans. Elect. Dev.* **51**, 1441 (2004).

[61] M. A. Schmidt, F. L. Terry, B. P. Mathur, and S. D. Senturia, *IEEE Trans. Elect. Dev.* **35**, 1627 (1988).

[62] S. Sun, Y. Sun, Z. Liu. D. Lee, S. Peterson and P. Pianetta, *Appl. Phys. Lett.* **88** 021903 (2006).

[63] J. Mitard, B. De Jaeger, F. E. Leys, G. Hellings, K. Martens, G. Eneman, D. P. Brunco, R. Loo, J. C. Lin, D. Shamiryan, T. Vandeweyer, G. Winderickx, E. Vrancken, C. H. Yu, K. De Meyer, M. Caymax, L. Pantisano, M. Meuris, and M. M. Heyns, *IEDM Tech. Dig*, p.873 (2008).

[64] T. Yamamoto, Y. Yamashita, M. Harada, N. Taoka, K. Ikeda, K. Suzuki, O. Kiso, N. Sugiyama, and S. Takagi, *IEDM Tech. Dig*. 2007, p. 1041.

[65] N. Taoka, W. Mizubayashi, Y. Morita, S. Migita, H. Ota, and S. Takagi, *2009 Symposium on VLSI Tech. Dig*. p. 80 (2009).

[66] C. G. Van de Walle and R. M. Martin, *Phys. Rev. B* **34**, 5621 (1986).

[67] C. H. Lee, T. Tabata, T. Nishimura, K. Nagashio, K. Kita, and A. Toriumi, *Appl. Phys. Exp.* **2**, 071404 (2009).

[68] M. Kobayashi, G. Thareja, M. Ishibashi, Y. Sun, P. Griffin, J. McVittie, P. Pianetta, K. Saraswat, and Y. Nishi, *J. Appl. Phys*. **106**, 104117 (2009).

[69] G. Lucovsky, Y. Wu, H. Niimi, V. Misra, and J. C. Philips, *Appl. Phys. Lett*. **74**, 2005 (1999).

[70] A. Dimoulas, D. P. Brunco, S. Ferrari, J. W. Seo, Y. Panayiotatos, A. Sotiropoulos, T. Conard, M. Caymax, S. Spiga, M. Faniculli, Ch. Dieker, E. K. Evangelou, S. Galata, M. Houssa, and M. M. Heyns, *Thin Solid Films* **515**, 6337 (2007).

[71] E. K. Evangelou, G. Mavrou, A. Dimoulas, and N. Konofaos, *Solid State Elect.* **51**, 164 (2007).

[72] G. Mavrou, S. F. Galata, A. Sotiropoulos, P. Tsipas, Y. Panayiotatos, A. Dimoulas, E. K. Evangelou, J. W. Seo, and Ch. Dieker, *Microelect. Engin.* **84**, 2324 (2007).

[73] D. P. Norton, J. D. Budai, and M. F. Chisholm, *Appl. Phys. Lett.* **76**, 1677 (2000).

[74] M. Houssa, G. Pourtois, M. Caymax, M. Meuris, and M. M. Heyns, *Appl. Phys. Lett.* **92** 242101 (2008).

[75] Hans Lüth, *Surfaces and Interfaces of Solids,* (Springer-Verlag, Berlin Heidelberg New York, 1993).

[76] W. Shockley, *Phys. Rev*. **56**, 317 (1939).

[77] I. Tamm, *Phys. Z. Soviet Union* **1**, 733 (1932).

[78] R. Cao, K. Miyano, T. Kendelewicz, I. Lindau, W. E. Spicer, J. *Vac. Sci. Tech. B* **5**, 998 (1987).

[79] W. Mönch, *Rep. Prog. Phys.* **53**, 221 (1990).

[80] W. Mönch, *Europhys. Lett.* **7** (3), 275 (1988).

[81] M. Prietsch, M. Domke, C. Laubschat, G. Kaindl, *Phys. Rev. Lett*. **60**, 436 (1988); M. Prietsch, M. Domke, C. Laubschat, T. Mandel, C. Xue, G. Kaindl, *Z. Physik* **74**, 21 (1989).

[82] S. H. Pan, D. MO, G. W. Petro I. Lindau, and W. E.Spicer, *J. Vac. Sci. Technol. B* **1**, 1593 (1983).

[83] K. Stiles, A. Kahn, Phys. Rev. Lett. 60, 440 (1988); K. Stiles, D. G. Kilday, G. Margaritondo, *J. Vac. Sci. Tec. B* **5**, 987 (1987); K. Stiles, S. F. Horng, A. Kahn, J. McKinley, D. G. Kilday, G. Margaritondo, *J. Vac. Sci. Tech. B* **6**, 1392 (1988).

[84] G. Hughes, and R. Ludeke, *J. Vac. Sci. Tech. B* **4**, 1109 (1986); G. Hughes, R. Ludeke, F. Schaffler, D. Rieger, *J. Vac. Sci. Tech. B* **4**, 924 (1986).

[85] R. Ludeke, G. Landgren, *Phys. Rev. B* **33**, 5526 (1986).

[86] E. H. Rhoderick, and R. H. Williams, *Metal-Semiconductor contacts,* (Clarendon Press, Oxford, 1988), p. 47.

[87] N. D. Lang, and W. Kohn, *Phys. Rev. B* **3**, 1215 (1971).

[88] S. V. Jagadeesh Chandra, Mi-Ra Jeong, K. H. Shim, H. B. Hong, S. H. Lee, K. S. Ahn, and C. J. Choi, *J. Electrochem. Soc*. **157** (5), H546 (2010).

[89] R. Jhn, J. Gurganos, Y. H. Kim, R. Choi, J. Lee, and V. Misra, *IEEE Elect. Dev. Lett.* **25** (6), 420 (2004).

[90] K. Kita, and A. Toriumi, *IEDM Tech. Dig.*, p.29 (2008).

[91] W. Schottky, Phys. Z. 113 367 (1940); N. F. Mott, *Proc. Cambridge Philos. Soc.* **34**, 568 (1938).

[92] R. L. Andersen, *Solid-State Electron.* **5,** 341 (1962).

[93] J. Bardeen, *Phys. Rev*. **71**, 717 (1947).

[94] V. Heine, *Phys. Rev.* **A138**, 1689 (1965).

[95] S. G. Louie, and M. L. Cohen, *Phys. Rev. B* **13**, 2461 (1976); S. G. Louie and J. R. Chelikowsky, and M. L. Cohen, *Phys. Rev. B* **15**, 2154 (1977).

[96] J. Tersoff, *Phys. Rev. Lett*. **52**, 465 (1984).

[97] J. Robertson, *J. Vac Sci Tech. B* **18**, 1785 (2000); P. W. Peacock, and J. Robertson, *J. Appl. Phys.* **92**, 4712 (2002).

[98] W. Mönch, *Surf. Sci.* **299/300**, 928 (1994).

[99] J. Tersoff, *Phys. Rev. B* **32**, 6968 (1985).

[100] E. Louis, F. Yndurain, and F. Flores, *Phys. Rev. B*, **13**, 4408 (1976); S. Tejedor, and F. Flores, *J. Phys. C*, **11**, L19 (1978).

[101] M. Cardona, and N. E. Christensen, *Phys. Rev. B* **35,** 6182 (1987); N. E. Christensen, *Philos. Mag. B* **70**, 567 (1994).

[102] A. Baldereschi, *Phys. Rev. B* **7**, 5212 (1973); D. J. Chadi, and M. L. Cohen, *Phys. Rev. B* **8**, 5747 (1973).

[103] L.N. Pauling, *The Nature of the Chemical Bond,* (C'ornell University, Ithaca, 1939).

[104] A. R. Miedema, F.R. de Boer and P.F. de Chatel, *J. Phys. F: Metal Phys.* **3**, 1558 (1973).

[105] A. R. Miedema, *J. Less-Common Metals*, **32**, 117 (1973).

[106] A. H. Nethercot, *Phys. Rev. Lett.* **33**, 1088 (1974).

[107] W. Gordy, and W. J. O. Thomas, *J. Chem. Phys.* **24**, 439 (1956).

[108] A. Zur, T. C. McGill, and D. L. Smith, *Phys. Rev. B* **28**, 2060 (1983); A. Zur, T. C. McGill, and D. L. Smith, *J. Vac. Sci. Tech. B* **2**, 440 (1984).

[109] J. Tersoff, *J. Vac. Sci. Tech.* ***B*** 3 (4), 1157 (1985).

[110] R. T. Tung, *Phys. Rev. B.*, **64**, 205310 (2001); R. T. Tung, *Phys. Rev. Lett.,* **84**, 6078 (2000).

[111] F. Capasso and G. Margaritondo, *Heterojunction band discontinuities: Physics and device applications.* (Elsevier Science Publishers, 1987).

[112] V. V. Afanas'eV, and A. Stesmans, *J. Appl. Phys*. **102**, 081301 (2007).

[113] S. Zafar, E. Cartier, and E. P. Gusev, *Appl. Phys. Lett.* **80**, 2749 (2002).

[114] E. A. Kraut, R. W. Grant, J. R. Waldrop, and S. P. Kowalczyk, *Phys. Rev. B* **28**, 1965 (1983).

[115] E. A. Kraut, R. W. Grant, J. R. Waldrop, and S. P. Kowalczyk, *Phys. Rev. Lett.* **44**, 1620 (1980).

[116] S. A. Chambers, T. Droubay, T. C. Kaspar, and M. Gutowski, *J. Vac. Sci. Tech.* **22**, 2205 (2004).

[117] S. Y. Chiam, W. K. Chim, C. Pi, A. C. H. Huan, S. J. Wang, J. S. Pan, S. Turner, and J. Zhang, *J. Appl. Phys.* **103,** 083702 (2008).

[118] H. F. Okorn-Schmidt, *IBM J. Res. Develop*. **43**, 351 (1999).

[119] T. Deegan, G. Hughes, *Appl. Surf. Sci.* **123/124,** 66 (1998).

[120] S. A. Suleiman, H. J. Oh, A. Du, C. M. Ng, and S. J. Lee, *Electrochem. and Solid-state Lett.* **13 (10),** H336 (2010).

[121] T. E. Cook Jr., C. C. Fulton, W. J. Mecouch, K. M. Tracy, R. F. Davis, E. H. Hurt, G. Lucovsky, and R. J. Nemanich, *J. Appl. Phys.* **93**, 3995 (2003).

[122] L. M. Wong, S. Y. Chiam, J. Q. Huang, S. J. Wang, J. S. Pan, and W. K. Chim, *J. Appl. Phys.* **108**, 033702 (2010).

[123] K. Y. Lee, W. C. Lee, Y. J. Lee, M. L. Huang, C. H. Chang, T. B. Wu, M. Hong, and J. Kwo, *Appl. Phys. Lett.* **89**, 222906 (2006).

[124] J. R. Arthur, *Surf. Sci.* **500**, 189 (2002).

[125] R. A. Swalin, *Thermodynamics of solids*, (John Wiley and Sons, New York, 1972).

[126] Obtained from Veeco website: www.veeco.com

[127] Obtained from Oxford vacuum science website :www.oxford-vacuum.com

[128] S. Hüfner, *Photoelectron Spectroscopy: Principles and Applications, (Springer, Berlin, 1995, 2nd edition).*

[129] C.N. Berglund, W.E. Spicer, *Phys. Rev.* **136,** A1030 and A1044 (1964).

[130] A. Einstein, *Annalen der Physik* **17**, 132 (1905).

[131] J. C. Vickerman, *Surface Analysis – The Principal Techniques*, Wiley, Chichester, England 1997) pp. 9-98.

[132] T. S. Koopmans, *Physica* **1**, 104 (1934).

[133] K. Siegbahn, C. Nordling, A. Fahlman, R. Nordberg, K. Hamrin, J. Hedman, G. Johansson, T. Bergmark, S. E. Karlsson, I. Lindgren, and B. Lindberg, *Nova Acta Regiae Societatis Scientiarum Upsaliensis, Ser.* IV, **20**, 5-282 (1967).

[134] K. Horn, *Surf. Sci.* **269/270**, 938 (1992).

[135] H. Öfner, R. Hoftmann, J. Kraft, and F. P. Netzer, *Phys. Rev. B* **50**, 15120 (1994).

[136] R. Hoftamnn, W. A. Henle, H. Öfner, M. G. Ramsey, F. P. Netzer, W. Braun, and K. Horn, *Phys. Rev. B* **47**, 10407 (1993).

[137] Catherine A. Dukes, and Raul A. Baragiola, *Surf. Interface Anal.* **42**, 40 (2010).

[138] J. Cazaux, *J. Appl. Phys.* **59**, 1418 (1986).

[139] R. A. Stratton, *Electromagnetic Theory* (McGraw-Hill, New York, 1961).

[140] J. Cazaux, *J. Elect. Spect. and Rel. Phen*. **176**, 58 (2010).

[141] R. S. Muller, and T. I. Kamins, *Device Electronics for Integrated Circuits*, (Wiley, New York, 1986), p. 496.

[142] B. Veal and A. Paulikas, *Phys. Rev. B* **31**, 5399 (1985).

[143] M. Scrocco, *Phys. Rev. B.* **32,** 1301 (1985); M. Scrocco, *Phys. Rev. B.* **32**, 1306 (1985).

[144] S. Miyazaki, *J. Vac. Sci. Tech. B* ***19***, 2212 (2001).

[145] S. Miyazaki, and M. Hirose, *AIP Conf. Proc.* **550**, 89 (2000).

[146] B. Mayer, St. Uhlenbrock, and M. Neumann, *J. Elect. Spect. and Rel. Phen.* **81**, 63 (1996).

[147] A. Kotani, and H. Ogasawara, *J. Elect. Spect. and Rel. Phen.* **60**, 257 (1992).

[148] D. A. Shirley, *Phys. Rev. B* **5,** 4709(1972).

[149] J. H. Scofield, *J. Elect. Spect. and Rel. Phen*. **8**, 129 (1976).

[150] C. D. Wagner, L. E. davis, M. V. Zeller, J. A. Taylor, R. H. Raymond, and L. H. Gale, *Surf. and Int. Anal*. **3**, 211 (1981).

[151] A. Jablonski, and C. J. Powell, *J. Elect. Spect. and Rel. Phen*. **100**, 137 (1999).

[152] P. J. Cumpson, and M. P. Seah, *Surf. and Int. Anal.* **25**, 430 (1997).

[153] C. J. Powell, *Scanning Electron Microsc. IV* 1649 (1984).

[154] G. A. Somorjai, *Introduction to Surface Chemistry and Catalysis*, (Wiley, New York, 1994), p. 383.

[155] P. Koke, A. Goldmann, W. Mönch, *Surf. Sci.* **152/153**, 1001 (1985).

[156] Y. Takeda, T. Ohtani, K. Ojima, T. Urano, and S. Hongo, *J. Elect. Spect. and Rel. Phen.* **88-91**, 619 (1988).

[157] A. S. Duwez, J. Riga, J. Ghijsen, J. J. Pireaux, and J. J. Verbist, *J. Elect. Spect. and Rel. Phen*. **76**, 523 (1995).

[158] E. Bersch, S. Rangan, R. A. Bartynski, E. Garfunkel, and E. Vescovo, *Phys. Rev. B.* **78**, 085114 (2008).

[159] G. Ertl, and J. Kuppers, *Low energy electrons and surface chemistry*, (VCH, Weinheim, Germany, 1985).

[160] Y. Park, V. Choong, Y. Gao, B. R. Hsieh, and C. W. Tang, *Appl. Phys. Lett.* **68**, 2699 (1996).

[161] D. B. Williams, and C. B. Carter, *Transmission Electron Microscopy* (Plenum, New York, 1996).

[162] D. K. Schroder, *Semiconductor material and device characterization* (Wiley-Interscience, 1998).

[163] P. W. Hawkes, *Principles of Electron Optics*, Vols. 1 and 2 (Academic Press, London, 1989).

[164] B. Fultz, and J. Howe, *Transmission electron microscopy and diffractometry of materials*, (Springer-Verlag, Berlin, Heidelberg, New York, 2001).

[165] T. T. Sheng, *Analytical Techniques for Thin Film Analysis* (K.N. Tu and R. Rosenberg, eds.) pp. 251-296 (Academic Press, Boston, 1988).

[166] W.R. Runyan and T.J. Shaffner, *Semiconductor Measurements and Instrumentation,* (McGraw-Hill, New York, 1998).

[167] N. W. Ashcroft, and N. D. Mermin, *Solid State Physics,* p. 96 (Thomson Learning, America, 1976).

[168] H. G. Tompkins, E. A. Irene, *Handbook of Ellipsometry,* (Springer, William Andrew, 2005).

[169] E. H. Nicollian, J. R. Brews, MOS (Metal Oxide Semiconductor) *Physics and Technology*, (New York: Wiley, 1982).

[170] J. R. Brews, *Solid State Elect.* **26,** 711 (1983).

[171] K. Martens, C. O. Chui, G. Brammertz, B. D. Jaeger, D. Kuzum, M. Meuris, M. M. Heyns, T. Krishnamohan, K. Saraswat, H. E. Maes, and G. Groeseneken, *IEEE Trans. Elect. Dev*. **55**, 547 (2008).

[172] K. Martens, B. D. Jaeger, R. Bonzom, J. V. Steenbergen, M. Meuris, G. Groeseneken, and H. Maes, *IEEE Elect. Dev. Lett*. **27**, 405 (2006).

[173] M. A. Lampert, *Phys. Rev***. 103**, 1648 (1956).

[174] F. C. Chiu, H. W. Chou, and H. Y. M. Lee*, J. Appl. Phys*. **97**, 103503 (2005).

[175] M. A. Lampert, and P. Mark, *Current injection in Solids* (Academic, New York, 1970).

[176] A. Rose, *Phys. Rev*. **97**, 1538 (1955).

[177] S. M. Sze, and K. K. Ng, *Physics of Semiconductor Devices*, (Wiley-Interscience, Hoboken, New Jersey, 2007).

[178] P. Li, and T. –M. Lu, *Phys. Rev. B* **43**, 14261 (1991).

[179] D. Stieler, V. L. Dalal, K. Muthtukrishnan, M. Noack, and E. Schares, *J. Appl. Phys.* **100,** 036106 (2006).

[180] J. Robertson, *J. Vac. Sci. Tech. B* **27**, 277 (2009).

[181] K. Kita, and A. Toriumi, *Appl. Phys. Lett*. **94**, 132902 (2009).

[182] K. Kakushima, K. Okamoto, M. Adachi, K. Tachi, P. Ahmet, K. Tsutsui, N. Sugii, T. Hattori, and H. Iwai, *Solid state Elect.* **52**, 1280 (2008).

[183] D. F. Mullica, C. K. C. Lok, H. O. Perkins, and V. Young, *Phys. Rev. B* **31**, 4039 (1985).

[184] J. Sugar, *Phys. Rev. A* **6**, 1764 (1972).

[185] L. F. Edge, D. G. Schlom, S. A. Chambers, E. Cicerrella, J. L. Freeouf, B. Hollander, and J. Schubert, *Appl. Phys. Lett.* **84**, 726 (2004).

[186] J. L. Alay and M. Hirose, *J. Appl. Phys.* **81**, 1606 (1997).

[187] S. Iwata, and A. Ishizaka, *J. Appl. Phys.* **79**, 6653 (1996).

[188] J. W. Keister, J. E. Rowe, J. J. Kolodziej, H. Niimi, H. –S Tao, T. E. Madey, and G. Lucovsky, *J. Vac. Sci. Tech. A* **17**(4), 1250 (1999).

[189] Y. Y. Mi, S. J. Wang, J. W. Chai, J. S. Pan, A. C. H. Huan, M. Ning, and C. K. Ong, *Appl. Phys. Lett.* **89**, 202107 (2006).

[190] E. Bersch, M. Di, S. Consiglio, R. D. Clark, G. J. Leusink, and A. C. Diebold, *J. Appl. Phys.* **107,** 043702 (2010), and refs. cited therein.

[191] V. V. Afanas'ev, A. Stesmans, C. Zhao, M. Caymax, T. Heng, J. Schubert, Y. Jia, D. G. Schlom, and G. Lucovsky, *Appl. Phys. Lett*. **85**, 5917 (2004).

[192] H. Kobayashi, T. Kubota, H Kawa, Y. Nakato, and M. Nishiyama, *Appl. Phys. Lett.* **73**, 933 (1998).

[193] C. D. Wagner, *Faraday Disc. Chem. Soc.* **60,** 291 (1975).

[194] G. Moretti*, J. Elect. Spect. and Related Phenom.* **95,** 95-144 (1998).

[195] S. -J. Oh, G. -H. Kim, G. A. Sawatzky, and H. T. Jonkman, *Phys. Rev. B* **37,** 6145 (1988).

[196] W. –D. Schneider, B. Delley, E. Wuilloud, J. –M. Imer, and Y. Baer, *Phys. Rev. B* **32**, 6819 (1985).

[197] P. S. Bagus, A. Wieckowski, and H. Freund, *Chem. Phys. Lett.* **420,** 42 (2006).

[198] R. Browning, M. A. Sobolewski, and C. R. Helms, *Phys. Rev. B* **38**, 13407 (1988).

[199] K. Hirose, H. Kitahara, and T. Hattori, *Phys. Rev. B.* **67,** 195313 (2003).

[200] Optical dielectric constants are obtained from the square of the refractive index (measured by ellipsometer) of the material; For LAO = 1.8^2; SiO_2 =1.45^2.

[201] R. Schlaf, H. Murata, Z. H. Kafafi, *J. Electron Spect. and Rel. Phen*. **120,** 149 (2001).

[202] Y. Liang, J. Curless, C. J. Tracy, D. C. Gilmer, J. K. Schaeffer, D. H. Triyoso, and P. J. Tobin, *Appl. Phys. Lett.,* **88**, 072907 (2006).

[203] K. Sugiyama, H. Ishii, Y. Ouchi, and K. Seki, *J. Appl. Phys.* **87**, 295 (2000).

[204] C. A. Dukes, and R. A. Baragiola, *Surf. Interface Anal.* **42**, 40 (2010).

[205] J. Kim, and K. Yong, *J. Vac. Sci. Tech.* **B 24** (3), 1147 (2006).

[206] J. S. Kim, B. Lagel, E. Moons, N. Johansson, I. D. Baikie, W. R. Salaneck, R. H. Friend, and F. Cacialli, *Synthetic Metals* **111**, 311 (2000).

[207] G. Betz and G. K. Wehner, *Sputtering by particle bombardment II* (Springer Verlag, Berlin, 1983), R. Behrisch (Ed.), Chapter 2 - Sputtering of multi-component materials, pp. 11-90.

[208] J. J. Yeh, *Atomic calculation of photoionization cross sections and asymmetry parameters*, Gordon and Breach Science, Publishers, Langhorne, PA, 1993.

[209] J. Robertson and B. Falabretti, *J. Appl. Phys.* **100**, 014111 (2006) and references cited therein.

[210] L. Becerra, C. Merckling, M. El-Kazzi, N. Baboux, B. Vilquin, G. Saint-Girons, C. Plossu, and G. Hollinger, *J. Vac. Sci. Tech.* **B** 27, 384 (2009).

[211] W. Xiang, H. Lu, L. Yan, H. Guo, L. Liu, Y. Zhou, G. Yang, J. Jiang, H. Cheng, and Z. Chen, *J. Appl. Phys.* **93**, 533 (2003).

[212] J. Robertson, *J. Appl. Phys*., **92**, 4712 (2002).

[213] W. Mönch, *Electronic properties of semiconductor interfaces* (Springer Berlin, 2004); W. Mönch, *App. Surf. Sci.* **92**, 367 (1996); W. Mönch, *Phys. Rev. Lett.* **58**, 1260 (1987).

[214] W. Mönch, *Appl. Phys. Lett*., **91**, 042117 (2007); W. Mönch, *Appl. Phys. Lett.*, **86**, 122101 (2005); W. Mönch, *J. Appl. Phys.* **107**, 013706 (2010).

[215] V. V. Afanas'ev, A. Stesmans, R. Droopad, M. Passiack, L. F. Edge, and D. G. Schlom, *Appl. Phys. Lett.*, **89**, 092103 (2006).

[216] N. Goel, W. Tsai, C. M. Garner, Y. Sun, P. Pianetta, M. Warusawithana, D. G. Schlom, H. Wen, C. Gaspe, J. C. Keay, M. B. Santos, L. V. Goncharova, E. Garfunkel, and T. Gustafasson, *Appl. Phys. Lett.*, **91**, 113515 (2007).

[217] Y. N. Tan, W. K. Chim, J. B. Cho, and W. K. Choi, *IEEE Trans. Elect. Dev*., **51**, 1143 (2004).

[218] A. Schleife, F. Fuchs, C. Rodl, Furthmuller, and F. Bechstedt, *Appl. Phys. Lett.* **94**, 012104 (2009).

[219] M. W. Allen, and S. M. Durbin, *Phys. Rev. B.* **82**, 165310 (2010) and references therein.

[220] M. Levinshtein, L. Kronik. B. Mishori, Y. Shapira, C. M. Hanson, A. R. Clawson, and P. Ram, *Appl. Phys. Lett.* **69**, 257 (1996).

[221] X. Wang, K. Han, W. Wang, X. Ma, D. Chen, J. Zhang, J. Du, Y. Xiong, and A. Huang, *Appl. Phys. Lett*., **97**, 062901 (2010).

[222] K. Shiraishi, K. Yamada, K. Torii, Y. Akasaka, K. Nakajima, M. Konno, T. Chikyow, H. Kitajima, and T. Arikado, *Jap. J. Appl. Phys*. **43**, L1413 (2004).

[223] J. K. Schaeffer, D. C. Gilmer, C. Capasso, S. Kalpat, B. Taylor, M. V. Raymond, D. Triyoso, R. Hegde, S. B. Samavedam, and B. E. White Jr, *Microelect. Engin*. **84**, 2196-2200 (2007).

[224] E. J. Lim, W. W. Fang, F. Liu, T. P. Lee, G. Samudra, D. L. Kwong, and Y. C. Yeo, *Appl. Phys. Lett*. **91**, 172115 (2007).

[225] P. D. Kirsch, P. Sivasubramani, J. Huang, C. D. Young, M. A. Quevedo-Lopez, H. C. Wen, H. Alshareef, K.Chi, C. S. Park, K. Freeman, M. M. Hussain, G. Bersuker, H. R. Harris, P. Majhi, R. Choi, P. Lysaght, B. H. Lee, H. –H. Tseng, R. Jammy, T. S. Boscke, D. J. Lichtenwalner, J. S. Jur, and A. I. Kingon, *Appl. Phys. Lett.* **92**, 092901 (2008).

[226] H. N. Alshareef, M. Quevedo-Lopez, H. C. Wen, R. Harris, P. Kirsch, P. Majhi, B. H. Lee, and R. Jammy, *Appl. Phys. Lett*. **89,** 232103 (2006).

[227] Z. C. Yang, A. P. Huang, L. Yan, Z. S. Xiao, X. W. Zhang, Paul K. Chu, and W. W. Wang, *Appl. Phys. Lett,* **94**, 252905 (2009).

[228] W. Mönch, *J. Appl. Phys.* **109**, 113724 (2011), and references cited within.

[229] S. Rangan, E. Bersch, R. A. Bartynski, E. Garfunkel, and E. Vescovo, *Phys. Rev. B* **79**, 075106 (2009).

[230] J. Robertson, and K. Xiong, *Rare Earth Oxide Thin Films*, vol. 106, pp.313-329, (Springer, Berlin Heidelberg, 2006).

[231] K. R. Jeon, S. J. Lee, C. Y. Park, H. S. Lee, and S. C. Shin, *Appl. Phys. Lett.* **97**, 111910 (2010).

[232] C. C. Fulton, G. Lucovsky, and R. J. Nemanich, *J. Appl. Phys*. **90**, 063708 (2006).

[233] X. P. Wang, M. F. Li, A. Chin, C. X. Zhu, J. Shao, W. Lu, X. C. Shen, X. F. Lu, R. Chi, C. Shen, A. C. H. Huan, J. S. Pan, A. Y. Du, Patrick Lo, D. S. H. Chan, and D-L. Kwong, *Solid-State Elect*. **50**, 986 (2006).

[234] W. Wang, K. Akiyama, W. Mizubayashi, T. Nabatame, H. Ota, and A. Toriumi, *J. Appl. Phys.* **105**, 064108 (2009).

[235] V. Narayanan, V. K. Paruchuri, N. A. Bojarczuk, B. P. Linder, B. Doris, Y. H. Kim, S. Zafar, J. Stathis, S. Brown, J. Arnold, M. Copel, M. Steen, E. Cartier, A. Callegari, P. Jamison, J. -P. Locquet, D. L. Lacey, Y. Wang, P. E. Batson, P. Ronsheim, R. Yammy, M. P. Chudzik, M. Ieong, S. Guha, G. Shahidi, and T. C. Chen, *Tech. Dig. - Symp. VLSI Tech.*, p. 178 (2006).

[236] H. B. Park, C. S. Park, C. Y. Kang, S. C. Song, B. H. Lee, T. Y. Jang, T. W. Kim, J. K. Jeong, and R. Choi, *Appl. Phys. Lett.* **95**, 192113 (2009).

[237] H. Takahashi, H. Minakata, Y. Morisaki, S. Xiao, M. Nakabayashi, K. Nishigaya, T. Sakoda, K. Ikeda, H. Morioka, N. Tamura, M. Kase, and Y. Nara, *IEEE Int. Electron Devices Meet*., p. 398 (2009).

[238] Y. Kamimuta, K. Iwamoto, Y. Nunoshige, A. Hirano, W. Mizubayashi, Y. Watanabe, S. Migita, A. Ogawa, H. Ota, T. Nabatame, and A. Toriumi, *Int. Electron Devices Meet*., p. 341 (2007).

[239] K. Iwamoto, Y. Kamimuta, A. Ogawa, Y. Watanabe, S. Migita, W. Mizubayashi, Y. Morita, M. Takahashi, H. Ota, T. Nabatame, and A. Toriumi, *Appl. Phys. Lett*. **92**, 132907 (2008).

[240] C. X. Li, and P. T. Lai, *Appl. Phys. Lett.* **95**, 022910 (2009).

[241] H. X. Xu, J. P, Xu, C. X. Li, and P. T. Lai, *Appl. Phys. Lett*., **97**, 022903 (2010).

[242] S. Swaminathan, M. Shandalov, Y. Oshima, and P. C. Mcintyre, *Appl. Phys. Lett.,* **96**, 082904 (2010).

[243] S. Y. Chiam, W. K. Chim, Y. Ren, C. Pi, J. S. Pan, A. C. Huan, S. J. Wang, and J. Zhang, *J. Appl. Phys.* **104**, 063714 (2008).

[244] M. Liu, L. D. Zhang, Q. Fang, J. P. Zhang, X. J. Wang, and G. He, *J. Phys. D: Appl. Phys*. **42**, 195304 (2009).

[245] M. Houssa, V. V. Afanas'ev, and A. Stesmans, *Appl. Phys. Lett.* **77**, 1885 (2000).

[246] D. Spassov, E. Atanassova, and G. Beshkov, *Microelectronics Journal* **31,** 653 (2000).

[247] P. Ahmet, K. Nakagawa, K. Kakushima, H. Nohira, K. Tsutsui, N. Sugii, T. Hattori, and H. Iwai, *Microelect. Rel.* **48**, 1769 (2008).

[248] G. H. Chen, Z. F. Hou, X. G. Gong, and Q. Li, *J. Appl. Phys.* **104**, 074101 (2008).

[249] T. Gougousi, M. Jason Kelly, David B. Terry, and Gregory N. Parsons, *J. Appl. Phys*. **93**, 1691 (2003).

[250] M. Suzuki, A. Kinoshita, T. Schimizu, and M. Koyama, *J. Appl. Phys.* **105**, 064105 (2009).

[251] M. J. McNutt and C. T. Sah, *J. Appl. Phys.* **46**, 3909 (1975).

[252] J. Maserjian, G. Peterso, and C. Svensson, *Solid State Electron.* **17**, 335 (1974).

[253] S. Kar, *IEEE Trans. Electron* Devices, **50**, 2112 (2003).

[254] Quantum-Mechanical CV Simulator of University of California, Berkeley [Available online: http://www-device.eecs.berkeley.edu/qmcv/index.shtml].

[255] V. S. Kaushik, B. J. O'Sullivan, G. Pourtois, N. V. Hoornick, A. Delabie, S. V. Elshocht, W. Deweerd, T. Schram, L. Pantisano, E. Rohr, L-A. Ragnarsson, S. D. Gendt, and M. Heyns, *IEEE Trans. Electron Devices* **53**, 2627 (2006).

[256] R. L. Opila, G. D. Wilk, M. A. Alam, R. B. Van Dover, and B. W. Busch, *Appl. Phys. Lett.* **81**, 1788 (2002).

[257] B. Mereu, A. Dimoulas, G. Vellianitis, G. Apostolopoulos, R. Scholz, and M. Alexe, *Appl. Phys. A.* **80**, 253 (2005).

[258] A. H. Edwards, *Phys. Rev. B* **44,** 1832 (1991).

[259] N. Miyata, Y. Abe, and T. Yasuda, *Appl. Phys. Exp*. **2**, 035502 (2009).

[260] A. Stesmans, *Phys. Rev. B* **48**, 2410 (1993).

[261] R. W. I. de Boer, and A. F. Morpurgo, *Phys. Rev. B* **72**, 073207 (2005).

[262] K. B. Jinesh, Y. Lamy, E. Tois, and W. F. A. Besling, *Appl. Phys. Lett*. **94**, 252906 (2009).

[263] I. Y. K. Chang, Y. R. Hwang, P. C. Juan, and J. Y. M. Lee, *J. Electrochem. Soc*. **155** (12) G265 (2008).

[264] S. A. Shevlin, A. Curioni, and W. Andreoni, *Phys. Rev. Lett.* **94**, 146401 (2005).

[265] M. Haverty, Atsushi Kawamoto, Kyeongjae, and R. Dutton, *Appl. Phys. Lett.* **80**, 2669 (2002).

[266] *Advanced Gate Stacks for High-Mobility Semiconductors*, edited by A. Dimoulas, E. Gusev, P. C. McIntyre, and M. M. Heyns, p. 73 (Springer, Berlin, 2007).

[267] L. K. Chu, W. C. Lee, M. L. Huang, Y. H. Chang, L. T. Tung, C. C. Chang, Y. J. Lee, J. Kwo, and M. Hong, *J. Cryst. Growth* **311**, 2195 (2009).

[268] J. J. Chambers, and G. N. Parsons, *J. Appl. Phys*. **90**, 918 (2001).

[269] J. Kwo, M. Hong, A. R. Kortan, K. L. Queeney, Y. J. Chabal, R. L. Opila, Jr. D. A. Muller, S. N. G. Chu, B. J. Sapjeta, T. S. Lay, J. P. Mannaerts, T. Boone, H. W. Krautter, J. J. Krajewski, A. M. Sergnt, and J. M. Rosamilia, *J. Appl. Phys.* **89**. 3920 (2001).

[270] A. Dimoulas, A. Travlos, G. Vellianitis, N. Boukos, and K. Argyropoulos, *J. Appl. Phys.* **90**, 4224 (2001).

[271] M. V. Fischetti, D. A. Neumayer, and E. A. Cartier, *J. Appl. Phys.* **90**, 4587 (2001).

[272] B. Laikhtman, and P. M. Solomon, *J. Appl. Phys*. **103**, 014501 (2008).

[273] A. C. Rastogi, and R. N. Sharma, *Semicond. Sci. Tech*. **16**, 641 (2001).

[274] L. K. Chu, T. D. Lin, M. L. Huang, R. L. Chu, C. C. Chang, J. Kwo, and M. Hong, *Appl. Phys. Lett*. **94**, 202108 (2009).

[275] C. W. Nieh, Y. J. Lee, W. C. Lee, Z. K. Yang, A. R. Kortan, M. Hong, J. Kwo, and C. -H. Hsu, *Appl. Phys. Lett.* **92**, 061914 (2008).

[276] S. C. Choi, M. H. Cho, S. W. Whangbo, C. N. Whang, S. B. Kang, S. I. Lee, and M. Y. Lee, *Appl. Phys. Lett.* **71**, 903 (1997).

[277] A. Dimoulas, G. Vellianitis, A. Travlos, V. Ioannou-Sougleridis, and A. G. Nassiopoulou, *J. Appl. Phys.* **92**, 426 (2002).

[278] L. Lamagna, G. Scarel, and M. Fanciulli, *J. Vac. Sci. Tech. A* **27** (3), 443 (2009).

[279] *High-k Gate Dielectrics,* edited by M. Houssa, pp. 29-37 (Institute of Physics Publishing, Bristol and Philadelphia, 2004).

[280] E. Landemark, C. J. Karlsson, L. S. O. Johansson, and R. I. G. Uhrberg, *Phys. Rev. B* **49**,16523 (1994).

[281] W. Mönch, *J. Vac. Sci. Tech. B* **6**, 1270 (1988); *Appl. Surf. Sci.* **41/42**, 128 (1989).

[282] A. Pellissier, R. Baptist, and G. Chauvet, *Surf. Sci.* **210**, 99 (1989).

[283] S. Y. Chiam, W. K. Chim, A. C. H. Huan, J. Zhang, and J. S. Pan, *J. Vac. Sci. Tech. A.* **25,** 500 (2007).

[284] M. Ohno and G. A. van Riessen, *Journal of Electron Spectroscopy and Related Phenomena* **128**, 1 (2003).

[285] P. Gas and F. M. d'Heurle, *Appl. Surf. Sci.* **73**, 153-161 (1993).

[286] T. Nakayama, S. Itaya, and D. Murayama, *J. Phys.: Conf. Series* **38**, 216-219 (2006).

[287]S. Y. Chiam, W. K. Chim, A. C. H. Huan, J. S. Pan, and J. Zhang, *Appl. Phys. Lett.* **88,** 011904 (2006).

[288] Y. Baba, T. A. Sasaki, and I. Takano, *J. Vac. Sci. Technol. A* **6**, 2945 (1988).

[289] R. Baptist, A. Pellissier, and G. Chauvet, *Solid State Commun*. **68**, 555 (1988).

[290] C. S. Hüfner, *Photoelectron Spectroscopy: Principles and Applications,* 2nd ed. (Springer, Berlin, 1995), p. 112.

[291] A. Dimoulas, P. Tsipas, A. Sotiropoulos, and E. K. Evangelou, *Appl. Phys. Lett.* **89**, 252110 (2006).

[292] T. Nishimura, K. Kita, and A. Toriumi, *Appl. Phys. Lett.* **91**, 123123 (2007).

[293] H. B. Michaelson, *IBM J. Res. Develop*. **22**, 72 (1978).

[294] J. Tersoff, *Phys. Rev. B* **30**, 4874 (1984).

[295] B. E. Coss, W. –Y. Loh, R. M. Wallace, J. Kim, P. Majhi, and R. Jammy, *Appl. Phys. Lett.* **95**, 222105 (2009).

[296] R. M. C. de Almeida, I. J. R. Baumvol, *Surf. Sci. Rep.* **49**, 1 (2003).

[297] D. Schmeisser, R. D. Schnell, A. Bogen, F. J. Himpsel and D. Rieger, *Surf. Sci.* **172**, 455 (1986).

[298] M. Gurvitch, L. Manchanda, and J. M. Gibson, *Appl. Phys. Lett.* **51**, 919 (1987).

[299] I. Barin, *Thermochemical Data of Pure Substances*, third edition, (VCH Verlagsgesllschaft mBH, Weinheim, Germany, 1995).

[300] O. M. Ndwandwe, Q. Y. Hlatshwayo, and R. Pretorius, *Mat. Chem. and Phys.* **92**, 487 (2005).

[301] R. Pretorius, J. M. Harris, and M. A. Nicolet, *Solid-State Elect.* **21**, 667 (1978).

[302] C. Durang, C. Dubourdieu, C. Vallee, V. Loup, M. Bonvalot, O. Joubert, H. Roussel, and O. Renault, *J. Appl. Phys.* **96,** 1719 (2004).

Appendix I: Derivation of MIGS equation

In this section, the MIGS model equation is briefly derived. Firstly, one assumes a continuum of interface states with a constant density of states D_S across the band gap, with Φ^p_{CNL} defined as the energy distance from the valence band maximum to the charge neutrality level (CNL) as shown in Fig. I-1(a). For energies above (below) the CNL, the interface states have acceptor (donor) characters as illustrated in Fig. I-1(b). Considering a p-type semiconductor, with hole Schottky barrier height (Φ^p_{SBH}), the interface charges (Q_{is}) formed as a result of the occupancy of the interface states (determined by relative position of E_F to CNL) is given by

$$Q_{is} = -qD_{is}(\Phi^p_{SBH} - \Phi^p_{CNL}) = -Q_m. \qquad \text{(I-1)}$$

If $\Phi^p_{SBH} > \Phi^p_{CNL}$, then the overall interface charge will be negative from Eq. (I-1), which agrees with Fig. I-1(b), and vice versa.

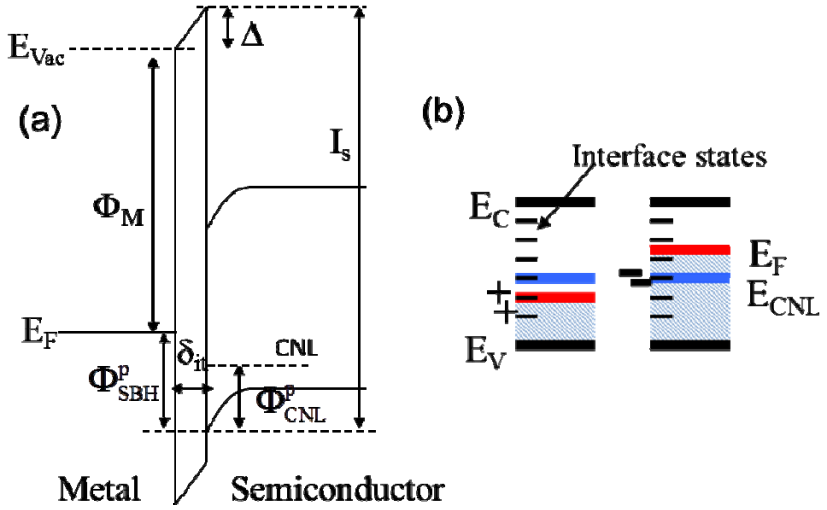

Fig. I-1: (a) Energy band diagram illustrating the concept of intrinsic gap states on interface dipoles; (b) Schematic illustrating how occupancy of the interface states affects the overall interface charges, Q_{is}. Note that the red and blue lines represent the Fermi level (E_F) and charge neutrality level (E_{CNL}), respectively.

Since the interface dipole, Δ, involves the separation of charges (i.e. by distance of δ_{it}), one can model it as a parallel plate capacitor:

$$q\Delta = Q/C = q(qD_{is})(\Phi^{p}_{SBH} - \Phi^{p}_{CNL})(\delta_{it}/\varepsilon_{it}), \quad \text{(I-2)}$$

whereby ε_{it} is the permittivity at the interface and δ_{it} is the width of the interface region. From the band diagram, it can be seen that to maintain energy conservation,

$$\Phi^{p}_{SBH} = I_s - \Phi_m - q\Delta. \quad \text{(I-3)}$$

By combining Eqs. (I-2) and (I-3), one is then able to derive the MIGS equation,

$$\Phi^{p}_{SBH} = S(I_s - \Phi_m) + (1-S)\Phi^{p}_{CNL}, \quad \text{(I-4)}$$

whereby $S = (1+(q^2\delta_{it}D_s/\varepsilon_{it}))^{-1}$. The physical implication of this equation is that for a large amount of D_{is}, S approaches zero (i.e. Bardeen limit), while for small values of D_{is}, S approaches one (i.e. Schottky-Mott limit). On the other hand, a higher permittivity, ε_{it}, S is increased (closer to Schottky-Mott limit), due to increased screening effect of the interface dipole, Δ.

The pinning parameter, S is dependent on both the densities of states (D_s) and the width of the interfacial region (δ_{it}) which can be approximated by the charge decay length, given by ($1/2q_s$). These two parameters can be calculated using theoretical approaches.

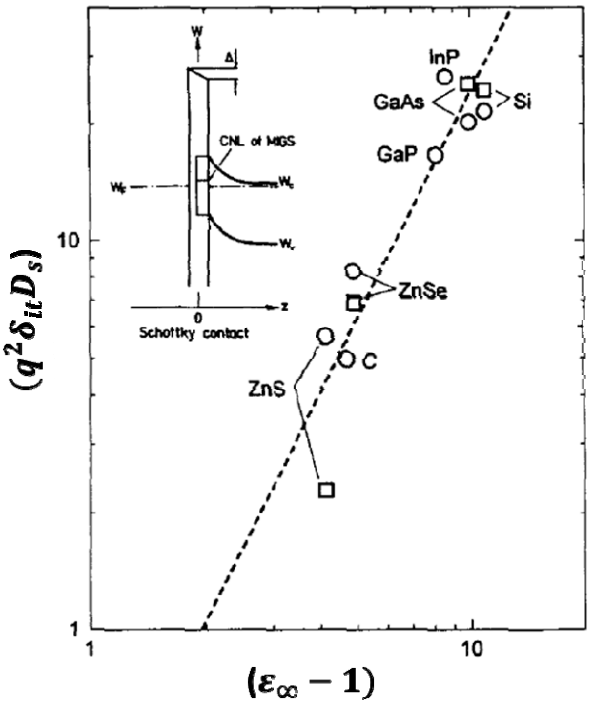

Fig. I-2: Theoretical values of $(q^2\delta_{it}D_s/\varepsilon_{it})$ as a function of the experimental electronic susceptibilities. These data are obtained from ref. 213.

Figure I-2 shows the product of these two parameters as a function of the experimentally obtained electronic susceptibilities, i.e. $\varepsilon_\infty - 1$. It is seen that one can obtain a semi-empirical relationship using a least-squares fit of the data, i.e. $(q^2 D_s / 2q_s) \propto (\varepsilon_\infty - 1)^{1.91\pm0.24}$.[213] Since 1.91 is close to 2, this forms the basis justifying the semi-empirical relationship, i.e.

$$S = \frac{1}{1 + 0.1(\varepsilon_\infty - 1)^2}. \qquad \text{(I-5)}$$

Appendix II: Calibration of Omicron EFM3

The Omicron EFM3 is equipped with a flux monitor which can be used to determine the deposition thickness. This requires, however, prior calibration through the measurement of the actual thickness using the quartz crystal modulator (QCM). The rod to sample distance is kept fixed at 22 cm in our depositions. Figure II-1(a) shows a plot of the deposition rate versus flux at different filament currents. It is seen that the deposition rate varies even for the same flux under different filament current. As such, we fix the filament current (i.e. at 1.3 A) for all our depositions. Figure II-1(b) shows that the deposition thickness varies linearly with time for a fixed flux of 1.3 A.

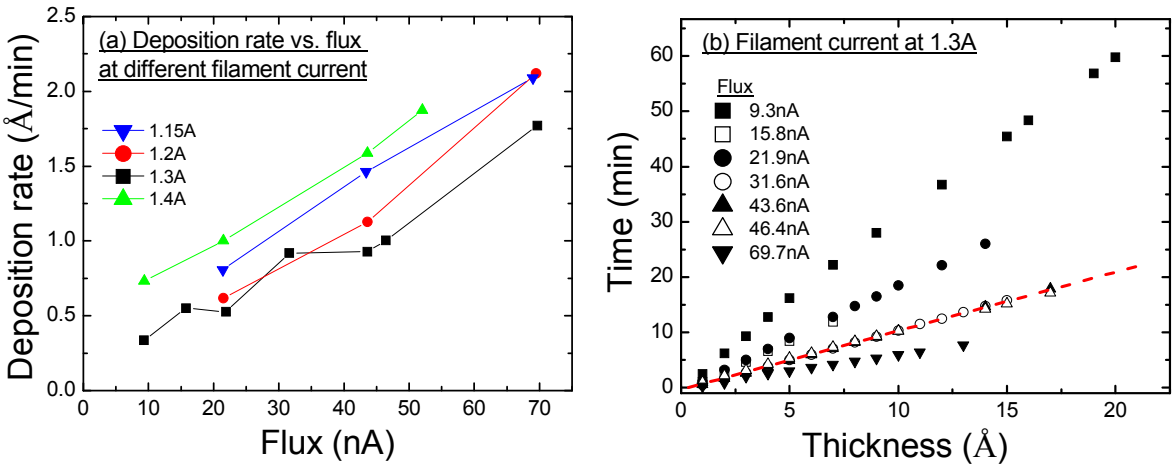

Fig. II-1: Calibration plots of (a) deposition rate vs. flux at different filament current and (b) deposition time vs. thickness, given a fixed filament current of 1.3 A.

In this study, we choose a deposition flux of 31.6 nA under filament current of 1.3 Å because it is able to give a reasonably sufficiently high and stable deposition rate. This rate is calculated to be ~0.96 Å/min from the slope (red dotted line in Fig. II-1 (b)).

Appendix III: Attenuation equations

Consider an overlayer film on a substrate as shown in Fig. III-1.

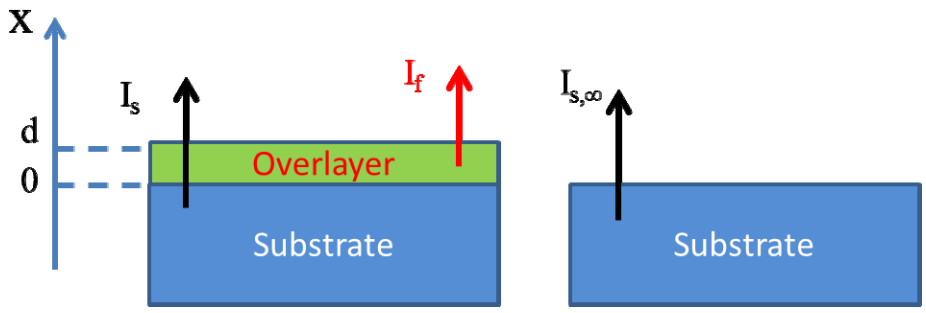

Fig. III-1: Simple diagram to consider the attenuation of photoemission signals, where I_f represents the signals from the overlayer film, and I_s represents the signals from the substrate film. Note that $I_{s,\infty}$ represents the signal from an infinitely thick substrate, i.e. without any overlayer film.

The intensity from a thin film with thickness, d, is given by

$$I_f = k\int_0^d FD\sigma y \exp(-x/\lambda_f \cos\theta)dx. \qquad \text{(III-1)}$$

where

k: spectrometer factor including transmission function of the analyzer and electron detection efficiency

F: X-ray flux

D: Atomic density of the element contributing to the photoemission peak

σ: Photoionization efficiency of the sample

y: Efficiency of sample to produce electrons of characteristic energy without energy loss due to, e.g. plasmons

λ_f: Mean free path of photoelectrons from the film

θ: Angle between the sample normal and emission direction of analyzed electrons

By integrating Eq. (III-1) and replacing the constants with $I_{f,\infty} = kFD\sigma y\lambda_f$, one can obtain the expression for the intensity of the film photoelectron signal as:

$$\begin{aligned} I_f &= k\int_0^d FD\sigma y \exp(-x/\lambda_f \cos\theta)dx \\ &= I_{f,\infty}\int_0^d \exp(-x/\lambda_f \cos\theta)dx \\ &= I_{f,\infty}[1-\exp(-d/\lambda_f \cos\theta)]. \end{aligned} \quad \text{(III-2)}$$

Similarly, the substrate signals can simply be expressed as the attenuation of the signal of an infinitely thick substrate, $I_{s,\infty}$ by the overlayer film of thickness, d,

$$I_s = I_{s,\infty} \exp(-d/\lambda_s \cos\theta). \quad \text{(III-3)}$$

Taking the ratios of Eqs. (V-2) and (V-3) and because $\lambda_f = \lambda_s$, one obtains

$$\frac{I_f}{I_s} = \frac{I_{f,\infty}}{I_{s,\infty}}[\exp(d/\lambda_s \cos\theta) - 1]. \quad \text{(III-4)}$$

Arranging the terms, the thickness of the overlayer film can then be derived as

$$d = \lambda_s \cos\theta . \ln(1 + \frac{I_{f,}}{I_s}\frac{I_{s,\infty}}{I_{f,\infty}}). \quad \text{(III-5)}$$

Appendix IV: Interpretation and selection of relevant core level peaks

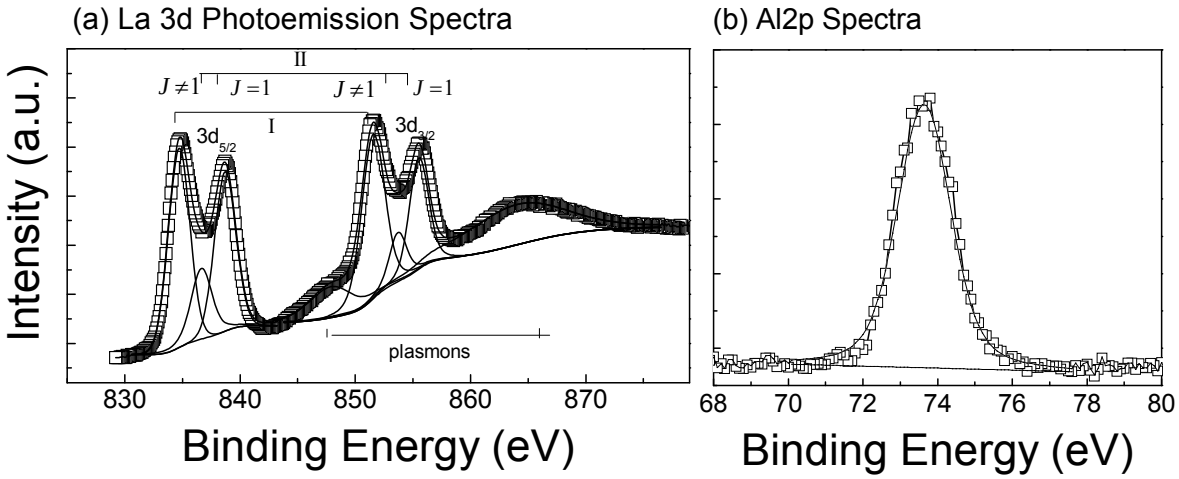

Fig. IV-1: High-energy resolution XPS narrow scans showing (a) La3d and (b) Al2p spectra. Due to many-body effects, the La3d photoelectron spectrum shows multiplet splitting; two final states I La^{4+} $3\underline{d}^{1}4f^{0}$ and II La^{3+} $3\underline{d}^{1}4f^{1}$ are created (satellite peaks). Due to electron-hole exchange for the satellite peaks, $J = 1$ term (strong signal) and $J \neq 1$ (a cluster of weak signals) can be observed. The spin-orbit split peak, which is separated by ~17 eV is also observed. In addition, two plasmon peaks can be identified.

Correct interpretation and selection of appropriate orbitals are necessary in order to obtain reliable information from the XPS spectrums. This is especially important for elements such as rare earth metals (i.e. lanthanum in LAO/Si and LAO/Ge heterostructures used in this study) because of the presence of various satellite peaks that complicate their spectrums. Figure IV-1 shows the (a) La 3d and (b) Al 2p photoemission spectrums of a thick (~15 nm) LAO sputtered film. At this thickness, these spectrums represent the bulk oxide film because the photoelectrons from the underlying substrate cannot escape due to their small mean free path. The Al 2p peaks have binding energy (BE) at ~73.6 eV with a full width at half maximum (FWHM) of ~1.7 eV, while $La3d_{5/2}$ peaks have BE of ~835 eV with a FWHM of ~2 eV.

It might be useful to briefly account for the many peaks for the La 3d spectra seen in Fig. IV-1, which is a result of many body effects observed in lanthanide compounds. In the photoionization of the 3d core level of La compounds, two final states, **I** La^{4+} $3\underline{d}^{1}4f^{0}$ and **II** La^{3+} $3\underline{d}^{1}4f^{1}$, are created.[183] While both final states have a core hole in the 3d orbital, the final state **II** (satellite) has a transfer of an electron from the O_{2p} valence band to an empty 4f orbital in La. Furthermore, the spin-orbit coupling creates a doublet peak (j = 3/2 and 5/2) with a core-level separation of ~17 eV for each final state. Finally, due to electron-hole exchange coupling, besides the stronger signal from the $J = 1$ term, there exists clusters of weaker signals (i.e., $J \neq 1$ term) with different total spins, resulting in a centroid located at a lower binding energy as compared to the $J = 1$ line.[184] In this dissertation, the La $3d_{5/2}$ peak (satellite **I**) is chosen to represent the $LaAlO_3$ and La_2O_3 films since the background of the $La3d_{3/2}$ peak is more affected by the two plasmon peaks. On the other hand, other orbitals, such as the La 4d spectrum, are not preferred due to their lower intensity and presence of additional multiplet coupling effects.

Next, we consider the core level peaks used to represent the substrate in this study. Amongst the orbitals with sufficient photoionization cross section (Ge 2p, Ge 3p and Ge 3d), Ge $3d_{5/2}$ is chosen to represent the underlying substrate for the VBO measurement of LAO/Ge. Photoelectrons from the Ge 2p orbitals are not used because these have a much lower mean free path than Ge 3d, resulting in low intensity when the overlayer films are thicker than ~4 nm. The Ge 3p photoelectron spectrum suffers from smaller signal-to-noise ratio as compared to that of Ge 3d due to the higher background signals. In addition, the overall

spectrum line shape of Ge 3p is harder to deconvolute due to the relatively large FWHM of ~2.3 eV for each of its doublets, which are spaced 4 to 5 eV apart. As such, it is difficult in this case to distinguish chemical shifts of the interfacial layer that are typically 2 to 3.3 eV. Although Ge 3d peaks are located at a low BE (~30 eV), these do not exhibit significant hybridization effects in our work. This is because the substrate signals have a narrow and consistent FWHM of ~0.7 eV without the presence of additional satellite features that will presumably result from hybridization. On the other hand, the Si 2p photoelectron peak is chosen to represent the substrate in the VBO measurement of LAO/Si since it has the highest intensity. However, to obtain chemical information for LAO/Si samples, Si 2s spectrum is used instead since the SiO components of Si 2p overlap with the La 4d spectrum.

Appendix V: Derivation of interface dipole using intrinsic gap states models

Due to the explicit dependence of the dipole on the magnitude of the final Schottky barrier height (SBH) (see Eq. (I-2)), the gap states model (i.e. MIGS model) dictates that the system behaves like a negative feedback to dampen the changes in the metal work function. Manipulating Eq. (I-2) to make Δ the subject matter and replacing Φ_{SBH}^{p} using Eq. (I-3) , it is seen that:

$$\begin{aligned}\Delta &= (D_{is})(\Phi_{SBH}^{p} - \Phi_{CNL}^{p})(\delta_{it} / \varepsilon_{it}) \\ &= (1-S)(I_s - \Phi_{CNL}^{p} - \Phi_m - \Delta) / S \\ &= (1-S)(\Phi_{CNL}^{Vac} - \Phi_m - \Delta) / S. \\ S\Delta &= (1-S)(\Phi_{CNL}^{Vac} - \Phi_m) - (1-S)\Delta,\end{aligned} \tag{V-1}$$

whereby $q^2\delta_{it}D_s / \varepsilon_{it} = (1-S)/S$ and $\Phi_{CNL}^{Vac} = I_S - \Phi_{CNL}^{p}$. Rearranging, one obtains

$$\Delta = (1-S)(\Phi_{CNL}^{Vac} - \Phi_m). \tag{V-2}$$

This derivation highlights the underlying concept behind this model, i.e. that the intrinsic dipole is governed by the charge transfer due to work function difference, mediated by the slope parameter. This is analogous to the contact potential difference between two metals. A similar derivation can be shown for the case of a semiconductor/oxide heterojunction, in which:

$$\Delta = (1-S)(\Phi_{CNL,semi}^{Vac} - \Phi_{CNL,oxide}^{Vac}). \tag{V-3}$$

List of Publications

Publications related to work in this thesis

1. Z. Q. Liu, S. Y. Chiam, W. K. Chim, J. S. Pan, and C. M. Ng, "Effects of thermal annealing on the band alignment of lanthanum aluminate on silicon investigated by X-ray photoelectron spectroscopy" *J. Appl. Phys*. **106**, 103718 (2009).

2. Z. Q. Liu, S. Y. Chiam, W. K. Chim, J. S. Pan, and C. M. Ng, "Thermal stability improvement of the lanthanum aluminate/silicon interface using a thin yttrium interlayer", *J. Electrochem. Soc*. **157**, G250-257 (2010).

3. Z. Q. Liu, W. K. Chim, S. Y. Chiam, J. S. Pan, and C. M. Ng, "Ambiguity of the magnitude and direction of the derived interface dipole at lanthanum aluminate heterostructures using photoemission techniques", *J. Appl. Phys.* **109**, 093701 (2011).

4. Z. Q. Liu, W. K. Chim, S. Y. Chiam, J. S. Pan, and C. M. Ng, "Evaluating the use of electronegativity in band alignment models through the experimental slope parameter of lanthanum aluminate heterostructures", *J. Appl. Phys*. **110,** 093701 (2011).

5. Z. Q. Liu, W. K. Chim, S. Y. Chiam, J. S. Pan, and C. M. Ng, "Formation of the yttrium / germanium interface: Fermi-level pinning and intermixing at room temperature", *Appl. Phys. Lett*. **100,** 092110 (2012).

6. Z. Q. Liu, W. K. Chim, S. Y. Chiam, J. S. Pan, and C. M. Ng, "Interface dipole predictive model for high-k dielectric/semiconductor heterostructures using the concept of dipole neutrality point", *J. Mater. Chem.* **22**, 17887 (2012).

7. Z. Q. Liu, W. K. Chim, S. Y. Chiam, J. S. Pan, S. R. Chun, Q. Liu, and C. M. Ng, "Interfacial-layer-free growth of yttrium oxide on germanium by understanding initial surface reactions", *Surf. Sci.* **606**, 1638 (2012).

8. Z. Q. Liu, W. K. Chim, S. Y. Chiam, J. S. Pan, and C. M. Ng, "Band gap, band offsets and dielectric constant improvements by addition of yttrium into lanthanum aluminate", *Thin Solid Films* submitted (2012).

9. S. Y. Chiam, Z. Q. Liu, J. S. Pan, K. K. Manippady, L. M. Wong, and W. K. Chim, "Effects of electric field in band alignment measurements using photoelectron spectroscopy", *Surf. Interface Anal., ECASIA special issue paper,* 2011. doi: 10.1002/sia.3851.

Other publications

10. C. Pi, Y. Ren, Z. Q. Liu, and W. K. Chim, "Unipolar Memristive Switching in Yttrium Oxide and RESET current reduction using a yttrium interlayer", *Electrochem. and Solid-State Lett*., **15** (3), G5-7 (2012).

11. H. L. Qin, Z. Q. Liu, C. Troadec, K. E. Johnson Goh, M. Bosman, B. S. Ong, S. Y. Chiam, K. L. Pey, "Barrier height determination of Au/Oxidized Ga As/n-GaAs using ballistic electron emission spectroscopy" *J. Vac. Sci. Tech. B* **30** (1), 011805 (2012).